Workshop on Polarized Electron Sources and Polarimeters

October 1 -3, 2008
Jefferson Lab, Newport News, VA 23606 USA
Organizers: J. Grames, M. Stutzman, R. Suleiman, M. Poelker

Published in the Proceedings of the 18th International Spin Physics Symposium (SPIN 2008, Charlottesville, Virginia, USA), edited by D. Crabb et al., AIP Conference Proceedings 1149, Melville, New York 2009.

Workshop on Polarized Electron Sources and Polarimeters

Status Report of the New Darmstadt Polarized Electron Injector…
Y. Poltoratska, R. Barday, U. Bonnes, M. Brunken, C. Eckardt, R. Eichhorn, J. Enders, C. Heßler, C. Ingenhaag, W. F. O. Müller, M. Platz, M. Roth, B. Steiner, M. Wagner, and T. Weiland - *Page 983*

Status of 200keV Beam Operations at Nagoya University ….
M. Yamamoto, T. Konomi, S. Okumi, Y. Nakagawa, N. Yamamoto, M. Tanioku, X. Jin, T. Ujihara, Y. Takeda, F. Furuta, H. Matsumoto, M. Yoshioka, M. Kuriki, C. Shonaka, and T. Nakanishi - *Page 987*

Recent Polarized Photocathode R&D at SLAC and Future Plans…
F. Zhou, A. Brachmann, T. Maruyama, and J. C. Sheppard - *Page 992*

High Intensity Polarized Electron Gun Studies at MIT-Bates…
E. Tsentalovich - *Page 997*

Atomic Hydrogen Cleaning of Superlattice Cathodes….
V. Tioukine, K. Aulenbacher, and E. Riehn - *Page 1002*

Ultra Cold Photoelectron Beams for Ion Storage Rings….
D. A. Orlov, C. Krantz, A. Shornikov, M. Lestinsky, J. Hoffmann, A.S. Jaroshevich, S.N. Kosolobov, A.S. Terekhov, and A. Wolf - *Page 1007*

Optimization of Semiconductor Superlattice for Spin-Polarized Electron Source…
L. G. Gerchikov, Yu. A. Mamaev, V. V. Kuz'michev, Yu. P.Yashin, V. S. Mikhrin, A. P. Vasiliev, and A. E. Zhukov - *Page 1017*

Study of the Activated GaAs Surface for Application as an Electron Source in Particle Accelerators…
N. Chanlek, J.D. Herbert, L.B. Jones, R.M. Jones, and K.J. Middleman - *Page 1022*

Recent Progress toward Robust Photocathodes…
G. A. Mulhollan and J. C. Bierman - *Page 1027*

Surface Analysis of Damaged Superlattice Photocathode…
M. L. Stutzman and J. Grames - *Page 1032*

Polarized Photocathode Development at SVT Associates….
Aaron Moy, T. Maruyama, F. Zhou and A. Brachmann - *Page 1038*

High Brightness Electron Source Using a Superlattice Photocathode with Long Life NEA-Surface….
T. Nishitani, M. Tabuchi, Y. Takeda, Y. Suzuki, K. Motoki, and
T. Meguro – *Page 1047*

High Brightness and High Polarization Electron Source Using Transmission Photocathode…
N. Yamamoto, X. Jin, A. Mano, Y. Nakagawa, T. Nakanishi,
T. Ujihara, S. Okumi, M. Yamamoto, T. Konomi, Y. Takeda,
T. Ohshima, T. Saka, T. Kato, H. Horinaka, T. Yasue, and
T. Koshikawa – *Page 1052*

Cooled Transmission-Mode NEA-Photocathode with Band-Graded Active Layer for High–Brightness Electron Source…
L. B. Jones, S. A. Rozhkov, V. V. Bakin, S. N. Kosolobov,
B. L. Militsyn, H. E. Scheibler. S. L. Smith, and A. Terekhov - *Page 1057*

K2CsSb Photocathodes…
John Smedley, Triveni Rao, and E. Wang - *Page 1062*

Photoemission Spectroscopic Study of Cesium Telluride Thin Film Photocathode…
H., K. Ogawa, Junpei Azuma, K. Takahashi, and M. Kamada - *Page 1067*

Status Jefferson Lab FEL High Voltage Guns…
C. Hernandez-Garcia, S. V. Benson, G. Biallas, D. Bullard,
P. Evtushenko, K. Jordan, M. Klopf, D. Sexton, C. Tennant,
R. Walker, and G. Williams - *Page 1071*

Status Cornell High Voltage Gun…
K. Smolenski, I. Bazarov, B. Dunham, H. Li, Y. Li, X. Liu,
D. Ouzounov, and C. Sinclair - *Page 1077*

Status of the ALICE Energy-Recovery Linac…
L. Jones, S. P. Jamison, Y. M. Saveliev, K. J. Middleman, and
S. L. Smith - *Page 1084*

Photocathode Preparation System for the ALICE Photoinjector Gun…
K. J Middleman, I. Burrows, R. Cash, B. Fell, L.B. Jones,
J. McKenzie, B. Militsyn, and A.S. Terekhov - *Page 1089*

Development of an Electron Gun for an ERL Based Light Source in Japan…
N. Nishimori, R. Nagai, H. Iijima, Y. Honda, T. Muto, M. Kuriki, M Yamamoto, S. Okumi, T. Nakanishi, and R. Hajima - *Page 1094*

KSI's Cross Insulated Core Transformer Technology…
Uwe Uhmeyer - *Page 1099*

Low Emittance Gun for XFEL Application…
C. Gough, M. Paraliev and S. Ivko - *Page 1104*

Ion Bombardment in RF Guns: Analytical Approach…
E. Pozdeyev, D. Kayran, and V. N. Litvinenko - *Page 1109*

High-Fidelity RF Gun Simulations with the Parallel 3D Finite Element Particle-In-Cell Code Pic3P…
A. Candel, A. Kabel, L. Lee, Z. Li, C. Limborg, C. Ng,
G. Schussman, and K. Ko - *Page 1114*

The Superconducting RF Photoinjector at Elbe – First Operational Experience…
J. Teichert, A. Arnold, H. Büttig, D. Janssen, M. Justus,
U. Lehnert, P. Michel, P. Murcek, A. Schamlott, C. Schneider,
R. Schurig, F. Staufenbiel, R. Xiang, T. Kamps, J. Rudolph, M. Schenk, G. Klemz, and I. Will - *Page 1119*

Measurements of the Rossendorf SRF-Gun Cavity Characteristics…
A. Arnold, H. Büttig, D. Janssen, M. Justus, T. Kamps, G. Klemz,
U. Lehnert, P. Michel, K. Möller, P. Murcek, J. Rudolph,
A. Schamlott, M. Schenk, Ch. Schneider, R. Schurig,
F. Staufenbiel, J. Teichert, V. Volkov, I. Will, and R. Xiang - *Page 1125*

The BNL Polarized SRF gun…
J. Kewisch, I. Ben-Zvi, T. Rao, A. Burril, D. Pate, E. Wang,
R. Todd, H. Bluem, D. Holmes, and T. Schultheiss - *Page 1133*

NEG Pump Technology…
P. Manini - *Page 1138*

Ultrahigh Vacuum Ion Pump Power Supply with Sensitive Current Monitoring Capability…
J. Hansknecht, P. Adderley, M. L. Stutzman and M. Poelker - *Page 1143*

High Brightness and High Polarization PES for SPLEEM and/or High Brightness PES with Transmission Photocathode…
T. Nakanishi, N. Yamamoto, A. Mano, Y. Nakagawa, T. Konomi, M. Yamamoto, S. Okumi, X. Jin, T. Ujihara, Y. Takeda, T. Ohshima, T. Kohashi, T. Yasue, T. Koshikawa, T. Saka, and T. Kato - *Page 1148*

Ab Initio Calculation of Effective Sherman Function in MeV Mott Scattering…
K. Aulenbacher and V. Tioukine - *Page 1155*

Compton Polarimeter at Bonn….
W. Hillert, B. Aurand, and J. Wittschen - *Page 1160*

Hall A Compton Polarimeter – DC Green Light and Optical Storage Cavity…
A. Rakhman, S. Nanda, P. Souder - *Page 1165*

Polarimetry and Planned Experiments at the Superconducting Darmstadt Electron Linac S-DALINAC…
C. Eckardt, R. Barday, U. Bonnes, M. Brunken, R. Eichhorn, J. Enders, C. Heßler, W. F. O. Müller, M. Platz, Y. Poltoratska, B. Steiner, M. Wagner, and T. Weiland - *Page 1170*

Benchmark Studies Among Own and Commercial Beam Tracking Codes on Fundamental Conditions…
N. Yamamoto, A. Mizuno, K. Masuda, K. Kan, S. Matsumoto, and M. Yamamoto - *Page 1174*

3D Modeling of the ALICE Photoinjector Upgrade…
J.W. McKenzie, B.L. Militsyn, and Y.M. Saveliev - *Page 1179*

Polarized Positron Source at Jefferson Lab….
J. Dumas, J. Grames, E. Voutier - *Page 1184*

Summary Report of PESP2008 -The Workshop on Polarized Electrons and Polarimeters….
M. Poelker - *Page 1189*

Status Report of the New Darmstadt Polarized Electron Injector

Y. Poltoratska*, R. Barday*, U. Bonnes*, M. Brunken*, C. Eckardt*, R. Eichhorn*, J. Enders*, C. Heßler*, C. Ingenhaag*, W.F.O. Müller†, M. Platz*, M. Roth*, B. Steiner†, M. Wagner* and T. Weiland†

*Institut für Kernphysik, Technische Universität Darmstadt, Germany
†Institut für Theorie Elektromagnetischer Felder, Technische Universität Darmstadt, Germany

Abstract. We present the status of the polarized injector for the superconducting Darmstadt electron linear accelerator S-DALINAC. An offline teststand of the source was built to test all components of the S-DALINAC polarized injector SPIN. The new electron source will deliver a 100 keV polarized beam and complement the present thermionic source operating at 250 kV. Results of the beam properties measurements will be introduced and an outlook on the upcoming installation of the new injector at the S-DALINAC will be given.

Keywords: S-DALINAC, strained superlattice GaAs, Mott polarimeter, Wien filter
PACS: 85.60.Ha, 79.60.-i, 29.27.Hj

INTRODUCTION

The superconducting Darmstadt electron linear accelerator S-DALINAC [1] is one of very few electron accelerators devoted to nuclear structure physics, including electron-scattering experiments. To complement the present scientific programm with the experiments that are focused on the investigation of violation of parity in the nuclei and breakup reactions of light nuclei [2] the new S-DALINAC Polarized injector (SPIN) was designed. It will provide - complementary to the existing 250 kV thermionic electron gun 100 keV polarized beams with polarization of 80 %, a mean current of 60 μA and 3 GHz cw or subharmonic time structure. The concept of the MAMI Gun [3] was used as a starting point for SPIN. To test the new developed polarized electron source independently from the operation of the S-DALINAC, an standalone teststand has been developed. In this contribution we describe the current status of the teststand and present the results of the measurements of the different beam properties.

TEST STAND OF THE POLARIZED INJECTOR

Figure 1 shows an schematic overview over the teststand of the polarized injector. The electrons are produced at a GaAs cathode by photoemission. As cathode material the strained superlattice crystals [4] are foreseen to achieve high degrees of polarization of more than 80%. Due to the limited space in the accelerator hall a very compact source had to be constructed, and major modifications from the Mainz design were necessary. One spin direction is selected by using circularly polarized light from diode laser system

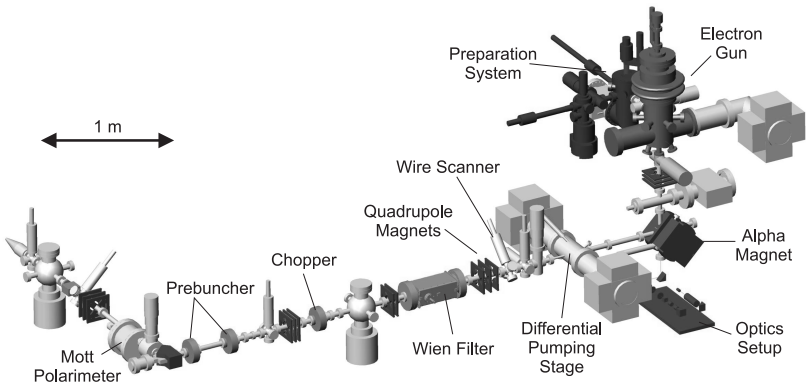

FIGURE 1. Schematic drawing of the teststand.

below the electron source focussed onto the photocathode surface. The photocathode crystal is installed at the front end of a highly polished stainless-steel electrode. The form of the electrode was designed following numerical simulations [5] and deviates from usual Pierce geometry [6]. To extract the electrons from the conduction band of the cathode crystal to the vacuum negative electron affinity (NEA) is needed. Therefore prior to installation into the cathode chamber the cathode is cleaned and activated by depositing thin CsO layer in a separate preparation chamber. With the aid of a load-lock system the photocathode activation can be handled quickly.

Afterwards the emitted electrons are accelerated electrostatically to an energy of 100 keV and injected by an alpha magnet into a horizontal beamline, where the beam properties are measured with various diagnostic elements. It is indispensable to create an ultra high vacuum conditions in the gun chamber to prevent a fast degradation of the NEA surface. After bake-out during 12 days at 220° C an end pressure of $< 2 \cdot 10^{-11}$ mbar has been achieved using non-evaporable getter (NEG) and ion-getter pumps.

Transverse beam quality

The transverse beam properties can be investigated qualitatively by fluorescent screens and quantitatively by a wire scanner [7]. The transverse emittance is determined by measuring of the beam radius for different focussing strengths of a solenoid preceding the wire scanner. The normalized transverse emittance has been determined to $\varepsilon_{n,x} = (0.146 \pm 0.037)$ mm mrad and $\varepsilon_{n,y} = (0.197 \pm 0.089)$ mm mrad, respectively.

Time Structure

The produced polarized electron beam needs to be modulated with the frequency of the S-DALINAS's superconducting cavities of 3 GHz for cw operation. This is achieved by modulating a laser diode [8]. The time structure was verified for the laser beam

with a fast sensor and for the electron beam with an ultra-fast coaxial Faraday cup. For the capturing process of the beam into the superconducting accelerating structures the electron-bunch length need to be of the order of 5 ps. Therefore a new chopper and prebuncher system has been developed, based on a similar setup at MAMI [9].

Polarization manipulation and measurement

The degree of polarization of 100 keV electrons for the teststand is measured with a Mott polarimeter detecting count-rate asymmetries in electron scattering on nuclei due to the spin-orbit interaction. The asymmetry occurs only when the electron spin direction is not parallel to the scattering plane. Thus the initially longitudinal oriented spins must be rotated by 90° into the transverse direction. This is done by a Wien filter [10]. This device is also necessary tool for adjusting the spin orientation at different experimental areas of the S-DALINAC.

The ideal Wien filter acts as a drift space in the vertical plane, but its horizontal electron-optical properties are similar to those of a quadrupole: It focusses the electron beam. This effect was minimized: the focus has been set inside the filter with help of newly designed compact quadrupole triplet in front of the Wien filter. An additional quadrupole doublet installed after the device compensates its influence on the beam. The installed spin rotator can provide 100 degree spin rotation.

The 100 keV Mott polarimeter [11] houses 4 silicon-surface-barrier detectors which are oriented in two perpendicular scattering planes to measure both transverse polarization components simultaneously. As targets self-supporting gold foils of the thickness in the range from 42.5 nm to 500 nm are utilized. The polarimeter contains also a BeO viewer to control the beam position and one empty target for background measurements. The scattering angle of $(120 \pm 1.5)^\circ$ is determined by an aluminum collimator with 2 mm diameter. This angle matches the broad maximum of the analyzing power or so-called Sherman function at this angle. The typical energy resolution of the detector is

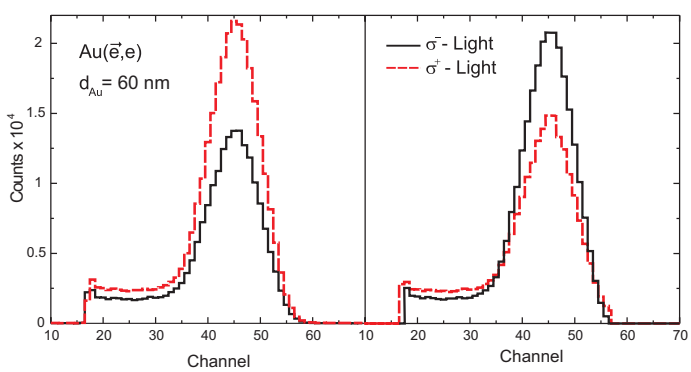

FIGURE 2. Measurement of Mott spectra with the two detectors of a scattering plane for reversing electron helicities. The helicity can be switched by reversing the polarization of the laser light.

about 20 keV and the peak-to-background ratio is found to be 14 : 1 for the 122 nm gold foil. The polarization of the electrons can be switched from parallel to antiparallel to the electron momentum by changing the incident light helicity.

To be independent from possible instrumental asymmetries two different measurements with opposite beam polarization must be performed.Typically measured spectra are shown in Fig. 2. From the measured data a degree of polarization was determined to be $(33.4 \pm 1.6)\%$ for bulk GaAs cathode and $(86 \pm 3)\%$ for strained superlattice cathode. Thereby the finite target thickness was taken into account by performing an extrapolation procedure to zero target thickness. A detailed explanation is given in reference [12].

SUMMARY AND OUTLOOK

In this paper we showed that the teststand for the S-DALINAC polarized injector has successfully been set up and put into operation. The measured transverse beam properties is comparable with others electron sources and the measured degrees of polarization for different cathode types is in good agreement with the literature. The next steps are the test of the chopper and prebuncher systems and implementation of the source at the S-DALINAC [13].

ACKNOWLEDGMENTS

We would like to thank K. Aulenbacher for useful discussions about Mott Polarimeter. Our thanks also due to SPIN 2008 organizing committee for financial support. This work is supported by the Deutsche Forschungsgemeinschaft through SFB 634.

REFERENCES

1. A. Richter, “Operational experience at the S-DALINAC”, EPAC’96, Sitges, 1996, p. 110.
2. C. Eckardt et al., these proceedings.
3. K. Aulenbacher et al., *Nucl. Instrum. Methods in Phys. Research A* **391**, 1997, p. 498.
4. Yu. A. Mamaev et al.,“Spin polarized electron transport and emission from strained semiconductor heterostructures”, SLAC-PUB-8391, 2000.
5. B. Steiner et al., “Recent Simulation Results of the Polarized Electron Injector (SPIN) of the S-DALINAC”, EPAC’06, Edinburgh, 2006 p. 2188.
6. D. Pierce and F. Meier, *Phys. Rev. B*, **13**, 1976, pp. 5484.
7. C. Eckardt, “Emittanzmessung an der Quelle spinpolarisierter Elektronen am S-DALINAC”, Diploma Thesis, TU Darmstadt, 2007, unpublished.
8. C. Heßler, “Commisioning of the offline-teststand for the S-DALINAC polarized injector SPIN”, EPAC’08, Genoa, 2008, p. 1476.
9. V. I. Shvedunov et al., “Design of a Prebuncher for Increased Longitudinal Efficiency of MAMI”, EPAC’96, Sitges, 1996, p. 1556.
10. B. Steiner et al.,“Wien filter as a spin rotator at low energy”, PAC’07, Albuquerqe, 2007, p.170.
11. Y. Poltoratska, “ Design and setup of a compact Mott polarimeter for the future S-DALINAC polarized injector”, Diploma thesis, Kharkiv Karazin National University and TU Darmstadt, 2005, unpublished.
12. R. Barday et al., “Electron beam polarimetry at S-DALINAC”, EPAC’08, Genoa, 2008 p. 1476.
13. Y. Poltoratska et al. “Polarized electrons in Darmstadt: recent developments”, these proceedings.

Status of 200keV Beam Operations at Nagoya University

M. Yamamoto[a], T. Konomi[a], S. Okumi[a], Y. Nakagawa[a], N. Yamamoto[b], M. Tanioku[b], X. Jin[b], T. Ujihara[b], Y. Takeda[b], F. Furuta[c], H. Matsumoto[c], M. Yoshioka[c], M. Kuriki[d], C. Shonaka[d], and T. Nakanishi[a]

[a]*Graduate School of Science, Nagoya University, Furo-cho, Chikusa-ku, Nagoya, Aichi, Japan 464-8602*
[b]*Graduate School of Engineering, Nagoya University, Furo-cho, Chikusa-ku, Nagoya, Aichi, Japan 464-8603*
[c]*High Energy Accelerator Research Organization (KEK), 1-1 Oho, Tsukuba, Ibaraki, Japan 305-0801*
[d]*Graduate School of Advanced Sciences of Matter, Hiroshima University, 1-3-1 Kagamiyama, Higashi-Hiroshima, Hiroshima, Japan 739-8530*

Abstract. We have developed a 200keV polarized electron source for generating high bunch charge of >3.2nC within ~1ns bunch duration for the International Linear Collider (ILC) and >7.7pC within 30ps bunch duration for a basic source study of an Energy Recovery Linac (ERL). In order to improve gun operation voltage and an operational lifetime, we have employed new electrode materials of molybdenum and titanium to eliminate field emission dark current, and restructured a beam transport vacuum systems. As a beam generation for the ERL, bunch charge of up to 28pC was generated by irradiating with sliced laser pulse trains. The details are described in this report.

Keywords: Electron source; Polarized beams; Vacuum systems
PACS: 29.25.Bx; 29.27.Hj; 07.30.Kf

200KEV GUN AND BEAM TRANSPORT SYSTEM

A 200-keV polarized electron source has been developed for generating highly polarized electron beams with high bunch charge for requirements of ILC [1]. Remaining problems of this source are photocathode QE lifetime in the condition with actual beam current of more than 50μA and stable gun high voltage operation.

An ultra high vacuum ($\leq 10^{-9}$ Pa) environment of a beam transport system as well as of the gun is important to maintain NEA surface during beam operation. In order to avoid vacuum increase due to outgassing from a beam dump, we have applied four NEG modules (WP950) and a 100 L/s ion pump to the beam dump system, and two NEG pumps (GP100MK5) to a differential pumping system (DPS). The vacuum pressure of the beam transport line is important information for a photocathode QE lifetime measurement. The DPS vacuum pressure was monitored by an extractor-type

vacuum gauge (AxTRAN X-11,ULVAC). By comparison of the DPS base pressure with and without NEG modules in a condition with 20μA beam dumping for ~10 minutes, the DPS base pressure of 1.2×10^{-9} Pa was increased to 1.7×10^{-9} Pa and 1.4×10^{-8} Pa, respectively.

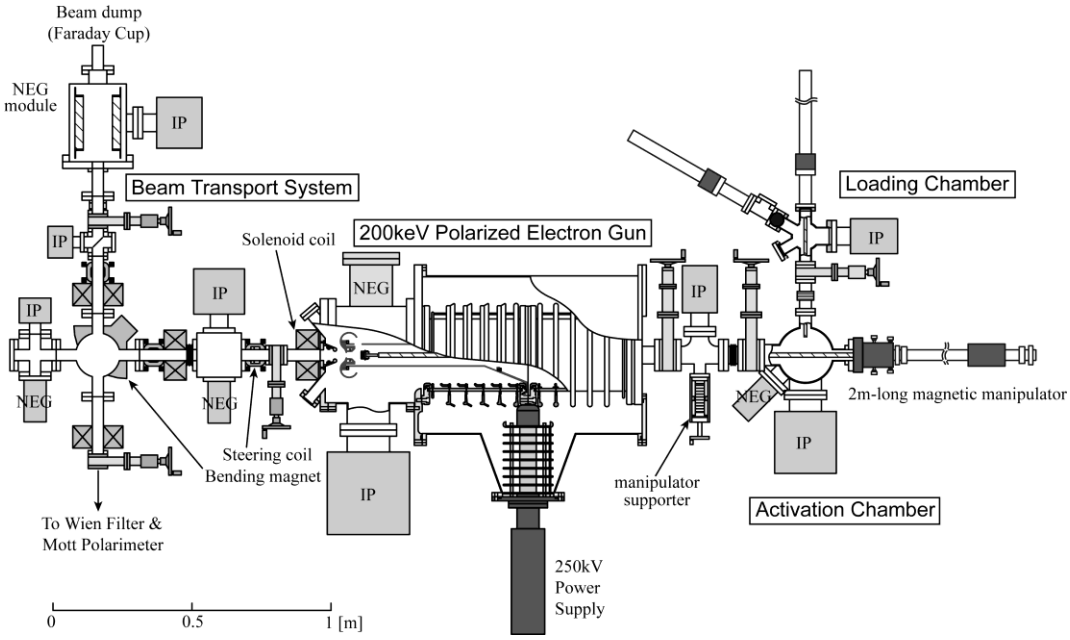

FIGURE 1. Schematic view of the 200keV polarized electron source and beam transport system.

To reduce the dark current in a high field gradient condition, we have employed a molybdenum cathode and titanium anode (Mo-Ti) [2]. A result of Mo-Ti electrode conditioning is shown in Fig. 2a.

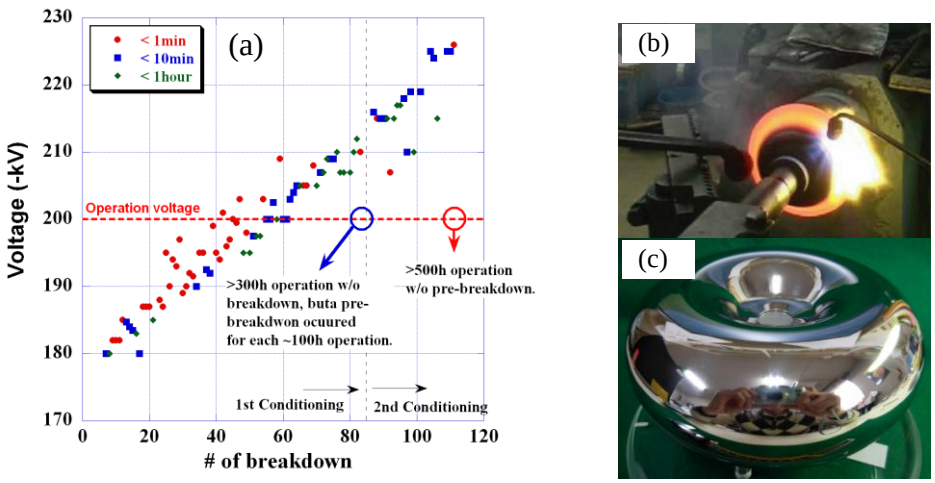

(b)

FIGURE 2. Result of electrode conditioning (a). Red circles, blue squares and green diamonds show high voltage duration less than 1 minute, 10 minutes and 1 hour respectively. The pictures show molybdenum cathode electrode fabrication processes of hot squeezing (b) and finished electrode (c).

The gradual increase of dark current observed before a breakdown in the SUS electrode was hardly detectable at a resolution of 1 nA, and breakdowns occurred

suddenly. Thus, HV-conditioning was performed repeatedly by increasing the bias voltage up to the previous breakdown voltage. The breakdown voltage grew by ~0.4 kV per discharge. No significant damage was observed on either the Mo or Ti surface after more than 100 discharges. This feature is a great advantage of the new electrode.

After the 80 conditionings, the breakdown voltage had grown to 215 kV, though the dark current remained below 1 nA for this surface state under 200-kV operation. However, a pre-breakdown phenomenon was observed for this surface at a rare rate of once per 100 hours, causing fatal damage to the PC surface. In order to avoid this problem, the conditioning voltage was increased to 225 kV, for which the pre-breakdown phenomenon completely disappeared for more than 500 hours at 200-kV operation.

LIFETIME MEASUREMENT AND 50μA BEAM OPERATION

A dark-lifetime for bulk-GaAs PC with a -200 kV bias voltage applied to the cathode was measured under a vacuum of 2.3×10^{-9} Pa in the gun chamber (Fig. 3a). The dark current of the 200 kV electrode was well suppressed to be less than 1nA level during the measurement. The QE was once decreased for about 10 hours after the NEA surface activated, and it gradually increased again in several tens hours until the measurement was stopped. The initial QE was maintained for several hundred hours, showing that the effects of dark current and residual molecules adsorption are sufficiently suppressed in our 200-keV gun.

An operational-lifetime was measured under this vacuum condition with an extraction current of 50 μA. The laser diameter on the photocathode was adjusted to be 1 mm to maintain high beam transportation efficiency to the beam dump, and then the transportation efficiency of 96% was obtained at this experiment. The result of the operational lifetime was shown in Fig. 3b. The initial DPS vacuum pressure $1.2\text{x}10^{-9}$ Pa was slightly increased to $2.8\text{x}10^{-9}$ Pa and the initial QE of 4.3% was decreased to 1/e value for ~120 hours.

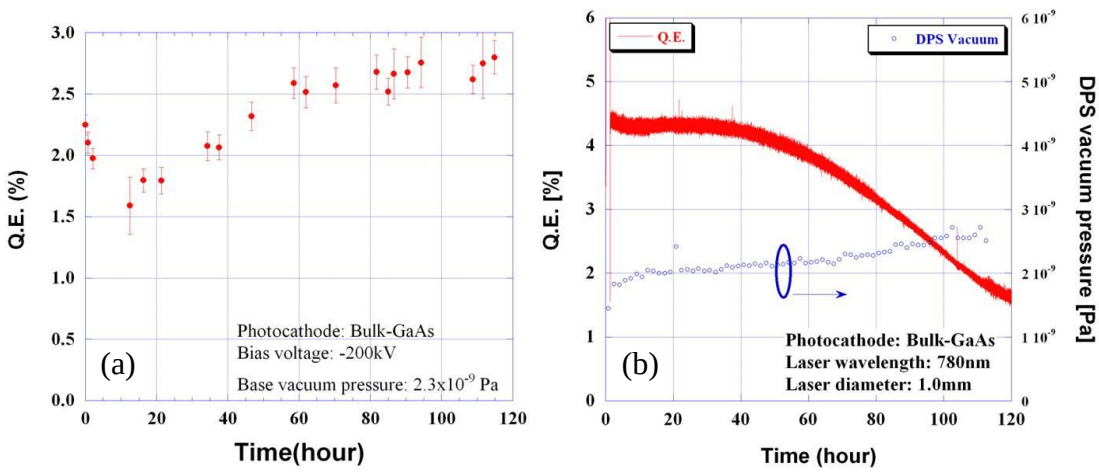

FIGURE 3. Results of dark-lifetime measurement with connecting beam transport line (a), and operational-lifetime measurement in the condition of 50μA constant beam current (b).

In order to research QE degradation behavior, a QE scan was done at the activation chamber. A laser light for scanning QE was transported by a single mode optical fiber and focused on ϕ 0.1 mm at the photocathode. The optical fiber system was fixed on the XY micro-motion stage and scanned for every 1 mm-steps for each direction. The Fig. 4a shows a flat QE distribution of 5~6% after NEA activation process, and Fig. 4b shows a degraded QE distribution after 50 μA beam operation. Comparing the data, it is clear that the damaged NEA surface region of ~ϕ10 mm is too large, while the electron emission area is considered to be as small as ϕ1 mm. It is presumed that the NEA damage is caused by back-bombardment not only by positive ions produced along the beam path between the HV electrodes but also by ions or outgases produced by the beam losses in the beam transport chambers [3,4].

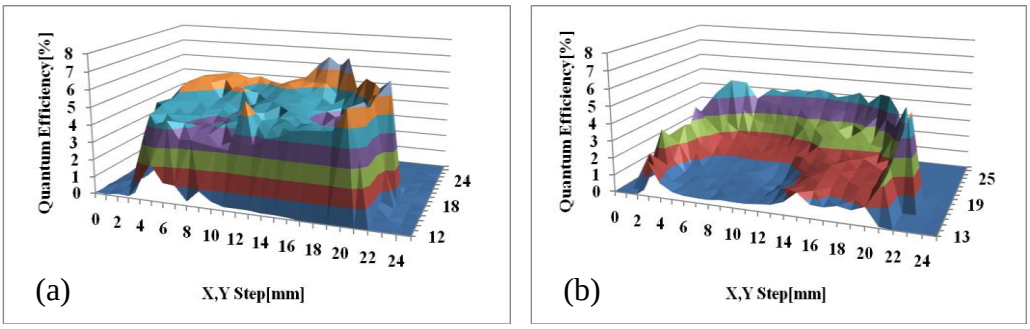

FIGURE 4. Result of QE scans after NEA activation (a) and 50μA beam operation (b).

PICO-SECOND BUNCH GENERATION

A high voltage DC-gun with an NEA-GaAs photocathode is considered to be major candidate to generate ultra-low emittance ($\varepsilon_{n.rms}$ < 1 mm.mrad) beams for the ERL. A pepper-pot (PP) method has been applied to measure the initial beam emittance of bulk-GaAs and GaAs-GaAsP superlattice photocathode by using the 200-keV gun system [5]. A duty factor controlled Ti:Sapphire mode-lock laser was employed because a thin film scintillator of the PP system is easy to charge up and to be damaged by a discharging under the beam average current of the order of more than micro-amperes. The Ti:Sapphire mode-lock (frequency of 81.25 MHz) laser output was sliced out 6.3 μs width with 20 Hz repetition. Since the rise and fall time of the pockels cell is less than 30 ns, less than 5 imperfect pulses contained in one sliced pulse-train which consists of ~500 pulses. By irradiating these sliced pulse trains with pulse length of ~30 ps and wavelength of 807 nm, the bunch charge of 28 pC could be generated from the gun (Fig. 5).

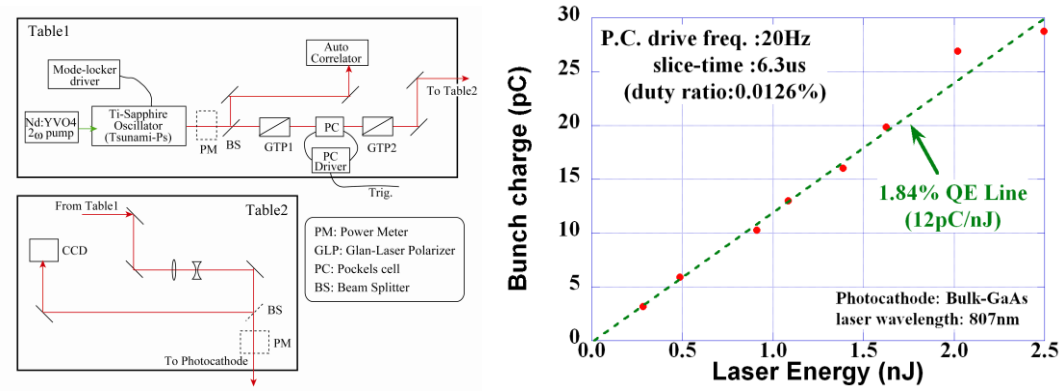

FIGURE 5. A schematic view of the Ti:Sapphire mode-lock laser system and the pulse slice system (left). A result of bunch generation from bulk-GaAs by illuminating sliced laser pulse trains (right).

CONCLUSION

The 200keV load-lock gun have been developed and operated more than 500 hours under condition with a low dark current of <1nA. The operational-lifetime measurement of 50 μA beam current was done and obtained ~120 hours that is available operation level for the ILC electron source. For the pico-second bunch generation, the bunch charge of 28 pC from bulk-GaAs could be emitted by irradiating sliced laser pulse trains. The emittance measurement with the bunch charge of more than 7.7 pC is underway.

ACKNOWLEDGMENTS

We wish to thank Mrs. K.Yamauchi, T.Katoh (Yorodu-Shibori Co., Ltd), T.Sashida, H.Uemori (Tosei Electrobeam Co., Ltd.), K.Satoh (Ultra Finish Technology Co., Ltd.), N.Takayama (SAKURAI Co., Ltd), T.Gotoh, M.Katsuki and K.Itoh (Technical Center of Nagoya University) for kindness support for fabricating the molybdenum and titanium electrode.

This work was has been supported partially by Grant-in-Aid for Scientific Research (No. 15204019, No. 20740129) and a research fund of KEK for cooperative development (No.2006-022, No.2007-023).

REFERENCES

1. T. Nakanishi et al., KEK Report 97-01 (1997) p.36-48
2. F. Furuta et al., Nucl. Instru. Meth. A538 (2005) p.33-44.
3. K. Aulenbacher et al., Proceedings of SPIN2004 p975-979
4 C.K. Sinclair et.al., Phys. Rev. ST Accel. Beams 10, 023501 (2007).
5 N. Yamamoto et.al., J. Appl. Phys. 102, 024904 (2007)

Polarized Photocathode R&D for Future Linear Colliders

F. Zhou, A. Brachmann, T. Maruyama, and J. C. Sheppard

SLAC National Accelerator Laboratory, 2575 Sand Hill Road, Menlo Park, CA 94025, USA.

Abstract. It is a challenge to generate full charge electrons from the electron sources without compromising polarization for the proposed ILC and CLIC. It is essential to advance polarized photocathodes to meet the requirements. SLAC has worldwide unique dedicated test facilities, Cathode Test System and dc-Gun Test Laboratory, to fully characterize polarized photocathodes. Recent systematic measurements on a strained-well InAlGaAs/AlGaAs cathode at the facilities show that 87% polarization and 0.3% QE are achieved. The QE can be increased to ~1.0% with atomic hydrogen cleaning. The surface charge limit at a very low current intensity and the clear dependence of the polarization on the surface charge limit are observed for the first time. On-going programs to develop photocathodes for the ILC and CLIC are briefly introduced.

Keywords: photocathode, photoemission, polarized beam.
PACS: 85.60.Ha, 79.60.-i, 29.27.Hj.

CHALLENGES OF THE ILC AND CLIC: HIGH-CURRENT HIGH-POLARIZATION ELECTRON SOURCES

Extensive developments on high-current high-polarization electron sources for the proposed International Linear Collider (ILC) and CERN Compact Linear Collider (CLIC) are being carried out at the SLAC and JLAB in the United States. Table 1 summarizes the major parameters of the polarized electron sources for the linear colliders. The major challenge for the ILC electron source is to generate full charge 1-ms-long macropulse without compromising polarization while the one for the CLIC is to generate a train of only-100-ps-long full-charge micropulses. In principle, the full charge production could be limited by space charge and/or surface charge effects in the linear colliders. A high quality polarized photocathode is required to overcome the surface charge limit, while a high-voltage dc-gun is needed to suppress the space charge effect. In addition, the high average beam current from the dc-gun sources for the linear colliders may cause serious ion-back bombardment onto the cathode, which may badly affect the QE lifetime due to the deterioration of the cathode. It requires us to explore solutions to reduce ions onto the cathode, such as cryo-pumping – condensing the gases onto the wall by cooling down the gun to a very low temperature, typically at 20-30 K. The major goals of the photocathode developments at the SLAC for the ILC and CLIC: 1) demonstration of full charge production without space charge and surface charge limit; 2) >85% polarization; 3) ~1% QE and long QE lifetime.

TABLE 1. Major parameters of the ILC and CLIC high-current high-polarization electron sources.

Parameters	ILC	CLIC
Electrons Per Microbunch	$3x10^{10}$	$6x10^{9}$
Number Of Microbunch	2625	312
Width Of Microbunch	1 ns	100 ps
Time Between Microbunches	360 ns	500.2 ps
Width Of Macropulse	1 ms	156 ns
Macropulse Repetition Rate	5 Hz	50 Hz
Charge Per Macropulse	12600 nC	300 nC
Average Current From Dc-Gun	63 μA	15 μA
Peak Current Of Microbunch	4.8 A	9.6 A
Current Intensity (1cm Radius)	1.5 A/cm^2	3.0 A/cm^2
Polarization	>80%	>80%

COMPLETE EXPERIMENTAL CHARACTERIZATIONS OF A STRAINED-WELL InAlGaAs/AlGaAs

Strained-well InAlGaAs/AlGaAs structures designed and manufactured by St. Petersburg in Russia have the following advantages [1]: 1) larger valence band splitting due to the combination of deformation and quantum confinement effects in the quantum well; 2) a sharp band-bending-region; and 3) a reasonably thick working layer without strain relaxation. The measurements in Russia show that the structures have excellent performance – 1% QE and 90% polarization. To cross-check the Russian data and also provide all key performance of the cathode including charge limitation, polarization, QE and QE lifetime, the InAlGaAs/AlGaAs structures have been characterized at the SLAC cathode and gun test facilities.

Polarization and quantum efficiency were firstly measured at the SLAC Cathode Test System (CTS) [2]. The CTS is an ultra-high vacuum system equipped with a load-lock chamber through which samples can be introduced without venting the system vacuum. Polarization measurements are made using an electron transport column, an electrostatic spin-rotator and a 20 kV Mott polarimeter. Prior to the cathode installation, the sample is processed via standard chemical and heat cleaning methods. The CTS measurements for the InAlGaAs/AlGaAs sample demonstrate 0.3% QE and 87% polarization. The sample used at the SLAC is not a fresh one and may have some degradation of near-surface region and As-cap. The degradation could not be removed by the standard chemical and heating cleaning techniques. However, the QE of the InAlGaAs/AlGaAs cathode was recovered to 1% with atomic hydrogen cleaning [3].

The SLAC Gun Test Laboratory (GTL) [4] is capable of characterizing all parameters including the surface charge limit, QE and QE lifetime, and polarization. The GTL beamline consists of an ultra-high vacuum, high-voltage electrostatic dc-gun, a load-lock chamber for cathode transfer and activation, and a beamline with magnetic components for electron beam transport. With the cathode biased at 120 kV, the gun is capable of producing a space-charge-limited current of 15 A from the 20 mm diameter cathode. An electrically isolated, optically coupled nanoammeter is used to measure the average photoemission current. A fast Faraday Cup (FARC) is employed to measure the temporal profile of the electron beam from which the surface

charge limitation can be measured. The electron beam is transported to the Mott chamber for polarization measurements. Fig. 1 shows the comparison of polarization spectrum of the InAlGaAs/AlGaAs cathode measured at St. Petersburg and at SLAC. It is shown that the polarization spectrum measured at the SLAC CTS and GTL is very close although there is a constant wavelength shift between them. The shift is probably caused by a wavelength calibration error in the CTS. The maximum polarization measured at the SLAC CTS/GTL is ~87% versus ~91% measured in Russia. The polarization difference is attributed to systematic differences in the measurement systems.

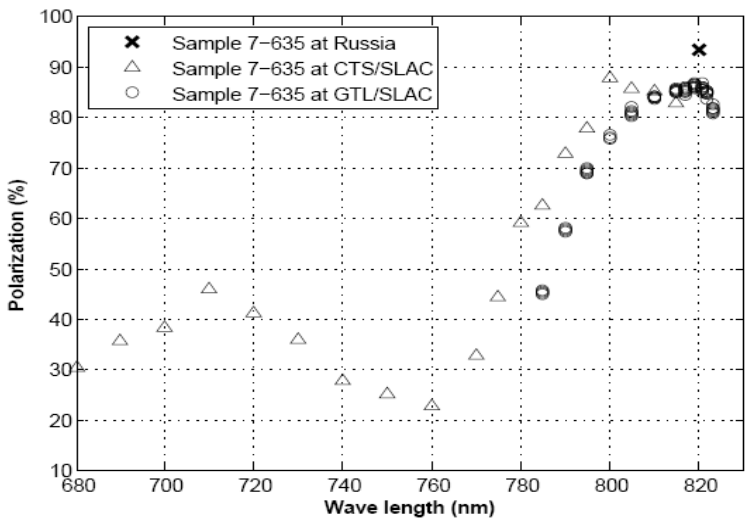

FIGURE 1. The comparison of the polarization spectrum measured at St. Petersburg in Russia, CTS/SLAC and GTL/SLAC.

The surface charge limit on the cathode is seen in Fig. 2 as the drop off of intensity during the current pulse. The limit is caused by the lower doping level in the surface layer, only $7x10^{18}/cm^3$ in the cathode. Further studies show that the onset of surface charge limitation occurs at a very low current intensity, only 0.06 A/cm^2. Increasing the doping level to $2\text{-}5x10^{19}/cm^3$ in the surface layer can effectively suppress surface charge limit [5].

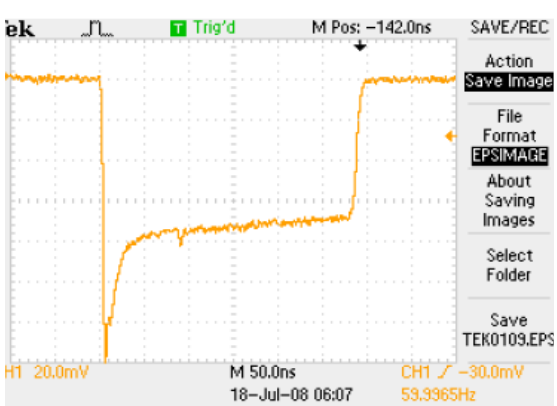

FIGURE 2. Observation of surface charge limit at $2.5x10^{10}$ electrons at 10 mm laser full size on the cathode. The abscissa is time, and the ordinate is the beam signal from Faraday Cup.

The dependence of the polarization on the surface charge limit is clearly observed for the first time. During the observations, only the laser position on the cathode is changed. At different laser positions A and B on the cathode, different levels of the surface charge limit are observed, as shown in Fig. 3(a) and 3(b), respectively. The surface charge limit at the laser position A is more severe than at position B. The beam generated at laser position B has a higher polarization, 2-3% more than at position A, as shown in Fig. 4. At the laser position A, the cathode is driven into saturation, and the electrons photoexcited into conduction band still can escape if they diffuse to a non-saturated region. Thus, these electrons spend a longer time inside the structure so it is likely that they suffer spin greater relaxation than at position B, which results in reduced polarization.

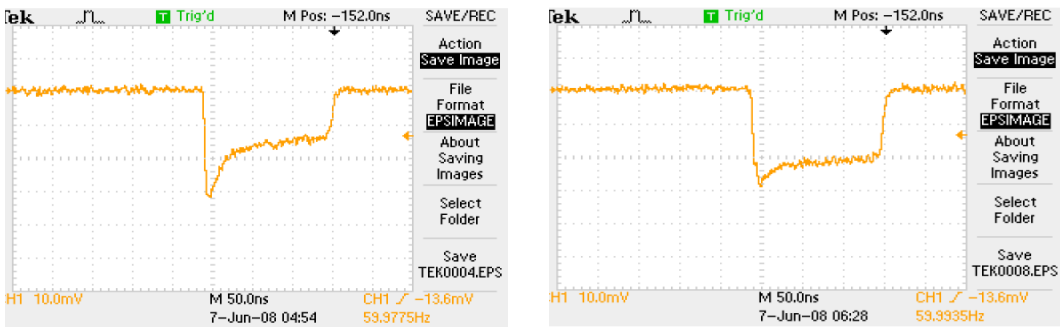

(a) (b)

FIGURE 3. Different degree of surface charge limit of the electron beam at different laser position on the cathode; (a) and (b) correspond to the laser position on the cathode at A and B, respectively. The abscissa is time, and the ordinate is the beam signal from Faraday Cup.

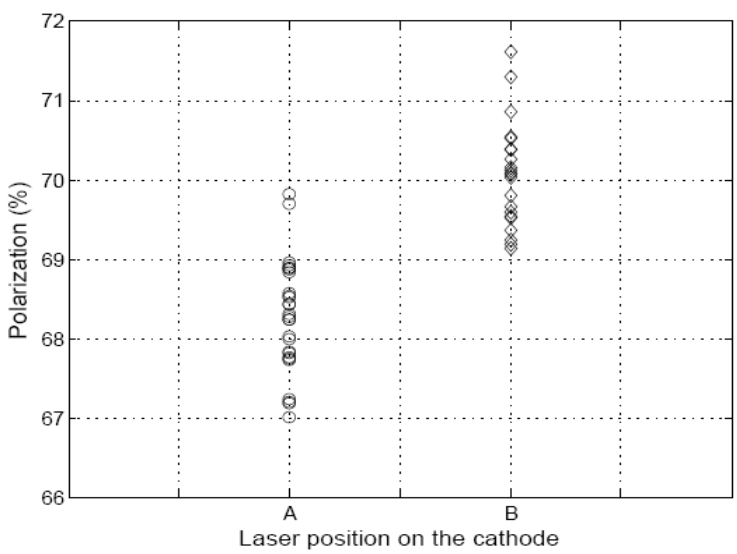

FIGURE 4. Polarizations corresponding to different laser position; data is taken at 800 nm wavelength.

SUMMARY AND PLANS

It is challenging to generate the ILC and CLIC full charge without compromising polarization. Advancing polarized photocathode technology to increase polarization, QE and QE lifetime along with reduced space charge and surface charge limit is one of the major factors to guarantee the success. Recent measurements at the SLAC test facilities show that the InAlGaAs/AlGaAs can produce 87% polarization, 0.3% QE. The QE can be recovered to ~1% with atomic hydrogen cleaning. Serious surface charge limit is observed at a very low current intensity. The clear dependence of the polarization on the surface charge limit is observed for the first time.

SLAC continues to be actively engaged in the development of improved polarized photocathodes through studies of the doping level in the structure of superlattice and of gradient doping in the active layer of the superlattice. Both QE and polarization are expected to be improved using these two techniques. The ILC laser prototype is expected to come online at the SLAC in 2009. This allows us demonstrate the ILC full charge production. In addition, the studies on ion effects on the QE lifetime are also being pursued.

ACKNOWLEDGMENTS

We would like to thank Jym Clendenin for his contributions and Y. Mamaev for the fruitful collaborations. The work is supported by U.S. DOE contract DE-AC03-76SF00515.

REFERENCES

1. Yu. A. Mamaev, et al., “InAlGaAs/AlGaAs superlattices for polarized electron photocathodes”, SLAC-PUB-11403, August 2005.
2. G. A. Mulhollan, “Low energy polarized electron source test facilities”, 1993 (unpublished).
3. V. Tioukine, “Atomic hydrogen cleaning of superlattice cathodes”, Workshop on sources of polarized electrons and high brightness electron beams, Jefferson Laboratory, Newport News, VA, October 1-3, 2008.
4. P. J. Saez, “Polarization and charge limit studies of strained GaAs photocathodes”, Ph. D thesis, SLAC-R-501, March 1997.
5. T. Maruyama, et al., “A very high charge, high polarization gradient-doped strained GaAs photocathode”, SLAC-PUB-9133, March 2002.

High Intensity Polarized Electron Gun Studies at MIT-Bates

E. Tsentalovich

MIT-Bates Linear Accelerator Center, Middleton, MA

Abstract. A proposed new high-luminosity electron-ion collider requires a polarized electron source of extremely high intensity. An ion back bombardment of the cathode is the main factor limiting the intensity of modern polarized electron guns. This study examines the possibility of building a very high intensity polarized electron gun.

Keywords: Polarized electron source, ion bombardment
PACS: 29.25.Bx, 29.27.Hj

INTRODUCTION

Modern polarized electron sources [1-6] routinely produce average current of hundreds of μA with a polarization approaching 90%. This intensity satisfies the requirements of the existing accelerator facilities. New advances in nuclear physics are expected with the development of a high luminosity electron-ion collider (EIC). The concept of such a collider has been discussed in the nuclear physics communities around the world for the past decade. Several conceptual designs have been proposed. Brookhaven National Laboratory (BNL) develops two different versions of eRHIC [7], based on the existing Relativistic Heavy Ion Collider (RHIC) complex. ELIC project [8] is developed at Thomas Jefferson National Accelerator Facility (TJNAF). These EIC projects require a significantly higher intensity from a polarized electron source. The linac-ring version of eRHIC produces the most challenging requirements with an average current of up to 250 mA. MIT-Bates, in collaboration with BNL, is investigating the possibility of building a very high intensity polarized electron gun.

MAJOR CHALLENGES

Two main problems must be solved in order to build a polarized electron gun with a very high average current. The first challenge is the heat load on the cathode. Tens or even hundreds of Watts of laser power must be deposited on a high polarization (strained or superlattice) GaAs cathode in order to extract a current of hundreds of mA. Cathode holders in the existing guns can absorb less than 1W without temperature rise. Active cooling of the cathode is necessary to avoid overheating of the crystal. The cooling system must be compatible with the high voltage applied to the cathode and with UHV conditions of the polarized electron gun, and presents a formidable engineering challenge.

The most difficult task is to achieve the high average current with a reasonable lifetime. The main problem is ion back bombardment. An electron beam ionizes molecules of the residual gases in the vacuum chamber; positive ions accelerate in the cathode-anode gap and strike the cathode, damaging the surface of the crystal. The effect is proportional to the product of the average electron current and the pressure in the gun chamber. It is difficult to expect a significant improvement of the vacuum conditions over present state-of-the-art installations, and the effect limits the average current in existing guns to several hundreds of μA.

Both problems could be addressed with increased cathode area. Heat transfer can be done more efficiently, and the ion damage will be distributed over a larger area, resulting in a higher lifetime of the cathode.

Measurements conducted at TJNAF [9] with a green laser indicated that the lifetime increased by a factor of ~10 when the laser spot diameter was increased by factor of 4. In a simplified picture, the average current that could be extracted from the cathode, with the same lifetime, is proportional to the emitting area. In reality, the picture is more complicated. Negatively charged electrons and positive ions follow a somewhat different trajectory, and ions tend to damage mostly the central area of the cathode. Existing electron guns are using the Gaussian shaped laser beams, with the maximum beam intensity near the cathode center, where the ion damage is most significant. For a high-intensity gun, it could be beneficial to form a ring-shaped laser beam, so the majority of the laser power is applied to the peripheral area of the cathode. The major difficulty in this approach is to avoid beam losses in the gun and its vicinity. Very detailed simulations including space charge effects must be conducted to design a large area cathode with a ring-shaped emission.

ION INDUCED DAMAGE STUDIES

The measurements have been conducted with the existing test beam line described in [6]. This beam line was designed for cathode tests and certification at very low current. It includes Mott polarimeter with silicon detectors and Mylar-backed golden foils. This section of the beam line cannot be baked at high temperature, and thus the vacuum in the whole beam line is rather inferior. The beam line has narrow apertures, and beam losses of 5-10% are typical. These losses produce out-gassing at high current, and degrade vacuum conditions even farther, resulting in a relatively short lifetime of the cathode. However, the poor performance of the test beam line at high current was beneficial for our studies. The ion damage accumulated quickly, and the measurements could be conducted in a relatively short time.

A fiber-coupled diode laser with a wavelength of λ=808nm was used for photoemission. The laser beam coming out of the fiber (0.4 mm diameter) has very large divergence (full open angle ≈25.4°). The first focusing lens L1 produced an almost parallel laser beam. An axicon (conical lens) in conjunction with the second focusing lens L2 formed a ring-shaped laser beam in the location of the cathode. With the axicon removed from the system, lenses L1 and L2 formed a point-to-point focusing between the output of the laser fiber and the cathode, resulting in a very small laser spot. A longitudinal translation of L2 allowed varying the beam spot size. The L2 lens was mounted on a translation stage for a precise translation in both

transverse directions. With the axicon removed and the laser beam focused, one could scan the surface of the cathode using these translations and map the QE of the crystal.

The following procedure was used during the measurements. The crystal was heat-cleaned and activated. With the axicon removed, a very small diameter laser beam was scanned across the surface of the crystal, mapping the QE. The cathode was biased to only -64V during the mapping. Then the optical system was tuned to a certain configuration (small or large laser beam, ring-shaped beam etc.). The cathode was biased to -60kV, and the laser intensity was adjusted to produce a current of ≈120 μA. Each run continued for several days, and an integrated charge of 12-18 C was accumulated during each run. As the QE of the cathode decreased, the laser intensity was adjusted to keep the average current at about 100 μA. After the run the QE of the crystal was mapped again. The ratio of those two maps represents the change in the QE during the run.

Figure 1 shows the results of the runs in four different configurations: a) small Gaussian laser beam (σ≈0.15 mm) in the center of the cathode, b) large Gaussian beam (σ≈2 mm), c) ring-shaped laser beam and d) small Gaussian beam parked in the corner of the cathode.

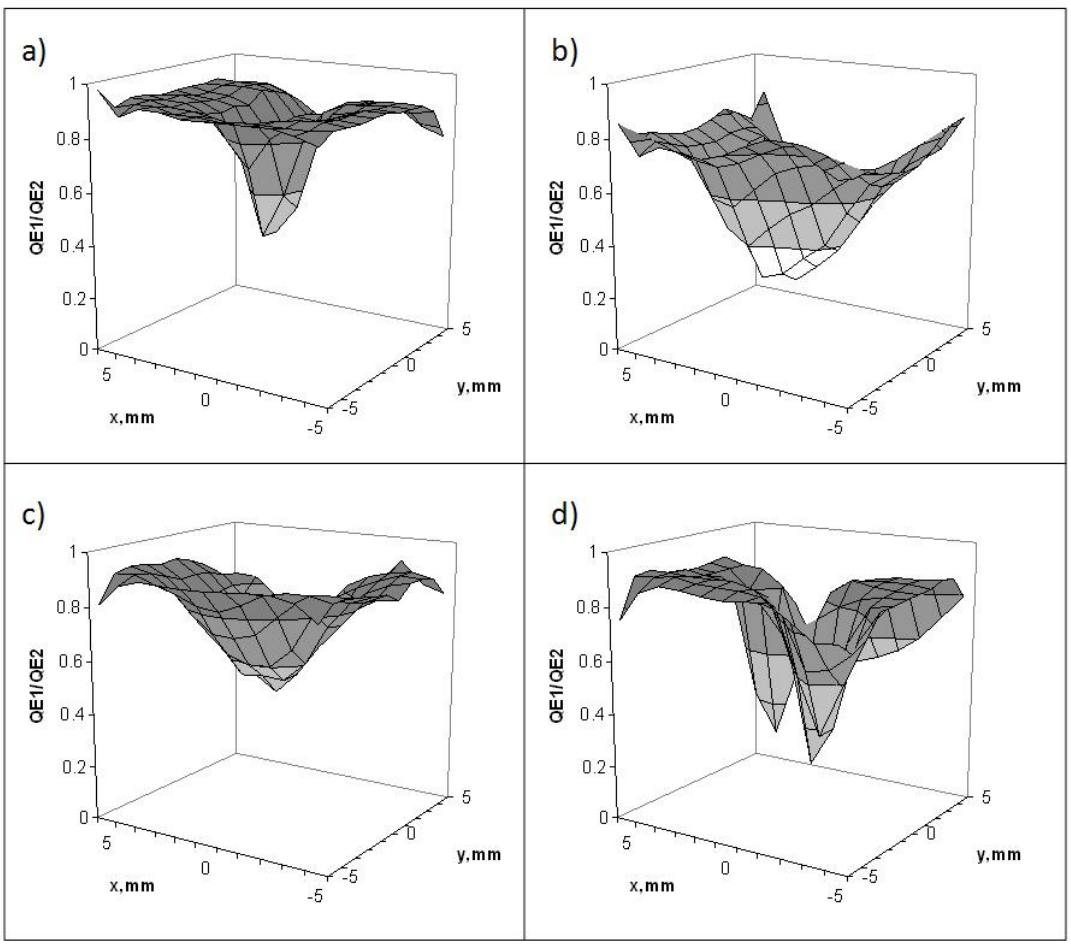

FIGURE 1. Map of the QE degradation after the run with a) – small centered beam, b) – large beam, c) – ring-shaped beam and d) – small beam parked at the corner of the cathode.

The run with a small laser spot centered on the cathode produced a deep "hole" in the QE distribution. Naturally, the "`hole" was located in the center of the crystal; the ions damaged mostly the area where the electrons have been emitted from. However, in the case of the ring-shaped beam, most of the damage occurred in the center of the crystal again, although the laser intensity was negligibly low there. The ring-shaped area where the electrons were emitted from actually received less damage than the central part.

The damage produced by a large Gaussian beam corresponds roughly to the beam shape, but the total amount of the damage is much higher. The Gaussian beam has tails, and significant amount of the electrons are emitted from the very edge of the cathode, where the transverse focusing forces are very large. Those electrons follow the extreme trajectories and get lost in the vicinity of the gun, causing out-gassing and increasing the ion-related damage. In contrast, an axicon-formed ring-shaped laser beam has very sharp edges with low tails and produces very few electrons with extreme trajectories.

A small laser beam parked in the corner of the cathode produced a “hole” in the emitting spot, a groove of damage extending toward the center of the crystal, and the second “hole” located on this groove slightly over the cathode center.

All these features can be understood by ion trajectory calculations. It should be noted that the anode hole acts as a defocusing element for the electrons, and a focusing element for ions. The ions produced in the vicinity of the cathode experience basically the same transverse forces as the electrons and follow approximately electron trajectories toward the cathode. The ions produced closer to the anode are affected by focusing fields of the anode at the part of the trajectory where their energy is still very low and the transverse forces are more effective. As a result, those ions tend to be focused toward the center of the cathode. The ions produced in the anode area are actually overfocused, but still damage mostly the central area of the crystal. These high energy ions are most likely responsible for the second “hole” on Fig.1d, giving a strong indication that although most ions are produced near cathode (due to high ionization cross section at low energy of the electrons), high energy ions produced near anode give a very significant contribution in ion-related damage.

The measurements have been conducted with CW beam, and ion trapping must be considered. The ions produced in the beam line after the anode could be trapped in the electron beam, travel toward the gun, get accelerated in the cathode-anode gap and strike the cathode. The preliminary measurements at TJNAF [10] indicated that this process could be important and that it can be suppressed by biasing the anode.

An additional run was conducted with the anode biased to +1kV and ring-shaped laser beam. A significant reduction in ion-related damage was measured, especially in the center area of the cathode, where most of the trapped ions are expected to be directed.

SIMULATIONS AND CATHODE COOLER

The simulations of the new gun and the beam line are under way. The simulations assume the current of up to 100 mA and gun voltage of 120 kV. The cathode diameter is 25 mm. The beam line includes two 90° dipole magnets, solenoidal lenses and a

beam dump. The main purpose of the simulations is to minimize beam losses, especially in the gun vicinity. The losses are required to be less than 10^{-6} in the first straight section and less than 10^{-5} in the rest of the beam line with different emission pattern (flat-shaped beam, Gaussian beam, ring-shaped beam).

Additionally, the ion trajectories are calculated and the expected damage pattern estimated. The gun geometry and the emission pattern will be optimized to reduce the overlap of the emission pattern and the damage pattern.

A special test chamber is designed to study the cathode cooling. The cooling agent (fluid with very low electrical conductivity) will be delivered to the cathode via ceramic tubes. High Voltage and Ultra High Vacuum compatibilities will be tested, as well as a cooling efficiency.

ACKNOWLEDGMENTS

The work is partially supported by DOE grant DE-FG02-94ER40818. The author would like to thank the staff of Bates laboratory for a constant help and support. The author is grateful to C. Sinclair for his comments.

REFERENCES

1. R. Alley et al, *Nucl Instr. and Meth*. **A365**, p.1 (1995).
2. K. Aulenbacher et al, *Nucl. Instr. and Meth.* **A391**, p.498 (1997).
3. M. J. J. van den Putte et al, *Nucl. Instr. and Meth.* **A406**, p.50 (1998).
4. J. Grames et al, *AIP Conf. Proc.* **675,** p. 1047 (2002).
5. Wolther von Drachenfels et al, *AIP Conf. Proc.* **675,** p. 1053 (2002).
6. E.Tsentalovich et al , *Nucl. Instr. and Meth*. **A582**, p.413 (2007).
7. V.Ptitsyn, Proc. of the Particle Accelerator Conference. 2007, p.1927.
8. Y. Zhang et al., Proc. of the Particle Accelerator Conference, 2007, p.1935.
9. M.Poelker and J.Grames, Proc. of 11th Intern. PST Workshop, Tokyo, 2005, p.127.
10. J. Grames et al, Proc. of 12th Intern. PST Workshop, Upton, 2007, p.110.

Hydrogen Cleaning of Superlattice Photocathodes

V. Tioukine, K. Aulenbacher, E. Riehn

Institut für Kernphysik der Universität Mainz,
J.J. Becherweg 45, D-55099 Mainz, Germany, F. R.

Abstract. Surface cleaning with a beam of thermally dissociated hydrogen atoms was applied to superlattice cathodes which resulted in a considerable improvement of quantum efficiency. Compared to untreated samples no significant reduction of polarization of the emitted electrons was observed.

Keywords: Superlattices, Polarized beams, Surface Cleaning
PACS: 78.67.Pt 29.27.Hj 81.65.Cf

INTRODUCTION: AGING PROBLEM

Activation of photocathodes towards the state of negative electron affinity requires a clean surface before a deposition of cesium and oxygen takes place. Typically this condition is realized by the application of a passivation layer, e.g. elemental arsen, directly after the growth of the wafer. The sample may then be exposed to air and stored for long time. The As-layer can be removed by heating the sample up to 400 °C in Ultra High Vacuum (UHV) prior to an activation. So far, this strategy proved successful for our strained layer- and also for some superlattice (SL-) cathodes. However, a different behavior was observed for $InGaAlAs/GaAlAs$ samples which were designed at St. Petersburg State Technical University and grown by the Joffe Institute (see fig. 2). If measured directly after the growth, these samples offer attractive parameters [1]. However, we initially achieved only about 1/10 of the quantum efficiency (q.e.) values reported in [1]. Moreover, saturation effects were observed which increased the discrepancy at the high laser intensities necessary at our accelerator. We assumed an aging problem due to the fact that the samples were stored for about three months. This was supported by our collaborators in St. Petersburg who also observed similar effects after long term storage. In order to explain this we suspect insufficient passivation of the cathode surface. This will lead to formation of Arsenoxide (As_2O_3) on the surface immediately after the venting of the growth apparatus. As_2O_3 can effectively be removed at relatively low temperatures ($\approx 500\,^{\circ}C$) thus explaining the good results achieved directly after growth. However, it was demonstrated [2] that As_2O_3 transforms into gallium oxides (Ga_2O_3), this reaction happening within months at room temperature. It cannot be avoided by storing the samples under inert gases or vacuum since the oxides are already present at the surface. Ga_2O_3 can not be effectively removed by heat treatment alone which can explain the problems observed. Alternative ways of surface cleaning must cope with the requirement to remove exclusively the oxides, since the functional structures close to the surface of the SL are extremely thin (fig. 2). Andreev et al. [3] studied several methods

of surface cleaning for NEA photoemitters. Good results were achieved if a thermal hydrogen cracker was used, which may be due to the absence of energetic ions and neutrals in the atomic beam of this source.

HYDROGEN CLEANING APPARATUS

We have set up a dedicated apparatus, called HABS - Hydrogen Atomic Beam Source - which allows for the following operations

- Hydrogen cleaning by a beam of thermally cracked hydrogen atoms.
- Activation to NEA state and q.e. measurement in order to test cleaning effect.
- Transfer of samples under UHV to other apparatuses for further investigations.

The apparatus consists of a bakeable all metal UHV system (fig. 1). The hydrogen source is a commercial one, similar to the design in [4]. It consists of a heated tungsten capillary which reaches a temperature of about 2150 C at a heating power of 300 watts. H_2 flowing through the hot capillary is dissociated. A beam of atomic hydrogen then hits the sample surface which is located at a distance of about 10 cm from the end of the capillary. The dissociator is enclosed in a water cooled copper shielding which reduces the radiative heating of the inner surfaces and of the sample itself. Clean hydrogen is provided by using pure H_2 gas and further purification is achieved by letting it stream through a getter. H_2 is then stored in an all metal enclosure and introduced by a leak valve. Hydrogen pressure during treatment was $2 \cdot 10^{-6}$ mbar stabilized by a turbo pump (fig. 1). Typical exposure times were about 5 minutes during which the samples are heated to 550 °C. Then, the activation procedure is started, consisting of a 30 minute long heat treatment at 550 °C and co-deposition of cesium and oxygen after cooling down the sample. The q.e. achieved may be compared with the one from untreated samples (fig. 3). Once a promising result is achieved, the samples are cleaned again without subsequent activation. Afterwards they are transported to one of the 100 keV sources in our labs for further investigations which are not possible within HABS (e.g. polarimetry). For this purpose the samples are transferred into the transport vessel by a manipulator. The vessel is equipped with an ion pump. An intermediate loading chamber is pumped by the turbo already mentioned above. After shutting off the transfer vessel by a valve the loading chamber is vented and the vessel may be removed. Meanwhile, another (closed) valve allows to keep the vacuum in the HABS chamber. The vessel is then transported to one of the electron sources where similar loading chambers exist. All stages of the transport are performed under UHV.

HABS RESULTS

Photocathodes: The structure of the superlattice (SL-)cathodes labelled 7-395 and 7-396 is presented in fig. 2. In both cases the working layer consists of 12 periods of double layers with a composition $In_{.2}Al_{.19}Ga_{.61}As/Al_{.4}Ga_{.6}As$, yielding a total thickness of 91 nm for the working layer of the cathode. Due to the fact that all layers contain Al it is necessary to inhibit interaction with oxygen by placing a very thin layer of GaAs on top

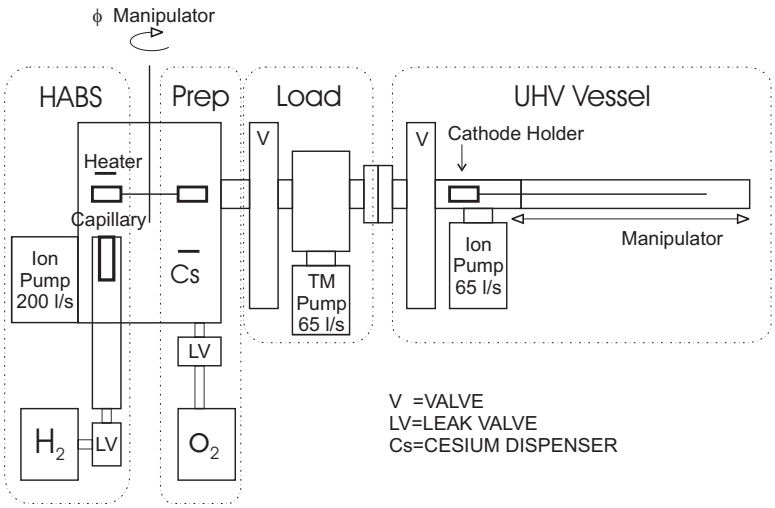

FIGURE 1. Schematic of hydrogen cleaning apparatus.

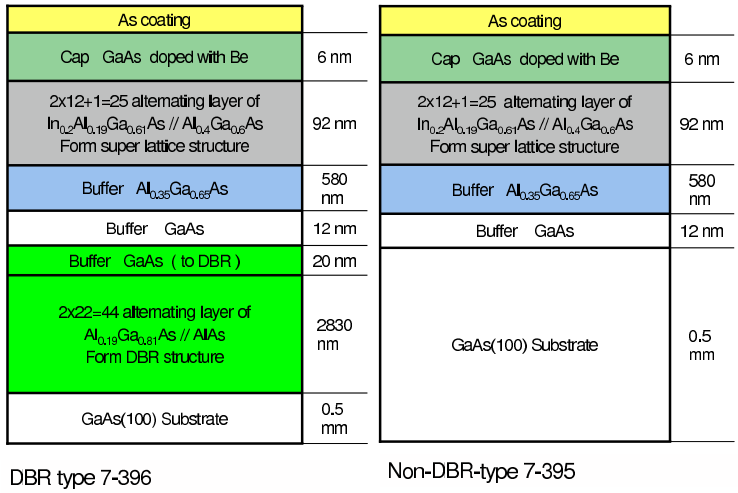

FIGURE 2. InAlGaAs/AlGaAs Superlattices. The As capping may not be fully present in our case.

of the SL. In contrast to the working layer, the GaAs is heavily p-doped, thus providing a thin band bending region which is essential for efficient emission in conjunction with low polarization losses. The SL 7-396 has an additional feature since it is grown on top of another superlattice (DBR) which reflects the incoming light. Together with the semiconductor/vacuum interface (Reflectivity $\approx$0.3) the DBR forms an optical cavity which allows to increase the internal absorbtion if the incoming wavelength corresponds to a cavity resonance. Both types suffered from the aging effect, which limited their q.e. to $\leq 1\%$ for light of $\lambda = 650\,\text{nm}$ which was used for the activation tests in HABS.

Activation results in HABS apparatus: The vertical bars in fig. 3 indicate when a cathode was hydrogen cleaned in addition to heat cleaning before the activation. The first two samples tested were bulk GaAs (activations 1-16). In both cases hydrogen cleaning resulted in an increase of q.e. by more than a factor of five. Following this,

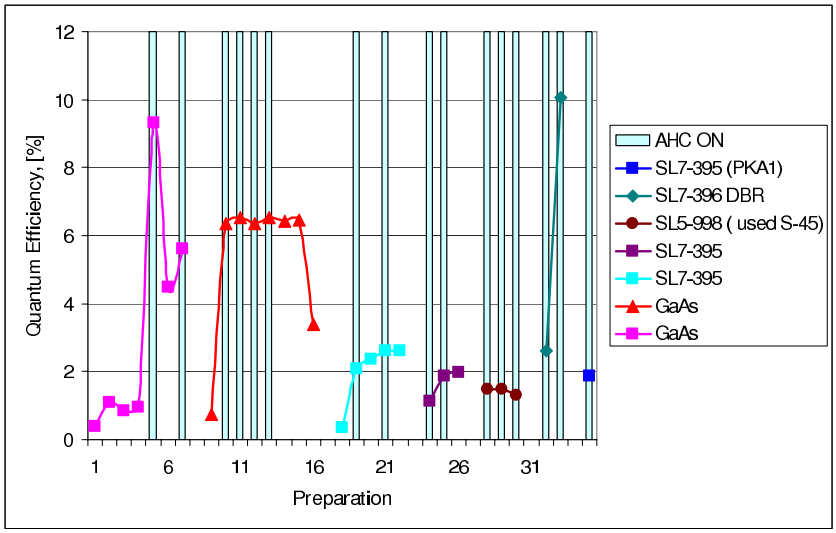

FIGURE 3. Sequence of activations in the HABS apparatus

maximum q.e. seems to remain constant for a few activations, even without further treatment, before a reduction is observed, see activations 12-16. The behavior of the SL's concerning hydrogen treatment is similar to bulk GaAs. The DBR cathode 7-396 has achieved the highest q.e., yielding more than 10% at 650 nm. 7-395/7-396 cathodes were transferred to our test source, a 7-395 went to the source at the MAMI accelerator.

Results in Production source: These tests were performed with a high intensity laser system operated at wavelengths of 785 and 802 nm, close to the maximum polarization response of the cathode. We observed a ten times increased q.e. at low intensities for the HABS treated sample if compared with an untreated one. Moreover, the saturation effects at high intensities had disappeared resulting in a factor 50 gain of maximum current. Tests were performed at a q.e. of 0.6% and 200 μA of average current (density of $\approx 200 mA/cm^2$) without showing nonlinear effects. Beam polarization was measured with a Mott polarimeter that offers a reproducibility of about 1%, whereas the absolute accuracy is $\Delta P/P = \pm 4\%$. After one week of operation at the accelerator the q.e. had dropped by a relative 15% which resulted in a relative increase of polarization by 6%, yielding an absolute value of $P = 85.5 \pm 3.2\%$. This value is within the highest ever observed at our production source.

Results in test source: Comparisons of maximum polarization for treated/untreated samples were done at the test source. We found no difference (at the 3% (relative) level) between the different samples once the initial q.e. of the hydrogen cleaned one was slightly reduced (see above). This provides evidence that hydrogen treatment has no detrimental effect on the bulk properties of the superlattice structure. A tunable laser was used for spectrally resolved measurements. The lower curve in figure 4 shows the results for an untreated sample of 7-395, the upper one those from a fresh one measured at St. Petersburg. The results for a hydrogen treated sample are close to the St. Petersburg measurements. Again, saturation effects were present for the non treated sample which would make the discrepancy in figure 4 even larger at high laser intensities. The DBR

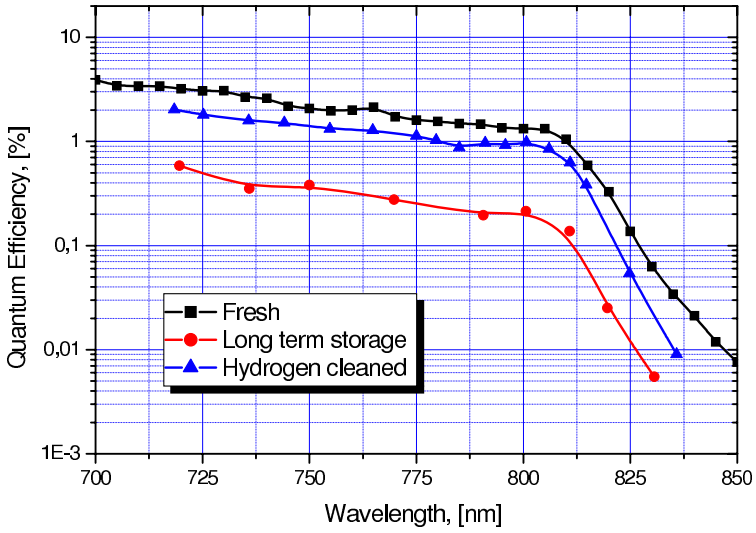

FIGURE 4. Comparison of results achieved under different conditions

sample 7-396 (not shown in fig. 4) achieved almost twice the q.e. of the non DBR sample 7-395 in figure 4, yielding q.e.=1.2% at the wavelength of maximum polarization which is even larger than the result obtained directly after growth.

CONCLUSION

We have demonstrated the usefulness of hydrogen cleaning for superlattice cathodes with very thin functional structures. We find no evidence for a depolarization with respect to untreated samples. The success of the method may be promoted by the specific technology of atomic hydrogen generation, based on thermal dissociation, which eliminates fast ions or neutral particles which may damage the surface.

ACKNOWLEDGMENTS

This work was supported by the SFB 443 of the Deutsche Forschungsgemeinschaft. We especially want to thank Yuri Mamaev and Yuri Yashin for stimulating discussions on the various aspects of surface treatment and semiconductor fabrication.

REFERENCES

1. Y. A. Mamaev et al., *Appl. Phys. Lett* **93**, 081114 (2008).
2. D. A. Allwood et al., *Thin Solid Films* **412**, 76 (2002).
3. V.E. Andreev et al., "Atomic and electronic engineering of p-GaAs-(Cs,O)-vacuum interface," in *SPIN 2000, AIP Proceedings Vol. 570*, edited by K. Hatanaka et al. , AIP, Melville, N.Y., 2001, p. 901.
4. U. Bischler and E. Bertel, *JVST A* **11**, 458 (1992).

Ultra Cold Photoelectron Beams for Ion Storage Rings

D. A. Orlov[a], C. Krantz[a], A. Shornikov[a], M. Lestinsky[a], J. Hoffmann[a], A.S. Jaroshevich[b], S.N. Kosolobov[b], A.S. Terekhov[b] and A. Wolf[a]

[a] *Max-Planck-Institut für Kernphysik, 69117, Heidelberg, Germany*
[b] *Institute of Semiconductor Physics, 630090, Novosibirsk, Russia*

Abstract. An ultra cold electron target with a cryogenic GaAs photocathode source, developed for the Heidelberg TSR, delivers electron currents up to a few mA with typical kinetic energies of few keV and provides unprecedented energy resolution below 1 meV for electron-ion recombination merged-beam experiments. For the new generation of low-energy electrostatic storage rings, cold electron beams from a photocathode source can bring additional benefits, improving the cooling efficiency of stored ions and making it possible to cool even heavy, slow molecules by electron beams of energies of only a few eV or even below.

Keywords: photocathode, electron beams, electron cooling, electron target, storage ring.
PACS: 52.25.Xz , 29.25.Bx, 29.20.D, 85.60.Ha, 34.80.Lx, 37.10-x

INTRODUCTION

Semiconductor photoemitters with negative electron affinity (NEA) are widely used in various scientific experiments for the generation of spin-polarized, short bunched high-density electron beams. Photoelectron sources also offer the possibility to employ extremely cold electrons with emission energy spread of about the cathode temperature, which can be as low as 7 meV at 100 K [1]. One of the main difficulties is to keep the beam cold as a space charge causes beam divergence at high currents. To avoid this heating, high magnetic guiding field is used in the electron coolers of storage rings, which decouples transverse and longitudinal electron motions. Electron-ion merged beams at storage rings have also opened a new domain for electron-ion recombination studies where ultra cold photoelectron sources can bring great benefits in high-resolution measurements. A cryogenic photocathode target was developed [2,3,4] for recombination measurements at the Heidelberg Test Storage Ring (TSR) and is in operation since 2002 delivering *dc* electron beams of mA currents and with ultra-cold temperatures below 1 meV [4,5]. For the upcoming electrostatic Cryogenic Storage Ring (CSR), where the cooling of stored slow ions has to be performed at typical electron energies of 10 eV down to the sub-eV range, the impact of the cold photocathode source can be of high additional importance. Indeed, at low energies of 1-100 eV the electron current drops down to the μA range due to a limited gun perveance, which strongly decreases the cooling efficiency. To make cooling possible, electron beams of low temperatures have to be used [6]. In this paper, we present the

Heidelberg photoelectron target and demonstrate the performance of the cryogenic GaAs-photocathode source.

MAGNETIZED ELECTRON BEAMS FOR STORAGE RINGS

A cold magnetically guided electron beam, overlapped in a straight section of the ring with the stored hot ions moving at the same average velocity, provides efficient cooling of the ions [7]. Merged electron and ion beams can also be used for collision experiments if the electron energy is for a short time period detuned from the cooling velocity and recombination products (neutral or ions) are detected downstream. In the case of the Heidelberg TSR (see Fig.1) with a maximum magnetic rigidity of about 1.4 Tm, ions are injected at the ring with typical energies of 0.1-8 MeV/u, which corresponds to electron cooling energies (for singly charged ions) from about 50 eV up to 4.4 keV.

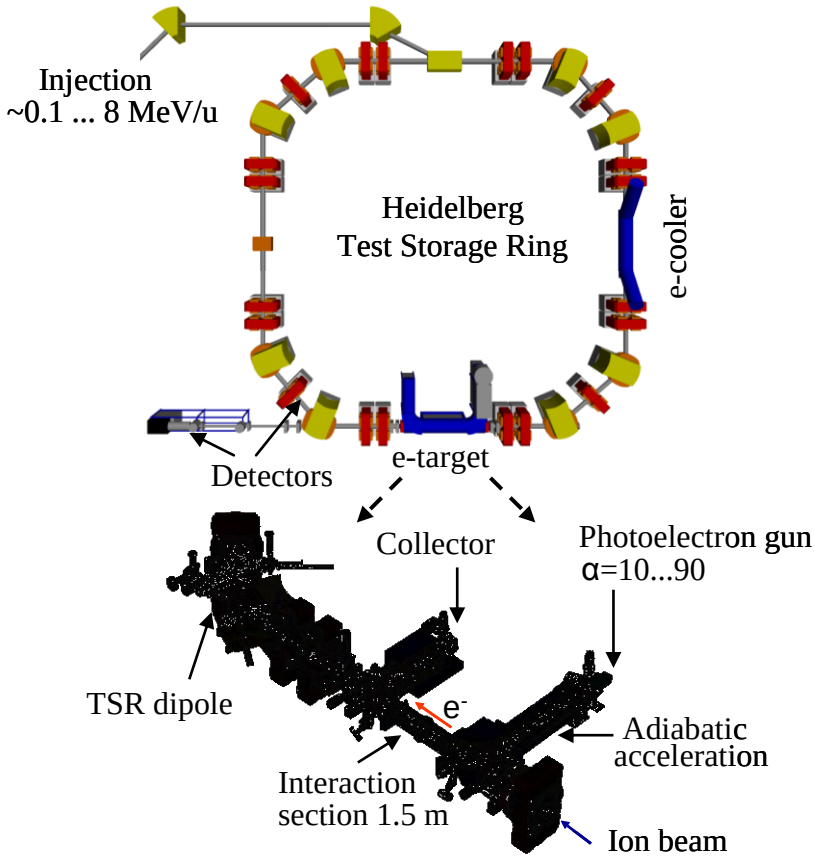

FIGURE 1. Schematic view of the Heidelberg TSR (top) and close up view of the e-target (bottom).

The TSR is the only storage ring equipped with two independent electron beam facilities, which allowed us to perform electron collision experiments at variable relative energies avoiding the resolution loss caused by the interruption of the electron cooling and by dragging of ions to the detuned electron energy [8]. The TSR electron cooler is equipped with a thermocathode source capable to deliver electron currents up

to 0.3 A, while the electron target is dedicated to high resolution measurements with typical currents below one mA. A cryogenic GaAs photocathode source, developed for the electron target [2,3,4], delivers electron beams up to few mA with an emission energy spread of about 10 meV. By subsequent adiabatic magnetic expansion and acceleration electron beam temperatures below 1 meV are obtained [5,6]. A schematic view of the TSR electron target is also shown in the Fig.1. The photocathode vacuum setup (not shown here) is attached to the electron gun. Electrons are extracted from the cathode in a strong magnetic field up to 4 T, which is reduced in field strength by a factor of 20-40 (typically) to decrease the transverse temperature. Guided by the resulting final magnetic field of 0.02-0.1 T, the drifting electron beam is bent by a toroid field to overlap collinearly with the stored ion beam for a distance of about 1.5 m. After the interaction section, electrons are demerged from the ion beam by the second toroid and then follow the guiding field which brings them to a collector, where the beam profiles and energy distributions of electrons can be measured with the help of a retarding field energy analyzer.

Electron Beam Temperatures

Beam densities as well as electron temperatures are the key parameters of the electron beams used for electron cooling and for merged electron-ion beam experiments. The guiding magnetic field of a strength given above helps to avoid space-charge divergence of the beam, to provide adiabatic transport of electrons from the gun to the interaction area, and to suppress transverse longitudinal relaxation in the electron plasma. The decoupling of transverse and longitudinal electron motion results in a strongly anisotropic energy distribution of the electron beam with a longitudinal temperature $kT_{\parallel}$ of about 0.05-0.1 meV, which is much smaller than the transverse one $kT_{\perp}$ of about 1-10 meV.

Initially $kT_{\perp}$ is given by the cathode temperature T_C and is reduced by an adiabatic magnetic expansion to $kT_{\perp}=kT_C/\alpha$, where α is the expansion coefficient [9,10]. The longitudinal temperature $kT_{\parallel}$ of electrons in the co-moving frame (we have electron beams as the reference frame) is given by:

$$kT_{\parallel} = \frac{(kT_C)^2}{E_{kin}} + C\frac{e^2}{4\pi\varepsilon_0} n_e^{1/3}. \qquad (1)$$

It is reduced due to kinematic transformation, when the beam is accelerated, to the first term in Eq. (1), where E_{kin} is the electron energy in laboratory frame. In this expression it is also taken into consideration that for $\alpha >> 1$ a large part of the transverse energy is transferred to the longitudinal one during adiabatic magnetic expansion, which increases the first term by a factor of about 2. The second term, with n_e representing electron densities, appears due to the relaxation of the internal energy of the moving plasma forming the electron beam, where the parameter C describes the quality of the acceleration [11]. It amounts to about 1.9 for fast acceleration and of about 0.7-0.8 for the TSR target using an adiabatic acceleration scheme. For electron energies *above* 100 eV, the kinematic term is small and the longitudinal temperature is defined mainly by the electron density and independent on emission energy spread.

However, it is emphasized here that for lower energies the situation reverses with the longitudinal temperature becoming strongly dependent on the cathode temperature.

Collision Energy Resolution, Cooling Efficiency

In recombination experiments, the electron temperatures lead to an asymmetric broadening δE of the observed cross-section resonances. The low-energy side of the resonance is broadened by $kT_\perp$, while $kT_\parallel$ effects in broadening the resonance symmetrically by $4(E_r\, kT_\parallel \ln 2)^{1/2}$, with E_r being the resonance energy [12]. Thus, the highest resolution (of about $kT_\perp$) is obtained at lowest energies typically below 0.1 eV.

The cooling time of the stored ions strongly depends on the electron density as well as on the transverse and the longitudinal temperatures of the electron beam, and on the charge Z_e and mass M_{ion} of the ions. The longitudinal momentum spread of the ions and the transverse emittance of the ion source, as well as the space-charge induced momentum spread of the electrons are also important to calculate cooling times. Assuming that ion beams are injected into the ring with a momentum spread lower than the electron momentum spread (as is typical for TSR), a first approximation of cooling times τ can be done in the model of a non-magnetized electron beam [13] with an electron temperature kT_e identical to the transverse temperature, yielding

$$\tau = \frac{3mc^3(4\pi\varepsilon_0)^2}{8\sqrt{2\pi}e^4}\,\frac{M_{ion}}{n_e \cdot Z^2 \cdot L_C}\cdot\left(\frac{kT_e}{m\,c^2}\right)^{3/2}, \qquad (2)$$

where L_c is the Coulomb logarithm. The cooling time can be reduced further by using a magnetized electron beam with small longitudinal temperatures [14], which also defines the size of the cooled ion beam.

The cooling force of the TSR cooler is typically much stronger than for the target due to its higher electron currents. However, at low cooling energies below 100 eV, when the electron current is limited by gun perveance to values below 1 mA, the electron target cools the slow ions much faster due to the high quality (low temperatures) of its electron beam [15].

PHOTOCATHODE SETUP

The photocathode vacuum setup consists of three chambers (see Fig. 2): the photoelectron gun chamber (basic pressure $1.2\cdot10^{-11}$ mbar), the photocathode preparation chamber ($4\cdot10^{-12}$ mbar) and combined loading and atomic hydrogen chamber ($2\cdot10^{-9}$ mbar). The chambers are connected via all metal gate valves with photocathodes being transferred between the chambers by magnetically-driven manipulators. In the electron gun, the photocathode is cooled by continuously flowing liquid nitrogen, regulated by a mass-flow-control unit, which allows the cathode temperature to be changed in the range from 80 K up to 300 K.

We are using transmission–mode GaAs–photocathodes, consisting of a two–layer ($GaAs/Al_{0.5}Ga_{0.5}As$) semiconductor heterostructure, covered with an antireflection coating and bonded to a thick sapphire base plate via a thin (10 - 20 µm) glass layer [16]. Before loading, photocathodes are cleaned in a HCl – isopropanol solution in a glove-box filled by pure nitrogen and are then transferred to the loading chamber

inside of a nitrogen–filled transfer vessel without any contact to the laboratory atmosphere. After attachment of the transfer vessel to the loading chamber and after pumping it out, photocathodes are moved into the preparation chamber and mounted on a carousel capable of keeping four cathodes. The carousel can be rotated into different positions for heat cleaning and (Cs,O) activation to NEA – state. This scheme of the photocathode preparation reproducibly provides photocathodes with high quantum efficiencies (QE) of ~ 20%. The main drawback of the scheme is that only ~ 3-4 restorations of degraded photocathodes by heat-cleaning and reactivation are possible. During the following cycles of heating and activation the QE drops strongly. In addition, the effect of current limitation due to surface photovoltage is observed for multiply recleaned cathodes. Formerly it was required to remove cathodes from the vacuum chamber for the chemical cleaning in the glove-box to restore their emission properties. With the low-energy atomic hydrogen treatment, multiple refreshings of the photocathodes within the UHV set up became possible.

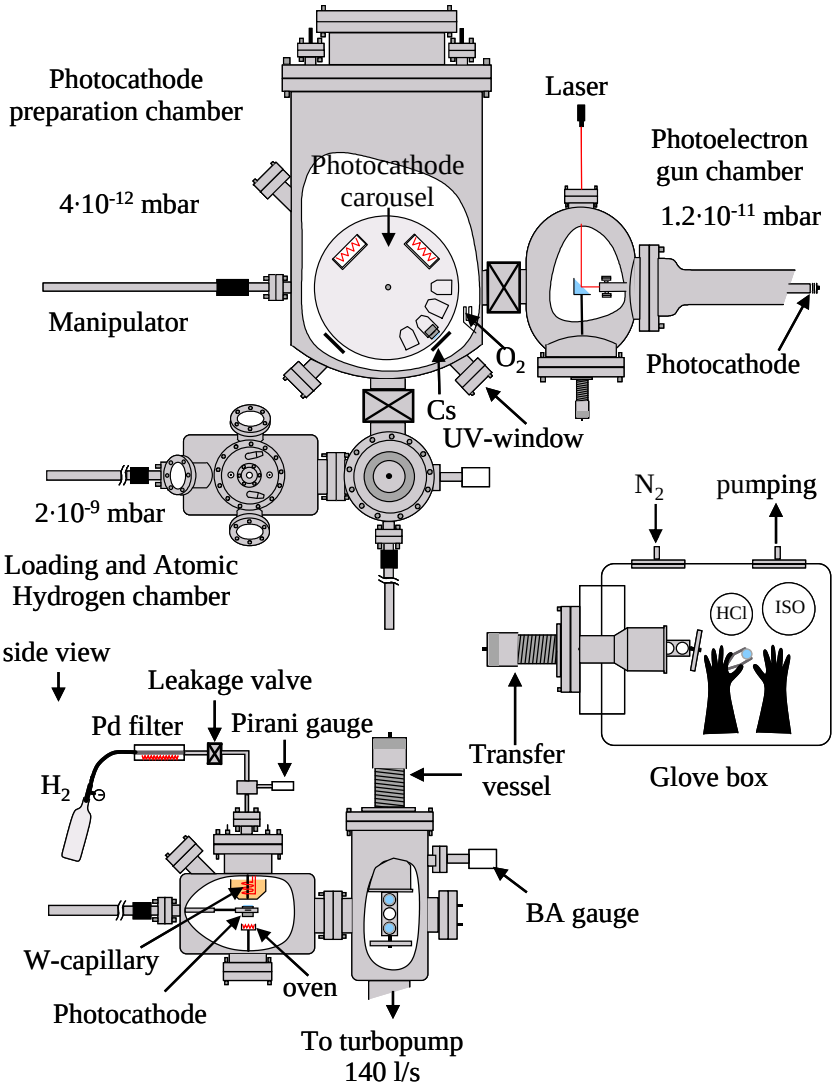

FIGURE 2. Schematic view of the photocathode treatment setup.

Atomic Hydrogen Treatment

Atomic hydrogen (AH), produced by thermal cracking of H_2-molecules inside a hot tungsten capillary, was implemented for the cleaning of transmission-mode GaAs–photocathodes with high quantum efficiency in a UHV multi–chamber photoelectron gun of the electron target. In contrast to previous measurements, where AH from RF sources was used [17,18], the low-energetic hydrogen from the capillary source was proved to be an efficient tool for *multiple* in-situ recleanings of the high QE cathodes without generating a "fatal" concentration of recombination centers within the near-surface region.

The design of our source (see Fig. 2) follows ideas presented in the paper [19] where a long tungsten capillary served as a high efficiency thermal cracker. Molecular hydrogen is brought into the hydrogen chamber through a heated palladium filter attached to the inlet of the capillary. We used a 60-mm-long capillary of 0.6 mm inner diameter. A 15-mm-part of the capillary near its outlet was heated by 21 W electron bombardment resulting in a capillary temperature of (1610 ± 25) ^{0}C. This temperature was high enough to crack 3-5% of the hydrogen molecules passing through the capillary, and was still sufficiently low to avoid a pollution of the GaAs surface by tungsten vapor. The pressure of molecular hydrogen at the inlet of the capillary was varied with a leakage valve in the range of 0.005-0.75 mbar, while the corresponding change of the pressure in the loading chamber, pumped by a 140 l/s TPU 180 H Balzers turbopump, was 10^{-7}-10^{-5} mbar. The exposure time was varied in the range of 2-15 minutes. For the AH treatment the cathode was heated to 450 ^{0}C. Afterwards the valve at the inlet of palladium filter was closed, and the heating filaments of the oven and of the capillary were turned off. The following activation of the cathode by (Cs,O) in the preparation chamber typically resulted in quantum efficiencies of 10% -15% at $\hbar\omega$ = 1.86 eV. It was also found experimentally that additional thermal annealing of the AH–treated photocathodes at about 450 ^{0}C during 30 min within the preparation chamber, increases the achievable QE to 15% - 20%, and up to 20-25% using two-step-activation (with a maximum value of 35%). After degradation during the cathode operation in the electron gun, the photocathodes were heat-cleaned and activated 3-4 times with the maximum QE typically being obtained for the second activation. After that, the AH cleaning was required to recover the emission properties. UV photoelectron spectroscopy was used to optimize and to control the efficiency of the atomic hydrogen and heat treatments. It was found that an atomic hydrogen exposure of 50-200 L is sufficient to remove the degraded activation layer from the GaAs surface.

Since 2002 AH–cleaning is routinely used for the refreshing of GaAs photocathodes at the TSR electron target. Ten photocathodes from two groups were used, two of which were grown by liquid phase epitaxy (LPE) and the others by metal–organic chemical vapor deposition (MOCVD). Photocathodes from the same group behaved in a similar way with respect of multiple AH-cleaning, but there was a difference between the groups. The LPE grown photocathodes, after cleaning with HCl–isopropanol, heat-cleaning and subsequent activation showed a maximum QE of about 15 – 25% achieved with two-step activation. A serious of AH treatments, each with a typical dose of about 400 L, was used for the LPE grown photocathode with a

total exposure as high as 5800 L. Within some uncertainties, no degradation of the QE was observed. Photocathodes from the MOCVD group showed a different evolution of the quantum efficiency. With these photocathodes higher initial QE of about 25 - 30% were routinely obtained. Moreover, the first AH cleaning typically resulted in an increase of the QE with an obtained highest value of 35 %. However, further AH cleanings (21 with total exposure of 5100 L for the sample with longest history) and reactivations of these photocathodes lead to a slow, steady decay of the QE with a saturation value at about 15 %. We varied hydrogen exposures within 100 - 440 L but did not see strong improvements. The refreshing of the surface with HCL treatment inside glove box did not rise QE value proving that the surface cleanness is not responsible for the steady QE degradation along with the number of AH treatments. The possible reason of the degradation is believed to be due the insertion of a dislocation network inside the semiconductor structure during multiple heat-cleaning cycles of up to 450 ^{0}C. Indeed, transmission – mode GaAs photocathodes on glass or sapphire substrates are mechanically strained and potentially have a risk to develop a dislocation net along with heat-treatment cycles even at moderate temperature treatment due to the different thermal expansion coefficients of the semiconductor heterostructure and the sapphire base plate. Study of the surface morphology of degraded photocathodes with an atomic force microscope indeed revealed the existence of a mesh – like structure resulting from the dislocation network which is inserted into the heterostructure during multiple high temperature treatments under the influence of mechanical strain. More studies are needed to minimize the dislocation density in strained photocathodes.

TSR ELECTRON TARGET PERFORMANCE

Using the cryogenic photocathode source, ultra cold electron beams were obtained, with transverse and longitudinal temperatures of <1 meV and 0.03 meV, respectively [4,5]. By controlling and systematically reducing different degradation effects like cryosorption, back stream of ionised rest gas, and pressure rise due to electron-induced gas desorption from the chamber walls, the lifetime of the photocathodes was strongly improved. Presently, the lifetime at high currents is limited by back-stream of ions and amounts to about 24 hours at 1 mA current. A large number of high resolution recombination measurements on atomic and molecular beams were performed using the cryogenic photoelectron source [5,20,21]. Below we demonstrate the performance of the photoelectron beam device in the TSR source as a high resolution electron target as well as an efficient cooler for low-energy ion beams.

Dielectronic Recombination of $^{45}Sc^{18+}$: QED Test Bench for Li-like Ions

In dielectronic recombination (DR) between atomic ions and electrons a free electron is resonantly captured into a Rydberg state, accompanied by the excitation of electrons already bound by the target ion (core excitations). Radiative decay of this intermediate autoionizing state completes the recombination. DR takes place when the electron collision energy equals the difference of the core excitation energy and the

Rydberg binding energy. In many cases of lithium-like and beryllium-like systems, binding energies of high Rydberg states can be calculated with high accuracy. In these cases, measurements of the DR rate coefficient at high energy resolution are tools to precisely derive the transition energies of the core valence electrons. The highest precision is reached when studying resonances of low energies (ideally below ~ 0.1 eV). In this case the experimental resolution reaches an optimal value close to the transverse electron temperature $kT_{\perp}$, which is better than 1 meV for the TSR's ultra cold electron target.

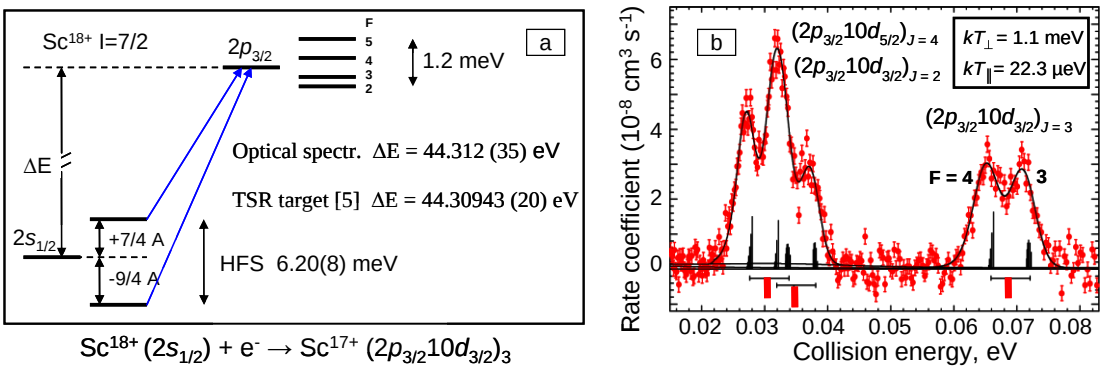

FIGURE 3. a) Energy level scheme for the $2s$-$2p_{3/2}$ transition of lithiumlike Sc^{18+}; b) high-resolution experimental DR rate coefficient spectrum of Sc^{18+} forming Sc^{17+} [5].

Measurements of low-energy DR resonances of lithium-like Sc^{18+} (see Fig.3), performed at the Heidelberg Test Storage Ring (TSR) with a cold photoelectron target, allowed us to determine the $2s_{1/2}$-$2p_{3/2}$ transition energy with an accuracy of 4.6 ppm, less than 1% of the few-body effects on radiative corrections [5]. The high resolution for the first time allows hyperfine components of DR resonances to be resolved in an electron collision experiment, revealing the hyperfine doublet of the $2s_{1/2}$ ground state due to the I=7/2 nuclear spin of ^{45}Sc. The analysis of the more complex hyperfine structure for the Rydberg DR resonances allows us to determine the resonance term energies from the hyperfine-split experimental peaks. The $2s_{1/2}$-$2p_{3/2}$ transition energy is found from these terms using relativistic many-body perturbation theory (RMBPT) and yielding the Rydberg binding energies to ~0.0001 eV.

CF^+ Cooling by 53 eV Electrons

Electron cooling experiments at low energies were performed at the TSR target on a CF^+ beam of energy 3 MeV (about 97 keV/u) [15]. The corresponding electron cooling energy is of about 53 eV. The diameter of the magnetically expanded electron beam was 13 mm (α=20), the electron current was limited by gun perveance to about 0.34 mA (electron density 3×10^6 cm^{-3}). In the case of the slow CF^+ ion beam the electron target was found to be by far stronger in cooling force than the TSR's e-cooler, providing much shorter cooling times. The CF^+ current in the storage ring after injection was estimated to be of a few 100 pA and the lifetime of the ion beam was about 4 s.

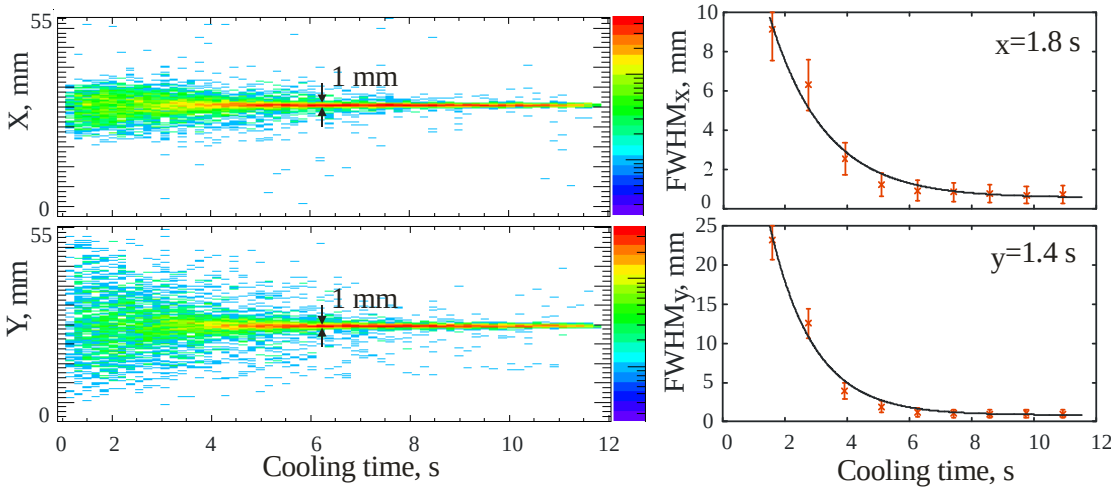

FIGURE 4. Transverse electron cooling of 97 keV/u CF^+ [15]. Centre-of-mass positions of the C and F neutral fragments vs time, recorded 12 m downstream of the electron target by the imaging detector and indicating rms divergence angles of about $3{\cdot}10^{-5}$.

Imaging detectors 12 m downstream of the electron target were used to measure neutral recombination fragments and to analyze the dissociation dynamics. The transverse momentum of the dissociation fragments is recorded event by event using a spatially resolving multi-hit detector (two-dimensional fragment imaging) [22].

For atomic ion beams the spatial profile of the neutral atoms produced by recombination in the electron target directly reflects the angular divergence of the ion beams [23]. For molecules, the imaging profile can not be used directly to monitor transverse ion beam properties during the phase space cooling due to the significant kinetic energy release in the dissociation process. However, this can be achieved by monitoring the centre-of-mass of all fragment hit positions for a given recombination event, which reflects the direction of the molecular ion before it captured an electron in the target [24].

Figure 4 (left) shows the distribution spread of the centre-of-mass as a function of the cooling time derived from correlated two-hit events for both transverse directions. The FWHM of the centre-of-mass distribution vs time is also shown in Fig. 4 (right). A transverse cooling time below 2 s was achieved, demonstrating a high cooling efficiency of the photocathode electron beam. An estimation of the cooling time from Eq. (2), assuming an isotropic electron beam with 1 meV temperature, L_c=3.3 and the length of the target to be about 2.2% of the ring circumference, gives a value of about 1.5 s for a cold ion beam and 6 s for a hot ion beam (with a diameter of the injected ion beam about 2 times larger than that of the electron beam). After 6 s a FWHM of the centre-of-mass distribution of 1 mm (horizontally) and 0.7 mm (vertically) was measured by the imaging detector. Assuming a longitudinal ion spread of about $5{\cdot}10^{-5}$ and using the horizontal TSR dispersion of 2 m and the β functions of 3.9 m (horizontal) and 1.5 m (vertical) at the target section, the divergence and size of the ion beam can be derived. The divergence was found to be of about $3{\cdot}10^{-5}$ in both transverse directions and the 1σ size was about 0.04 mm (vertically) and 0.2 mm (horizontally). The larger size of the ion beam in the horizontal direction arises from

the ring dispersion and from fluctuations of the power supplies for dipole magnets and cathode voltage.

Thus, the short cooling times and the very small equilibrium beam size obtained in these experiments demonstrate the high potential of cryogenic photocathode electron beams for electron cooling of slow ions, in particular for electrostatic Cryogenic Storage Ring under construction at the Heidelberg MPI-K [25,26].

CONCLUSIONS

Ultra-cold photoelectron beams from a cryogenic GaAs electron gun, developed for the Heidelberg TSR target, was found to be excellent tool for high-resolution recombination measurements at storage rings as well as for eV-cooling of low-energy ions. The source can deliver electron currents up to few mA with a typical lifetime of about 24 hours and provides unprecedented energy resolution below 1 meV. Atomic hydrogen treatment, developed for in-situ refreshing of the high quantum efficiency GaAs photocathodes inside of the gun vacuum setup, provides conditions necessary for non-stop operation of the electron target.

REFERENCES

1. D.A. Orlov et al., *Appl. Phys. Letters* **78**, 2721-2724 (2001).
2. D.A. Orlov et al., *NIM A*, **532**, 418-421 (2004).
3. U. Weigel et al., *NIM A*, **536**, 323-328 (2005).
4. D.A. Orlov et al., *J.Phys.: Conf. Ser.* **4**, 290-295 (2005).
5. M. Lestinsky et al., *Phys. Rev. Lett.* **100**, 033001 (2008).
6. D.A. Orlov et al., "Ultra-cold electron beams for the Heidelberg CSR and TSR," in *Beam cooling and related topics*, edited by S. Nagaitsev and R.J. Pasquinelli, AIP Conference Proceedings 821, American Institute of Physics, Melville, NY, 2006, pp. 478-487.
7. N.Meshkov, *Phys. Part. Nucl.* 25, 631-661 (1994).
8. F. Sprenger et al., *NIM A*, **532**, 298-302 (2004).
9. T.M. O'Neil and P.G. Hjorth, *Phys Fluids*, **2**8, 3241-3252 (1985)
10. S. Pastuszka et al., *NIM A*, **369**, 11-22 (1996).
11. N.S. Dikansky, Preprint **88-61**, Institute of Nuclear Physics, Novosibirsk, 1988.
12. Al-Khalili et.al., *Phys. Rev. A*, **68,** 042702 (2003).
13. L. Spitzer, "Physics of fully ionized gases", Inter-science, New York, 1956.
14. Ya.S. Derbenev, A.N. Skrinskii, *Sov. Phys. Rev.* **1**, 165-237 (1981).
15. D.A. Orlov et al., "*Electron cooling with photocathode electron beams applied to slow ions at TSR and CSR*", in *Proceedings of COOL 2007*, edited by R.W. Hasse and V. RW Schaa, Bad Kreuznach, Germany, 2007, pp.230-233.
16. Developed and manufactured in the group of Prof. A.S. Terekhov.
17. T. Maruyama et al., *Appl. Phys. Letters* **82**, 4184-4186 (2003).
18. M. Baylac et al., *Phys. Rev. ST AB* **8,** 123501(2005)
19. U. Bischler, E. Bertel, *J. Vac. Sci. Technol. A* **11**, 458-460 (1993)
20. H. Kreckel et al., *Phys. Rev. Lett.* **95**, 263201 (2005).
21. S. Novotny et al., *Phys. Rev. Lett.* **100**, 193201 (2008).
22. Z. Amitay, *Phys. Rev. A* **54,** 4032-4050 (1996)
23. G.I. Budker et al., Part. Accel. **7** 197-211 (1976).
24. A. Wolf et al., NIM A **532,** 69-78 (2004).
25. D. Zajfman et al., *J.Phys.: Conf. Ser.* **4**, 296-299 (2005).
26. A. Wolf et al., "The Heidelberg CSR: Stored Ion Beams in a Cryogenic Environment," in *Beam cooling and related topics*, edited by S. Nagaitsev and R.J. Pasquinelli, AIP Conference Proceedings 821, American Institute of Physics, Melville, NY, 2006, pp. 473-477.

Optimization of Semiconductor Superlattice for Spin Polarized Electron Source

L. G. Gerchikov[a], Yu. A. Mamaev[a], V. V. Kuz'michev[a], Yu. P.Yashin[a], V. S. Mikhrin[b], A. P. Vasiliev[b], A. E. Zhukov[b]

[a]*St. Petersburg State Polytechnic University, Russia*
[b]*A. F. Ioffe Physicotechnical Institute RAS, Russia*

Abstract. Optimized AlInGaAs/AlGaAs superlattice with strained quantum wells has been developed, fabricated and studied. The choice of hetero-layer composition and thicknesses is based on calculations of Sl's band energy spectrum, photoabsorption spectrum and transport properties. Electron emission from the developed photocathodes demonstrates maximal polarization above 90%.

Keywords: Polarization, Photoemission, Superlattice.
PACS: 72.25.Fe,73.21.Cd,79.60.-i

INTRODUCTION

The use of short-period superlattices (SL) opens up wide possibilities for band structure engineering of photoemitter working layer. The optimal choice of SL's layers composition and thickness providing the high energy splitting of the valence band together with good transport properties for photoelectrons have made it possible to design photocathodes with electron polarization above 90% [1-3]. Photocathodes based on GaAs/GaAsP [1] and AlInGaAs/GaAlAs [2] SL structures with strained quantum wells (QW), GaAs/AlInGaAs-based SLs [3] with strained barriers, and so-called compensated SLs based on AlInGaAs/GaAsP SL structures with opposite strains in the wells and barriers [4] have been developed.

These studies have also revealed several fundamental difficulties for achieving further progress. High electronic polarization, *P*, is achieved at the expense of quantum efficiency, *QE*. Indeed, the maximal spin orientation of photoelectrons takes place at the photoabsorption threshold where the light absorption coefficient is rather small. Maximal polarization of photoelectrons is limited by the mixture of light and heavy hole states which takes place even at the absorption edge due to the broadening of the valence band energy spectrum and smearing of the valence band edge. The mixture of light and heavy hole states can be reduced by increasing the energy splitting ΔE_{hh-lh} between the *hh* and *lh* subbands. However the splitting of SL valence band due to the deformation is limited by some critical value. Deformation beyond this level results in structural defects, smaller residual strain and lower polarization.

The valence band splitting ΔE_{hh-lh} in SL cannot exceed the valence band offsets. Therefore, to create a significant splitting $\Delta E_{hh-lh} \approx 100$ meV, SL with large band offsets at the heterointerfaces must be used. In this case, high barriers of hundreds of meV usually appear in the conduction band that complicates the transport of photoelectrons to the photocathode surface. Low electron mobility along the SL axis reduces the *QE*. This leads to a partial loss of spin orientation by electrons during their transport to the surface due to D'yakonov–Perel' mechanism [5] for spin relaxation.

Thus, choosing the optimal structure of a SL to provide large ΔE_{hh-lh} splitting in the absence of strain relaxation and in combination with good transport properties is a difficult problem. The solution requires a reliable method to calculate the energy spectrum of the SLs on the basis of ternary and quaternary III–V semiconductor compounds. In addition, the maximum value of photoelectron polarization depends crucially on the structural quality of the SLs, which imposes heightened requirements on the technology of their growth.

VALENCE BAND SPLITTING

The initial polarization of the photoelectrons can be increased by choosing structures with a high valence band splitting. The SL structures with strained QW layers where heavy and light hole minibands, in addition to the strain splitting, are moved aside due to different light and heavy-hole confinement energies in the QW, are the best for this purpose. However strain induced splitting and splitting caused by quantum confinement do not combine additively and the resulting energy splitting is a complicated function of SL composition and layer thickness. Deformation splitting of the QW's valence band edge increases the QW depth for heavy holes and decreases it for the light holes. Thus the increase of deformation splitting reduces the quantum confinement contribution to ΔE_{hh-lh}. Fig. 1 illustrates the choice of optimal QW thickness for $Al_{0.19}In_{20}Ga_{0.61}As/Al_{0.4}Ga_{0.6}$ As SL with strained QW and 2.1nm thick barriers. Here we show the positions of the highest hole minibands together with the energy splitting ΔE_{hh-lh}. calculated within multiband Kane model [6] as a function of the QW width a. For our structure we have chosen the QW width a = 5.4nm because the increase of ΔE_{hh-lh} at $a > 5.4$ nm saturates while the risk of strain relaxation increases.

The deformation of QW layer and hence the deformation energy splitting of the valence band edge linearly varies with In concentration. The chosen for our structure In concentration 0.2 corresponds to 76meV of deformation splitting that together with quantum confinement contribution results in ΔE_{hh-lh} = 87eV. This valence band splitting is sufficient to provide the initial polarization of photoelectrons of up to 97% [2].

Aluminum concentration in the QW layer does not affect the deformation but changes the energy gap value. We have chosen it equal to 0.19 to adjust the photoabsorption threshold of SL and hence the position of the main polarization maximum to λ = 820nm. The Al concentration in the barrier layer 0.4 was chosen to achieve sufficiently high barriers in the SL's valence band in order to provide large ΔE_{hh-lh}. On the other hand the conduction band barriers should be transparent enough for effective electron transport. This was achieved by the choice of the barrier width b

= 2.1nm. For the chosen SL's composition the barriers for electrons, heavy and light holes are equal to 339 meV, 149 meV and 77 meV, respectively.

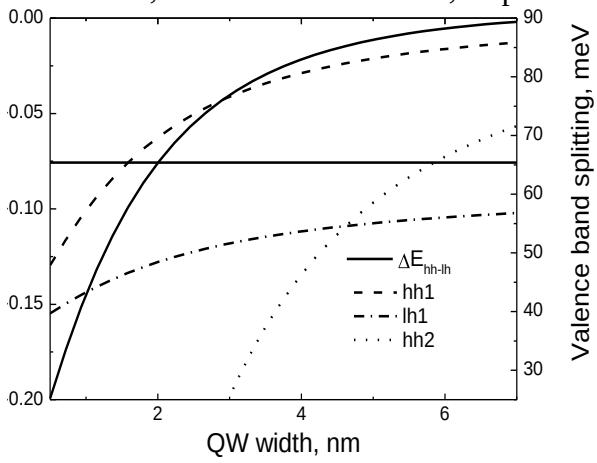

FIGURE 1. Edges of the first two heavy hole minibands, hh1 and hh2, and the first light hole miniband, lh1, are shown together with the energy splitting between hh1 and lh1 minibands ΔE_{hh-lh} as a functions of the QW width for $Al_{0.19}In_{20}Ga_{0.61}As/Al_{0.4}Ga_{0.6}As$ SL. The miniband energies are counted from the position of the heavy hole valence band edge of the QW layer. The position of the light hole valence band edge spitted by QW deformation is shown by horizontal line.

ELECTRON TRANSPORT

Optimization of electron transport along the SL axis is crucially important for SLs with strained QW because of the presence of relatively high barriers in the conduction band. To determine the transport properties of the SL we calculate the electron tunneling probability along the SL axes neglecting any electron collisions with phonons and impurities. In Fig. 2 we show the tunneling probability together with the tunneling time, τ, calculated as a function of electron energy within the range of the first electron miniband. We consider the stationary electronic current incidents on the SL and determine the tunneling time as the ratio of number of electrons inside the SL to the electron current penetrated through the SL. Each resonance peak of tunneling probability curve corresponds to electronic state localized within the SL. The resonance width Γ is proportional to the inverse tunneling time, $\Gamma = \hbar/\tau$. The energy distance between the resonances ΔE is proportional to the inverse period of electronic motion within the SL, $\Delta E = \hbar/\tau_{SL}$. Since $\Gamma << \Delta E$ the total tunneling time is much larger than the time of electron motion within the SL, $\tau >> \tau_{SL}$, i.e. τ is determined mainly by the tunneling through the last barrier. It is quite natural because the tunneling between the neighboring QWs is a resonant process and its probability is proportional to the first order of the tunneling exponent $\exp(-\kappa b)$, where κ is the electronic wave vector under the barrier and b is the barrier width. The tunneling through the last barrier is a non resonant process and its probability is much smaller since it is proportional to the second order of the tunneling exponent $\exp(-2\kappa b)$. It is clear that the optimal design of the SL providing equal probability for each tunneling

will be achieved by taking the last barrier of half width *b*/2 [7]. In Fig. 2 we show by dash-dotted and dotted lines tunneling probability and tunneling time calculated for such optimized SL. In this case the tunneling resonances overlap, at least at the middle of the miniband, and the total tunneling time is decreased.

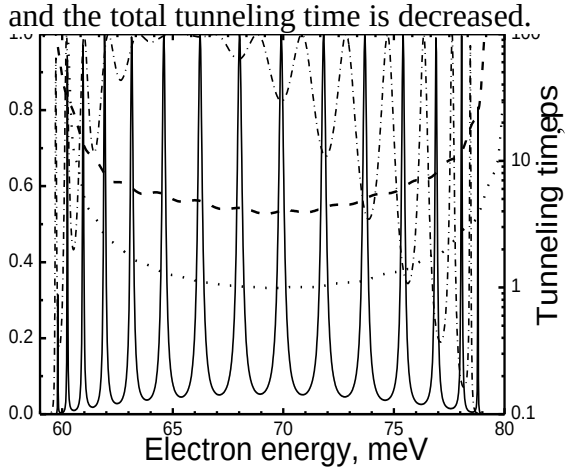

FIGURE 2. Tunneling probability (solid line) and tunneling time (dashed line) calculated for 15 periods $Al_{0.19}In_{20}Ga_{0.61}As$(5.4nm)/$Al_{0.4}Ga_{0.6}$ As(2.1nm) SL. Electron energy is counted from the bottom of electronic QW. Dash-dotted and dotted lines show the results obtained for the same SL with the last barrier of 1nm width.

The calculated tunneling time even for the optimized SL is larger by the order of magnitude than the typical collision time for electrons within the QW $\tau_p \approx 10^{-13}$s. Thus, to evaluate the real transport time one should take into account electron collisions with phonons and impurities. We do it by solving the kinetic equation within the constant relaxation time approximation. In the case of stationary optical pumping we derive the following expression for the transport time

$$\tau = \frac{(N-1/2)(N-1)}{6\tau_p}\tau_b^2 + N\tau_f, \qquad (1)$$

where N is the number of SL's periods, τ_b and τ_f are the tunneling times for the barriers within the SL and the last barrier, respectively. According to Eq.(1), the transport time is a sum of diffusion time within the SL given by the first term in r.h.s. of Eq.(1) and the time $N\tau_f$, taken to penetrate through the last barrier to the band bending region (BBR). Note, that obtained Eq.(1) is similar to the corresponding expression of the bulk case [8]. The first term in Eq.(1) corresponds to the diffusion term with diffusion coefficient $D = 2d^2\tau_p/\tau_b^2$ and the second term corresponds to the surface recombination term with surface recombination velocity $S = d/\tau_f$, $d = a + b$ is the SL period. For the developed $Al_{0.19}In_{20}Ga_{0.61}As$(5.4nm)/$Al_{0.4}Ga_{0.6}$ As(2.1nm) SL their values, D = 12 cm^2/s and $S = 3*10^6$ cm/s, are three times smaller than in the case of bulk GaAs. For 12 periods SL Eq. (1) gives the transport time τ = 5ps. The main contribution, 3ps, comes from the last tunneling. The use of last barrier with half width 1nm could make

the time of the last tunneling five times smaller, $N\tau_f$ = 0.6ps, and hence considerably decrease the total transport time, τ = 2.6ps.

SUMMARY AND OUTLOOK

We have developed an optimized InAlGaAs/AlGaAs SL with strained quantum wells for photocathode working layer. The optimal SL design provides maximal valence band splitting ΔE_{hh-lh} = 87eV with minimal risk of strain relaxation and good transport properties. Electron emission from the best photocathode based on the developed SL demonstrates the highest level of polarization of the photoelectrons P = 92% in combination with the largest quantum efficiency at polarization maximum QE = 0.85%. Further progress in development of polarized electron sources can be based on new structures with better structural quality and optimized transport properties. However maximal values of P and QE are limited by unavoidable losses of electrons and their polarization in BBR. Also, QE is strongly limited by the fact that the most part of incoming light is absorbed in the substrate. The use of Distributed Bragg Reflector can resolve this problem and considerably increase the QE of photocathode.

ACKNOWLEDGMENTS

This work was supported by Russian Ministry of Education and Science under grant N.P. 2.1.1.2215 and by Swiss National Science Foundation under grant SNSF IB7420-11111.

REFERENCES

1. T. Nishitani, T. Nakanishi, M. Yamamoto, S. Okumi, F. Furuta, M. Miyamoto, M. Kuwahara, N. Yamamoto, K. Naniwa, O. Watanabe, Y. Takeda, H. Kobayakawa, Y. Takashima, H. Horinaka, T. Matsuyama, K. Togawa, T. Saka, M. Tawada, T. Omori, Y. Kurihara, M. Yoshioka, K. Kato, T. Baba, *J. Appl. Phys* **97**, 094907 (2005).
2. Yu. A. Mamaev, L. G. Gerchikov, Yu. P. Yashin, D. A. Vasiliev, V. V. Kuzmichev ,V. M. Ustinov, A. E. Zhukov, and V. S. Mikhrin, *Appl.Phys.Lett*. **93**, 81114 (2008).
3. L. G. Gerchikov, Yu. A. Mamaev, A. V. Subashiev, Yu. P. Yashin, D. A. Vasil'ev, V. V. Kuz'michev, A. E. Zhukov, E. S. Semenova, A. P. Vasil'ev and V. M. Ustinov, *Semiconductors*, **40**, 1326 (2006).
4. A. V. Subashiev, L. G. Gerchikov, Yu. A. Mamaev, Yu. P. Yashin, J. S. Roberts, D.-A. Luh, T. Maruyama, and J. E. Clendenin, *Appl. Phys. Lett*. **86,** 171911 (2005).
5. *Optical Orientation*, edited by F. Meier and B. P. Zakharchenya, North-Holland, Amsterdam, 1984.
6. A.V. Subashiev, L.G. Gerchikov, and A.I. Ipatov. *J. Appl. Phys.*, **96**, 1511 (2004).
7. V. A. Tkachencko, V. E. Andreev, O. A. Tkachenko, V. L. Alperovich, A. S. Proc. *10th Intern. Symp. on High Energy Spin Physics*, Nagoya, Japan, 1992, p.857-860.
8. K. Aulenbacher, J. Schuler, D. v. Harrach, E. Reichert, J. Roethgen, A. Subashev, V. Tioukine, Y. Yashin, *J. Appl. Phys*., 92, 7536 (2002).

A Study of the Activated GaAs Surface for Application as an Electron Source in Particle Accelerators

N. Chanlek[a,b], J.D. Herbert[b] , L.B. Jones[b] , R.M. Jones[a] and K.J. Middleman[b]

[a]*University of Manchester, Manchester, M13 9PL, United Kingdom*
[b]*STFC Daresbury Laboratory, Warrington, WA4 4AD, United Kingdom*

Abstract. The use of type III-V semiconductor materials as photocathodes has in recent years become a focus for the High Energy Physics community. Once activated to a negative electron affinity (NEA) state and illuminated by a laser, these materials can be used as a high-brightness source of both polarised and un-polarised electrons in some modern accelerators, for example, ALICE (Accelerators and Lasers in Combined Experiments) at Daresbury Laboratory. This paper will focus on the use of gallium arsenide (GaAs) as a photocathode, and detail the re-configuration and re-commissioning of two vacuum systems that support standard surface science techniques such as ultraviolet/X-ray photoelectron spectroscopy (UPS/XPS), low energy electron diffraction (LEED) and auger electron spectroscopy (AES). The paper will present details of cleaning GaAs in order to maximise quantum efficiency and will provide evidence from XPS and LEED to demonstrate what is happening at the atomic level.

Keywords: negative electron affinity (NEA), gallium arsenide (GaAs), photocathode, x-ray photoelectron spectroscopy (XPS) and low energy electron diffraction (LEED)
PACS: 29.20.-c, 29.25.Bx, 61.05.cj, 61.05.jh

INTRODUCTION

Gallium arsenide (GaAs) photocathodes are being used as electron sources for various modern particle accelerators and next generation light sources. For example, the ALICE ERL prototype, a 35 MeV energy recovery test facility, is currently under commissioning at Daresbury Laboratory [1]. The current design of this machine requires an electron source that can generate a continuous wave (CW) current of 6.5mA (electron beam) as a pre-cursor to the 100 mA injector with a normalised emittance of $< 2\,\pi$ mm mrad [2].

It is well known that once activated to a negative electron affinity (NEA) state, the GaAs photocathode can be used as a high-brightness, low emmitance electron source [3,4]. This state is prepared by depositing caesium and an oxidant (either O_2 or NF_3) onto its atomically clean surface. The preparation process involving handling, preparation and cleaning processes is an essential step in the performance of the NEA GaAs photocathode. However, the fundamental nature and mechanism of these processes is not well understood, and clarification has been the subject of research for many years.

In this article we report on the progress of the re-configuration and re-commissioning of two vacuum systems which will allow the study and investigation of the photocathode activation process using the surface science techniques available within the same vacuum system. We also present the preliminary results of an X-ray photoelectron spectroscopy (XPS) and low energy electron diffraction (LEED) study on the effects of heating temperature on the GaAs surface in the heat cleaning process.

EXPERIMENT SET UP

Figure 1 shows our present experimental chamber configured at the Cockcroft Institute, STFC Daresbury Laboratory. The chamber consists of three sections, a loading chamber, cathode preparation chamber and surface analysis chamber which are isolated by gate valves. The photocathode sample is introduced to the system through the loading chamber which is pumped down via a dry turbomolecular pumping system. Once a suitable pressure has been reached the sample can be transferred between the sections using a transfer arm. The cathode preparation chamber includes a manipulator with sample holder and all of the components needed to clean and activate a cathode to the NEA state. The sample holder is isolated from the chamber wall by a ceramic ring and connected to a UHV electrical feedthrough so that a bias voltage can be applied to the sample. The chamber is also equipped with a caesium dispenser and a hydrogen gas cracker. The chamber is kept at a base pressure of 1×10^{-10} mbar by a dry turbomolecular pumping system, a DI ion pump and additional NEG pumping modules. The surface analysis chamber is equipped with a twin anode X-ray source, a hemispherical analyser for ultraviolet/X-ray photoelectron spectroscopy (UPS/XPS) technique, a LEED optics for low energy electron

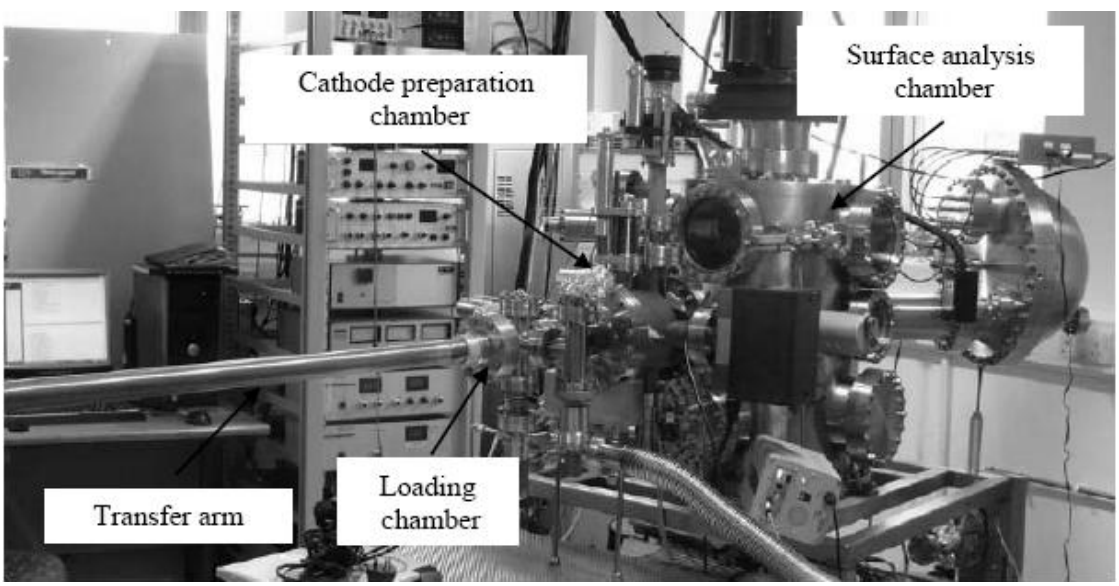

FIGURE 1. Picture of Photocathode experimental chamber which has been set up at the Cockcroft Institute, STFC Daresbury Laboratory.

diffraction (LEED) and auger electron spectroscopy (AES) technique, ion gun for sample sputter cleaning and RGA for residual gas analysis. This chamber is maintained at a base pressure of 1×10^{-10} mbar via a turbopump connected directly and supported by a turbomolecular drag dry pump system and two NEG pumps.

RESULTS AND DISCUSSION

For preliminary results, the heat cleaning procedures for a GaAs photocathode were studied. Bulk VGF (vertical gradient freeze) GaAs samples of p-type doping (Zn) without any chemical cleaning were loaded in order to leave native contaminants on the surface. The samples were heated to five different temperatures; 450, 500, 550, 600 and 625 °C for 60 minutes in the surface analysis chamber. During heating, the temperature of the sample surface was monitored via an infrared pyrometer which has the resolution of ±15 °C. Note that this error comes from the rough calibration because, presently, no accurate emissivity of the GaAs photocathode could be estimated. The XPS spectra of the GaAs surface excited by Al $K\alpha$ (1486.6 eV) radiation were taken before and after heat cleaning process. The typical contaminants for GaAs such as oxygen, carbon and chlorine were observed on the dirty sample surface [5]. The removal by heat cleaning of oxides which are the main coverage contaminants on the GaAs surface was studied, with representative results as shown in Fig. 2.

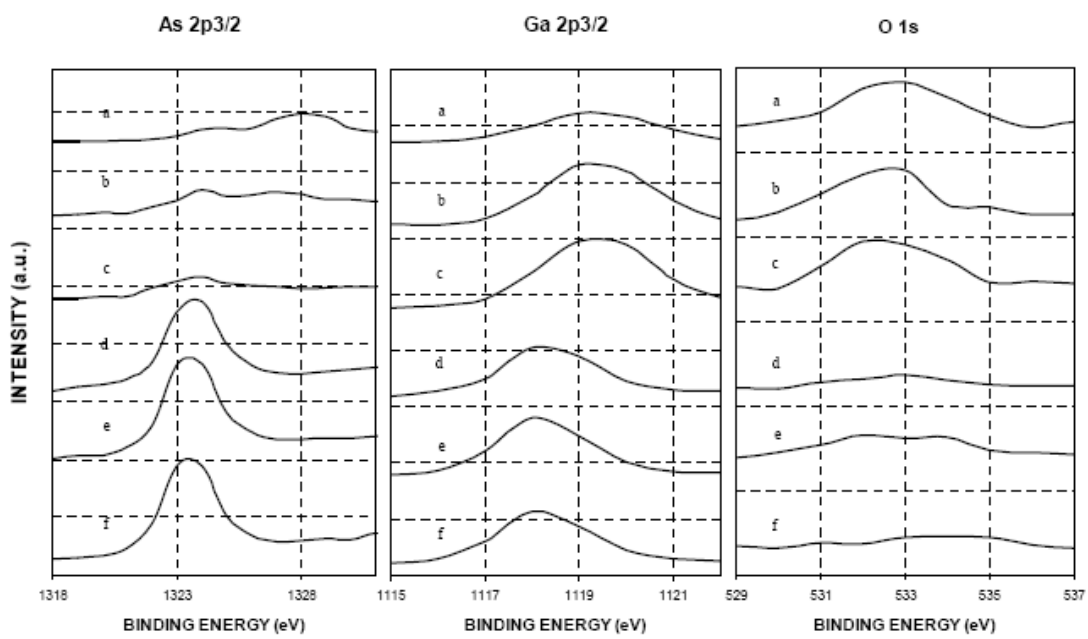

FIGURE 2. XPS spectra of the As $2p_{3/2}$, Ga $2p_{3/2}$ and O 1s for (a) the initial dirty sample, (b) after heating to 450°C for 60 min, (c) 500°C for 60 min, (d) 550°C for 60 min, (e) 600°C for 60 min and (f) 625°C for 60 min.

The core-level energy of the As $2p_{3/2}$ (1324 eV), Ga $2p_{3/2}$ (1117 eV) were observed and the presence of As_2O_3 and Ga_2O_3 were determined by the core-level energy shifts of 3 and 1 eV toward higher energies, respectively [6, 7]. The XPS spectra show that the energy shifts of the As $2p_{3/2}$, Ga $2p_{3/2}$ peaks decreased when the heating temperature was increased, and at the same time the intensity of As core-level energies increased. These results indicate that the surface oxides are desorbed from the GaAs surface under heat cleaning, and are completely removed after heating to a temperature higher than 550 °C for 60 min. This is also consistent with the reduction in the O 1s intensity.

The activation to NEA surface and measurement of the quantum efficiency (QE) was made after heating the sample to each of the different temperatures. Caesium and oxygen were deposited onto the sample by using the standard "yo-yo" method [3]. The samples were illuminated with a HeNe laser at 632.8 nm during the activation process to drive the photocurrent and calculate the highest QE of the sample. The QE of the GaAs samples are shown in Fig. 3. As is clearly seen, the QE of the GaAs samples increases when the cleaning temperature is increased, agreeing with the XPS results that the oxide overlayer is removed under heat cleaning. A QE of 4.12% was obtained as a result of heating the sample at 600°C, however, the QE dropped to 3.81% after heating to 625°C. This result shows that heating to excessive temperatures might damage the properties of the GaAs, resulting in a detrimental effect on the QE.

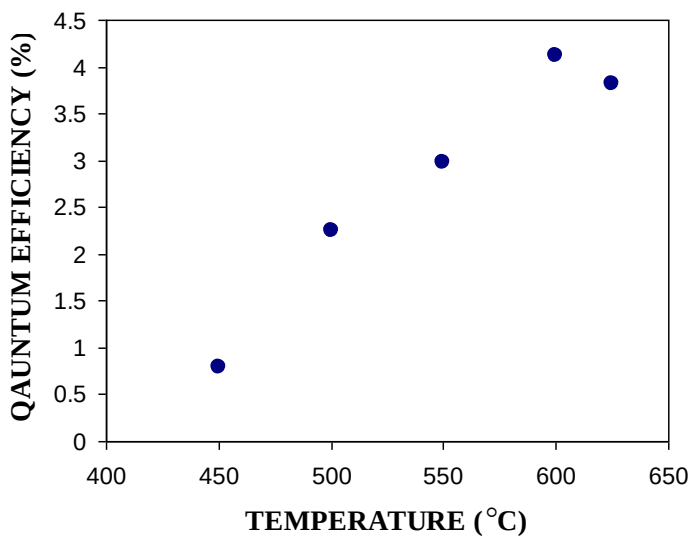

FIGURE 3. Quantum efficiency as a function of heat temperature in heat cleaning procedure.

To further our studies, the LEED pattern of the GaAs sample was also taken after heating to the different temperatures. It was found that a clear LEED pattern can be observed after heating the sample to a temperature of 550°C for 60 min, as shown in Fig. 4, indicating that the sample has a clean and well-ordered surface.

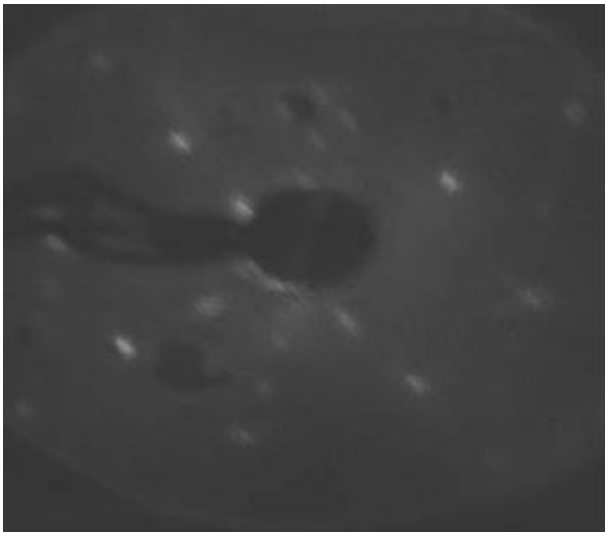

FIGURE 4. LEED pattern of the GaAs surface after heat the sample to 550°C for 60 min.

CONCLUSIONS

The amalgamation of two vacuum systems has been completed at the Cockcroft Institute, Daresbury Laboratory in order to study and investigate the photocathode material in detail. This experimental set up allows us to prepare and study the properties of the photocathode material using the application of surface science techniques such as ultraviolet/X-ray photoelectron spectroscopy (UPS/XPS), low energy electron diffraction (LEED) and auger electron spectroscopy (AES) within the same vacuum system.

The heat cleaning procedure for the NEA GaAs photocathode was studied. It was found that oxides from the GaAs surface can be removed after heating to a temperature higher than 550°C for 60 min. However, the heating temperature need to be optimized, as excessive temperatures can result in decreasing in the QE.

ACKNOWLEDGMENTS

The authors are grateful for support from ASTeC and STFC Daresbury Laboratory.

REFERENCES

1. Daresbury Laboratory, 4thGeneration Light Source, ERLP Construction, accesses September 2008, http://www.4gls.ac.uk/ERLP.htm
2. B.L. Militsyn (private communication).
3. D.T. Pierce and F. Meier, *Phys. Rev. B* **13**, 5484(1980).
4. T. Maruyama, D.-A. Luh, A. Brachmann, J.E. Clendenin, E.L. Garwin, S. Harvey, R.E. Kirby and C.Y. Prescott, *Appl. Phys. Lett.* **82**, 4184 (2003).
5. J. Uebbing, *J. Appl. Phys*. **41** 802(1969).
6. E. J. Petit and F. Houzay, *J. Vac. Sci. Technol. B.* **12**, 547(1994).
7. Z. Lu, M.T. Schmidt, D. Chen, R.M. Osgood, W.M. Holber, D.V. Podlesnik and J. Forster, *Appl. Phys. Lett.* **58**, 1143(1991).

Recent Progress toward Robust Photocathodes

G. A. Mulhollan and J. C. Bierman

Saxet Surface Science, Austin, TX 78744, USA

Abstract. RF photoinjectors for next generation spin-polarized electron accelerators require photocathodes capable of surviving RF gun operation. Free electron laser photoinjectors can benefit from more robust visible light excited photoemitters. A negative electron affinity gallium arsenide activation recipe has been found that diminishes its background gas susceptibility without any loss of near bandgap photoyield. The highest degree of immunity to carbon dioxide exposure was achieved with a combination of cesium and lithium. Activated amorphous silicon photocathodes evince advantageous properties for high current photoinjectors including low cost, substrate flexibility, visible light excitation and greatly reduced gas reactivity compared to gallium arsenide

Keywords: Photocathode, NEA, GaAs, Immunization, Photoyield decay, Amorphous silicon, FEL
PACS: 85.60.Ha, 29.25.Bx

INTRODUCTION

The motivations for robust photocathodes are manifold. Ideal photoemitters would perform well under very poor vacuum conditions. In practice, improved performance in operable vacuum is always desirable. It is well known that the environment in RF guns is still tough on photoemitters, though designs incorporating better pumping represent good progress. High electron spin-polarization photocathodes continue to demand ultra high vacuum (UHV) conditions for reliable operation. Better environmental immunity for these photocathodes is required for successful operation in RF guns, such as could be employed for the ILC. Photocathodes operated in high average current injectors manifest cumulative damage which limits operational lifetimes.

Photocathode environmental interactions may be viewed as stemming from either chemical reactions or charged particle fluence. The principal source for chemical reaction participants is the background gas. Electron beam induced desorption can increase the quantity of these reactants. Several gas species, such as CO_2, H_2O and O_2 are known to be harmful to the lifetime of negative electron affinity (NEA) photocathodes[1]. Detrimental charged particle fluences at photocathodes are primarily composed of ions. Low energy ions, most likely in RF guns, generate atomic displacements near the surface and can affect the activation layer as well as the near surface crystal structure. This damage can be annealed out and the photocathode activated again to an NEA state. High energy ions, such as found in DC guns can cause many displacements per particle if they impact the photocathode. The damage to the photocathode crystalline structure can be widespread and if the energy is large enough, the damage may not anneal out. Both high and low energy ion interactions can affect yield and the emitted electron spin-polarization.

HIGH POLARIZATION PHOTOEMITTER IMMUNIZATION

Generation of high spin-polarization electrons from III-V and related semiconductors mandates the emitter be crystalline. Both single strained-layers and superlattices (strained and unstrained) have been employed in this role. The use of an activation layer to achieve NEA is also a requirement in common. The first goal of this work was to achieve a level of immunity against background gas chemical reactivity for such emitters. Several groups have studied the decay process of NEA photocathodes. While good progress toward understanding the chemical makeup of diminished yield photocathode surfaces has been made[2], both in process and susceptibility, this information has not provided insight into the prevention of the decay process, aside from straightforward improvements in vacuum base pressure leading to increased lifetimes. Our approach to the problem was to attempt to de-activate potential reaction sites. The overlayers on activated GaAs(100) are amorphous. This can be partly attributed to the large covalent radius of cesium, $\sim$2.3 Å, compared to the GaAs nearest neighbor distance. In a billiard ball model, large gaps are present between the cesium atoms. In fact, they are large enough for a much smaller covalent radius atom, e.g., oxygen, $\sim$0.73 Å, to fit through them and bond to the semiconductor surface and/or cesium. This argument suggests that if access to the underlying surface could be blocked during or following the activation process, then absorbed gas induced decay could be inhibited. The true picture must be formulated in terms of electron charge density with the gaps actually being regions of low charge density. An obvious choice for a blocking atom is another, smaller covalent radius alkali. While all alkali atoms lower the GaAs(100) electron affinity, the best performance is from cesium. This indicates that blocking the surface reactivity is likely to incurr a cost in the yield.

An alkali source flange containing Cs, Rb, K, Na and Li getter channels was constructed to allow testing of each alkali's effects on yield and sensitivity to reactive gas exposure. This flange was installed into an existing photocathode test system, described elsewhere[3]. Activations were first performed with each alkali individually to establish the proper operating curents. Standard activations were performed by depositing alkali until a peak in photocurrent was achieved. Following the peak, the oxidizer gas was introduced. The oxidizer partial pressure was adjusted for maximim photocurent increase (co-deposition) until the final peak value was achieved. In all cases, the activation oxidizer gas was NF_3. Carbon dioxide was chosen as the archtype decay gas. It is a known strong reactant with NEA surfaces and is readily distinguishable in residual gas spectra. Dosing data were acquired under computer control. The cathode bias was disconnected between data points and the light source was shuttered when not in use. First, dark current values were acquired for each point, then the light source was unshuttered for the emission measurement. Data were recorded once a minute. Dosing consisted of three segments. In the first 30 minutes, the photocathode was exposed only to the normal background gas, base pressure $4\text{x}10^{-11}$ Torr, primarily H_2. In the second segment, the pressure, as measured by a nude ion gauge, was increased to $1.5\text{x}10^{-10}$ Torr by introduction of the dosing gas, and in the final segment the pressure was increased to $5.0\text{x}10^{-10}$ Torr.

In keeping with the above argument, activations using two alkali types were initially attemped by introducing the second, non-Cs alkali after the first photocurrent peak was

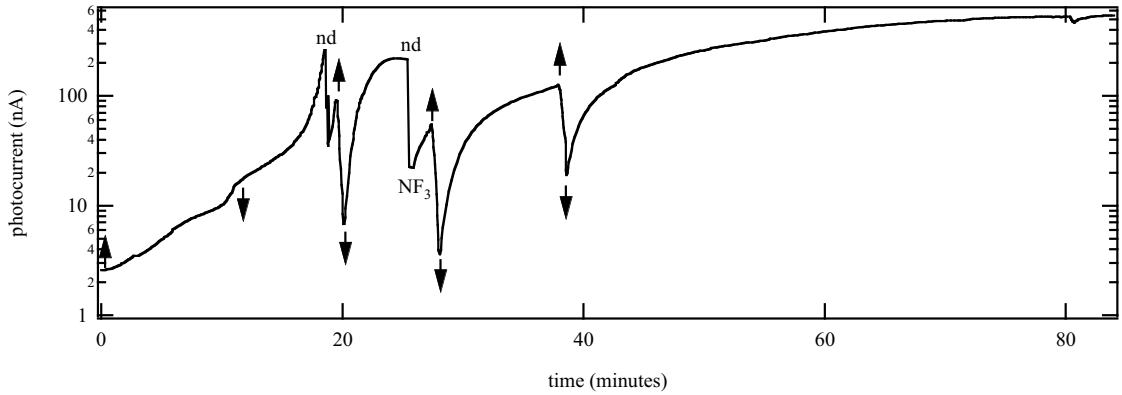

FIGURE 1. Activation curve for Cs + Li activated bulk GaAs. Up arrows indicate when the Li is on and down arrows when off. Neutral density filter insertion is indicated by 'nd'.

achieved. The second alkali was deposited at the rate required for the single alkali activations to complete in the same time as those using Cs alone. Both alkalis were used to complete the activation. These activations resulted in lower than normal photoyields and little resilience to the dosing gas. However, the decay curves for the Na and Li dual alkali activated photocathodes did evince a lower decay rate when dosed than the other combinations. By limiting the second alkali's exposure during most of the activation, reasonable yields were achieved and relatively better immunity to the dosing gas was achieved. An example of the activation with Li as the second alkali is shown in Fig. 1.

Figure 2 shows the yield decay upon dosing for bulk GaAs at 633 nm. The dual alkali activated photocathode maintained a yield $\sim$2x that of the standard activated GaAs after the low pressure dosing and $\sim$6x that of the standard activated GaA at the end of the high pressure dosing. Comparable, but not as dramatic results were observed for Cs and Na activated GaAs. Number and timing of deposition of the second alkali was investigated.

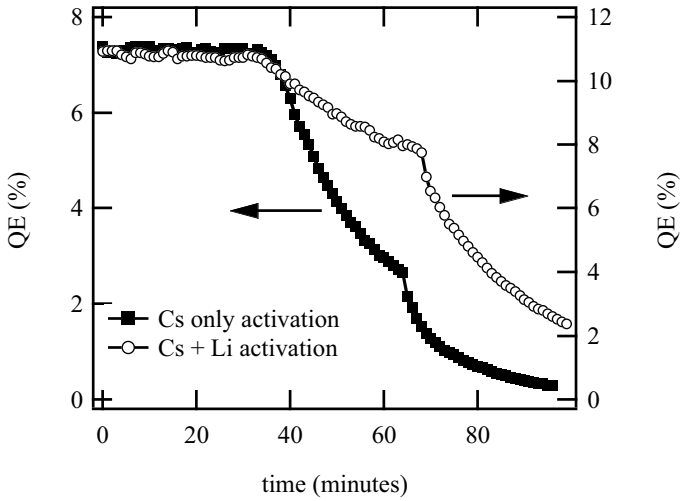

FIGURE 2. Comparison of yield decay at 633 nm for Cs only and Cs + Li activated bulk GaAs.

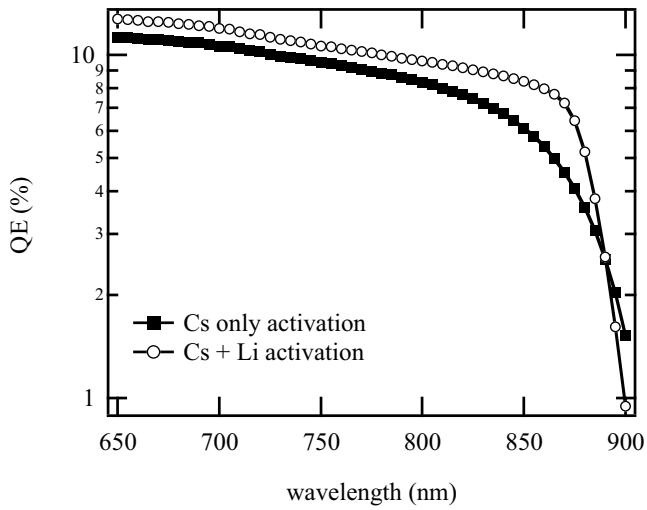

FIGURE 3. Yield curves for bulk GaAs activated with Cs only and Cs + Li.

Critical is the presence of the second alkali at the start of the activation. Subsequent depositions, both in timing and number, are less critical to achieve the best immunity. Yield data for standard Cs only activated and Cs + Li activated bulk GaAs are shown in Fig. 3. Overall the yield does not suffer from the addition of Li. Taking into account sample-to-sample variation, the numerous Cs + Li activated photocathodes, using the activation shedule of Fig. 1, all gave excellent photoyield. The yield curve, however, for the Cs + Li activated sample exhibits a much less rounded shape near the bandgap. This shape change is very repeatable and does not occur for the Cs + Na activated photocathodes. The addition of the Li changed not only the reactivity of the surface, but the shape of the surface barrier as well.

AMORPHOUS SiGe PHOTOEMITTERS FOR FEL SOURCES

Amorphous Si photocathodes have been grown in our laboratory both by sputter deposition and RF PECVD. Advantages of a-SiGe for use in an FEL injector gun include *ex situ* growth so that the growth apparatus is separated from the injector load system. Amorphous SiGe can be grown on many substrates including tantalum, glass, stainless steel and copper. The latter requires a diffusion barrier. Either transmission or reflection modes can be used. RF PECVD is a mature technology and a-SiGe can be grown to accommodate nearly any photocathode electrode shape. The chemical clean prior to vacuum introduction is easy, low cost and rapid. These photocathodes activate in a manner familiar to operators used to III-V photocathodes. The low temperature heat clean reduces stress on vacuum components and makes introduction systems simpler and less expensive. An a-SiGe photocathode can be reactivated without an additional heat clean if the yield is allowed to decay. Under background gas and ion exposure, a-SiGe photoemitters have shown considerably better performance than the III-V based photocathodes. As-grown photocathodes stored for 9 months activated as readily as freshly-grown samples. We have even demonstrated its use as a photoelectron source in stand-alone

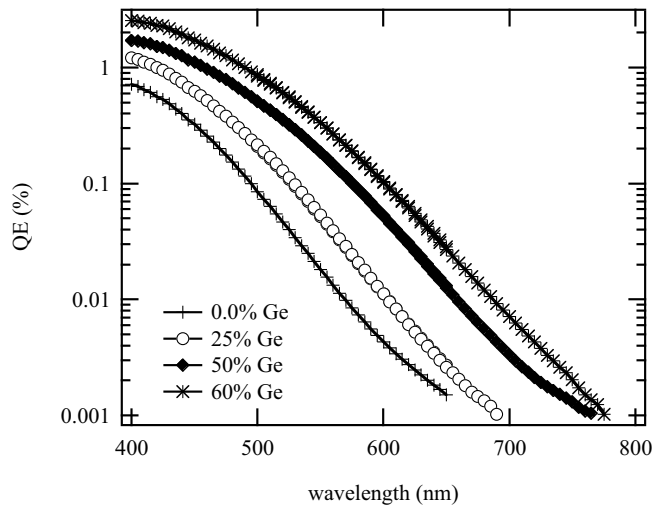

FIGURE 4. Yield curves from a-$Si_{(1-x)}Ge_x$ for various values of x.

vacuum tubes.

SUMMARY AND OUTLOOK

The addition of a second alkali to the activation of bulk GaAs has been shown to reduce its reactivity with carbon dioxide, a gas which shortens the lifetime of NEA GaAs. The addition of Li also provides an interesting modification to the surface barrier. Polarization measurements on dual activated bulk, thin unstrained and high polarization III-V photocathodes will take place soon. The surface chemistry will be studied with core level XPS. Measurements of the angular emission and charge density properties of a-Si are underway. Optimization of the material through growth parameter exploration continues. Amorphous SiGe holds great promise for use as a photoemitter in harsh environments and it may be feasible to employ it as the photoemitting layer for III-V photocathodes to provide them even greater environmental protection.

ACKNOWLEDGMENTS

This work was supported by the United States Department of Energy SBIR under Grants No. DE-FG02-06ER84475 and DE-FG02-07ER84832 and the United States Navy SBIR under Grant No. N65538-08-M-0126.

REFERENCES

1. T. Wada, T. Nitta, T. Nomura, M. Miyao and M. Hagino, *Jpn. J. Appl. Phys.* **29**, 2087–2091 (1990).
2. Z. Liu, Y. Sun, S. Peterson and Piero Pianetta *Appl. Phys. Lett.* **92**, 241107–241109 (2008).
3. G. A. Mulhollan and J. C. Bierman, *J. Vac. Sci. Technol. A* **26**, 1195-1197 (2008).

Superlattice Photocathode Damage Analysis

Marcy L. Stutzman and Joseph Grames

Center for Injectors and Sources
Thomas Jefferson National Accelerator Facility
12000 Jefferson Avenue, Newport News, VA 23606

Abstract. Jefferson Lab uses 100kV DC high voltage photoguns with high polarization strained superlattice GaAs photocathodes to achieve electron beam polarization over 80%. The photocathode is subjected to back-bombardment from ionized residual gasses during operation. We present surface analyses using transmission electron microscopy (TEM) and secondary ion mass spectrometry (SIMS) to characterize photocathode damage.

Keywords: Polarized electron source, superlattice photocathode, surface charge limit.
PACS: 29.25.Bx, 79.60.-i

PHOTOCATHODE DAMAGE: INTRODUCTION AND MOTIVATION

High polarization strained superlattice GaAs photocathode material is used inside 100kV DC high voltage photoguns at Jefferson Lab's CEBAF nuclear physics accelerator to generate electron beams with polarization over 80%. We use a GaAs/GaAsP superlattice structure developed in a partnership between SVT and SLAC [1]. This material is very reliable, with initial quantum efficiency (QE) near 1%, and minimal variation between batches [2]. Further, no degradation of the electron polarization has been observed over the course of experiments lasting many months and delivering hundreds of Coulombs at QE over 0.1% (Fig.1). (During operation with QE<0.1%, some degradation of polarization has been observed and is being investigated.)

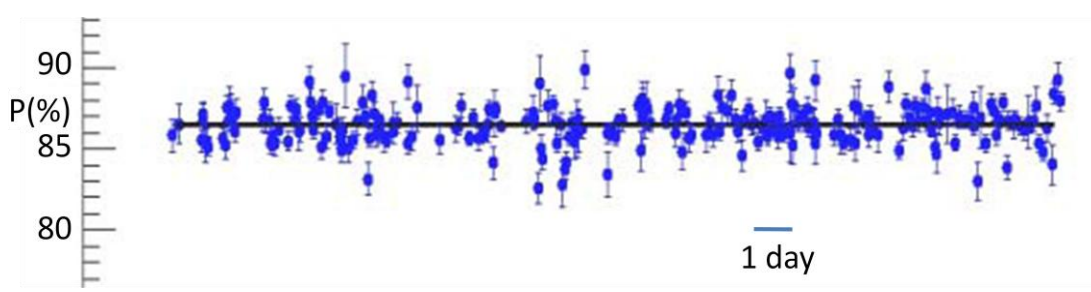

FIGURE 1. Electron beam polarization measurements from the Jefferson Lab Hall A Compton polarimeter [3] during a one month experimental run where 90 Coulombs were delivered. There is no significant variation in polarization. Note the QE is above 0.1% during this time.

In contrast with the electron polarization, we do observe a degraded "surface charge limit" (SCL) [4], where quantum efficiency of the photocathode decreases as a function of laser intensity (Fig. 2). Although the SCL effect has been observed at pulsed machines operating with bunch charge over 1 nC, it was not expected at the sub pC bunch charge used at CEBAF.

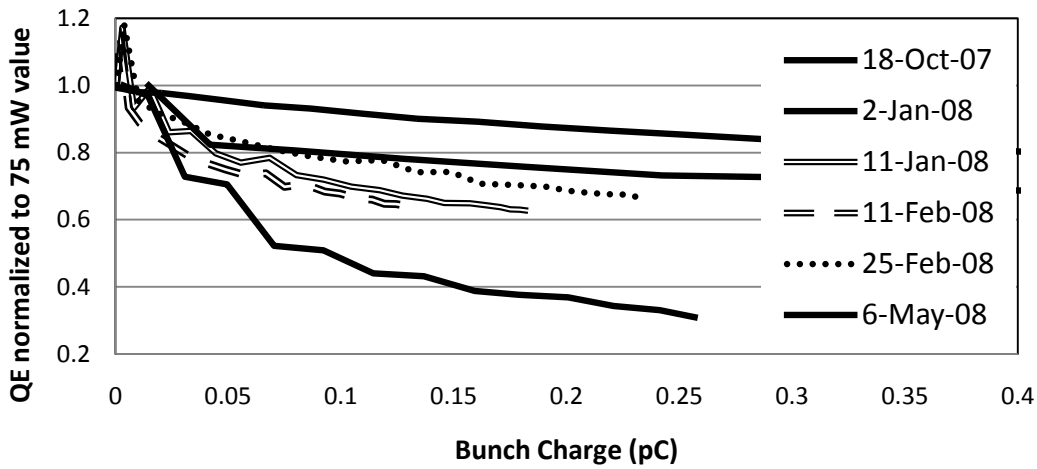

FIGURE 2 Surface charge limit measurements for a strained superlattice GaAs photocathode during its operational lifetime delivering beam in the CEBAF machine at Jefferson Lab. The total charge and charge since last heat/activation cycle are tabulated in Table 1.

TABLE 1. Summary of charge delivered from photocathode for data in Figure 1.

SCL Measurement	Total charge (C)	Charge since heat cycle (C)
October 18, 2007	2	2
January 2, 2008	256	0
January 11, 2008	305	49
February 11, 2008	422	166
February 25, 2008	444	0
May 6, 2008	618	167

Degradation of GaAs photocathodes has long been associated with the ionization of residual gasses in the photogun vacuum chamber and its acceleration into the photocathode material [5] where ions can affect both the surface chemistry and implant into the GaAs structure. The surface chemistry damage can be rejuvenated by simply adding cesium or by heating and reactivating the photocathode with cycles of Cs and an oxidant. For ions implanted into the photocathode material, thermal annealing is effective in repairing some of the damage. Measurements at Jefferson Lab using bulk GaAs indicate that extended heating (12 hours rather than a standard 2 hours at 525°C) are significantly more effective in rejuvenating the maximum yield from a photocathode, particularly in heavily damaged areas such as the electrostatic center where ions are focused.

Similarly there is evidence that heating the photocathode may be effective in reducing the effect of SCL, as shown in Fig. 2, where the photocathode was heated

and reactivated between February 11 and February 25 and the SCL effect decreased. Understanding and mitigating the SCL effect is critical for future high current experiments planned at Jefferson Lab; at high currents, the photocathode is damaged more quickly by the higher rate of ion back-bombardment, and the SCL in a damaged photocathode will prevent adequate photocurrent delivery with laser powers that would otherwise be sufficient, requiring unacceptably frequent photocathode changes.

Presented here are the initial results from surface analyses of damaged strained superlattice GaAs photocathode that was removed from the CEBAF photoinjector after more than a year of beam delivery, using two complementary techniques: transmission electron microscopy (TEM) of a focused ion beam (FIB) prepared cross section of the material, and secondary ion mass spectrometry (SIMS) analysis of the composition of ions implanted in the used photocathode material.

SURFACE ANALYSIS TECHNIQUES AND RESULTS

Transmission Electron Microscopy

The first technique used to study the damage to the strained superlattice photocathode material is transmission electron microscopy (TEM). Sample preparation for TEM analysis of the strained superlattice structure was performed at North Carolina State University using a focused ion beam (FIB) milling and lift-out technique to prepare the samples without damaging the superlattice structure [6]. The GaAs is first protected through coating with an evaporative layer of gold and palladium, next a thicker layer of platinum is sputter coated using the FIB. The FIB is then used to mill a sample for TEM analysis. The FIB milled sample is a depth cross section of the superlattice photocathode and the substrate, where the layers of the superlattice are seen in cross section. Lattice dislocation are evident (see Fig. 3a) and present in both new and used material. Areas of significant darkening, typical of ion implantation damage, can be seen in the used sample, but are not evident in the unused control sample (Fig 3b).

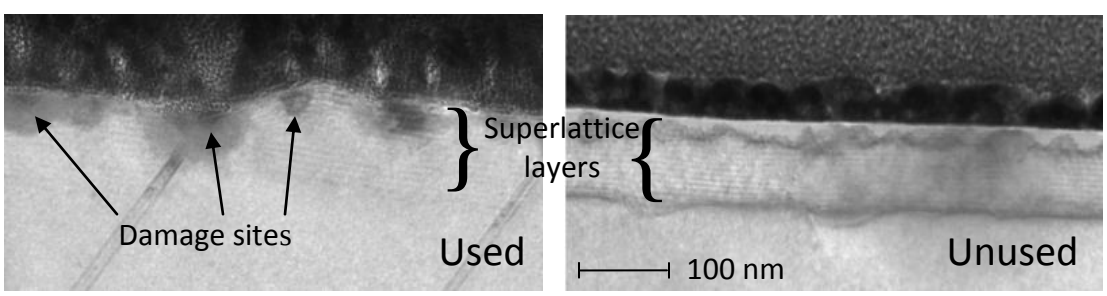

FIGURE 3: TEM images of used (left) and unused (right) superlattice photocathode material. The dark areas at the top are the Au/Pd and Pt protective layers. The 100 nm thick superlattice of 3 and 4 nm layers of GaAs/GaAsP can be seen. The used cathode shows deep "stains", which are not evident in the unused sample on the right. Blurring at the top of the unused cathode is due to a slight tilt during TEM imaging which images the gold overlayer as well as the cathode.

The damage is non-uniform across the surface of the material at this length scale. The laser spot is ~500μm diameter, far larger than the distance scales observed on this TEM image. The nature of this non-uniformity is not understood at this point.

Secondary Ion Mass Spectrometry

Secondary ion mass spectrometry (SIMS) was used to analyze composition of the ions implanted in the material. A cesium ion beam was used at several positions across the surface of the photocathode, and the secondary ions liberated were measured. As expected, the main components found in the sample are the residual gasses in the chamber: hydrogen, oxygen, carbon (from CO and CO_2) and fluorine which comes from the NF_3 used to activate the photocathode in this system.

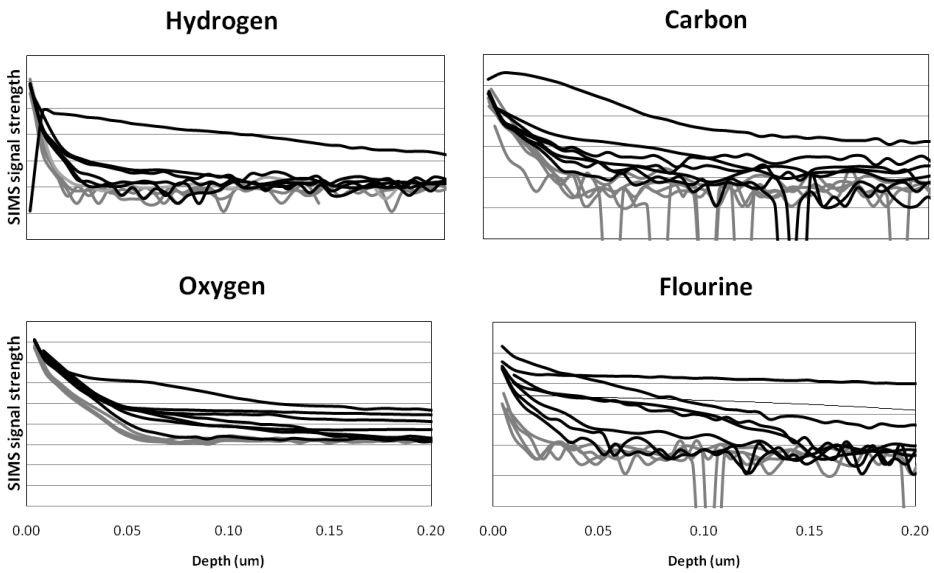

FIGURE 4. SIMS data for various species as a function of depth through the photocathode. Traces in black are from various spots across the damaged photocathode, and gray traces are from spots across the unused control sample. Signal strength is in arbitrary units, depths into the photocathode material are identical for all graphs, with the GaAs/GaAsP superlattice structure 0.1 μm thick.

FIGURE 4 shows an increased signal strength in the traces from the used samples (black lines) over the control unused samples (gray lines). Direct measurement of the common residual gasses implanted in the used photocathode is further evidence that the residual gasses are being implanted in the photocathode. The anomalously high data trace in the hydrogen, carbon and oxygen graphs is from the same position on the cathode, most likely corresponding to the electrostatic center of the photocathode, where ions are focused by the fields of the cathode/anode electrodes.

The damage analysis studies were performed on photocathode material that was used for more than a year in the single chamber horizontal gun where the photocathode is activated in the high voltage chamber, making fluorine a significant component of the residual gas. The SCL data presented above is from a new load-locked system where photocathode preparation is separate from the high voltage chamber and fluorine is no longer expected to be a significant residual gas.

Discussion of SIMS data and Comparison to Theory

Programs such as SRIM [7] can be used to calculate the depth of implantation for various residual gas species as a function of voltage. Comparison between the SRIM calculation and the SIMS data can provide an estimate of the energy of the implantation. In the case of hydrogen, energies as low as 10 kV are sufficient to implant to depths greater than the 100 nm superlattice structure from which electrons are photoemitted. The hydrogen SIMS data shows an increased hydrogen signal at depths less than 100 nm, indicating that low energy hydrogen ions implant in the photocathode. Oxygen shows increased signal strength from near the surface through to depths greater than 100 nm, while most of the carbon data shows no increase in signal until over 50 nm. SRIM simulations show a mean implantation depth of 50 nm for both carbon and oxygen at energies near 30 kV. Consequently, increasing gun voltage or decreasing cathode-anode gap, to reduce the volume of gas that ionizes at these intermediate range energies, may decrease photocathode damage.

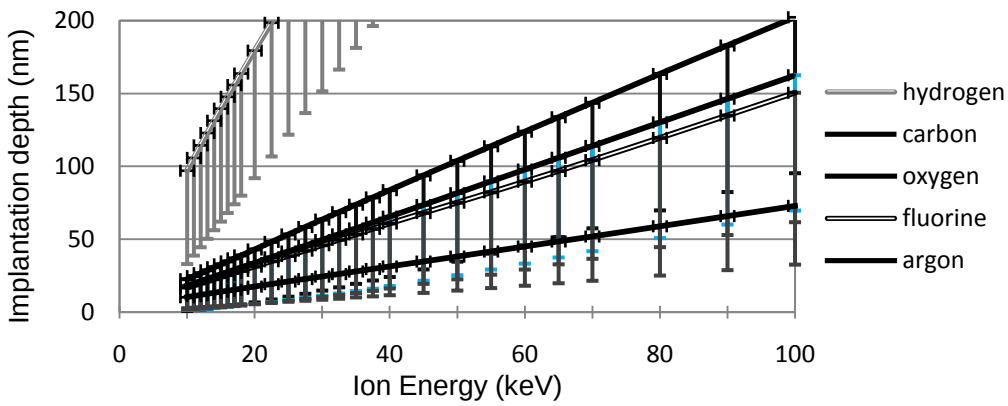

FIGURE 5. SRIM calculations showing mean stopping depths anticipated for various ion species implanted in GaAs.

CONCLUSIONS

Surface analyses of strained superlattice photocathode material used in a 100kV DC photogun show that the predominant residual gas species are implanted in the material, indicative of the ion back-bombardment model, and also provide information on the energy of the implanted ions. The non-uniform nature of the implantation sites is puzzling. We hope to perform studies of the diffusion of the beryllium dopant and any broadening of the interface between the GaAs/GaAsP superlattice layers using SIMS with an oxygen beam, which is more sensitive to the depth scale and species and aim to better understand and mitigate the observed surface charge limit effect.

ACKNOWLEDGMENTS

We would like to acknowledge the help of collaborators at North Carolina State University, Dr. Fred Stevie and Dr. Dale Batchelor, for the surface analysis techniques and interpretation of the results. Authored by Jefferson Science Associates, LLC under U.S. DOE Contract No. DE-AC05-06OR23177.

REFERENCES

1. T. Maruyama et al., Appl. Phys. Lett **85**, 2640 (2004)
2. P. Adderley et al., In the Proceedings of Particle Accelerator Conference (PAC 07), Albuquerque, New Mexico, 25-29 Jun 2007, pp 3130.
3. K.A. Aniol, et al., Phys. Lett. B 635 (2006) 275
4. T. Maruyama et al., PESP 2002 AIP Conf. Proc **675** 1083(2003).
5. K. Aulenbacher, SLAC 432-Rev., SLAC, Stanford, CA, 1994, p. 1.
6. F.A. Stevie et al., Surf. Interface Anal. 2001 **31** 345.
7. SRIM calculation program: the Stopping and Range of Ions in Matter. http://www.srim.org/

MBE Growth of Graded Structures for Polarized Electron Emitters

Aaron Moy,[a] T. Maruyama,[b] F. Zhou[b] and A. Brachmann[b]

[a]*SVT Associates, Eden Prairie, MN.*
[b]*SLAC National Accelerator Laboratory, Menlo Park, CA*

Abstract. SVT Associates, in collaboration with SLAC, has investigated two novel photocathode design concepts in an effort to increase polarization and quantum efficiency. AlGaAsSb/GaAs superlattice photocathodes were fabricated to explore the effect of antimony on device operation. In the second approach, an internal electrical field was created within the superlattice active layer by varying the aluminum composition in AlGaAs/GaAs. A 25% increase in quantum efficiency as a result of the gradient was observed.

Keywords: Polarized electrons, high polarization photocathode
PACS: 29.25.Bx, 29.27.Hj

INTRODUCTION

Polarized electrons have been essential for high-energy parity-violating experiments and measurements of nucleon spin structure, and polarized electron beams will be required for all future linear colliders. Polarized electrons are readily produced by GaAs photocathode sources. When a circularly polarized laser beam tuned to the bandgap minimum is directed to the negative-electron-affinity (NEA) surface of a GaAs crystal, longitudinally polarized electrons are emitted into vacuum. The electron polarization is easily reversed by reversing the laser polarization. The theoretical maximum polarization of 50% for natural GaAs was first exceeded in 1991 using the lattice mismatch of a thin InGaAs layer epitaxially grown over a GaAs substrate to generate a strain in the former that broke the natural degeneracy between the heavy- and light-hole valence bands [1].

In a previous collaboration between SVT Associates and SLAC, photocathodes were developed based on $GaAs_{0.64}P_{0.36}$/GaAs superlattice. These devices demonstrated polarizations as high as 86%, with quantum efficiencies exceeding 1% [2]. Two known factors limit the polarization of these cathodes: 1) a limited band splitting; and 2) a relaxation of the strain in the surface epilayer since the 10-nm critical thickness for the 1% lattice-mismatch is exceeded.

In an effort to advance photocathode operating characteristics, two different device structures were examined. The first design employed $Al_xGa_{1-x}As_ySb_{1-y}$ material to reduce depolarization. A second design employed an $Al_xGa_{1-x}As$/GaAs superlattice where the aluminum content was varied during the growth. This graded $Al_xGa_{1-x}As$ thus created an internal electrical field that would serve to accelerate electrons to the surface, increasing quantum efficiency.

ANTIMONIDE-BASED PHOTOCATHODE STRUCTURES

To address material-specific spin-depolarization and increase the photocathode robustness which is essential for an RF gun, a strained superlattice structure based on GaAs and $Al_xGa_{1-x}As_ySb_{1-y}$ was explored. In this structure, the $Al_xGa_{1-x}As_ySb_{1-y}$ layers serve as energy barriers. The GaAs layers are wells and are strained. The addition of antimony (Sb) to the material was thought to have two benefits. Firstly, antimony has 3 orders of magnitude lower diffusivity than gallium and 2 orders of magnitude lower diffusivity than arsenic [3]. Diffusion is one of the main reasons for structural and surface decomposition of cathodes, especially during heat cleaning and surface bombardment.

Secondly, antimony has higher spin orbit coupling than As, so the effect of spin orbit coupling on depolarization can be studied. The increased spin orbit coupling allows structures with larger HH-LH separation, which can increase the polarization of the photocathode effectively. Thus it is believed that antimony-based photocathodes could play an important role in spin polarized RF guns because they can combine high polarization and high robustness in poor vacuum environment

Figure 1 displays a diagram of the AlGaAsSb/GaAs superlattice structure explored. Polarized emission continues from the GaAs layers in this structure, with the strain and barrier energies being defined by the $Al_xGa_{1-x}As_ySb_{1-y}$ alloy composition. The addition of antimony (Sb) atoms in the material growth was a novel approach to the design of photocathodes with polarized electron emission.

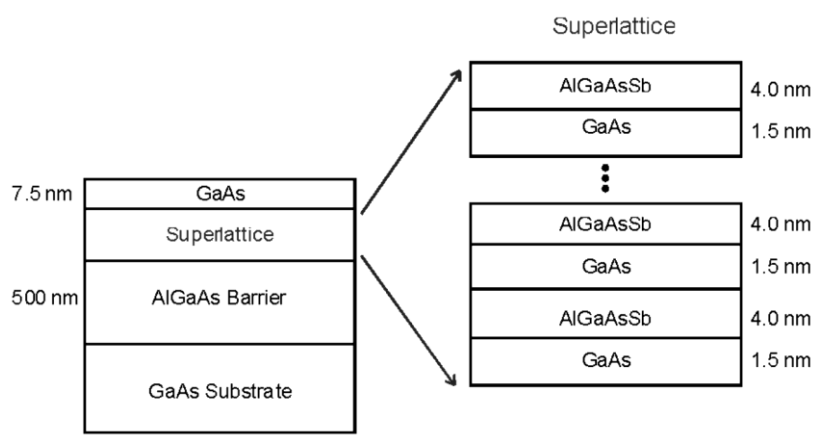

FIGURE 1. Diagram of the basic photocathode structure studied utilizing a superlattice consisting of GaAs wells and AlGaAsSb barriers.

The spin orbit (SO) coupling is more pronounced in superlattice structures due to heterointerface asymmetries. A 10-15nm GaAs layer of high p- doping (5x19 cm^{-3}) at the cathode surface is desirable in order to achieve NEA reliably. The SL structure should have low p-doping (~1x17 cm^{-3}) in order to increase mobility and avoid depolarization due to scattering. The increased doping at the surface results in an elevated CB at the surface that can be compensated by the SL miniband as long as the

conduction miniband is higher that the conduction band level at the surface. The entire structure was grown on a GaAs substrate with an AlGaAs energy barrier layer.

In principle, the $Al_xGa_{1-x}As_ySb_{1-y}$ quaternary alloy provides design flexibility. The percentage of Sb can be used to experiment with the effect of spin orbit coupling and band lineup and the Al percentage can be used to control the band offsets and LH, HH valence band splitting.

Three device structures were grown on 2" diameter GaAs substrates by molecular beam epitaxy (MBE). The structures all utilized $Al_xGa_{1-x}As_{0.82}Sb_{0.18}$ alloy in the superlattice, where the aluminum composition was changed between the samples being x = 5, 10 or 15%.

X-ray diffraction was performed on the device wafer to confirm and measure the superlattice (Fig. 2). A simulation of the structure was also calculated assuming 100% strain in the structure. The superlattice peaks are observed in the measured data, as expected from the superlattice layers. However, the location of the sideband peaks is slightly shifted, indicating that some relaxation in the material may have occurred.

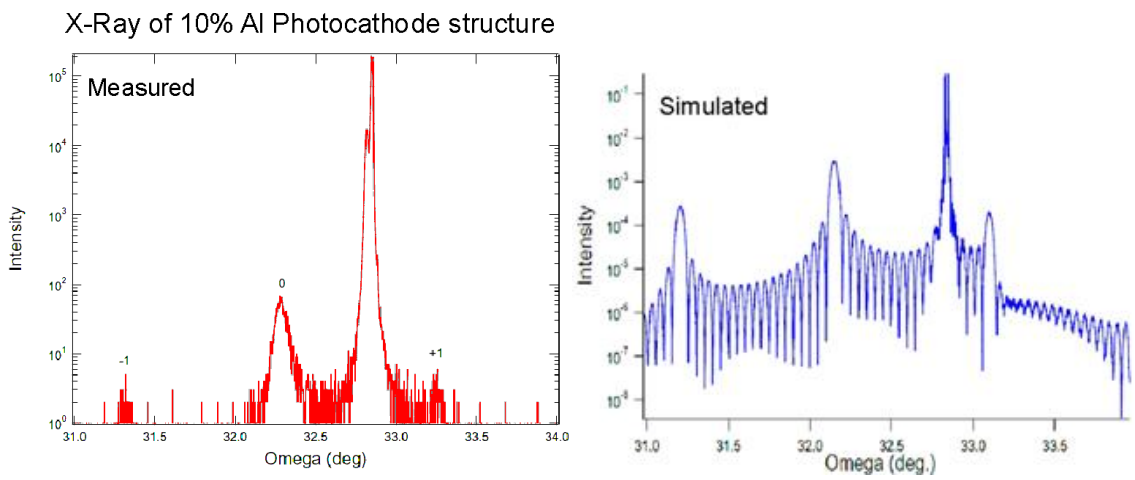

FIGURE 2. X-ray diffraction measurement and simulation of AlGaAsSb/GaAs superlattice photocathode structure. The simulation assumes 100% strain.

The wafers were sent to SLAC where they were cut into discs and cesium-activated. Prior to installation in the test system, the sample is degreased in a boiling solution of trichloroethane. After the protective oxide layer is removed in ammonium hydroxide, the sample is rinsed in distilled water and methanol. The cathode activation method used to obtain a negative-electron-affinity (NEA) surface consists of heat cleaning to 600° C for 1 hour, cool-down for an hour, followed by application of cesium until the photo-yield peaks, and then cesium and nitrogen-trifluoride co-deposition until the photo-yield is again maximized. The heat-cleaning temperature is monitored via an infrared pyrometer. The cathode is activated while monitoring the photo-yield with a white light and a 670 nm diode laser. Once a red response is observed from the diode laser, the white light is turned off and the diode laser is used to complete the activation. The absolute QE is measured using the diode laser at a photon wavelength of 670 nm. A tungsten lamp and a monochrometer are used to

measure the relative QE as a function of photon wavelength, and these measurements are then normalized to the diode laser measurement at 670 nm.

Measurement of the quantum efficiency (QE) from the 10% aluminum sample was very low, ~0.01% at 650 nm excitation wavelength. Such emission was too low to measure polarization. The 5 and 15 % aluminum composition samples did yield higher currents, with QE of 0.2% and 0.1%, respectively. Polarization was measured from the 5% aluminum sample, but demonstrated polarization less than 50% (Fig. 3).

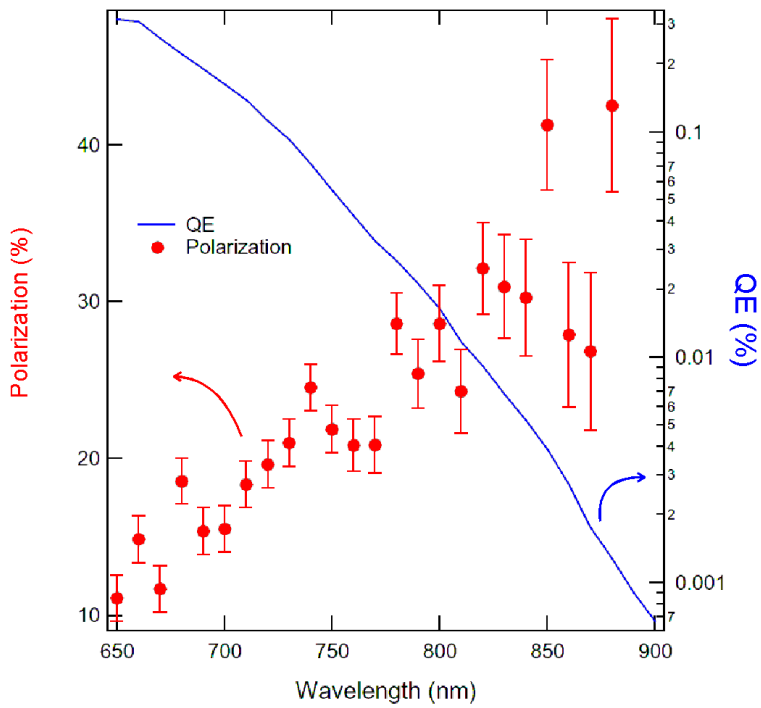

FIGURE 3. Quantum efficiency and polarization measurements from the AlGaAsSb/GaAs superlattice photocathodes with 5 % aluminum composition.

Unfortunately, the device results for antimony-based $Al_xGa_{1-x}As_{0.82}Sb_{0.18}$/GaAs photocathode were not as anticipated. Both quantum efficiency and polarization values were very low. This could be a result of this superlattice design and not wafer quality. The hypothesis is that the confinement energy around the quantum wells was too high, trapping electrons inside and hampering their contribution to the photoemission. Another possibility is that the compressively-strained AlGaAsSb layers, which are normally grown at temperatures below 500 °C, could have been damaged during thermal removal of surface native oxide at 600 °C before surface activation process.

GRADED ALUMINUM GALLIUM ARSENIDE SUPERLATTICE PHOTOCATHODES

Another approach to increasing quantum efficiency is to create an electrical field internal to the photocathode active layer to accelerate electrons toward the negative electron affinity (NEA) surface. Figure 4 displays the concept, where the conduction band of the superlattice has a sloped gradient field to influence electron flow, as opposed to a typical design where the barrier heights exist at a constant level. To achieve such a gradient, $Al_xGa_{1-x}As$ alloys were used as barriers. This $Al_xGa_{1-x}As$ material permitted wide latitude in changing the bandgap energy by varying the composition x during growth, without creating undo changes to the overall lattice constant.

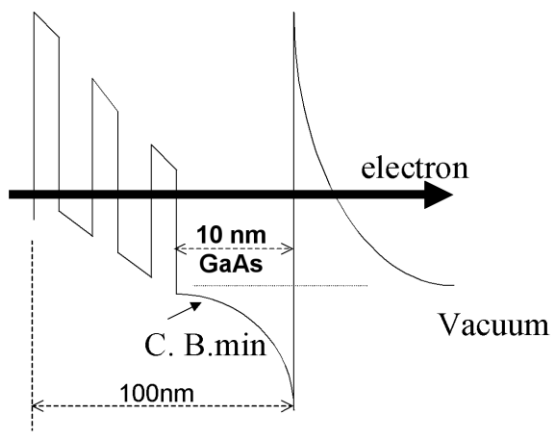

FIGURE 4. Diagram of the concept to create an accelerating field internal to the photocathode structure in order to drive electrons to the surface for increased quantum efficiency.

In the presence of such accelerating field, the electron transport time decreases by an order of magnitude to less than 1ps as it has been estimated by Monte Carlo simulations and verified experimentally [4, 5, 6]. The decrease of the transport time by an order of magnitude not only increases the current density that is required for an RF gun by the same amount but it also increases the polarization. In the case of thin films (<100nm) the polarization can increase by decreasing the transport time of the electrons and decreasing the total number of scattering events (Eq. 1) [7].

$$\frac{P_2}{P_1} = \frac{1+\dfrac{\tau_{em1}}{\tau_{s1}}}{1+\dfrac{\tau_{em1}}{\tau_{s1}}\left(\dfrac{s_2}{s_1}\dfrac{\tau_{em2}}{\tau_{em1}}\right)} \qquad (1)$$

where τ_{em} is time of electron emission in vacuum, P is electron polarization upon excitation with circularly polarized light and s is the total number of scattering events. Based on the simple model of Eq. (1), an increase of 5-10% in polarization can be achieved with accelerating the electrons.

The main objective of these experiments was to demonstrate an internal bias using an $Al_xGa_{1-x}As/GaAs$ superlattice structure. Figure 5 shows the reference sample layout, where the active layer consisted of 19 periods of superlattice layers, with 11 monolayers of $Al_xGa_{1-x}As$ and 7 monolayers of GaAs in each pair. For the reference sample, the aluminum composition x was held constant at 0.35. An internal bias was introduced into subsequent photocathodes by varying the aluminum fraction, x, throughout the active layer. By slightly varying the aluminum fraction between each pair through the superlattice, a graded field was created. This type of design, however, adds complexity to the epitaxial growth, as atomic mole fraction must be quickly and precisely varied.

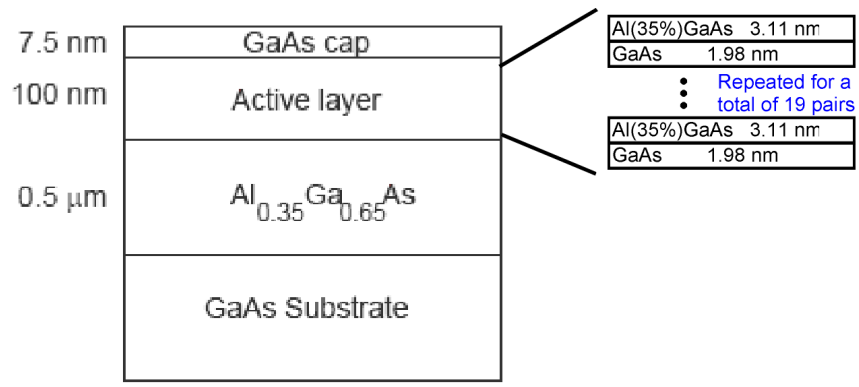

FIGURE 5. Schematic structure of the reference AlGaAs/GaAs superlattice photocathode.

The superlattice band structure was studied using the **k·p** envelope function method. Figure 6(a) shows the mini-band energies as a function of the superlattice well width for a fixed barrier width (7 monolayers). The two highest energy valence bands correspond to the heavy- and light-hole mini-bands, and the maximum energy splitting was expected to be about 28 meV. Figure 6(b) shows the expected polarization and QE as a function of the excitation wavelength. The band gap wavelength was expected at 760 nm.

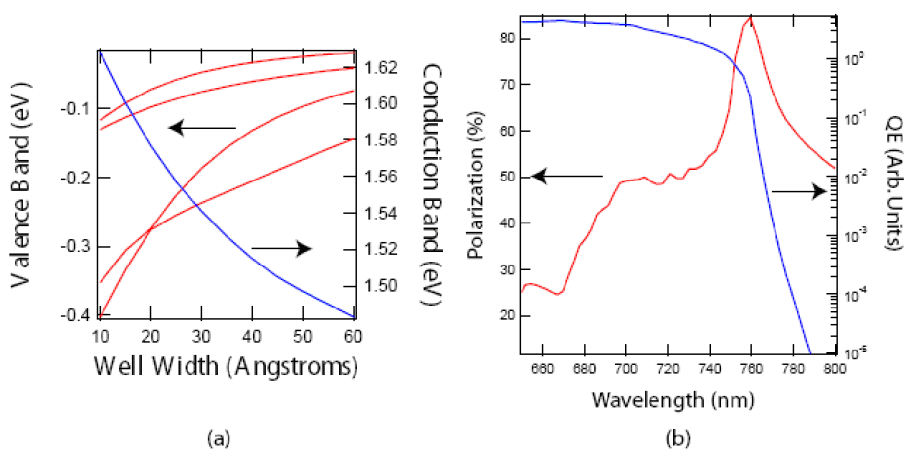

FIGURE 6. (a) Superlattice mini-band energies as a function of the well width. (b) Theoretical predictions for the polarization and QE.

Three wafers were grown with different aluminum grading values in the active layer: 1) no grading with x=0.35, 2) 10% grading from x=0.35 to 0.25, and 3) 20% grading from x=0.35 to 0.15. Because of the thin amount of the active layer and the extremely low lattice mismatch between the Al and Ga atoms, the x-ray diffraction simulation predicted two weak, widely spaced satellite peaks (Fig. 7) for the superlattice. Actual measured x-ray data of the grown wafer were in close agreement with the simulation (Fig. 8).

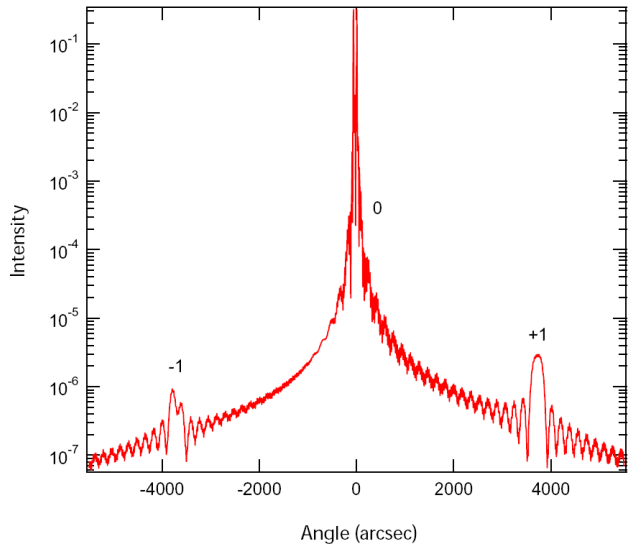

FIGURE 7. Simulation of anticipated x-ray diffraction curve based on the graded AlGaAs/GaAs superlattice structure.

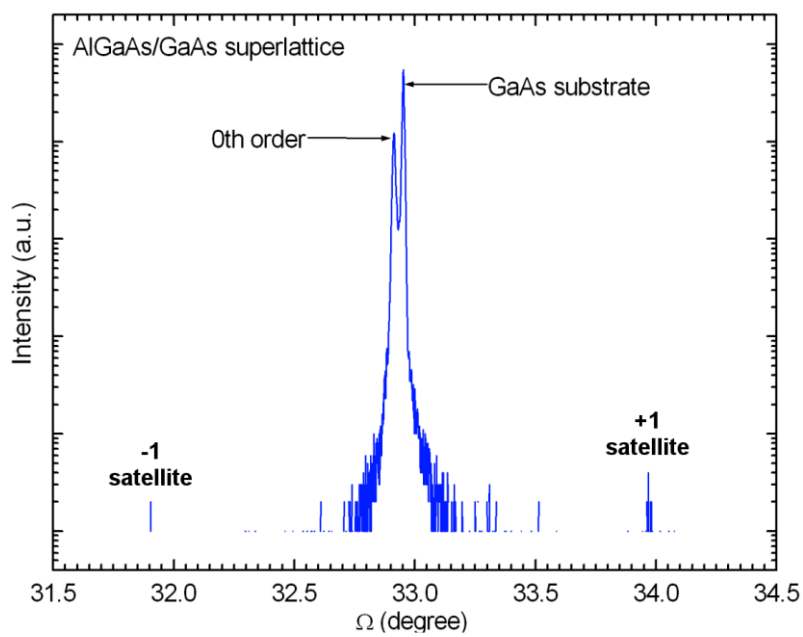

FIGURE 8. Measured x-ray diffraction curve of the grown AlGaAs/GaAs superlattice structure.

The photocathode wafers were cleaned and activated as described in the previous section. Figure 9 shows the QE at 650 nm for the three samples. As the internal bias is increased by increasing the aluminum grading, the QE increases as much as 25%. This is the first demonstration that an electric field can be incorporated in the conduction band and a QE enhancement is possible.

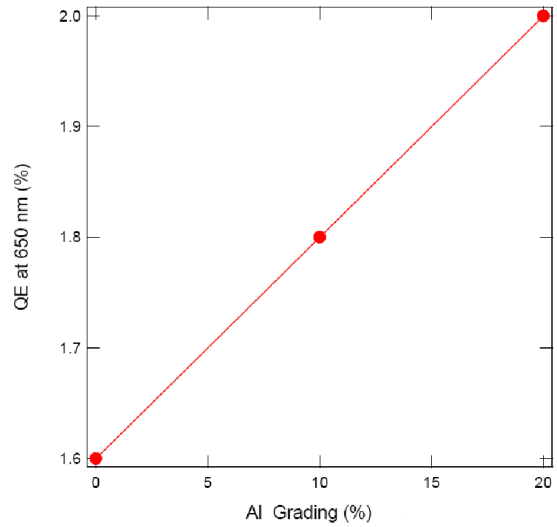

FIGURE 9. QE at 650 nm as a function of aluminum grading in AlGaAs/GaAs superlattice photocathodes.

Figure 10 shows QE and polarization as a function of wavelength for the three samples tested. As the aluminum grading was increased, the peak polarization decreased. Furthermore, the wavelength dependence of QE became steeper, eliminating the QE gain in the short wavelength region. This is a consequence of the structural change in the superlattice active layer. As the aluminum fraction is decreased, the effective bandgap energy gets smaller and the heavy- and light-hole splitting is reduced.

CONCLUSION

Two novel device structures were studied to improve the operating characteristics of photocathodes with polarized electron emission. $Al_xGa_{1-x}As_ySb_{1-y}$/GaAs superlattices were created to take advantage of the lower diffusivity and higher spin orbit coupling of antimony atoms. These photocathodes in this instance yielded low quantum efficiency, attributed to the extremely deep well energy. Further investigation can continue in the future with a modified design.

The second approach was to create a superlattice with a self-generated internal electric field to accelerate electrons toward the photocathode surface. This was accomplished by varying the aluminum composition in a $Al_xGa_{1-x}As$/GaAs superlattice. Quantum efficiency was observed to increase by up to 25% compared to a control sample that lacked an internally graded field. The low strain in $Al_xGa_{1-x}As$/GaAs materials resulted in mild polarization values, but the internal gradient concept can be applied to other high polarization photocathodes.

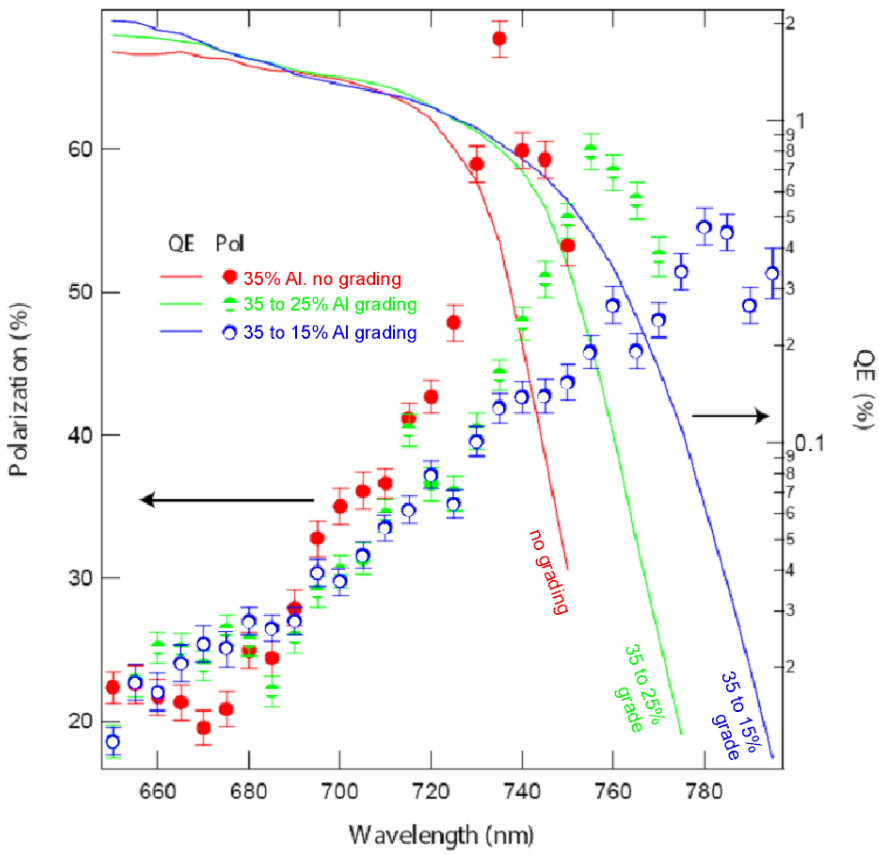

FIGURE 10. Polarization and QE as a function of the excitation wavelength for three AlGaAs/GaAs superlattice photocathodes with internal gradient fields.

ACKNOWLEDGMENTS

This research was supported by Small Business Innovation Research (SBIR) grants from the U.S. DOE under contracts DE-FG02-07ER86329 and DE-FG02-07ER86330.

REFERENCES

1. T. Maruyama, E.L. Garwin, R. Prepost, G.H. Zapalac, J.S. Smith, and J.D. Walker, Phys. Rev. Lett. **66**, 2376 (1991).
2. T. Maruyama, D.-A. Luh, A. Brachmann, J.E. Clendenin, E.L. Garwin, S. Harvey, J. Jian, R.E. Kirby, C.Y. Prescott, R. Prepost, and A.M. Moy, Appl. Phys. Lett. **85**, 2640 (2004).
3. H. Bracht, S.P. Nicols, W. Walukiewitz, J.P. Silveira, F. Briones, E.E. Haller, "Large disparity between gallium and antimony self diffusion in gallium antimonide", Nature, **408**, 69 (2000).
4. Schuler,J., et al., Polarized sources conf., Nagoya 2000.
5. K. Ioakeimidi, et al., "Photoelectronic analog-to-digital conversion: sampling and quantizing at 100 Gs/s", *IEEE Trans. Microwave Theory and Techniques*, Vol. 53, Issue 1, Jan. 2005.
6. K. Ioakeimidi et. al., "Sub-picosecond jitter in picosecond electron bunches", *J. Vac. Sci. Technol. B*, Vol. **23**, (2005).
7. K. Ioakeimidi et al., "Transport Mechanisms in Spin Polarized Semiconductor Superlattices", *SPIN 2006*, 1-7 October 2006, Kyoto, Japan.

Superlattice Photocathode with High Brightness and Long NEA-Surface Lifetime

Tomohiro Nishitani[a], Masao Tabuchi[b], Yoshikazu Takeda[c], Yuji Suzuki[c], Kazuya Motoki[c], Takashi Meguro[a]

[a]*Beam Application Team, RIKEN, Wako, Saitama, 351-0198, Japan*
[b]*Venture Business Laboratory, Nagoya University, Nagoya, 464-8601, Japan*
[c]*Department of Crystalline Materials Science, Nagoya University, Nagoya, 464-8601, Japan*

Abstract. We have suggested that a small momentum spread of photoelectrons and high quantum efficiency can be obtained concurrently by a photocathode using a semiconductor with a superlattice instead of a bulk. We have begun to search for the suitable semiconductor material of a superlattice photocathode for maintaining the surface with a negative electron affinity state for a long time. We measured quantum efficiency degradation of photocathodes using GaAs and AlGaAs semiconductors with various electron affinities. The AlGaAs semiconductor had a quantum efficiency lifetime of 10 times long compared with the GaAs semiconductor. We found that the AlGaAs semiconductor was the suitable material for the superlattice photocathode with the surface maintaining a negative electron affinity state for a long time.

Keywords: GaAs semiconductor, photocathode, electron affinity, superlattice, long lifetime.
PACS: 85.60.Ha, 29.25.Bx

INTRODUCTION

GaAs photocathodes are well known as photoemitters with a surface of a negative electron affinity state (NEA-surface) using semiconductors related with a GaAs semiconductor. GaAs photocathodes have played very important roles as spin-polarized electron sources in several fields of fundamental science[1,2,3]. Recently, a GaAs photocathode was found to be useful a high brightness electron source for a high energy accelerator based on linac[4], because GaAs photocathode has the advantages of a large emission current (several mA[5]) and a small momentum spread (energy of ~0.2eV[6]) of extracted electrons. The key technology of GaAs photocathode is that an NEA surface enables excited electrons in the conduction band minimum to escape to a vacuum. However, the NEA surface of the conventional GaAs photocathode has the short lifetime problem for a large emission current of several mA[7]. To realize the electron source with beam performance for the next generation synchrotron light source based on a linac[4], we have developed photocathodes which simultaneously realizes a high brightness and an NEA surface with a long lifetime.

PHOTOCATHODE WITH NEA SURFACE USING SEMICONDUCTORS

An NEA surface of the conventional GaAs photocathode is realized by the band bending and an electric field by electric dipoles composed of cesium and gallium atoms on the surface as shown in FIGURE 1. When the surface of a GaAs semiconductor with a p-type doping is activated to be an NEA state by cesium, the electron affinity is given by the next formula:

$$\chi^{NEA} = \chi - \phi^{BB} - \phi^{D} < 0,$$

where χ is the electron affinity of the semiconductor, ϕ_{BB} is the surface band bending, ϕ_D is the electric field by the electric dipoles on the surface.

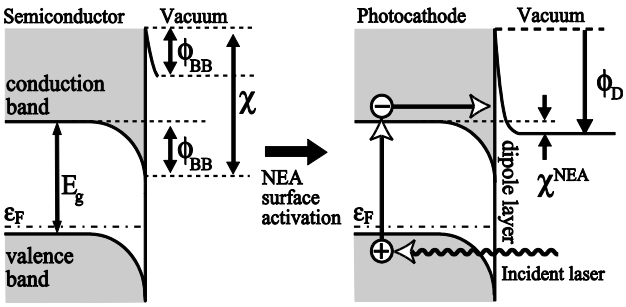

FIGURE 1. (a) The potential diagram of a GaAs semiconductor with a p-type doping. (b) The mechanism of photoemission illustrated on the potential diagram of a GaAs photocathode.

The χ^{NEA} of the conventional GaAs photocathode with a p-type doping GaAs semiconductor is -0.17eV[8] at room temperature. A GaAs semiconductor has electron affinity of 4.07eV and band gap energy of 1.42eV at a room temperature[9]. The ϕ_D can be estimated to be 3.5eV at a room temperature where it is assumed that the ϕ_{BB} of a GaAs semiconductor is a half of band gap energy. Therefore, a GaAs photocathode is possible to generate an electron beam with a small momentum spread of ~0.2eV by excitation photon energy tuned to band-gap energy of a semiconductor. However, quantum efficiency (QE) of a GaAs photocathode with a bulk structure at excitation photon energy tuned to its band-gap is low (3~4%) due to small electron energy density of state in the conduction band.

ALGAAS PHOTOCATHODE FOR MAINTAINING AN NEA STATE FOR A LONG TIME

An effective electron affinity (χ^{NEA}-ϕ^{BB}) of a semiconductor should be small for maintaining an NEA state (χ^{NEA}<0) for a long time. We considered that a semiconductor with a smaller electron affinity and larger band gap energy was a more suitable material of a photocathode for maintaining an NEA state for a long time. We fabricated test samples of GaAs and AlGaAs semiconductors with various Al fractions because the electron affinity of an AlAs semiconductor (3.50eV) is smaller than that of a GaAs semiconductor (4.07eV) and band gap energy of an AlAs semiconductor (2.95eV) is larger than that of a GaAs semiconductor (1.42eV) [10]. These samples have

the same surface structure of a thin GaAs layer with a thickness of 5nm. TABLE 1 shows a electron affinity and band gap energy for each sample.

TABLE 1. Electron affinity and band gap energy for each sample.

Sample	Al fraction	Electron affinity (eV)	Band gap energy (eV)
GaAs	0	4.07	1.42
$Al_{0.168}GaAs$	0.168	3.89	1.64
$Al_{0.283}GaAs$	0.283	3.76	1.79

We measured the QE degradation of these samples using the photocathode electron source facility at Japan Atomic Energy Agency[11]. In the measurements, the excitation laser photon energy was chosen at ~0.1 eV above band gap energy for each sample, and the applied voltage for the extraction of a photocurrent was as high as 200 V to degrade the NEA surface by ion back bombardment[12]. A QE lifetime of AlGaAs samples was 10 times long compared with that of the GaAs sample. The QE lifetime of $Al_{0.283}GaAs$ sample was longer than that of the $Al_{0.168}GaAs$ sample.

SUPERLATTICE PHOTOCATHODE

The advantage of superlattice structure

We have suggested a photocathode with a superlattice structure for a high brightness electron source[13]. We consider a superlattice structure has intrinsic advantages in realization of higher QE, a smaller momentum spread of photoelectrons and a longer QE lifetime than those of the conventional GaAs photocathode due to the following two reasons.

(1) By selecting an appropriate semiconductor material for each layer in the superlattice structure, a superlattice semiconductor is possible to have large band gap energy, a small electron affinity for a long QE lifetime.

(2) Electron energy density of state (DOS) for a superlattice structure is a step function of excitation photon energy due to a quantum confinement effect shown in FIGURE 2. QE of a GaAs photocathode is proportional to its DOS integrated from band gap energy to the excitation photon energy[14]. A GaAs semiconductor with a bulk structure, which has a monotonically increasing DOS function, requires rather higher energy photons to achieve high QE operation at the expense of a large momentum spread of electrons. A superlattice structure, on the other hand, enable one to achieve high QE and a small momentum spread (ΔE_{SL}) simultaneously by choosing photon energy (E_g^{SL}) just above step energy of DOS.

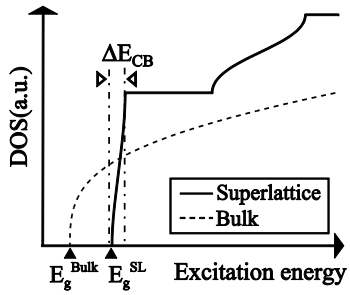

FIGURE 2. Dependence of DOS on excitation energy for a bulk and a superlattice structure.

AlGaAs-GaAs superlattice photocathode

We have decided to use AlGaAs and GaAs semiconductors as superlattice materials from our results of a QE lifetime using AlGaAs photocathodes. To optimize a superlattice structure for a small momentum spread of photoelectrons and a long QE lifetime, we estimated energy width of the conduction mini-band (Wcb) and the effective electron affinity for various superlattice structures. We calculated the dependence of these values on the well- (Lw) and barrier-layer (Lb) thickness of a GaAs-AlGaAs superlattice using Klonig-Penny-Bastard model[15]. FIGURE 3 shows the dependence of Wcb, the electron affinity and the band gap energy on Lw and Lb. Those layer thicknesses should be between 2 and 10nm for an effectively quantum confinement effect by a quality superlattice structure. We can see that superlattice structures with Lw = 2nm have the smallest electron affinity and the largest band gap energy. Superlattice structures with Lb more than 6nm have smaller Wcb than the thermal energy (26meV) at a room temperature. Superlattice structures with Lw = 2nm and Lb of 6~10nm have the almost same effective electron affinity of the AlGaAs photocathode with Al fraction of 0.168. From these results, we found that the superlattice photocathode with Lw = 2nm and Lb=6~10nm is a suitable photocathode for a smaller momentum spread of photoelectrons and longer QE lifetime than that of the conventional GaAs photocathode.

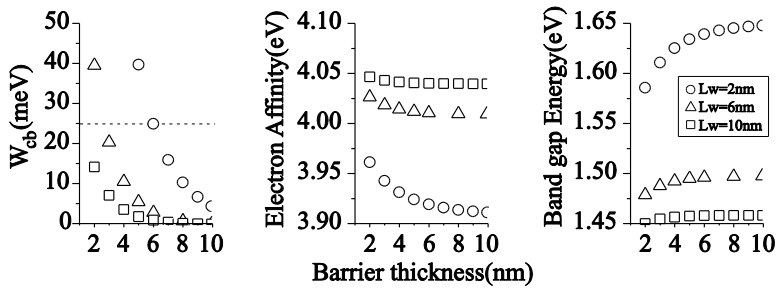

FIGURE 3. Dependence of energy width of the conduction mini-band, the electron affinity and band gap energy on the barrier and well layer thickness of the GaAs-AlGaAs superlattice with an Al fraction of 0.29.

For confirmation of improving a momentum spread of photoelectrons and a QE lifetime performance using superlattice photocathodes designed by our theoretical calculation, we fabricated test samples of the GaAs-AlGaAs superlattice with a well-layer thickness of 2nm and a barrier thickness of 6~10nm by a molecular beam

epitaxial facility at Nagoya university. We will measure the QE degradation under a large photocurrent and dependence of QE on excitation energy of these test samples by the 30keV photocathode electron gun at RIKEN.

SUMMARY

To conclude, we measured the QE degradation using GaAs and AlGaAs photocathodes and designed a superlattice structure using theoretical calculation of an energy band model. We found AlGaAs photocathodes has 10 times longer QE lifetime than that of a GaAs photocathode. The results of the QE degradation using GaAs and AlGaAs photocathodes agreed that a photocathode with a smaller electron affinity is more suitable for maintaining an NEA state for a long time. We found that the AlGaAs-GaAs superlattice with the well layer thickness of 2nm and the barrier thickness of 6~10nm is an eminently suitable photocathode for a small momentum spread of photoelectrons and a long QE lifetime.

ACKNOWLEDGMENTS

The authors thank Dr. Eisuke J Minehara, Dr. Ryoichi Hajima and the energy recovery linac development group member at Japan Atomic Energy Agency for the useful discuss and the use of the photocathode electron source facility. This work was supported in part by the Kazato Research Encouragement Prize from the Kazato Research Foundation and Grant-in-Aid for Scientific Research (18740253) from the Ministry of Education, Culture, Sports, Science and Technology.

REFERENCES

1. SLD Collaboration Phys. Rev. Lett. 70 17, pp.23-31 (1993)
2. J. Kirschner, D. Rebenstorff, and H. Ibach, Phys. Rev. Lett. 53, 698- 701 (1984)
3. J. Unguris, A. Seiler, R. J. Celotta, D. T. Pierce, P. D. Johnson, and N. V. Smith, Phys. Rev. Lett. 49, 1047- 1050 (1982).
4. Sol M. Gruner, et al., Review of Scientific Instruments, Vol. 73 Issue3 pp.1402-1406 (2002)
5. G. R. Neil, et al., Phys. Rev. Lett. 84, pp.662-665 (2000)
6. D.A. Orlov, et al., Nucl. Instrum. Methods A 532, 418 (2004)
7. J. Grames et al., Proceedings of Particle Accelerator Conference, pp. 2875-2877 (2005) http://accelconf.web.cern.ch/AccelConf/p05/
8. D.A. Orlov et al., Nuclear Instruments and Methods in Physics Research A 532 (2004) 418–421
9. Sadao Adachi, J. Appl. Phys. 58 (3), (1985) pp. R1-R12
10. S. Adachi, “GaAs and Related Materials: Bulk Semiconducting and Superlattice Properties”, World Scientific, (1994) pp. 145, 307
11. T. Nishitani, et al., Proceedings of International Free Electron Laser Conference, (2006) , pp.319-322, http://www.bessy.de/fel2006/proceedings/
12. J. Grames, P. Adderley, J. Brittian, J. Clark, J. Hansknecht, D. Machie, M. Poelker, E. Pozdeyev, M. Stutzman, and K. Surles-Law , AIP Conf. Proc. 980 (2008) pp. 110-117
13. T. Rao, A. Burrill, X.Y. Chang, J. Smedley, T. Nishitani, C. Hernandez Garcia, M. Poelker, E. Seddon, F.E. Hannon, C.K. Sinclair, J. Lewellen, D. Feldman, Nuclear Instruments and Methods in Physics Research A 557, pp.124–130, (2006)
14. T. Nishitani et al. J. Appl. Phys. 97 (2005) 094907
15. G. Bastard, Phys. Rev. B 24 5693 (1981)

High Brightness and high polarization electron source using transmission photocathode

Naoto Yamamoto*, Xiuguang Jin*, Atsushi Mano†, Yasuhide Nakagawa†, Tsutomu Nakanishi†, Toru Ujihara*, Shoji Okumi†, Masahiro Yamamoto†, Taro Konomi†, Yoshikazu Takeda*, Takashi Ohshima**, Takashi Saka‡, Toshihiro Kato§, Hiromichi Horinaka¶, Tsuneo Yasue‖ and Takanori Koshikawa‖

*Graduate School of Engineering, Nagoya University, Nagoya, Aichi,464-8602 Japan
†Graduate School of Science, Nagoya University, Nagoya 464-8602, Japan
**Central Research Laboratory, Hitachi Ltd., Tokyo 185-8601, Japan
‡Daido Institute of Technology, Nagoya 457-8531, Japan
§Daido steel Co. Ltd., Nagoya 457-8531, Japan
¶Faculty of Engineering, Osaka Prefecture University, Osaka 599-8531, Japan
‖Fundamental Electronics Research Institute, Osaka Electro-Communication University, Osaka 572-8530, Japan

Abstract. A transmission photocathode was fabricated based on GaAs-GaAsP strained superlattice layers on a GaP substrate and a 20kV-gun was built to generate the polarized electron beams with the diameter of a few micro-meter. As the results, the reduced brightness of 1.3×10^7 A/cm^2/sr and the polarization of 90 % were achieved.

Keywords: polarized electron source, high brightness, transmission photocathode
PACS: 21.10.Hw,29.25.Bx,87.64.Ee

INTRODUCTION

The GaAs-type semiconductor photocathode (PC) with a negative electron affinity (NEA) surface is currently used as a conventionally polarized electron source (PES) to produce a highly polarized electron beam. Polarized electron beams have been widely used in high energy electron accelerators for spin physics studies of fundamental particles or hadrons [1, 2, 3, 4, 5, 6].

To answer the needs of future high energy accelerators, several groups, including our own, have made long-term efforts to improve PES (PC+gun) performances. For examples, electron spin polarization (ESP) higher than 85% has been achieved by strained GaAs [7] and GaAs-GaAsP strained super-lattice (SL) layers [8] grown on a GaAsP buffer substrate. A quantum efficiency (QE) higher than 0.3% has been simultaneously obtained for the same PCs. We have recently demonstrated experimentally that thermal emittance can be minimized to as low as 0.15 π mm mrad for a beam radius of 1.0 mm, by using a GaAs-GaAsP strained SL layer PC installed in a 200-kV DC-gun [9].

High brightness is one of the most important PES performances for the application to electron microscopes. Several types of point-like sources have already been developed to produce a needle-like beam, although it can not produce a polarized beam. Field

emission sources can realize the highest brightness ($10^8 \sim 10^9$ A cm^{-2} sr^{-1}) and have been used for high space-resolution electron microscopes, such as scanning electron microscopes (SEM) where the radius of the W-tip is typically shaped to be as small as 100 nm.

For SEM applications, another source using an NEA-GaAs PC was developed to produce small energy spread beams by one of the co-authors (T. Ohshima) [10]. The electron generation from NEA-PC is based on two fundamental physical processes: 1) optical excitation to the conduction band and 2) electron emission through the surface potential barrier due to the NEA surface. In a conventional PC scheme, laser light is injected from the NEA surface side and the electrons are extracted to the same side. In contrast,to form a small diameter electron beam, they injected laser light from the back surface of a GaAs film grown on a glass sheet, with the excited electrons emitted into vacuum from the front NEA surface of the PC. Using this laser injection scheme, it is possible to decrease the distance between a focusing lens and the PC crystal and to minimize the laser spot size. Hereafter, we distinguish this PC from conventional PCs, by naming them “transmission PC (T-PC)” and “reflection PC (R-PC)”, respectively.

In order to achieve high brightness and high polarization performances for polarized electron beams, a 20–kV gun system (named JPES-1) was designed and built to install the newly designed T-PC at Nagoya University.

EXPERIMENTAL SETUP

20-kV Electron guns

The T-PC PES system (JPES-1) was developed at Nagoya University as a prototype SPLEEM gun to demonstrate its high brightness performance [11]. JPES-1 consists of five chambers: an NEA surface preparation chamber, a gun chamber, a brightness measuring chamber, a spherical condenser chamber and a 100-keV Mott polarimeter chamber [12].

Two important apparatus performances must be met for a high voltage PES gun: an extreamely high vacuum ($\leq 10^{-10}$ Pa) environment around the NEA-PC and an extremely low dark current ($\leq$ 10 nA) between the high voltage electrodes. These performances are required to protect the NEA surface and reduce its degradation speed to maintain a long PC lifetime ($\geq$ several tens hours).

The NEA surface is known to be easily degraded by the desorption of residual gas molecules and the back bombardment of positive ion produced by the beam itself. Therefore the vacuum pressure near the photocathode was maintained less than 1.0×10^9 Pa by using an 100 L/s ion pump and a 2000 L/s non-evaporable getter pump.

The accelerating electrodes was designed by using the simulation cord [13], which was developed to calculate envelops and profiles of charged particles precisely. The field gradient on a photocathode surface was estimated to be 4 MV/m at 20–kV bias. Since titanium electrodes were found to suppress field emission currents by our previous study [14], the titanium electrodes were installed to the gun chamber.

In the experiments, the beam lifetime performance was monitored during JPES-1 keeping extremely low vacuum pressure ($\leq 2 \times 10^{-9}$ Pa) and extremely low dark

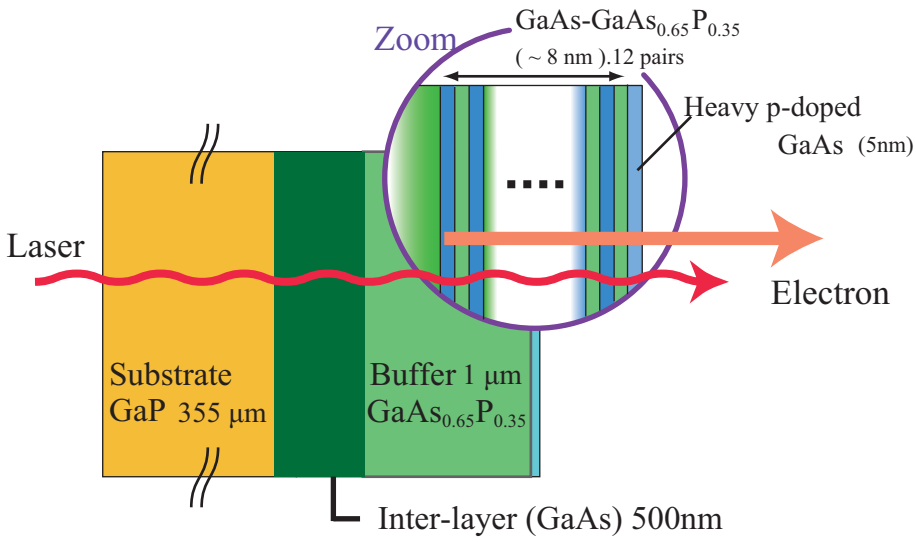

FIGURE 1. Details of the T-PC structure.

current ($\leq$ 1 nA) conditions. As typical data, an initial current of 3 μA extracted by 3.2-μm radius laser irradiation descreased exponentially with a lifetime of 36 hours, which corresponds to a charge lifetime density of 1.8×10^8 C/cm^2.

The ESP is measured using a standard 100-kV Mott polarimeter [12]. The Mott polarimeter has four different Au-foil targets of different thickness for self-calibration of the effective Sherman functions. The systematic error for the ESP measurement was estimated to be $\pm$ 6% (absolute value) at maximum.

Photocathode Design

The T-PCs were fabricated by using a low-pressure organometallic vapor phase epitaxy (OMVPE) system with a verticalcold-wall quartz reactor. The PC structure is shown in Fig 1, A commercially available GaP wafer with a Zn dopant of 1.4×10^{17} cm^{-3} was used as a substrate. To control the strain in the buffer and SL layers [15] [16], the GaAs inter-layer was grown on the GaP substrate. Then, 1 μm of the GaAsP buffer layer and 12 pairs of SL layers were grown with a Zn dopant consentration of 1.5×10^{18} cm^{-3}. Subsequently the SL structure was coated with a heavily doped 5nm layer of GaAs (Zn 6×10^{19} cm^3). This design effectively overcomes the surface charge effect that appears in the generation of a high current density beam [17],[18] and exhibits ESP and QE performances, as high as 92% and 0.5%, respectively [19].

RESULT & DISCUSSION

The beam performance of the T-PC was measured by JPES-1 with the laser focusing conditions. The full-width at half-maximum of the smallest laser spot was 1.3 μm. The highest brightness obtained under an extraction voltage of 20–kV was $(1.3 \pm 0.5) \times 10^7$

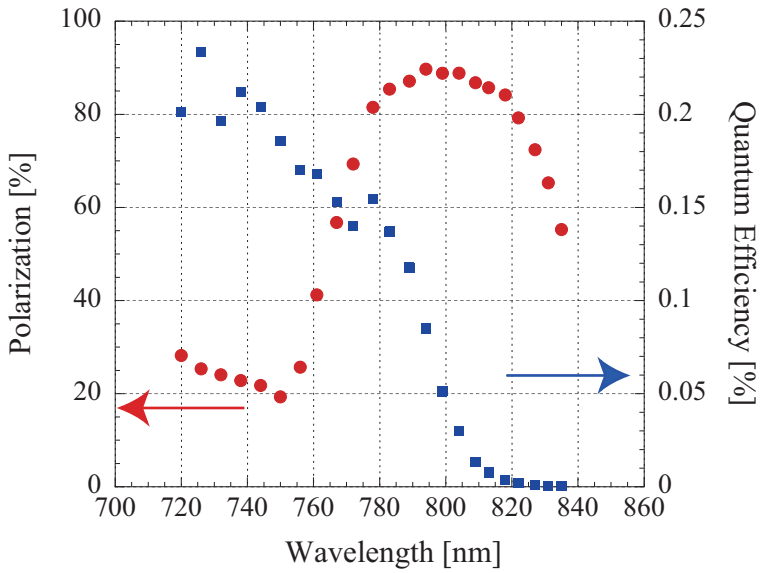

FIGURE 2. Observed ESP as a function of excitation laser wavelength.

A cm^{-2} sr^{-1} and the angular current density was 161 mA/sr. This brightness is large compared with those of un-polarized electron emitters. It is smaller than those of W-tip emitters by one or two orders, but one order higher than those of LaB_6 emitters.

ESP and QE spectra taken for the T-PC are shown in Fig. 2, where the closed circle and square points indicate ESP and QE, respectively. A maximum ESP of 90% with QE of 0.09% has been achieved at a wavelength of 794 nm. This ESP value is in the range of the values of our previous studies of R-PC. On the other hand, the QE value is smaller because the absorption of the pump laser light by a 500 nm-thick GaAs layer was about 50% and the QE performance was not optimized on this PC. Further efforts have been made in designing new T-PC samples with a higher QE.

SUMMARY

In order to achieve high brightness and high polarization performances for polarized electron beams, a 20–kV gun and T-PCs were developed. As the results, the brightness of $(1.3 \pm 0.5) \times 10^7$ A cm^{-2} sr^{-1} and the ESP of (90 ± 6)% were achieved. These performances are enough high for the applications to not only high energy electron accelerators but also electron microscopes.

The interference between the laser and electron beam lines in the conventional R-PC scheme is a serious problem for gun design and imposes a serious limit on beam performance. This T-PC scheme appears promising for applications of polarized beam in various types of high energy electron accelerators and microscopes, since there is sufficient free spaces along both the laser and electron beam lines to enable the optimization of design figures and parameters individually.

Furthermore, this T-PC scheme has an additional advantage for laser heating problem by high duty operation, such as Energy Recovery Linacs. In the electron generation

process of NEA-PC with SL layers, only a several % of the pump laser light is absorbed in the SL layers. In the case of R-PCs, the other of that are absorbed in its substrate and the absorbed power causes the heating problem for the PCs. On the other hand, in the T-PCs case, since the substate is transparent for the pump laser light, it can be possible to suppress the effect of laser heating.

ACKNOWLEDGMENTS

This work has been financially supported by Japan Science and Technology (JST) as a technology development program for advanced measurement and analysis (program leader: T. Nakanishi).

REFERENCES

1. D. T. Pierce, F. Meier, and P. Zürcher, Appl. Phys. Lett. **26**, 670 (1975).
2. C. Y. Prescott, W. B. Atwood, R. L. A. Cottrell, H. DeStaebler, E. L. Garwin, A. Gonidec, R. H. Miller, L. S. Rochester, T. Sato, D. J. Sherden, et al., Phys. Lett. B **77**, 347 (1978).
3. M. Meyerhoff, D. Eyl, A. Frey, H. G. Andresen, J. R. M. Annand, K. Aulenbacher, J. Becker, et al., Physics Letters, Section B: Nuclear, Elementary Particle and High-Energy Physics **327**, 201 (1994).
4. SLD colaboration, I. Abt, C. J. Ahn, T. Akagi, W. W. Ash, D. Aston, N. Bacchetta, K. G. Baird, C. Baltay, H. R. Band, et al., Phys. Rev. Lett. **74**, 2880 (1995).
5. S. Mayer and J. Kessler, Phys. Rev. Lett. **74**, 4803 (1995).
6. U. Kolac, M. Donath, K. Ertl, H. Liebl, and V. Dose, Review of Scientific Instruments **59**, 1933 (1988).
7. T. Nakanishi, H. Aoyagi, H. Horinaka, Y. Kamiya, T. Kato, S. Nakamura, T. Saka, and M. Tsubata, Physics Letters A **158**, 345 (1991).
8. T. Nakanishi, K. Togawa, T. Baba, F. Furuta, H. Horinaka, T. Kato, Y. Kurihara, H. Matsumoto, T. Matsuyama, T. Nishitani, et al., Nuclear Inst. and Methods in Physics Research, A **455** (2000).
9. N. Yamamoto, M. Yamamoto, M. Kuwahara, R. Sakai, T. Morino, K. Tamagaki, A. Mano, A. Utsu, S. Okumi, T. Nakanishi, et al., Journal of Applied Physics **102**, 024904 (2007).
10. T. Ohshima and M. Kudo, Japanese Journal of Applied Physics **43**, 8335 (2004).
11. N. Yamamoto, T. Nakanishi, A. Mano, Y. Nakagawa, S. Okumi, M. Yamamoto, T. Konomi, X. Jin, T. Ujihara, Y. Takeda, et al., Journal of Applied Physics **103**, 064905 (2008).
12. T. Nakanishi, K. Dohmae, S. Fukui, Y. Hayashi, I. Hirose, N. Horinaka, T. Ikoma, Y. Kamiya, M. Kurashina, and S. Okumi, Jpn. J. Appl. Phys **25**, 766 (1986).
13. N. Yamamoto, A. Mizuno, K. Masuda, K. Kan, and M. Yamamoto, this Proceedings (2009).
14. F. Furuta, T. Nakanishi, S. Okumi, T. Gotou, M. Yamamoto, M. Miyamoto, M. Kuwahara, N. Yamamoto, et al., Nuclear Inst. and Methods in Physics Research, A **538**, 33 (2005).
15. X. Jin, N. Yamamoto, Y. Nakagawa, A. Mano, T. Kato, M. Tanioku, T. Ujihara, Y. Takeda, S. Okumi, M. Yamamoto, et al., Applied Physics Express **1**, 45002 (2008).
16. X. Jin, T. Saka, M. Tanioku, S. Fuchi, T. Ujihara, Y. Takeda, N. Yamamoto, Y. Nakagawa, A. Mano, S. Okumi, et al., Journal of Crystal Growth **310**, 5039 (2008).
17. K. Togawa, T. Nakanishi, T. Baba, F. Furuta, H. Horinaka, T. Ida, Y. Kurihara, H. Matsumoto, T. Matsuyama, M. Mizuta, et al., Nucl. Instr. and Meth. A **414**, 431 (1998).
18. T. Maruyama, A. Brachmann, J. Clendenin, T. Desikan, E. Garwin, R. Kirby, D. Luh, J. Turner, and R. Prepost, Nuclear Instruments and Methods in Physics Research, A **492** (2002).
19. T. Nishitani, T. Nakanishi, M. Yamamoto, S. Okumi, F. Furuta, M. Miyamoto, M. Kuwahara, N. Yamamoto, K. Naniwa, O. Watanabe, et al., Journal of Applied Physics **97**, 94907 (2005).

Cooled Transmission–Mode NEA–Photocathode with a Band–Graded Active Layer for High Brightness Electron Source

L.B. Jones*, S.A. Rozhkov†, V.V. Bakin**, S.N. Kosolobov**, B.L. Militsyn*, H.E. Scheibler**, S.L. Smith* and A.S. Terekhov†,**

*STFC Daresbury Laboratory, Warrington, WA4 4AD, United Kingdom
†Novosibirsk State University, Novosibirsk, 630090, Russia
**Institute of Semiconductor Physics, Novosibirsk, 630090, Russia

Abstract. A Free–Electron Laser (FEL) places many exacting demands on a Negative Electron Affinity (NEA) photocathode, such as the need for an ultra–fast response time, low energy spread for emitted electrons, high quantum efficiency (*Q.E.*) and a high average photocurrent. However, these key requirements are conflicting, and cannot be fulfilled by conventional photocathode design. For example, to achieve ~ 10 ps response time, the photocathode active layer should be thinned to $\sim 100-150$ nm, but this thickness is insufficient to provide near–complete absorption of light with $h\nu \approx \varepsilon_g$ so high *Q.E.* cannot be achieved. Complete optical absorption and high *Q.E.* can be obtained using a thin active layer at higher photon energies, but this generates photoelectrons with excess kinetic energy within the semiconductor. These photoelectrons do not thermalise in a thin active layer, so yield a broad energy distribution in the emitted electrons. Moreover, cooling of the conventional semiconductor photocathode structure is ineffective due to its fragility, so it cannot be pressed firmly to a heat sink to attain good thermal contact. Consequently, the maximum CW photocurrent is limited to a few milliamps. The goal of our work is to develop a new design of NEA–photocathode which is optimised for FEL applications.

Keywords: GaAs, photocathode, photoelectron, FEL, NEA, transmission mode, reflection mode
PACS: 29.25.Bx, 41.60.Cr, 81.05.Ea, 85.60.Ha

METHODOLOGY & EXPERIMENTAL DETAILS

Our approach is to design a transmission–mode GaAs (Cs,O) photocathode with a *composite band–graded* (BG) *active layer* on a buffered sapphire substrate. The energy diagram for this photocathode is shown in fig. 1 (a). During operation, the photocathode is back–illuminated through the sapphire and buffer layer with photons of ~ 2.3 eV. The BG layer is grown from $Al_xGa_{1-x}As$ with x varied over the range $0 < x < 0.1$, which absorbs most of the incident photons. The thickness of the BG layer is ~ 300 nm, and is sufficient for effective thermalisation of photoelectrons within this layer over a period of ~ 0.1 ps. The variation of the Al content across the BG layer creates a variation in the energy of the conduction band minima, and consequently, creates a 'built–in' electric field whose strength is $\sim 4 \times 10^4$ V/cm.

It is known from the literature [1] that this electric field accelerates thermalised photoelectrons to the saturation velocity, typically around 10^7 cm/sec. Thus photoelectrons are 'ejected' from the BG layer into the GaAs 'emitting' layer over an estimated time of approximately 3 ps. It then takes ~ 5 ps for photoelectrons to diffuse across the GaAs

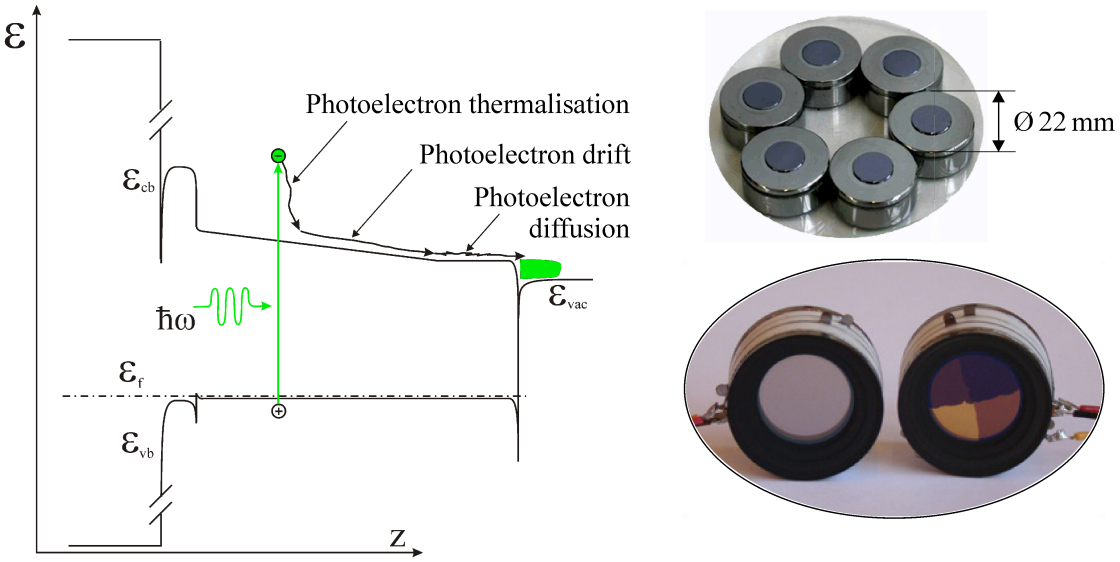

FIGURE 1. **(a)** Band–graded photocathode energy diagram. **(b)** Test photodiodes & photocathodes.

layer whose thickness is ~ 100 nm, and finally escape into the vacuum [2]. Therefore, the estimated time response of a BG–photocathode does not exceed ~ 10 ps.

To permit a comparative study of photoemission characteristics, a batch of test photocathodes were manufactured with both BG and homogenous (HM) active layers, with fig. 1 (b) showing the BG–photocathodes. The thickness of HM active layer was equal to 130 nm, so slightly exceeds the 100 nm GaAs layer present in the BG–photocathode. Both types of photocathode were hermetically sealed within test parallel plate photodiodes. The anodes of these photodiodes were made of glass, covered with transparent and conductive In_2O_3 layers, permitting photoemission to be studied in both transmission– and reflection–mode illumination geometries. Longitudinal energy distribution curves (LEDC) for the emitted photoelectrons were measured by applying a retarding potential between photocathode and anode [3]. *Q.E.*s were measured at low electric fields so that the influence of the Shottky effect could be neglected. Experiments were performed at both room and liquid nitrogen temperatures, specifically 300 K and 77 K respectively.

RESULTS

Q.E. spectra for two photocathodes with both HM and BG active layers, measured in both transmission– (TM) and reflection–mode (RM) illumination geometries are shown in fig. 2. One can clearly see that the *Q.E.*s for both photocathodes are low for photon energies close to the GaAs energy gap, but exceed 15 – 20% for $h\nu = 2.32$ eV ($\lambda = 532$ nm), when most of exciting photons are absorbed within the active layers. LEDC measured at room temperature in RM illumination geometry for photocathodes with HM and BG active layers are shown in fig. 3 (a) & (b) respectively. It is clear that for this illumination geometry, an increase in photon energy is accompanied by an increase in both amplitude and width of the high–energy tail of LEDC. This observation

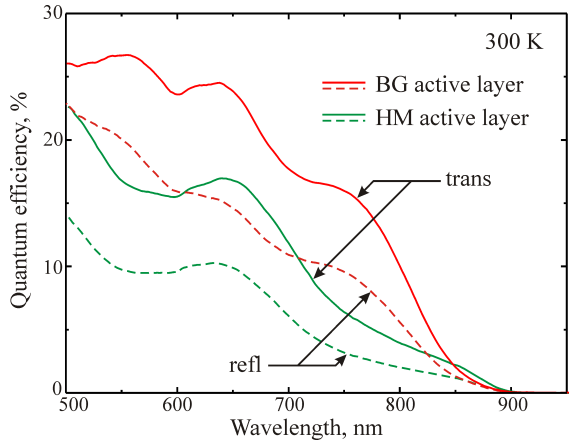

FIGURE 2. *QE* Spectra for photocathodes with both band–graded and homogeneous active layers in transmission–mode (*trans*) and reflection–mode (*refl*) illumination geometry.

is expected because at 'high' photon energies, the majority of photoelectrons with excess kinetic energy are generated in close proximity to the emitting surface. Consequently, a significant number of non–thermalised electrons are emitted before thermalisation, and their contribution to the photocurrent increases in tandem with the increase in photon energy. The BG layer cannot play any role in the RM illumination geometry, however the role of BG layer is changed significantly if the photocathode is illuminated in TM geometry.

Firstly, let us consider the photocathode with a HM active layer. If this photocathode is back–illuminated at 'high' photon energy, most of the photoelectrons with 'excess' kinetic energy are generated near the interface between the active and buffer layers. To be emitted into the vacuum, these photoelectrons must cross the active layer by diffusion. If the thickness of the active layer is approximately 100 nm, the diffusion process takes typically ~ 5 ps [2]. This time exceeds the photoelectron thermalisation time for p-doped GaAs [4], so a large portion of 'hot' photoelectrons generated near the back side of the HM active layer have to be thermalised during their diffusion to the emitting surface. The validity of this statement can be checked through analysis of the data presented on the fig. 4 (a) which shows the LEDC measured for the HM active layer in TM illumination geometry. One can see in fig. 4 that both the amplitude and width of the high–energy tail of the LEDC are approximately two times smaller than those shown in fig. 3 (a) which were measured from the same photocathode in RM illumination geometry. Nevertheless, it is shown that the thickness of the active layer (130 nm) is not sufficient for complete suppression of the 'hot' electron contribution to the photocurrent.

Analysis of data presented in fig. 3 (a) has shown that the thickness of the active layer of this photocathode is close to the optical absorption length for $h\nu = 2.32$ eV, and to the thermalisation length of 'hot' photoelectrons. This is the basis for the remarkable contribution from 'hot' electrons which is detected in the LEDC. To suppress photoemission of 'hot' photoelectrons from a conventional TM photocathode, one has to increase the thickness of HM active layer. However, if this is done, the response time of the photocathode increases rapidly because it is proportional to the squared thickness of the active

Left (a): Homogeneous (HM) layer **Right (b):** Band–graded (BG) layer

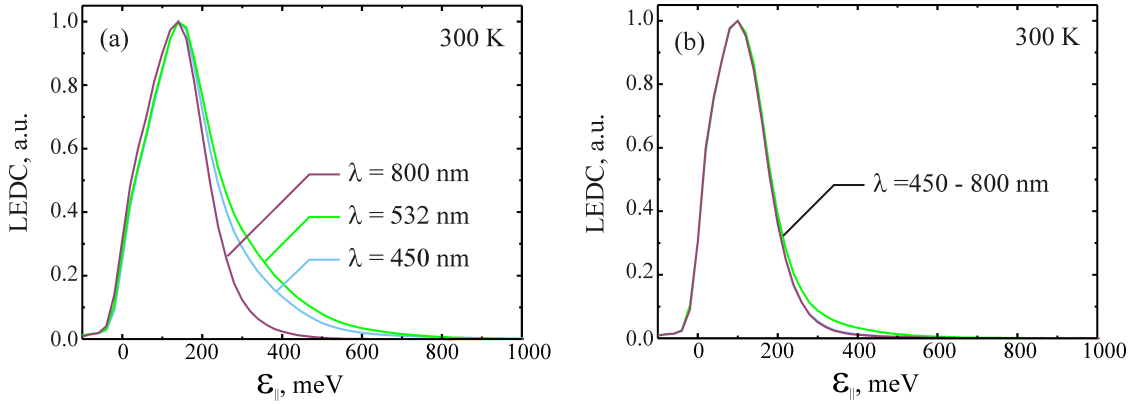

FIGURE 3. LEDC measured for the reflection–mode photocathode at room temperature.

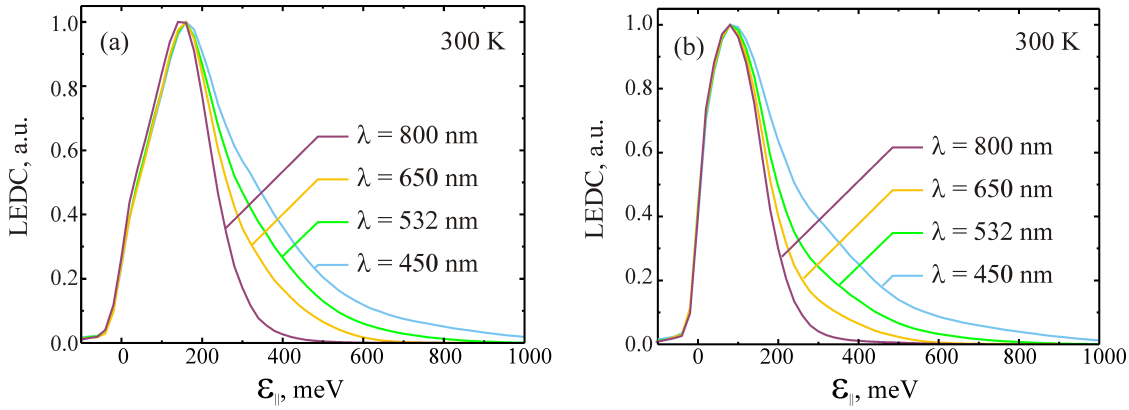

FIGURE 4. LEDC measured for the transmission–mode photocathode at room temperature.

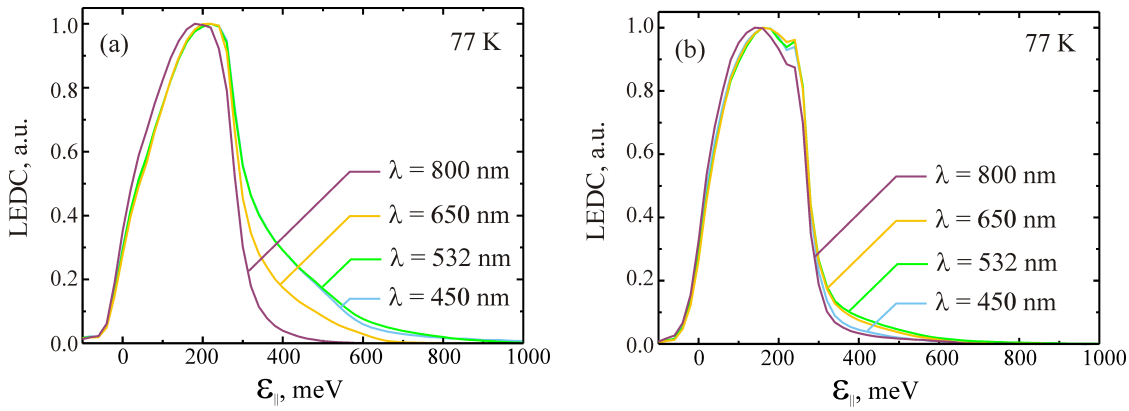

FIGURE 5. LEDC measured for the transmission–mode photocathode at liquid nitrogen temperature.

layer.

To overcome this problem, we have increased the total thickness of the active layer using the BG layer, thus creating the strong built–in electric field. This field is sufficient to accelerate photoelectrons to saturation velocity [1], boosting the photoelectron's 'slow' diffusion to a 'rapid' drift. Our estimate shows that it takes ~ 3 ps to extract photoelectrons from the BG layer and to inject them into the GaAs emitting layer. Therefore, use of a BG layer confers a low response time to the photocathode.

To check the effectiveness of the BG layer to suppress the 'hot' electron contribution, we have measured the LEDC for the photocathode with a composite active layer, as shown in fig. 4 (b). One can see from this figure that the 'hot' electron contribution in this photocathode is much less than those measured for the photocathode with a HM active layer. The similar data, shown in fig. 5 (a) & (b), were obtained for these two photocathodes at liquid nitrogen temperature. One can see, also, that the cooling of NEA–photocathode increases the width of the photoelectron energy distribution due to the increase of NEA–value.

SUMMARY

A new design for a cooled transmission–mode (TM) NEA photocathode on a sapphire base plate with a composite active layer, appropriate for FEL applications, is proposed and realised. To suppress the contribution of 'hot' photoelectrons in the broadening of the photoelectron energy distribution without loss of photocathode time response, a 'thick' band–graded (BG) layer with a strong built–in electric field was incorporated in the photocathode semiconductor structure. The estimated response time does not exceed 10 ps and *Q.E.* at $h\nu = 2.32$ eV exceeds 20%. Future plans include optimisation of the band–graded active layer parameters and measurement of response time.

ACKNOWLEDGMENTS

This work has been funded by the Science and Technology Facilities Council (STFC) as R&D in support of a possible fourth–generation light source facility in the United Kingdom. The work has been carried out by the Novosibirsk Institute of Semiconductor Physics and Novosibirsk State University, in collaboration with the Accelerator Science and Technology Centre at STFC Daresbury Laboratory.

REFERENCES

1. H. Arabshahi, M.R. Khalvati & M. Rezaee Rokn–Abadi, *Brazilian J. of Physics*, **38**, page 293 (2008).
2. K. Aulenbacher, J. Schuler, D.V. Harrach, E. Reichert, J. Rothgen, A. Subashiev, V. Tiokine & Y. Yashin, *J. Appl. Phys.*, **92**, page 7536 (2002).
3. A.S. Terekhov & D.A. Orlov, *Pis'ma Zh. Exp. Teor. Fiz.*, **59**, page 864 (1994).
4. *Optical orientation* edited by F. Meier & B.P. Zakharchenya, North–Holland publishing (1984).

K_2CsSb Cathode Development

John Smedley[a], Triveni Rao[a] and Erdong Wang[b]

[a]*Brookhaven National Laboratory, Upton, NY 11973*
[b] *Institute of Heavy Ion Physics, Peking University, Beijing, 100871, China*

Abstract. K_2CsSb is an attractive photocathode for high current applications. With a quantum efficiency of >4% at 532nm and >10% at 355nm, it is the only cathode to have demonstrated an average current of 35mA in an accelerator environment. We describe ongoing cathode development work for the energy recovery linac being constructed at BNL. Several cathodes have been created on both copper and stainless steel substrates, and their spatial uniformity and spectral response have been characterized. Preliminary lifetime measurements have been performed at high average current densities (>1mA/mm^2).

Keywords: Photoemission, Photocathode
PACS: 85.60.Ha

INTRODUCTION

Alkali antimonide cathodes have been used in photoinjectors for many years [1-2]. They have high quantum efficiency for visible light, but are challenging to implement in an accelerator; the lifetime of a K_2CsSb cathode in a normal-conducting (NC) RF cavity is measured in hours [1] due to the relatively poor vacuum in the injector. With the advent of superconducting (SRF) injectors, it may be possible to lengthen this lifetime considerably, as the cavity vacuum can be orders of magnitude better (~0.01nTorr in an SRF cavity, compared to ~1nTorr in an NCRF cavity).

One project based on such an SRF injector is the energy recovery linac (ERL) project at Brookhaven National Laboratory [3]. This machine has two modes of operation, with average currents of 50mA and 0.5A. The cathode being developed for 50mA operation is cesium potassium antimonide (K_2CsSb). The cathode will be mounted on the stalk of a ¼ wave choke filter, and will be kept at 77K to reduce the radiative heat load on the cavity. The laser spot on the cathode will be ~7mm in diameter, resulting in a design current density of 1.3mA/mm^2. For 0.5A operation, a diamond amplifier [4] will be used; in this case the average current required from the K_2CsSb photocathode is lower, but the cathode will be operated in transmission mode, with the laser incident from the back of the cathode through a transparent conductor.

This paper describes the current status of the cathode development for the ERL. Four cathodes have been created, and all have reached the design quantum efficiency (QE) of 10% at 355nm in reflection mode. The spectral response of each cathode has been measured, and preliminary measurements of lifetime at the design current density have been performed.

METHODS

The cathodes are created in a vacuum system with a base pressure of ~0.02nTorr. This vacuum is achieved using a 400l/s ion pump in conjunction with a titanium sublimation pump. The deposition geometry is vertical – the sources evaporate up onto the substrate, which is moved via a linear manipulator into position above each source sequentially. The antimony source is a tantalum boat packed with antimony pellets. The potassium and cesium sources are "V" sources from alvatech. The source to substrate distance is 4cm. A crystal monitor can be used to monitor the deposition rate of antimony and potassium. The cesium deposition rate is not measured; instead the QE is monitored during deposition by illuminating the cathode with a green laser (532nm), and the deposition ended when the QE stops increasing. In addition to the laser port used for deposition, the system has two horizontally aligned optical ports. After deposition, the cathode can be rotated to face one of these ports, with the back of the cathode facing the other. This arrangement allows the optical transmission of a transparent portion of the cathode substrate to be measured to check the deposition thickness, and it allows the QE to be measured in both transmission and reflection mode. Spectral response measurements are made through the reflection port by using a lamp (DH2000 from Ocean Optics) with a fiber-coupled monochromator (Edmond Optics) to illuminate the cathode. This source has a 2nm bandwidth, and a 5x5mm^2 spot on the cathode. The measurements with the lamp source require all external light sources to be off, as even the light from the filament of an ion gauge produces more current than the lamp. A 532nm CW laser can be used for lifetime and high current measurements.

For high current tests, the cathode can be moved in front of a wire mesh anode, with an electrode separation of 2.5cm. The anode can be biased to 5kV, allowing higher currents to be extracted from the cathode without space charge limitation. The parallel geometry of the cathode and anode in this case allows the electric field on the cathode to be estimated. The wire mesh is chosen to allow 100% transmission of the 532nm laser while maintaining a nearly uniform electric field between electrodes.

The copper cathode substrate is 2.5cm in diameter, polished with 1µm diamond polishing compound to a mirror finish. Portions of the copper substrate can be covered with shims made of other materials, allowing comparison of the QE for cathodes deposited on different substrates (to date, only copper and stainless steel have been measured). A 6mm diameter hole in the substrate exposes a glass slide covered with a transparent conductor. For the current measurements, 20-40nm of sputtered copper was used; indium-tin oxide (ITO) coated slides will be tested in the future. This 6mm region can be illuminated from either side, allowing the QE to be compared in reflection and transmission modes, and allowing the optical absorption of the cathode layer to be measured. The cathode is electrically isolated from the vacuum translation arm, enabling the cathode to be biased and the charge leaving the cathode to be measured. The arm includes a vacuum heater capable of raising the substrate to 150C, and liquid nitrogen (LN_2) cooling lines capable of cooling the cathode to -80C.

The cathode is deposited sequentially, following the general method of D. Dowell [1]. The substrate is at 150C for the antimony deposition, and the rate is set to ~0.5nm/s. 20nm of antimony is deposited, after which the substrate is cooled to ~140C

for the potassium deposition. 40nm of potassium is deposited, again with a rate of ~0.5nm/s. The substrate is cooled to 135C, and the substrate is biased to -20V. The cathode is illuminated with ~0.5mW of 532nm light, and the emitted current is monitored. Cesium is deposited until the emitted current stops rising, at which point the cathode is cooled to room temperature by flowing LN_2 through the arm.

RESULTS

Figure 1 shows the spectral response of cathode 2 deposited on both copper and stainless steel substrates. The spatial uniformity of this cathode is shown in figure 2. The QE was also measured on the unpolished copper fork which holds the substrate puck. To test the linearity of the response with flux, a 532nm CW laser was used to deliver 47.7mW to the cathode, resulting in 0.526mA of emitted current. The QE was the same as that measured with the lamp source, which provides 20nW and 226pA at 532nm. Cathode 2 was also cooled to -80C, with no change in the spectral response. Figure 3 shows the spectral response of 4 cathode depositions. Cathode 4 had a second cathode deposited on top of the first after the lifetime measurements, restoring its QE. Cathode 3 was deposited with the substrate at 120C (rather than 150C-135C); this exhibited somewhat inferior QE.

The performance of the cathodes in transmission mode depends strongly on the cathode thickness. Cathode 3 was the best, with a QE in transmission mode half that of reflection mode after accounting for the 20% transmission of the sputtered copper layer used to provide conduction.

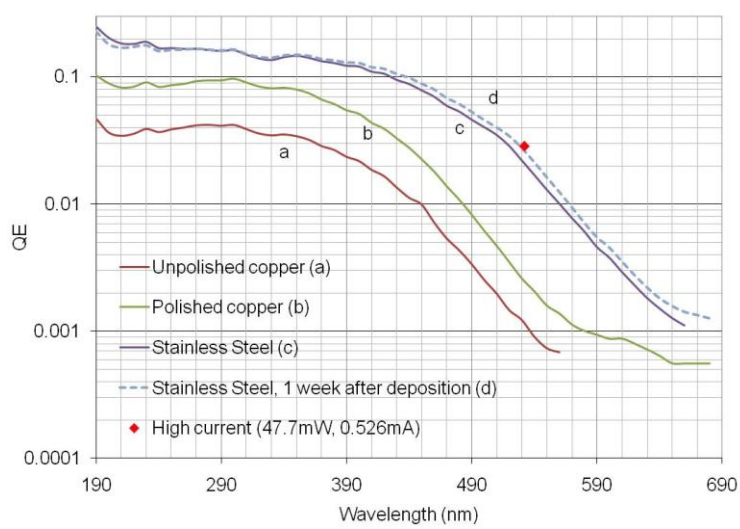

FIGURE 1. Spectral Response of a K_2CsSb cathode on copper and stainless steel substrates. The high current point was taken 8 days after deposition, immediately after response curve (d).

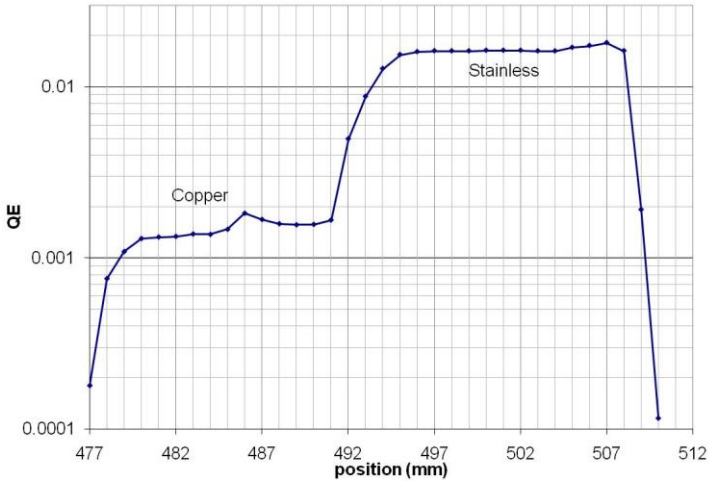

FIGURE 2. Spatial uniformity of cathode 2 measured with a laser (532mn).

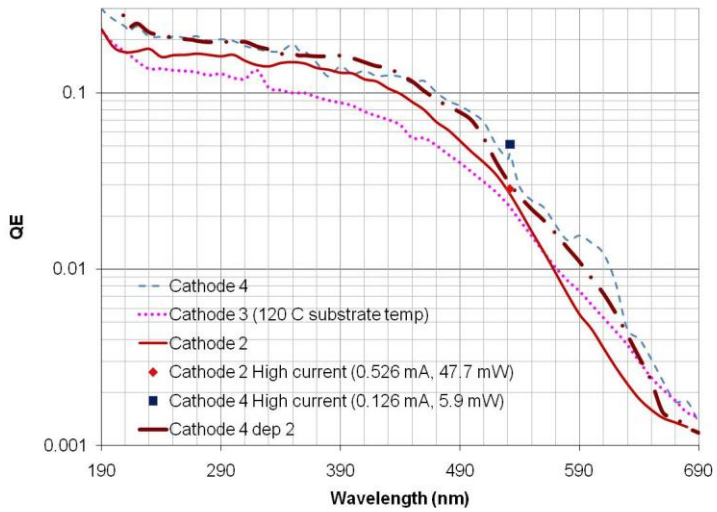

FIGURE 3. Spectral Response of a K_2CsSb cathodes on stainless steel substrates.

Lifetime

Cathode 4 was used to test the performance of K_2CsSb under continuous operation at the ERL current density. Tests on earlier cathodes have shown that the QE is unchanged after 40 days of storage in the chamber vacuum. The measurement station with the anode was used for these tests to achieve a field necessary to overcome space charge. The 532nm laser was focused to 80µm FWHM on the cathode to achieve a current density of up to 2.2mA/mm^2 with a bias of 3kV (1.45mW optical power, 10.9µA emitted current). The optical power was modulated to keep the current density near the ERL goal of 1.3mA/mm^2; for a 1kV bias on the anode, the cathode emission was space charge limited to 1.1mA/mm^2. Figure 4 shows the result of this test. For 2kV and 3kV anode bias, the QE decay is consistent with a 1/e lifetime of 100hrs; as the emission was space charge limited at 1kV, no estimate of lifetime can be made. A similar measurement was made with a 3mm diameter laser spot on the cathode and a

bias of 500V, with 60µA of emitted current. In this case the QE decayed from 2.3% to 2.0% in 40 hrs, yielding a 1/e lifetime of 360hrs. Two possible causes of this decay are ion bombardment of the cathode and local vacuum pressure rise near the cathode due to electron stimulated desorption from the anode (as the 1-3keV electrons strike the anode).

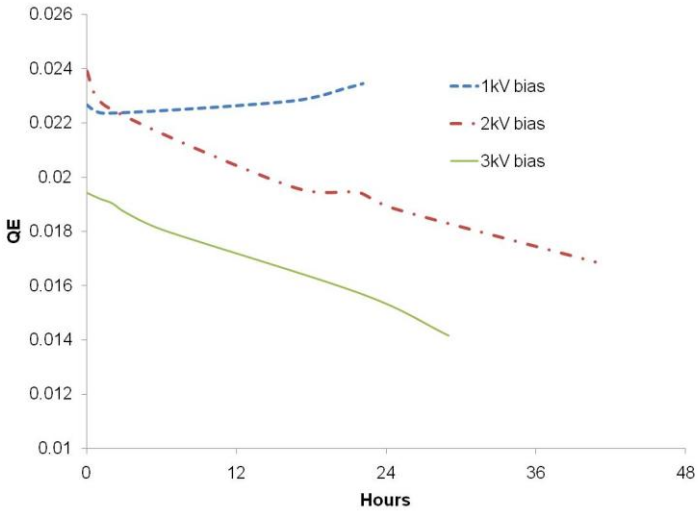

FIGURE 4. Decay of QE under continuous extraction of 1.3mA/mm^2.

CONCLUSIONS

K_2CsSb is an attractive cathode for high average current injectors. It has less stringent vacuum requirements than Cs:GaAs and has high QE for visible light. It has been shown to have a limited lifetime in a NCRF injector, but in the better vacuum of a SRF or DC injector, lifetimes of days to weeks should be possible, even at high current density. Cathodes have been fabricated that meet the QE and current density requirements of the BNL ERL.

ACKNOWLEDGMENTS

The authors would like to thank John Walsh for his expert technical assistance, Andrew Burrill for his advice and Veljko Radeka for his support. This work funded by the U.S DOE under Contract No. DE-AC02-98CH10886.

REFERENCES

1. D.H. Dowell, S.Z. Bethel and K.D. Friddell, *Nucl. Inst. and Meth. in Phys. Res.*, **A356** 167 (1995)
2. P. Michelato et al, "R & D Activity on High QE Alkali Photocathodes for RF Guns", Proceedings of PAC '95, p 1049 (1995). accelconf.web.cern.ch/AccelConf/p95/ARTICLES/WPC/WPC23.PDF.
3. V. Litvinenko et al, "R & D Energy Recovery Linac at Brookhaven National Laboratory", Proc. of EPAC '08, p 193 (2008). accelconf.web.cern.ch/AccelConf/e08/papers/mopc057.pdf.
4. J. Smedley, et al., "Diamond Amplified Photocathodes", in Diamond Electronics—Fundamentals to Applications II, Mater. Res. Soc. Symp. Proc. 1039, Warrendale, PA, (2007), 1039-P09-02.

Photoemission Spectroscopic Study of Cesium Telluride Thin Film Photocathode

Harue Sugiyama, Koji Ogawa, Junpei Azuma, Kazutoshi Takahashi, and Masao Kamada

Synchrotron Light Application Center, Saga University, 1 Honjo, Saga 840-8502, Japan

Abstract. The photoemission spectroscopy using synchrotron radiation has been carried out to study the high quantum efficiency and long working lifetime of cesium telluride (Cs_xTe_y) thin film photocathode. The electron affinity derived from the observed energy-distribution curves provides an important hint for long persistency of the photocathode.

Keywords: Cesium-Telluride, Photocathode
PACS: 29.25.Bx, 73.61.–r

INTRODUCTION

It has been known that Cs_xTe_y (cesium telluride) thin film photocathodes for RF guns have high quantum efficiency and long working lifetime. In fact, Cs_2Te thin film photocathodes have been used as RF-gun photocathodes for over 10 years [1]. Why do Cs_xTe_y thin films maintain such high quantum efficiency with long lifetime against the damage by grinding ion-bombardment under high RF-voltages? In order to understand this issue, we take up the first step to study Cs_xTe_y characteristics.

In the present study, Cs_xTe_y thin films were formed with vacuum evaporation. The photoemission spectroscopy was applied to measure the energy distribution of the electrons emitted from the films. The threshold energy or work function was estimated from the observed spectra of secondary electrons and valence-band photoelectrons. Finally, the electron affinity of Cs_xTe_y is discussed, giving an important hint for long persistency of the photocathode.

EXPERIMENT

Saga University has constructed a new beam line at BL13 of Saga Synchrotron Light Source (SAGA-LS), which has 1.4 GeV beam energy [2]. The BL13 consists of a VLS-type monochromator with a planar undulator and a PGM-type monochromator with bending radiation. The PGM monochromator provides photons in the energy range from few eV to 150 eV. The present photoemission study has been carried out at the PGM station.

The PGM station consists of three chambers and the transfer system. An air-lock chamber makes it possible to install samples quickly. A preparation chamber and an

analyzing chamber are used for sample preparation and analyses, respectively. Samples can be transferred in the ultra high vacuum (UHV) between them. In the preparation chamber, cesium and tellurium sources, a leak valve for oxygen gas, a thickness monitor, and an ion-sputtering gun are installed. The sample annealing and the total-yield measurement with a He-Ne laser are also conducted in the chamber. The analyzing chamber involves an OMICROM HR-125 hemi-spherical electron-analyzer and a PHI 10-155A/CMA Auger spectrometer, which can be used to measure the photoemission spectra and to check the surface contaminations, respectively. The drain current from the samples can be observed with a Keithley 616 pico-ammeter.

Cs_xTe_y thin films were formed with a vacuum evaporation method in the preparation chamber having a base pressure of 3×10^{-8} Pa. Molybdenum plates were used as sample substrates. The substrates were heated up to 550 °C in the preparation chamber before deposition. Cs_xTe_y thin films were formed at room temperature by first deposition of tellurium on the substrates and subsequent deposition of cesium. Tellurium bits of 99.9999 % in purity were purchased from Nilaco and installed in the deposition device, while a commercially available cesium dispenser was obtained from SAES getters. The details of the sample preparation have been already reported elsewhere [3]. The Cs_xTe_y thin films were transferred in UHV to the analyzing chamber. All measurements were carried out in the analyzing chamber having a base pressure of 3×10^{-8} Pa.

PHOTOEMISSION SPECTRA

The photoemission spectroscopy was applied to measure the energy distribution of the electrons emitted from the films. The observed spectra consist of secondary electrons and photoelectrons. The former is the majority of electrons emitted from the films, and then firstly we focus our attention on the secondary electrons. The cut-off energy of the secondary electrons corresponds to the vacuum level of the samples, while the threshold energy or the work function can be derived from the observed spectra of secondary electrons and valence-band maximum (VBM).

Figure 1 (a) shows the energy distribution curves of secondary electrons from the cesium telluride thin film. The distribution curves were measured in biased condition in order to observe the electrons of less energy than the analyzer work function with avoiding stray electrons in the chamber. The ordinate is normalized at the peak intensity and the abscissa is given relative to the vacuum level of the analyzer. Figure 1 (a) shows the spectra of the film (about 50 nm as total thickness) from fresh off to 6 days after the fabrication. It is found that the low energy cut-off is shifted from -3.3 eV (1 hour) to -2.5 eV (6 days). The vacuum levels from the Fermi level correspond to the value of 1.3 eV (1 hour) and 2.1 eV (6 days).

Figure 1 (b) shows valence-band spectra of the film. The arrows indicate the Fermi level that was calibrated with photoemission of gold. As seen in Fig. 1 (b) the VBMs of the film are observed at 2.5 eV lower than the Fermi level. It is noticed that the VBMs are not shifted within several days.

The present results of the photoemission spectroscopy indicate that the threshold energy is changed from 3.8 eV to 4.6 eV. A cesium telluride thin film as a

photocathode is irradiated with the laser, which has the energy of 4.7 eV in general. Therefore, the change in the electron affinity does not make any difference.

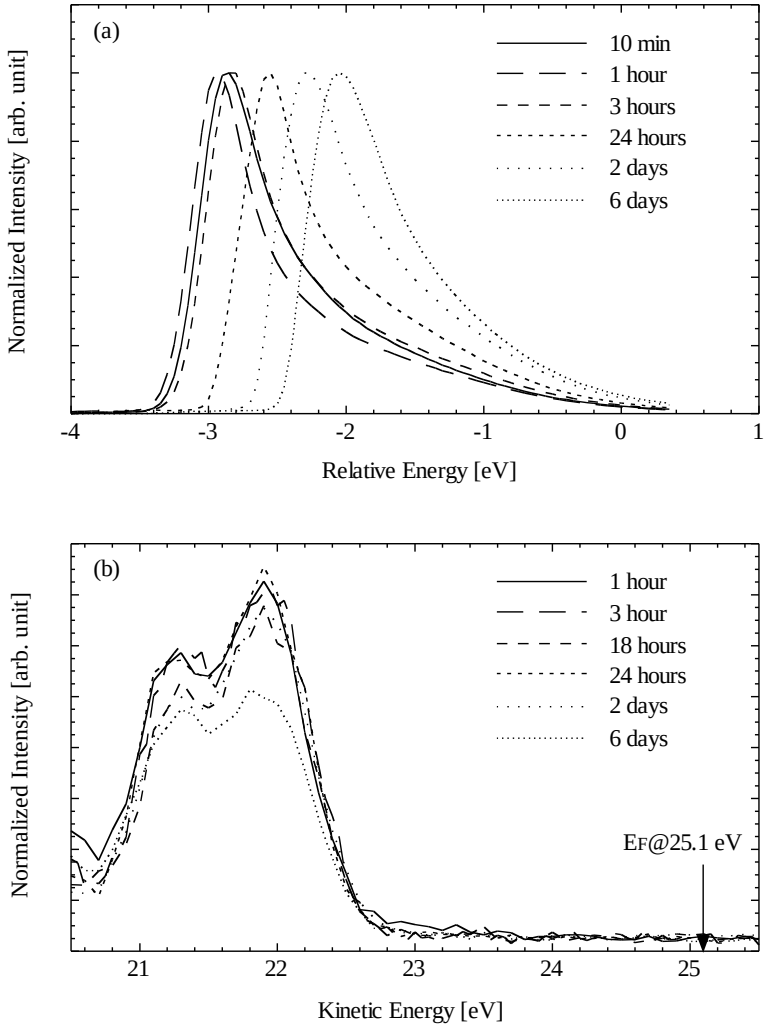

FIGURE 1. (a) Secondary electron spectra and, (b) valence-band spectra.

The VBMs are not shifted within several days. It is inferred from this result that the energy gap is not changed. It is possible to consider that the change of the low energy cut-off is attributed to the temporal changes in the electron affinity. The values of the electron affinity, that can be derived from the results of the photoemission spectroscopy and reported value of the energy gap [5] are 0.5 eV (1 hour) and 1.3 eV (6 days). The temporal change in the electron affinity and in the shape of valence-band are interesting observations, but need further analysis.

AUGER ELECTRON SPECTRA

Figure 2 shows the Auger-electron spectra of the same film as those shown in Fig. 1, and the substrate before a heat treatment by way of comparison. The Auger-electron

spectrum of the film was observed after the photoemission measurement. It is stressed that there were no peaks except for Te MNN and Cs MNN Auger peaks. The peaks originated from carbon or oxygen on the spectrum of the film were out of the detection limit. Therefore, a contamination on the surface is not a main cause of the temporal changes as shown in Fig. 1.

The elemental ratio between cesium and tellurium (Cs:Te) has been derived from the Auger spectra. The cross-section ratio of Cs MNN to Te MNN Auger peaks is about 1:5 in the literature [4]. As seen in Fig. 2, the peaks a and b, which are assigned as Te MNN and Cs MNN Auger peaks, respectively, show the intensity ratio of 7:5. Therefore, the elemental ratio is roughly designated as Cs_7Te.

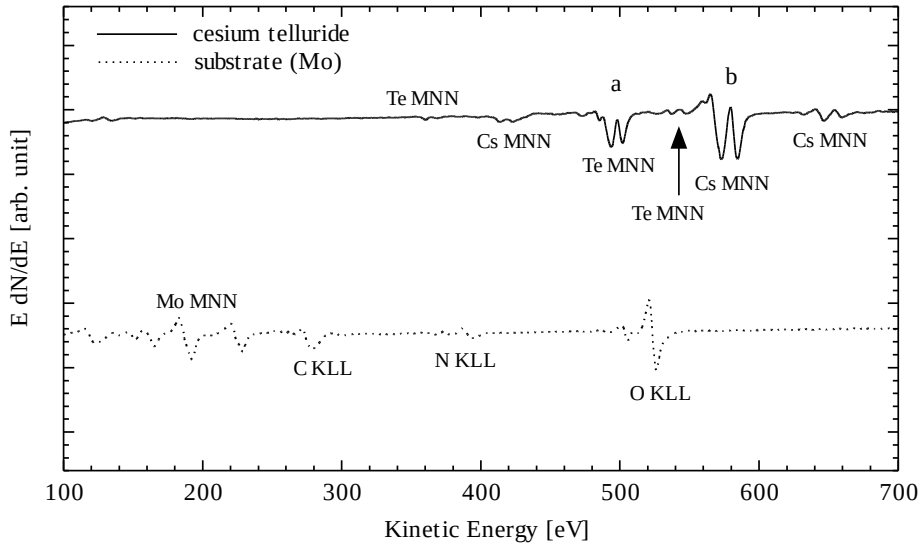

FIGURE 2. Auger-electron spectra.

ACKNOWLEDGMENTS

I express my greatest appreciation to everyone at Jefferson Lab for hosting the workshop and to all other people for giving me such a wonderful opportunity. This research was partially supported by the Ministry of Education, Science, Sports and Culture, Grant-in-Aid for Young Scientists (B).

REFERENCES

1. S. H. Kong, J. Kinross-Wright, D. C. Nguyen, and R. L. Sheffield, J. Appl. Phys. **77** (11), 6031 (1995).
2. K. Takahashi, Y. Kondo, J. Azuma, and M. Kamada, J. Elect. Spect. and Rel. Phenom. 144/147, 1093 (2005).
3. H. Sugiyama, "Characteristics of Cesium Telluride Thin Film Photocathode", Ph.D. Thesis, Nagoya University, 2005.
4. "Handbook of Auger Electron Spectroscopy" 3rd ed. (PHYSICAL ELECTRONICS, ISBN: 0-964824-0-1).
5. R. A. Powell, W. E. Spicer, G. B. Fisher, and P. Gregory, Phys. Rev. B **8**, 3987 (1973).

DC High Voltage Conditioning of Photoemission Guns at Jefferson Lab FEL

C. Hernandez-Garcia, S. V. Benson, G. Biallas, D. Bullard, P. Evtushenko, K. Jordan, M. Klopf, D. Sexton, C. Tennant, R. Walker, and G. Williams

Thomas Jefferson National Accelerator Facility, Newport News, VA 23606

Abstract. DC high voltage photoemission electron guns with GaAs photocathodes have been used to produce polarized electron beams for nuclear physics experiments for about 3 decades with great success. In the late 1990s, Jefferson Lab adopted this gun technology for a free electron laser (FEL), but to assist with high bunch charge operation, considerably higher bias voltage is required compared to the photoguns used at the Jefferson Lab Continuous Electron Beam Accelerator Facility. The FEL gun has been conditioned above 400kV several times, albeit encountering non-trivial challenges with ceramic insulators and field emission from electrodes. Recently, high voltage processing with krypton gas was employed to process very stubborn field emitters. This work presents a summary of the high voltage techniques used to high voltage condition the Jefferson Lab FEL photoemission gun.

Keywords: DC high voltage, photoemission electron guns, krypton processing.
PACS: 29.25.Bx, 81.65.Ps, 84.70.+p, 07.30.-t, 79.60.Bm

INTRODUCTION

The surface chemistry of the Cs:GaAs photocathode imposes extreme requirements on the vacuum environment in photoemission electron guns, while the need to extract electrons from the photocathode and create electrostatic focusing demands bias voltage at least ~ 100kV, with gradients as high as 5 MV/m. Besides the challenges to obtain and maintain extreme high vacuum conditions, another non-trivial challenge is presented by the ceramic insulator, which electrically isolates the electrode from ground. The insulator must be vacuum compatible and able to stand-off the voltage. Extreme care is taken in polishing and cleaning the electrodes to minimize field emission, which can puncture the insulator by charge build-up, as well as severely degrade vacuum conditions in the gun chamber. Surface preparation of the electrode structure is not sufficient to eliminate field emission. Once the gun is assembled in a clean environment and the electrodes are under ultra high vacuum conditions, the voltage needs to be increased slowly and systematically to prevent electrical breakdown. This is a time consuming but critical process before the gun can be operated at the desired voltage. In the process, field emitters are encountered and processed out. At higher voltages, gas desorption takes place with every kV increase, contributing to the complexity of the process. Once the field emission is extinguished, and the gas desorption no longer present, the gun is fully conditioned. Typically, the gun is conditioned to higher voltage than desired for nominal operations.

In the early 1990s, the DC photoemission gun technology used by the Continuous Electron Beam Accelerator Facility at Jefferson Lab (JLab) was adopted by the IR-

Demo Free Electron Laser (FEL) [1] to produce un-polarized electron beam, with charge per bunch ~100pC, which required voltages in excess of 300kV to mitigate space charge effects [2]. The JLab FEL has successfully conditioned two generations of electron guns to 425kV for operation at 350kV, albeit with a multitude of problems with punctured insulators and damaged electrodes [3,4].

The JLab FEL DC Photoemission Gun

In the JLab FEL gun [3,4], the high voltage cathode electrode is supported by a long tube, also at high voltage, that is coaxial to the cylindrical insulator as shown in Fig. 1. Field emission from the support tube can produce charge build-up in the bulk of the insulator. When the insulator discharges it creates micro-channels that eventually lead to vacuum failure. The ceramic cannot be repaired at that point. It is very expensive and requires highly skilled shops for the bracing of large diameter kovar rings. This is why high voltage processing must be done very carefully. Early in the JLab IR Demo FEL, the inside of the ceramic insulators were platinum implanted to mitigate the charge build-up by adding a conductive path to ground, although at very high resistivity (in the order of tens of Giga-Ohms across the length of the ceramic).

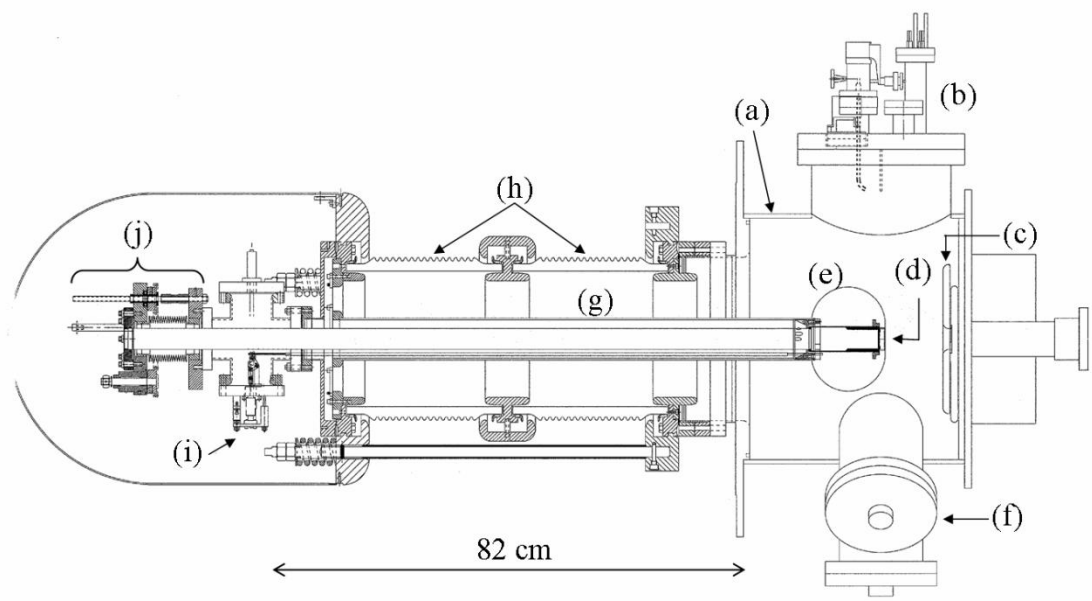

FIGURE 1. Schematic showing the JLab FEL DC photoemission gun. (a) vacuum chamber, (b) instrumentation, (c) anode, (d) 25 mm diameter GaAs photocathode, (e) ball cathode, (f) NEG pumps, (g) ball support tube, (h) ceramics, (i) shield door actuator mechanism, and (j) stalk retracting mechanism.

HIGH VOLTAGE CONDITIONING

High voltage conditioning in DC guns is nominally performed under vacuum conditions. Usually, the field emitters can be processed out by slowly increasing the

voltage to control the field emission current. There are commonly three cases of field emission: a) erratic current, b) current increasing rapidly with time, and c) steady current. In case a), the usual procedure is to sustain the voltage for a few minutes until the field emitter 'burns off', causing the field emission current to decrease or extinguish almost completely. For case b), while the voltage is held constant, the current reaches the trip limit turning off the high voltage power supply. In some occasions, enough energy is released to burn off the emitter when the voltage is restored; in other occasions, the field emitter can sharpen (by surface migration) leading to much larger current at the same voltage when originally generated. A sharp emitter is somewhat easy to burn off, by going to lower voltage limiting the field emission current and slowly increasing the voltage as the current decreases. Case c) is probably the most difficult to process. Since the field emission current can be sustained for hours at levels beyond 100 micro-amperes, at hundreds of kV there is enough power to heat the copper gaskets in the large diameter conflat flanges opening leaks, or worse, puncturing the ceramic insulator.

The diagnostics include: total current from the high voltage power supply, the ion pump current to monitor pressure and a residual gas analyzer (RGA) to look for potential leaks. Another diagnostic that proved essential in the recent FEL gun conditioning is radiation monitors. Two ionization chambers were installed next to the gun, one on the stainless steel vacuum chamber (closest to the ball cathode) and one more on the SF_6 aluminum tank to monitor field emission from the support tube electrode, which is coaxial to the ceramic insulator (See Fig. 1).

In the FEL gun, field emitters are typically encountered between 100kV and 250kV. Once the emitters are processed up to that voltage, a new phase in the processing begins; something we have called "voltage-induced gas desorption". With every 1 kV increment, the pressure in the gun vacuum chamber increases from low $1x10^{-10}$ Torr to mid $1x10^{-8}$ Torr. The time it takes for the vacuum to recover is voltage dependent: below 300 kV, it takes about 5 to 10 minutes but at 420 kV it can take up to one hour for each 1 kV step.

The RGA reports increased H_2, CH_4, CO and CO_2 partial pressure with each step up in voltage. This gas desorption phase is not fully understood yet, but it has been observed every time the gun has been conditioned, and it has a very sharp onset. For example, if the gun is fully conditioned to 350kV, it can operate for years at that voltage, but if the voltage is increased by 1 kV, then gas desorption is present again.

Despite these complications, the FEL gun has been successfully conditioned in several occasions to 450 kV, taking about 100-man hours in the process. However, during September 2008, high-voltage conditioning of the FEL gun took much longer. The first significant field emitter was encountered at 270 kV. After ~50 hours of processing under good vacuum conditions, the emitter could not be processed out. At that point it was decided to try gas processing.

High Voltage Processing with Helium Gas

When field emitters cannot be processed under the nominal conditioning (i.e. the excess current is above 100 uA at voltages below 150kV and is self-sustained for

hours, or if the emitter returns at the same voltage it first appeared after several hours of processing), an inert gas can be used in combination with the voltage.

Helium is commonly used and has shown good results for the Cornell gun [5]. However, there is always a risk to develop a leak especially in the ceramic insulator due to the lack of vacuum diagnostics at the $1x10^{-5}$ Torr level where the inert gas processing takes place. Note that this process is not a DC glow discharge, the pressure is too low for igniting a plasma. Most ion gauges do not operate at that pressure and the ion pumps need to be turned off. The NEG pumps keep pumping though, and do not pump inert gasses. Actually, at the $1x10^{-11}$ Torr range most of the pumping is provided by the NEGs and the ion pumps are mostly used as gauges. In the FEL gun, an RGA capable of operating up to the $1x10^{-4}$ Torr range was used to monitor the overall pressure with its integrated ion gauge, and its mass analyzer was used to monitor argon for potential leaks during the high voltage processing.

In the $1x10^{-5}$ Torr range, helium gas molecules are ionized by the field emission current and are accelerated towards the negatively biased electrode, effectively "back-ion" bombarding the field emitter until the geometry or the work function is altered. In the FEL gun, helium processing worked very effectively in the sense of processing field emitter at voltages below 270kV. The high voltage power supply current was at baseline and the voltage could then be increased up to 375kV. When the helium was pumped out and the voltage was ramped up back to where the field emission first started at 270kV, the gas desorption phase was observed, but at 274 kV the field emission started again and the emitter could not be processed out.

High Voltage Processing with Krypton Gas

Since processing with helium showed some improvement, but could not process the emitter at 270kV, it was proposed to use a heavier gas. Ideally one would start with neon. Argon could work better, but the problem is that the Argon peak is used to monitor for leaks during the processing. The only gas available at the time was krypton, which is about 20 times heavier than helium. For a detailed procedure on krypton processing, see Reference 6.

Starting with $5x10^{-6}$ Torr, krypton processing quickly burned off some emitters at voltages below 250kV. After one hour of processing between 290kV and 315kV, the current was at baseline and very stable, but the radiation was high. At that point a pattern was observed in the current and radiation with every 1 kV increase. The pattern resembled the gas desorption phase observed under nominal vacuum high voltage conditioning, only this time the diagnostic was the signal from the radiation monitors instead of the current from the ion pumps. The radiation tracked the current perfectly, showing a sharp rise and an exponential decay with every 1-kV step. The krypton processing was then successful in eliminating emitters and at the same time the processing had evolved into the gas desorption phase, which continued up to 375kV for tens of hours, but the field emitter at that voltage was not fully processed yet. The krypton was then pumped down and with the gun in nominal vacuum conditions, the voltage was ramped up effortlessly to 364 kV, where the first indication of gas desorption was observed. Krypton processing continued for tens of

hours up to 415kV followed by soaking at 365kV under vacuum for several hours, concluding successfully the gun high voltage conditioning.

GUN OPERATIONS AFTER KRYPTON PROCESSING

The GaAs wafer suffered surface damage after ~200 hours of high voltage conditioning. The cesiated photocathode exhibited large amounts of field emission seen on the phosphor screen downstream of the gun. This effect has been observed previously in the IR-Demo FEL, but heat cleaning the wafer for 5 hours proved back then to improve the cathode QE lifetime and to minimize field emission from the cesiated surface [6]. This time, the field emission from the wafer limited the gun operating voltage to 290kV, which proved insufficient to drive the FEL. It was decided to vent the gun and change the wafer, which showed the anodization area almost gone. The non-anodized area showed a myriad of small pits, but a thorough surface analysis needs to be done. No evidence of krypton in the wafer bulk was found with XPS.

Since the gun had been conditioned up to 365kV under vacuum conditions and up to 415kV with krypton, it was expected for the gun to remain conditioned after the wafer change-out and to exhibit mainly gas desorption, as it had been previously observed. However, during the initial conditioning after replacing the wafer, field emission in excess of 100 microamperes was present again at 270kV, as if no processing had occurred at all. It appears as the gun bake cycle at 250C had re-activated the field emitter.

The gun had to be re-conditioned again up to 375kV with krypton. Then under vacuum, the gun remained conditioned up to 360kV, until the wafer was heat cleaned at 550C as part of the photocathode activation process. We did not expect the heat clean, which is made in-situ by retracting the wafer inside the ball electrode, to affect the electrode conditioning, but it did. The field emission went from zero to 100 micro-amperes at 350kV, but this time the field emission was generated at the ball cathode, not the wafer. After a few weeks of operating the gun at 350kV, the field emission current slowly decreased and settled down to 10 microamperes. The gun has been operating with this field emission since November 2008, decreasing significantly the photocathode lifetime. The field emission is inducing some charge build-up in the ceramic insulator that discharges every 30 to 45 minutes. This has no effect on FEL operations, other than a pressure surge in the gun from $5x10^{-10}$ Torr to $1x10^{-9}$ Torr.

CONCLUSIONS

Kyrpton processing was very useful, and provided a means to achieve bias voltage unattainable using conventional HV processing techniques. Helium processing was less effective, in particular it did not contribute to raising the on-set voltage for field emission neither to the gas desorption phase. One speculation is that if the emitter is not processed, most of the available ‘energy’ is going through the field emission current, limiting the available energy for desorbing gas. Once the emitter was processed with krypton, the gas desorption phase continued as usual. It is not clear if

neon or argon would have helped processing the emitter in the same was as krypton did. At the pressures used for gas processing ($1x10^{-5}$ Torr), there is little chance for plasma formation and therefore sputtering on the electrodes surfaces. Besides, the electrodes are biased negatively. In plasma sputtering systems, the pressure is in the $1x10^{-3}$ Torr range and the electrodes are biased positively. Radiation monitors proved to be an essential diagnostics during the gun high voltage conditioning. High voltage processing with krypton gas works.

ACKNOWLEDGMENTS

This work supported by the Office of Naval Research, the Commonwealth of Virginia, and by DOE Contract DE-AC05-060R23177. Many thanks to Michael Kelley for doing the krypton analysis on the wafer, and to CEBAF's polarized source group for quickly making available for us a bottle of krypton gas.

REFERENCES

1. G. R. Neil, et al., *Physical Review Letters*, **84**, 4, 662-665 (2000).
2. D. Engwall, et al., 1997 Particle Accelerator Conference, Vancouver, B. C., Canada, IEEE, Piscataway, NJ, 1998.
3. T. Siggins, et al., *Nucl. Insttrum. Methods Phys Res., Sect. A* **475**, 549 (2001).
4. C. Hernandez-Garcia, et al., Proceedings of the 2005 Particle Accelerator Conference, Knoxville, TN, pp. 3117-3119.
5. B. Dunham (private communication).
6. C. Hernandez-Garcia, JLAB-TN-08-065.

Design and Performance of the Cornell ERL DC Photoemission Gun

K. Smolenski, I. Bazarov, B. Dunham, H. Li, Y. Li, X. Liu, D. Ouzounov, C. Sinclair

CLASSE, Cornell University, Ithaca, NY 14853, U.S.A.

Abstract. Cornell University is planning to build an Energy Recovery Linac (ERL) X-ray facility. For an ERL, it is well known that the x-ray beam brightness for the users is mainly determined by the initial electron beam emittance provided by the injector. To address technical challenges of producing very low emittance beams at high average current as required for an ERL, Cornell University has proposed a prototype injector with 5-15 MeV beam energy, 100 mA maximum average current and 77 pC/bunch. In this article, we describe the design, construction and initial results for a DC photoemission gun now under operation.

Keywords: DC high voltage GaAs photogun, Energy recovery linac.
PACS: 29.25.Bx, 81.65.Ps, 84.70.+p, 07.30.-t, 79.60.Bm

INTRODUCTION

An electron injector for an ERL-based light source has many challenges. To provide the x-ray beam quality that users demand for the future, the injector needs to meet the requirements show in Table 1 [1].

TABLE 1. Injector Requirements (values in ( ) are goals for the prototype system of this paper)

Beam Energy	10-15 (5-15) MeV
Charge per bunch	77 (77) pC
Average Current	100 (100) mA
Bunch Length	2-3 (2-3) ps
Transverse Emittance	0.3 (2) μm
Operating Frequency	1.3 (1.3) GHz

At Cornell University, we have undertaken a program to develop and test such an injector (see Fig. 1) towards realization of this difficult set of requirements. The design was based on detailed simulations using genetic algorithms to find the optimum solutions to the multi-parameter design space [2]. The electron source is a DC photoemission gun using a GaAs cathode, providing a 1.3 GHz bunch train of 77 pC/bunch with a 20-40 ps ‘beer can’ distribution. This is followed by a short section

for emittance compensation solenoids and a normal conducting buncher cavity [3]. The beam is then accelerated through a cryomodule containing five 2-cell niobium superconducting RF (SRF) cavities, each with individual control of phase and gradient. The cavities have two opposing 50 kW input couplers to feed in 100 kW per cavity. The available RF power allows for either 100 mA at 5 MeV or 33 mA at 15 MeV. After the SRF cavities, an extensive suite of diagnostics allows for a complete characterization of the transverse and longitudinal phase space of the beam. The beam is terminated in an aluminum dump with a capacity for disposing 600 kW of average power. The current status of the complete injector commissioning and beam performance has been reported elsewhere. [4]

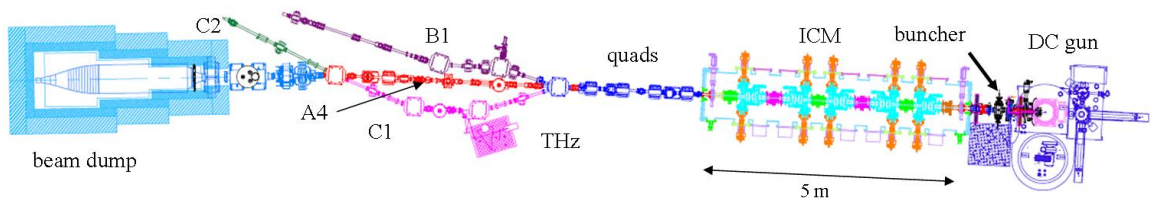

FIGURE 1. The layout of the Cornell prototype ERL injector.

DC PHOTOEMISSION GUN

Based on the experience of other labs [5] and of the authors, DC photoemission guns provide the best chance of producing the low emittance, high average power beam to meet the needs of an ERL. The present record for average current belongs to the Boeing normal conducting RF (NCRF) gun [6] at 32 mA (25% duty factor), and while other projects continue to push for higher current with NCRF guns, no improvements have been realized. Work on SRF guns has made excellent progress recently [7], but the prospect of obtaining 100 mA average current is still many years away. The DC gun used for the Jefferson Lab FEL project [5] has reliably provided 135 pC bunches at an average current of ~9 mA, and an extension of that technology is the most likely path to meet the needs of an ERL injector in the near future.

High Voltage Gun

Common sense dictates that high initial beam energy and high electric field at the cathode are necessary to overcome the space charge forces in bunched beams and obtain the best possible emittance. Simulations [2] show that higher gun voltage is important for obtaining low emittance up to a certain point, after which the improvement is relatively small. Thus, a DC gun operating in the range of 500-600 kV should meet the emittance goals with the appropriate cathode. To minimize dark current at the operating voltage, the gun must be processed to roughly 25% above the operating value; consequently the Cornell gun has been designed to withstand a 750 kV maximum voltage.

A schematic cutaway of the Cornell DC photoemission gun is shown in Fig. 2, and was designed to meet the requirements in Table 2. The gun was operated for over a year using a test beamline to measure the performance of the gun and cathode before

mating it to the rest of the injector. Details of these measurements have been published elsewhere [8, 9], with the main result that the emittance measurements at 77 pC/bunch and 250 kV beam energy match the simulations very closely, giving confidence that the simulations for the entire system are valid. Two difficulties observed involved the laser profile and laser stability. Tails in the phase space distribution were traced (through simulation) to non-uniformities and laser stability across the 'flat-top' laser distribution and variations in the distribution over time. The pointing stability of the laser at the cathode was also an issue, causing jumps in the phase space measurements. The laser itself is stable to 20-30 μm rms, but this increases upon demagnification to the cathode. We have since purchased an active position stabilization device (MRC Systems GmbH) which will reduce the position jitter at the cathode to < 10 μm rms.

TABLE 2. DC Gun and Laser Requirements

Operating voltage	500-600 kV
Maximum voltage	750 kV
Average Current	100 mA
Vacuum during operation	$< 1\times10^{-11}$ Torr
External SF_6 pressure	4 atm
Laser wavelength	520 nm
Laser pulse shape	'beer can'
Laser pulse length	20-40 ps
Phase jitter	< 1 ps

All guns of this type suffer from the problem of controlling field emitted electrons from the high voltage surfaces. These electrons can land on the insulator, and if the charge builds up punch-through can occur, causing a vacuum leak. We purchased an insulator with an internal resistive coating (CPI, Inc.) to bleed off these electrons, but it has only been successful up to 450 kV during processing, above which punch-through occurs. In addition, the coating has not adhered well, leaving a layer of dust on the electrodes, certain demise for reaching 750 kV. Two such insulators have been built and tested with similar damage occurring to both. Correlation between the location of edges of the segmented electrode support stalk and the vacuum breaches caused by punch-through have led to the adoption of a single piece stalk to replace the one shown in fig. 2.

Colleagues at Daresbury Lab [10] have built an insulator using a new material from Morgan Advanced Ceramics (AL-970CD) which is more resistant to field emitted electrons, at least up to 500 kV. We are in the process of obtaining a new insulator using this material, and are also investigating the use of segmented insulators [11] which completely block the line of sight between the electrodes and the insulator, but have a much more complicated mechanical structure. For now, we are limiting the gun voltage to 300 kV to reduce the chance of damage, until a spare is obtained.

If one can make electrodes that do not field emit, the insulator design is not so important – this is the Holy Grail for gun design (and for SRF cavities). We have built the present gun emulating the best techniques known for cavity cleaning, namely electro-polishing followed by high pressure rinsing. In a test chamber, gradients of 30 MV/m have been routinely reached on large area electrodes, but these results have not been reproduced in the real gun, most likely due to dust contamination from the insulator coating.

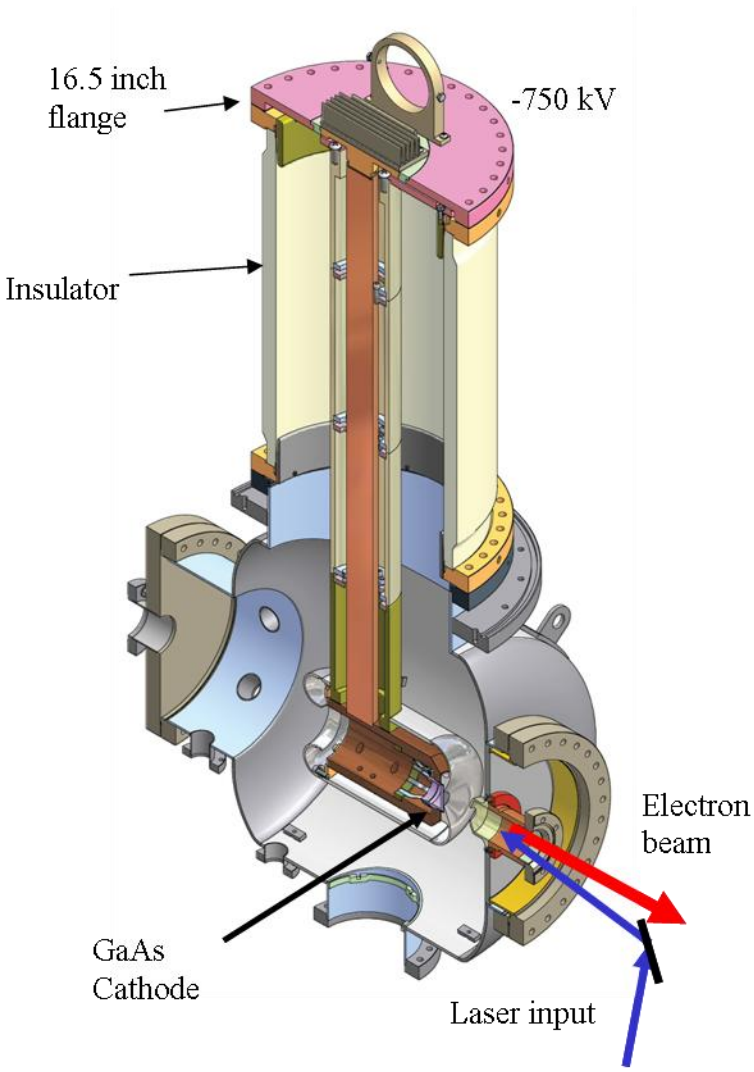

FIGURE 2. The Cornell Photoemission Gun.

Laser System

To produce 100 mA from a GaAs cathode with a 1% QE, over 20 Watts of laser power at 520 nm is required at the cathode (2 W for 10% QE). Accounting for possible losses in the laser transport and beam shaping, a laser with 40 W of average power is desired. The system must provide pulses at a repetition rate of 1.3 GHz

synchronized to the RF master clock (with a timing jitter < 1 ps), and a configurable pulse shape in time and space for minimizing the electron beam emittance.

We have chosen to use a Yb-doped fiber laser system to meet these requirements [12]. Initially, the oscillator was made in-house, but difficulties were encountered in accurately synchronizing it to the RF system. Subsequently, a commercial fiber laser 'clock' was purchased from PriTel Inc. They modified a standard product to work at our pulse repetition rate. The laser is triggered by the RF master clock signal, and the jitter between the output pulse the clock signal is less than 500 fs. The pulses are fed to a single mode fiber amplifier where the pulse energy is boosted to 150 nJ, low enough to prevent any nonlinear distortion. The pulse energy is further increased through amplification in a double clad large mode area fiber amplifier built to work in nearly single mode regime. Currently we have implemented only one such stage and achieved average power of 35 watts at 1040 nm (27 nJ pulse energy). The IR pulses are frequency doubled in a LBO crystal to produce pulses centered at 520 nm and energy of 9 nJ (12 W average power). Additional thermal management is needed to reach higher powers. Laser shaping of the pulses has been described in detail elsewhere in these proceedings [13].

Photocathode Materials

A perfect photocathode for an accelerator electron source would have high efficiency at a convenient laser wavelength, fast response time, long lifetime and a low thermal emittance. Unfortunately, no such cathode exists today, although the search continues. A number of different photocathodes meet some of these criteria, so tradeoffs have to be made depending on the requirements of the particular system. For an ERL, obtaining 100 mA average current means high quantum efficiency (QE) photocathodes are a necessity.

Semiconductor photocathodes are currently the best choice for high QE and low emittance. Examples are GaAs, Cs_2Te, GaN, and K_2CsSb. Both Cs_2Te and GaN show promise but require UV light but there are no laser systems available to produce enough average power in the UV. Both GaAs and K_2CsSb have 5-10% QE for ~520 nm light, where high average power lasers are readily available. At Cornell, we have chosen to use GaAs, but are still considering other cathodes depending on the application.

As mentioned earlier, it is possible to recover the intrinsic thermal emittance from the cathode using a carefully designed emittance compensation scheme for the bunch charges of interest to an ERL [2]. Of all the cathodes available, GaAs has the lowest thermal emittance [7], so is the cathode of choice for an ERL. Unfortunately, the QE is near a minimum when the thermal emittance is smallest (close to the band gap), thus unsuitable for high average current. In addition, it is well known that at ~780 nm a fast laser pulse will generate an electron beam with a 20-40 ps tail, which is not acceptable for low emittance operation. For shorter wavelengths (~520nm) recent measurements [10] show that the response time is quite fast (~1 ps) as long as the QE is not too high (< 10%). This points out some of the tradeoffs one has to make even when using GaAs, and we have chosen an operating wavelength of 520 nm as the best compromise between QE, thermal emittance and response time.

The last important parameter is cathode lifetime. The cathodes described above are all sensitive to chemical poisoning to some extent, and require ultra-high vacuum. GaAs is the most sensitive, unfortunately, requiring vacuum levels < 10^{-11} Torr for successful operation. An additional lifetime limiter is ion back-bombardment which further reduces QE. The electron beam can ionize residual gas molecules anywhere along their path, which can then be accelerated back towards the cathode surface. Jefferson Lab [14] has carried out extensive measurements at 10 mA average current, and has measured cathode lifetimes as high as 10^6 C/cm^2 (the amount of charge extracted per cm^2 when the QE has fallen by 1/e). One can use this data to estimate that a 10 W maximum power laser system should be able to provide 100 mA over 100 hours with a 1.8 mm diameter laser spot [15]. Such performance has not been demonstrated yet, and it is certainly an optimistic estimate.

Vacuum System

In order to meet the extreme vacuum levels required for sufficient cathode lifetime both reductions in outgassing and massive pumping have been implemented. The stainless steel vacuum vessel and all stainless internal components including the electrodes have been air-fired for 100 hours at 400°C to reduce their hydrogen outgassing rate, the primary residual gas constituent [16]. A typical 160°C vacuum bake follows assembly of the gun. The pumping scheme consists of a 400 l/sec Perkin-Elmer ion pump and 20 NEG modules lining the walls of the gun vessel. The NEG modules are of the WP1650-ST 707 type supplied by SAES Getters and provide approximately 15,000 l/sec of pumping for hydrogen. Typical static pressure in the gun is below 6×10^{-12} mbar.

Small vacuum leaks have opened at the Conflat flange joints between the insulator and the gun vessel during processing, perhaps caused by heating of the gasket by field emission. New triple point protection rings that cover the vacuum joint were installed and no further leaks have occurred.

Cathode Preparation System

A modular cathode preparation system is attached to rear of the gun vessel to load, clean, prepare, and store the semiconductor cathodes. Vacuum isolation between each chamber (load lock, hydrogen cleaning and heating, cathode surface preparation) allows for multiple cathodes to be accommodated at once. For example a backup cathode could be heat cleaned at the same time the primary cathode is being cesiated. Its design allows for flexibility in the cathode material and is extensible for future cathode material development. 1m long orthogonal manipulator arms transfer the cathode pucks between processing chambers and also move the prepared cathode into the electrode structure.

COMMISSIONING RESULTS AND PLANS

Processing of the electrode structure at a rate of 1kV/Hr. has been successful only to 450KV where punch through occurred (as described earlier). The gun typically

operates at 250 kV and we are not pushing the voltage higher until a backup insulator is acquired. Now in operation for two years, the gun routinely provides pulsed beams of varying bunch charge for diagnostic measurements. Average current as high as 20mA at 250kV has been achieved for short periods. The near term plans include extensive sets of phase space measurements along with the push for higher currents.

ACKNOWLEDGEMENTS

This work was supported by NSF grant PHY 0131508.

REFERENCES

1. S. M. Gruner and M. Tigner, Eds., "Study for a proposed Phase I Energy Recovery Linac (ERL) synchrotron light source at Cornell University", CHESS Technical Memo 02-003, Jefferson Laboratory Report No. JLABACT-01-04 (2001).
2. I.V. Bazarov, *et al.*, "Multivariate optimization of a High Brightness DC Gun Photoinjector", PRST AB, **8**, 034202 (2005).
3. S. Belomestnykh, *et al*., "Commissioning of the Cornell ERL Injector RF Systems", 2008 European Particle Acc. Conf., Genoa, Italy, 832-834 (2008).
4. B. Dunham, *et al*., "First Tests of the Cornell University ERL Injector", Linac 08 Proceedings, In Press (2008).
5. C. Hernandez-Garcia, *et al.*, "A High Average Current DC GaAs Photocathode Gun for ERLs and FELs", 2005 Particle Acc. Conf., Knoxville, TN, 3117-3119 (2005).
6. D. Dowell, *et al.*, Nucl. Instr. Meth. A **356**, 167 (1995).
7. A. Arnold, *et al.*, "Development of a Superconducting RF Photoinjector", Nucl. Instr. Meth., A **577**, 440 (2007).
8. I. Bazarov *et al*., "Thermal emittance and response time measurements of negative electron affinity photocathodes", J. Appl. Phys., **103** (2008) 054901.
9. I. Bazarov *et al.*, "Efficient temporal shaping of electron distributions for high brightness photoemission guns", PRST AB 11 (2008) 040702.
10. R.J. Smith, Daresbury Lab, personal communication.
11. J. Haimson, IEEE Trans. Nucl. Sci. **NS 22**, 1354 (1975.
12. D. Ouzounov, *et al.*, "The Laser System for the ERL Electron Source at Cornell", 2007 Particle Acc. Conf., Albuquerque, NM, 530-532 (2007).
13. D. Ouzounov, *et al.*, These Proceedings.

Status of the ALICE Energy Recovery Linac

L.B. Jones, S.P. Jamison, Y.M. Saveliev, K.J. Middleman and S.L. Smith

ASTeC – Accelerator Science and Technology Centre, Science and Technology Facilities Council, Daresbury Laboratory, Warrington WA4 4AD, United Kingdom

Abstract. The ERLP energy recovery linac prototype at Daresbury Laboratory has been re-branded, and is now called *ALICE* (**A**ccelerators and **L**asers **I**n **C**ombined **E**xperiments). This paper gives an overview of the project and its status, outlines some of the challenges experienced during the commissioning of the photoinjector and superconducting accelerating systems, and presents our photoinjector gun commissioning results. An outline is given of the planned photon science program for ALICE, and its under-pinning role in the EMMA NS–FFAG[1] project.

Keywords: superconducting, linac, photoinjector, GaAs, electron, FEL, CBS, THz
PACS: 29.20.Ej, 29.25.Bx, 29.27.Eg, 29.27.Fh, 41.75.Ht, 42.72.-g

INTRODUCTION

The ALICE ERL prototype was conceived as a test–bed for the key concepts and technologies expected to feature in the 4th Generation Light Source (4GLS). Despite the cancellation of 4GLS, it now has a broader role as an accelerator physics and technology test facility, and for developing fourth generation light source science. The facility is undergoing commissioning at present, and the past year has been a frustrating combination of progress and setbacks. A short productive period of gun commissioning has been book–ended with several gun vacuum problems. However in parallel to the beam commissioning work, progress has been made with the cryogenic and RF systems.

ALICE ACCELERATOR SYSTEMS OVERVIEW

The photoinjector is a DC photocathode gun operating at 350 kV, based on the Jefferson Laboratory IR-FEL gun [1]. It combines a caesiated gallium arsenide (Cs:GaAs) reflection–mode cathode (activated in–situ) with a laser system specified to deliver 80 pC per electron bunch. The gun uses a one–piece bulk–doped ceramic insulator, which has demonstrated extremely good high voltage performance during conditioning to 450 kV.

The drive laser is a *High Q* IC10000 Picotrain model, delivering $>$10 W at 1064 nm wavelength. The lasing medium is diode–pumped neodymium yttrium vanadate (Nd:YVO_4), mode–locked to generate 7 ps FWHM pulses at a repetition rate of 81.25 MHz, this being the 16th sub–harmonic of the 1.3 GHz RF frequency. The drive laser optical system [2] defines and delivers *macrobunches* to the cathode at a repetition rate up to 20 Hz, the length of which can vary from a single laser pulse up to a 100 μs

[1] Electron Model of Many Applications non–scaling Fixed–Field Alternating Gradient accelerator

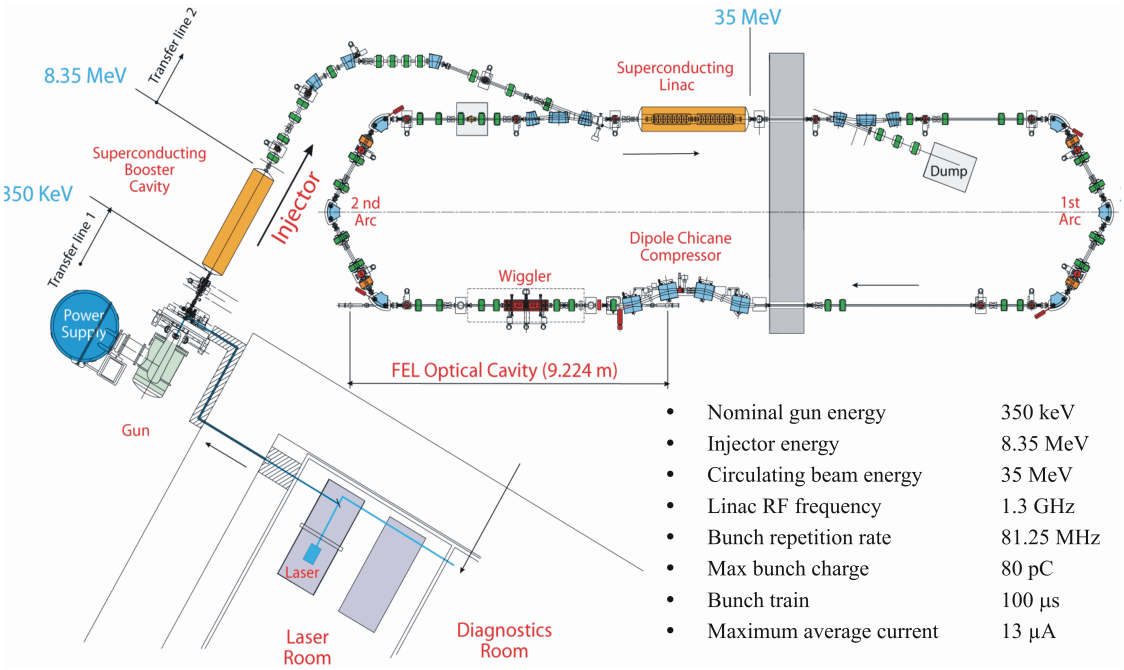

FIGURE 1. Schematic showing the layout of the ALICE machine and its main parameters.

pulse train. This constitutes a maximum duty cycle of 0.2% and represents a maximum average electron beam current of 13 μA.

Cryogenic system and accelerating modules

The cryogenic system [3] was installed during 2006 as a collaborative effort between Daresbury Laboratory, Linde, ACCEL and DeMaco, with both accelerating modules delivered in the first half of that year. Both modules were cooled to 2 K in December of 2006, and were tested with a simulated dynamic heat load of 112 W. Pressure stability of ± 0.03 mbar at 2 K and ± 0.10 mbar at 1.8 K has also been demonstrated, and the cryogenic system is now performing beyond its design specification.

ALICE uses two Stanford/Rossendorf cryomodules assembled by ACCEL, each containing 2×9-cell TESLA cavities with a total cryogenic load of ~ 180 W at 2 K. One module is configured as the *booster* and the other as the *main linac*, both using a JLab HOM coupler. The booster has up to 52 kW of RF power to provide a 4 MV/m gradient to accelerate the beam by 8 MeV. Due to energy recovery, the linac has only 16 kW of RF power to provide a 13.5 MV/m gradient accelerating the beam to 35 MeV.

Extreme levels of field emission were observed during RF commissioning at Daresbury, cavity performance being significantly worse than during vertical tests at DESY, as shown in table 1. This necessitated the re–location of sensitive equipment close to the booster linac, and installation of a lead shield around the main linac, with a long–term plan of aggressive cavity conditioning fitted around the beam commissioning program.

TABLE 1. Booster & main linac gradient test results.

	Booster		Linac	
	Cavity 1	Cavity 2	Cavity 1	Cavity 2
	Vertical tests at DESY, July – December 2005			
E_{acc} (MV/m)	18.9	20.8	17.1	20.4
Q_o	5×10^9	5×10^9	5×10^9	5×10^9
	Acceptance tests at Daresbury, May – September 2007			
Max E_{acc} (MV/m)	10.8	13.5	16.4	12.8
Measured Q_o	3.5×10^9 @ 8.2 MV/m	1.3×10^9 @ 11 MV/m	1.9×10^9 @ 14.8 MV/m	7.0×10^9 @ 9.8 MV/m
Limitation	FE Quench	FE Quench	RF Power	FE Quench

COMMISSIONING STATUS

The gun delivered first beam at 01:08 on Wednesday 16th August 2006, has been operated since then for several commissioning periods into a dedicated diagnostics beamline [4]. Problems were experienced with poor quantum efficiency (*Q.E.*) and cathode lifetime, but steady improvements have been achieved through better cathode handling and activation procedures, and improved vacuum. Additionally, beam halo, field emission and high voltage breakdown have been encountered during gun commissioning to–date, giving the ALICE team useful experience in dealing with these challenges. We have also suffered repeated failure of the one–piece ceramic at its flange welds, and are now using a smaller spare loaned to us by Stanford which limits our operating voltage to ~ 250 kV.

Commissioning goals achieved so far include: beam energy of 350 keV; bunch charge of > 80 pC; *Q.E.* of 3.7% with a $\frac{1}{e}$ lifetime of $\sim$100 hours; macrobunch length from a single 7 ps pulse to 100 μs train and train repetition rate up to 20 Hz.

ALICE EXPLOITATION AND UPGRADE PROGRAM

ALICE will drive a mid–IR FEL using a wiggler device loaned from Jefferson Laboratory. The gap will be tuneable (12 – 20 mm), which combined with a variable electron beam energy (24 – 35 MeV), will yield radiation tuneable over a range of $\lambda = 4 - 12\,\mu$m. Additionally, a multi–10 TW laser system will provide beams to generate X–rays through Compton backscattering (CBS), and for a longitudinal electro–optic (EO) electron bunch length diagnostic [5] which will be critical to optimise FEL performance. The CBS source will use head–on and side–on geometries in collisions with the electron beam, yielding $h\nu$ to 30 keV [6]. The bunch compressor will be an *intense* pulsed THz source, and will be used to study exposure in live biological cells [7].

In addition to the light derived directly from ALICE (mid–IR FEL, CBS X–rays & THz), an exciting research programme will also use *combinations* of these with a free–standing tunable femtosecond laser and the multi–10 TW laser, mainly for pump–probe experiments that will use a combination of light sources. ALICE exploitation capabilities will be extended into bioscience after completion of a tissue culture laboratory.

The photoinjector will be up–graded by adding a load–lock chamber and re–designed

cathode ball, permitting external activation of photocathodes, so improving its HV performance and reducing cathode–change downtime from several weeks to hours [8]. There are also plans to re–install a gun diagnostic beamline as a permanent feature. The ultimate upgrade comes in the form of EMMA: a prototype non–scaling FFAG electron accelerator which will use ALICE as its injector. It is hoped that NS–FFAG technology will provide a cost–effective means to build hadron therapy centres in the UK [9].

PHOTOINJECTOR GUN COMMISSIONING RESULTS

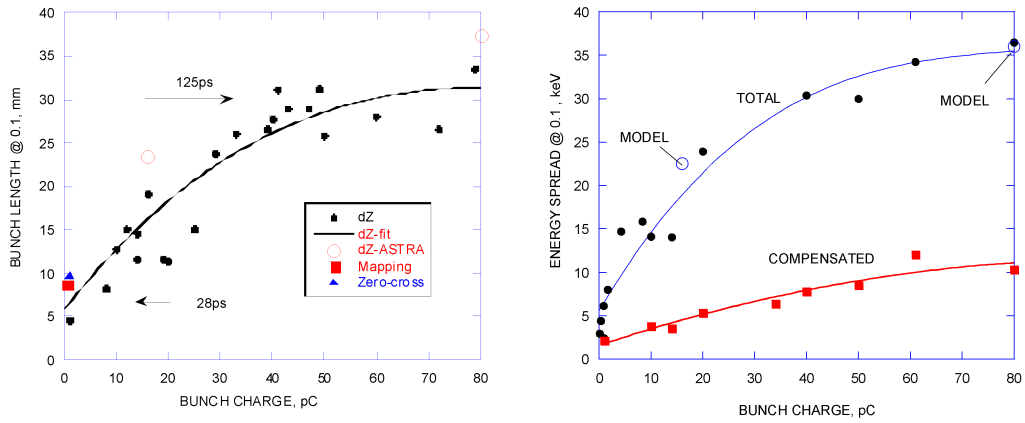

FIGURE 2. **(Left)** Bunch length at 10% of peak **(Right)** Total and tilt–compensated energy spread

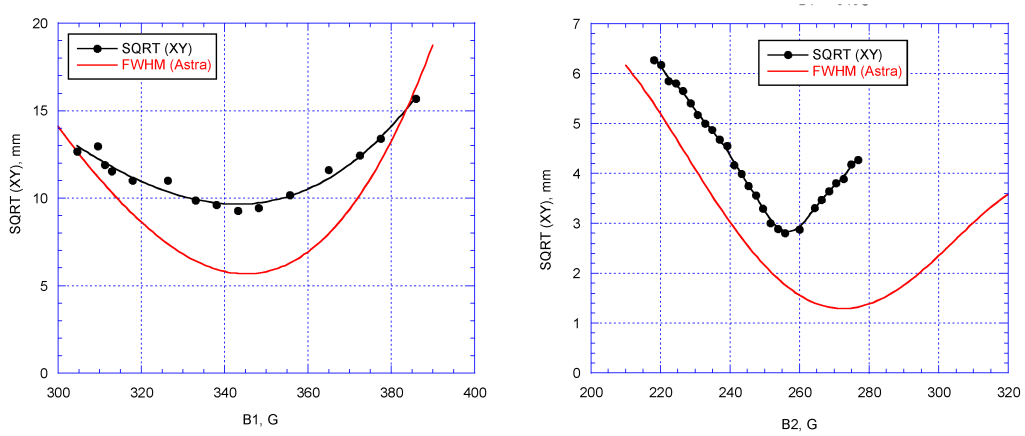

FIGURE 3. **(Left)** Beam size at the 1st solenoid **(Right)** Beam size at the 2nd solenoid

Having overcome the problems described earlier, an improved cathode activation process produced a QE of 3.5%, and a bunch charge of $> 100\,\mathrm{pC}$ was achieved. This allowed injector performance to be measured at high bunch charge, and several highly–productive weeks of measurements were made to characterise the gun until field emission from the cathode again became a problem [10]. This had been managed to that point by setting the solenoid parameters to sub–optimum values. In summary:

- The gun has been repeatedly HV conditioned to 450 kV;

- The beam was fully–characterised operating at 350 keV (emittance, bunch length and energy spectra) in a wide range of bunch charges from 1 to 80 pC [10];
- Despite sub–optimal experimental conditions (e.g., field emission and non–uniform cathode *QE*), good agreement between ASTRA simulations and experimental data was found for the bunch length and energy spread (figure 2) and beam size (figure 3);
- Figure 4 compares some of the bunch characteristics measured using 7 ps and 28 ps drive laser pulses, at a bunch charge of 16 pC. This indicated little difference in bunch quality, though appreciable improvement in emittance is expected with longer laser pulses at higher bunch charges, in the ideal case of a near flat–top laser pulse [11];
- A complete review of the commissioning results is contained in references [10, 11].

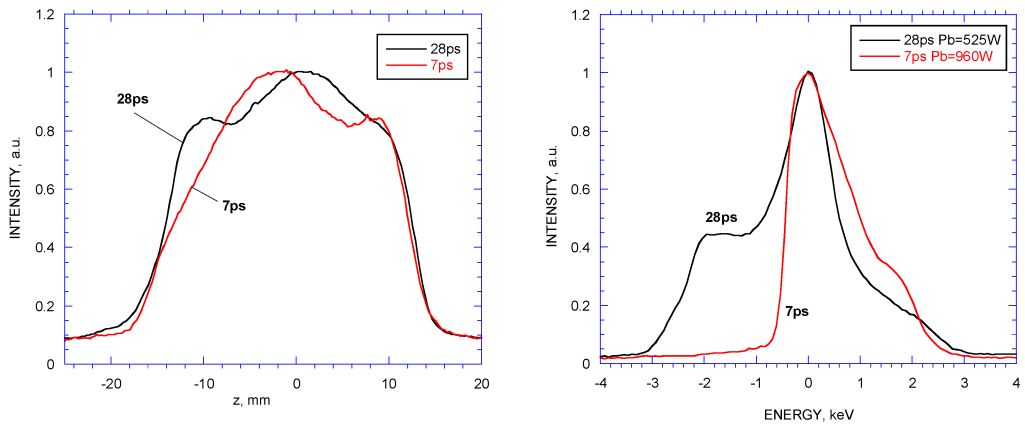

FIGURE 4. **(Left)** Bunch length with 7 and 28 ps laser pulses **(Right)** Compensated energy spread

REFERENCES

1. T. Siggins, C.K. Sinclair, C. Bohn, D. Bullard, D. Douglas, A. Grippo, J. Gubeli, G.A. Krafft & B. Yunn, *Performance of a DC GaAs photocathode gun for the Jefferson lab FEL*, Nuclear Instruments & Methods A; 475 (2001), pages 549–553.
2. L.B. Jones, *Status of the ERLP Drive Laser*, ERL '07 Proceedings, pages 212–213.
3. A.R. Goulden *et. al*, *Installation and Commissioning of the Superconducting RF Linac Cryomodules for the ERLP*, Advances in Cryogenic Engineering, 53B (2007), page 1573.
4. D.J. Holder *et. al*, *ERLP Gun Commissioning Beamline Design*, Proc. LINAC '04, page 93.
5. P.J. Phillips, W.A. Gillespie, S.P. Jamison, A.M. MacLeod, *Electro–optic diagnostics on the daresbury energy recovery linac*, TUPCH041, Proc. EPAC '06
6. G. Priebe, D. Laundy, M.A. MacDonald, G.P. Diakun, S.P. Jamison, L.B. Jones, D.J. Holder, S.L. Smith, P.J. Phillips, B.D. Fell, B. Sheehy, N. Naumova, I.V. Sokolov, S. Ter-Avetisyan, K. Spohr, G.A. Krafft, J.B. Rosenzweig, U. Schramm, F. Gruner, G.J. Hirst, J. Collier, S. Chattopadhyay & E.A. Seddon, *Inverse Compton backscattering source driven by the multi-10 TW laser installed at Daresbury*, Laser and Particle Beams 26 (4), doi:10.1017/S0263034608000700 (2008)
7. M.A. Bowler, M. Surman, F.M. Quinn, S.P. Higgins & A.D. Smith, *Radiation sources on the ERL Prototype at Daresbury Laboratory*, 9th Conf. on SR Inst., AIP Conf. Proc. 879 (2007), page 627.
8. K.J. Middleman, *Load–lock upgrade for the ALICE photoinjector*, these proceedings.
9. R. Edgecock *et. al*, *EMMA – The World's First Non–Scaling FFAG*, Proc. EPAC'08.
10. Y.M. Saveliev, D.J. Holder, B.D. Muratori & S.L. Smith, *Results from ALICE (ERLP) DC photoinjector gun commissioning*, MOPC062, Proc. EPAC '08.
11. Y.M. Saveliev, S.P. Jamison, L.B. Jones & B.D. Muratori, *Characterisation of electron bunches from ALICE DC photoinjector gun at two different laser pulse lengths*, MOPC063, Proc. EPAC '08.

Photocathode Preparation System for the ALICE Photoinjector

Keith J Middleman[a], I. Burrows[a], R. Cash[a], B. Fell[a], L.B. Jones[a], J. McKenzie[a], B. Militsyn[a] and A.S. Terekhov[b]

[a]*STFC Daresbury Laboratory, Keckwick Lane, Warrington, Cheshire, UK, WA4 4AD.*
[b]*Institute of Semiconductor Physics, Novosibirsk, 630090, Russian Federation*

Abstract. ALICE - Accelerators and Lasers in Combined Experiments - is a relatively new accelerator built at Daresbury Laboratory that will demonstrate the process of energy recovery by the end of 2008. The project is a research facility to develop the technology required to build a New Light Source (NLS) in the UK. This paper details the current ALICE photoinjector design and highlights the limitations before focusing on a photoinjector upgrade. The key component of the upgrade is a three-stage extreme high vacuum load-lock system that will be incorporated into the ALICE photoinjector in 2010. The load-lock system has *de facto* become a standard component of a type III-V semiconductor photocathode injector and comprises: 1) loading chamber to allow new photocathodes to be introduced, 2) cleaning chamber for atomic hydrogen cleaning of the photocathodes and, 3) a preparation and activation chamber where the photocathodes will be activated to the NEA state ready for use on the ALICE accelerator. Once commissioned the load-lock system will allow rapid transfer of photocathodes between the load-lock system and the ALICE photoinjector whilst maintaining the integrity of the vacuum system and providing many other benefits. The new load-lock system will not only remove the problems with the existing set-up, it will also permit a new vacuum chamber to be designed for the gun itself. This new design will also aim to improve vacuum performance by addressing some of the major vacuum associated problems ALICE has encountered in the past 2 years.

Keywords: photoinjector, load-lock, ALICE, photocathode, vacuum, GaAs, lifetime.
PACS: 29.20.Ej; 29.25.Bx; 81.05.Ea; 85.60.Ha.

INTRODUCTION

The current ALICE photoinjector is based on the Jefferson Laboratory IR-FEL injector design [1] which is a 350 kV DC injector with a single vacuum chamber design as shown in figure 1. The semiconductor GaAs is used as the electron source, although it requires activating to the negative electron affinity (NEA) state to maximise the electron emission (quantum efficiency: QE). The activation of the GaAs photocathode is done by depositing alternate layers of Cs/O_2 or NF_3 all of which has to be done inside the photoinjector. For successful operation the integrity of the vacuum system is critical to cathode performance [2], the vacuum requirements for the ALICE photoinjector were to achieve 5×10^{-11} mbar whilst ensuring the residual gas species are not detrimental to the GaAs photocathode.

The single-chamber design has a number of limitations some of which have been problematic during ALICE operations. The main limitation is the fact it is a single vacuum chamber design so only has the ability to accommodate one GaAs

photocathode. This limitation means that whenever a new GaAs photocathode is required the photoinjector must be vented to atmospheric pressure with dry nitrogen. Given that the vacuum integrity is critical then a minimum period of one month is required to condition the vacuum system back to its original state prior to venting. This conditioning requires an extensive bakeout to 250ºC and this itself can create further vacuum problems. The activation of the GaAs photocathode also impacts on vacuum performance and high voltage, operating Cs dispensers at high temperature whilst injecting O_2 or NF_3 through a fine leak valve meaning the vacuum recovery time can be a number of hours.

Given these basic design problems it was decided that a new multi-chamber design was required that would allow the introduction of photocathodes without compromising the ALICE photoinjector vacuum system. This new design would also allow the activation of the photocathode to be performed external to the ALICE photoinjector.

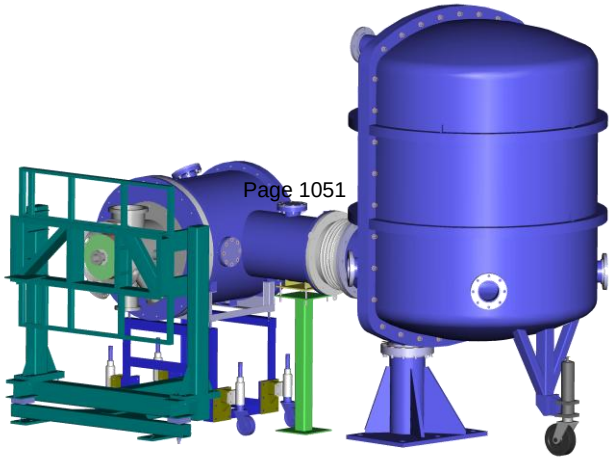

FIGURE 1. Current ALICE Photoinjector Based On JLab IR-FEL Design

New Multi Chamber Load-Lock Design

Figure 2(a) shows the new load-lock design with 2(b) showing a plan view of how it will be incorporated on to the ALICE photoinjector. It is a 3-stage load-lock design with each chamber having a purpose-designed function. There is a loading chamber where photocathodes will be introduced to the system, a hydrogen-cleaning chamber to remove contaminants from the photocathode surface and a preparation chamber where photocathodes will be activated to the NEA state before being transferred into the ALICE photoinjector. The system is primarily pumped using Sputter Ion Pumps (SIP) and Non Evaporable Getter (NEG) strips, and the vacuum specification was to achieve a minimum of $5e^{-12}$ mbar in the preparation chamber. To help achieve this, the system was vacuum fired at a temperature of 950ºC for 5 hours to deplete the 316LN Stainless Steel of hydrogen.

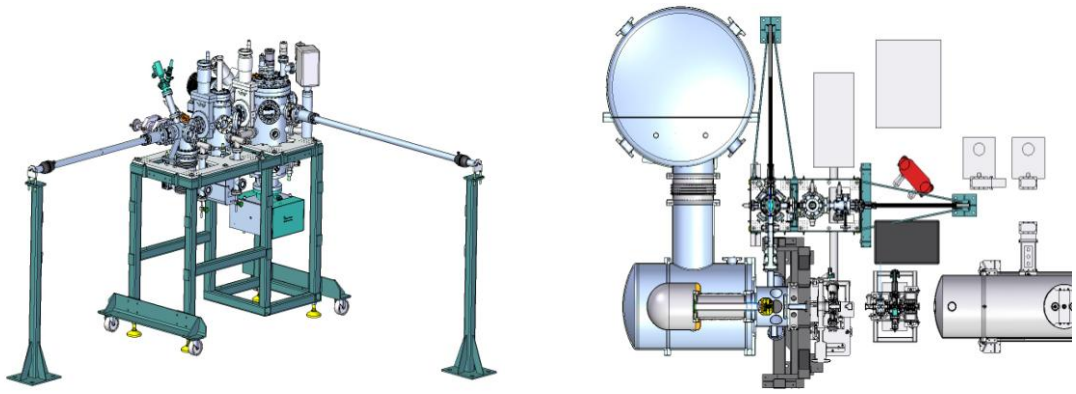

FIGURE 2. (a) New load-lock system, (b) plan view of ALICE photoinjector with new system

Loading Chamber Overview

Figure 3(a) shows a section through of the loading chamber, whilst 3(b) shows the z-translation stage with a magazine holder that can accommodate up to four photocathodes at any one time. To load new photocathodes the z-stage is removed from the loading chamber and transported under dry nitrogen to a nitrogen-purged glove box. The newly prepared photocathodes are inserted into the magazine holder, and the z-stage is closed such that the 'O' ring seals (Fig. 3(b)). The photocathodes are thus stored in a leak tight nitrogen environment. The z-stage is then re-inserted in to the loading chamber, the 'O' ring seal opened and the chamber evacuated to ensure the photocathodes are not exposed to any contaminants from the atmosphere.

(a) (b)

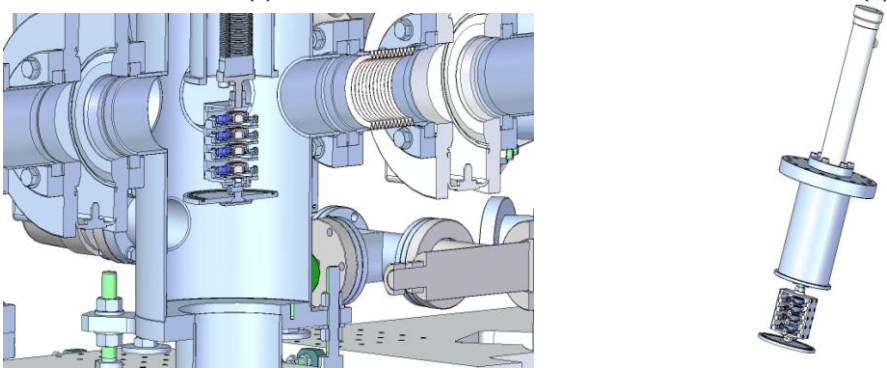

FIGURE 3. (a) Section-through of loading chamber, (b) Z-translation stage with magazine holder

Hydrogen Chamber Overview

Figure 4(a) shows the hydrogen cleaning chamber, whilst 4(b) shows a section through the chamber. Here the cathode is heated to an appropriate temperature ready for hydrogen cleaning (~300ºC). This heating process is done via the use of a 250W halogen bulb, shielded by tantalum to avoid any radiative heating of other components

whilst focusing the heat onto the photocathode, thus minimising the power requirements. The hydrogen cleaning process makes use of a thermal gas cracker that uses electron bombardment of a tungsten capillary to thermally dissociate the gas passing through it. Given the right conditions the thermal cracking efficiency of hydrogen is very high and this is important in order to minimise the number of H^+/H^- ions in the cleaning process. Once hydrogen cleaned the photocathode is then transferred through to the preparation chamber ready for activation.

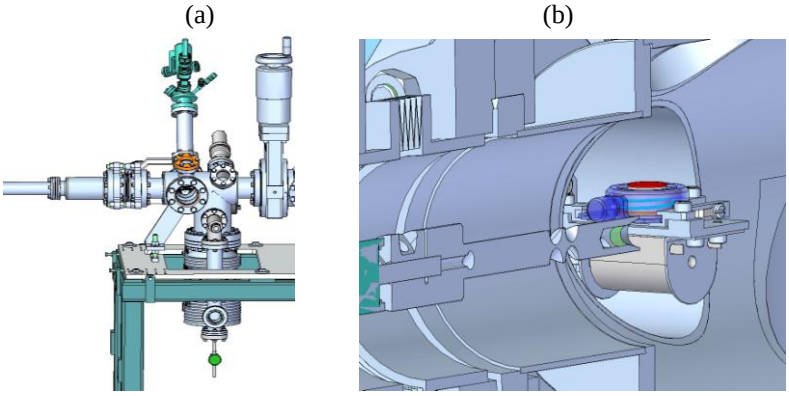

FIGURE 4. (a) Hydrogen cleaning chamber, (b) section-through hydrogen chamber

Preparation Chamber Overview

Figures 5 (a) and (b) show the preparation chamber, (a) showing the complete preparation chamber, with (b) showing a section through of the preparation chamber.

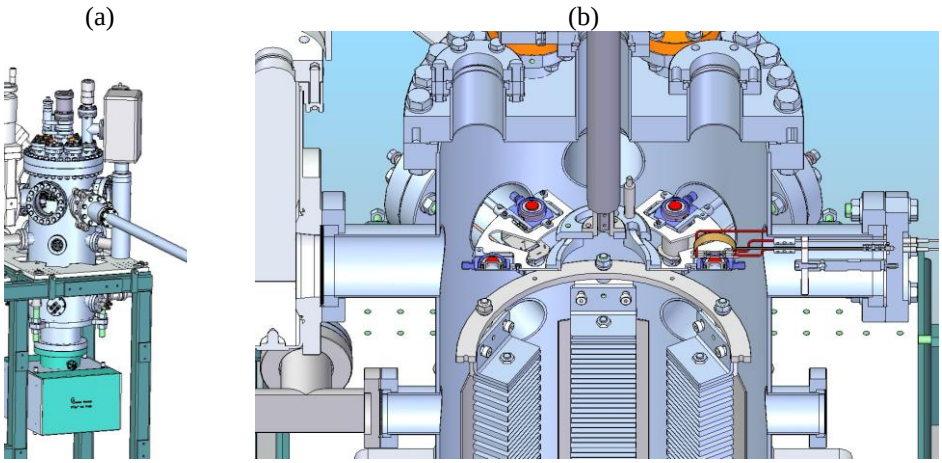

FIGURE 5. (a) Preparation chamber, (b) section-through view of preparation chamber

Once a photocathode has been loaded into the system and hydrogen cleaned, it is ready for a full activation in the preparation chamber using the standard 'yo-yo' method. As shown in Fig.5 the preparation chamber has a carousel with the capability to hold six photocathodes. There are two possible heating positions again using

halogen bulb heaters, they are in the 10 and 2 o'clock positions in Fig.5. After heating to ~560-580ºC for upto 3 hours [3] and cooling to room temperature the carousel is rotated such that the photocathode to be activated is in the 3 o'clock position in Fig.5. The Cs dispensers are positioned within 10mm of the photocathode surface, as is the charge collector used to measure the photocurrent. The O_2/NF_3 is injected into the system via a piezo-electric fine leak valve which is positioned on the 2.75 inch conflat flange that sits directly above the 3 o'clock position in Fig.5. Once activated to the NEA state the photocathode is ready for transport in to the ALICE photoinjector and is ready for use.

Insertion Of Photocathode Into ALICE Photoinjector

The activated photocathode will be transferred into the ALICE photoinjector via a side loading mechanism into the cathode ball. Figure 6(a) shows the slot in the cathode ball were the photocathode will be inserted [4] whilst Fig.6(b) shows the mechanism inside the cathode ball from the opposite side to Fig.6(a). A separate transfer arm will locate onto the small joystick shown in Fig.6(b) and through rotation of the joystick in a clockwise/anti-clockwise direction the photocathode can be moved forward or backward until it is located in its correct position. Once in position the activated photocathode is ready for use as an electron source.

(a) (b)

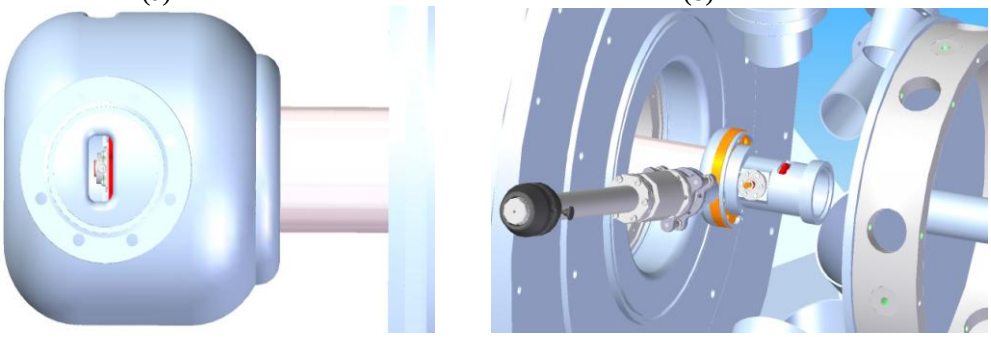

FIGURE 6. (a) Slot in cathode ball for insertion of photocathode, (b) internal mechanism for movement of photocathode

REFERENCES

1. T. Siggins, C.K. Sinclair, C. Bohn, D. Bullard, D. Douglas, A. Grippo, J. Gubeli, G.A. Krafft & B. Yunn, Performance of a DC GaAs photocathode gun for the Jefferson lab FEL, Nuclear Instruments & Methods A; 475 (2001), pages 549–553.
2. T. Reichelt *et al*, Applied Surface Science. 143 (1999) P319–322
3. N. Chanlek, Study of Activated GaAs Surface for Application as an Electron Source in Particle Accelerators, these proceedings.
4. J. McKenzie, 3D Modeling of the ALICE Photoinjector Upgrade, these proceedings.

Development of an electron gun for an ERL based light source in Japan

N. Nishimori*, R. Nagai*, H. Iijima*, Y. Honda†, T. Muto†, M. Kuriki**, M. Yamamoto‡, S. Okumi‡, T. Nakanishi‡ and R. Hajima*

*Japan Atomic Energy Agency (JAEA), Tokai, Naka, Ibaraki 319-1195, Japan
†High Energy Accelerator Research Organization (KEK), Oho, Tsukuba, Ibaraki 305-0801, Japan
**Hiroshima University, Kagamiyama, Higashihiroshima, Hiroshima 739-8530, Japan
‡Graduate School of Science, Nagoya University, Nagoya 464-8602, Japan

Abstract. We have developed a prototype DC photoemission electron gun for a future energy recovery linac (ERL) based light source in Japan. The prototype gun is operated at up to 250 kV and is designed to deliver up to 50 mA beam current. A diagnostic beam line for emittance and bunch length measurements has been constructed. We have also designed a new 500 kV DC gun which is capable of producing up to 10 mA electron current with emittance lower than 1 mm-mrad. The high voltage terminal will be isolated by ten ceramics stacked in series. The new gun will satisfy performance required as an injector for the compact ERL, which will be constructed at KEK site as a prototype of the future ERL light source.

Keywords: ERL, High brightness electron beam, Photoinjector
PACS: 29.25.Bx, 41.75.Hz, 07.30.Kf, 79.60.-i

INTRODUCTION

An electron gun capable of producing a high brightness electron beam with emittance lower than 1 mm-mrad and current up to 100 mA needs to be developed for next generation Energy Recovery Linac (ERL) light sources (LS). A DC gun equipped with a GaAs photocathode is considered to be the most promising candidate, since high current operation has been successfully demonstrated at Jefferson Laboratory. The DC gun for the JLab 10 kW IR Upgrade FEL provides a high current electron beam of 9.1 mA CW with normalized emittance lower than 8 mm-mrad [1]. The JLab 100 kV load locked electron gun delivers 10 mA CW electron beam with lifetime exceeding 2000 C [2].

A Japanese ERL light source project has been jointly launched by High Energy Accelerator Research Organization (KEK), Japan Atomic Energy Agency (JAEA), the Institute for Solid State Physics of the University of Tokyo and other laboratories [3, 4]. We are planning to construct together the Compact ERL as an ERL test facility at KEK site [5]. The tentative parameters for the Compact ERL are the beam current 100 mA, the injection energy 5 MeV, normalized emittance 1 mm-mrad, beam energy at main linac 60 MeV, and the bunch length 100 fs. We started to develop a photocathode DC gun for the ERL LS [6].

Hajima et al. have proposed to use this gun technology to develop a nondestructive assay system of nuclear waste [7]. The ERL technology will be employed to produce a high-flux Compton gamma ray and identify the nuclide in the nuclear waste using nuclear resonance fluorescence based detection system. Many other different applications

will be inspired by the gun development for ERLs.

In the present paper, we describe our current status of development of two photocathode DC guns. One is a 250 kV prototype gun, which will be used for demonstration purposes such as high current operation up to 50 mA, emittance and bunch length measurements. We have generated 1 μA beam from the prototype gun and constructed a diagnostic beam line downstream of the gun. The other is a 500 kV gun, which will be used as the gun for the Compact ERL. We have designed a 500 kV Cockcroft Walton power supply for generation of 10 mA beam, a segmented insulator tube where ten ceramics are stacked in series, and SF6 tank where the power supply and the insulator are placed.

DEVELOPMENT OF 250 KV PROTORYPE GUN

We have developed a 250 kV 50 mA DC gun equipped with an NEA photocahode shown in Fig. 1 [6]. A Cockcroft Walton power supply is used to apply high voltage to an insulator tube. A photocathode sample is introduced into a loading chamber and heat cleaned by an IR heater. The cathode sample is then transferred into the preparation chamber where cesium and oxygen are applied on the cathode. The activated cathode is finally transferred to the main chamber and the photoemitted electron beam is produced upon laser illumination.

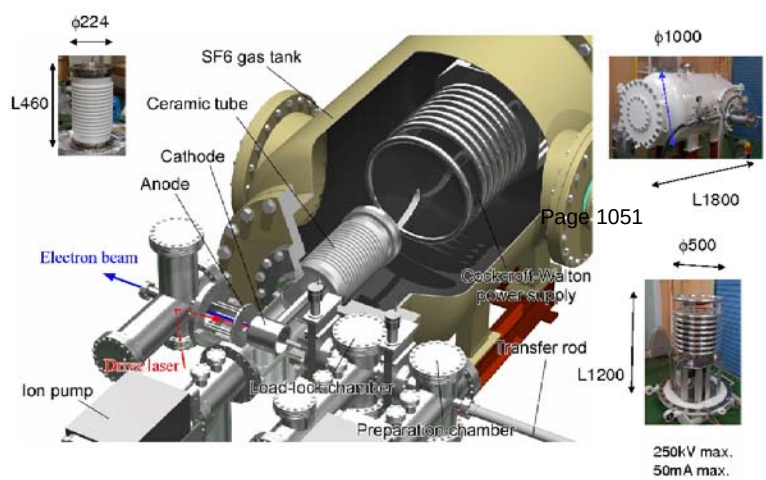

FIGURE 1. JAEA photocathode electron gun.

All the gun chambers are made of titanium which has outgassing rate significantly lower than stainless steel [8]. The flanges are made of a titanium alloy (KS100, Kobe Steel, Ltd.) with hardness of 230 Hv, which is higher than stainless steel (SUS304) of 190 Hv. A 300 l/s turbo pump and a 1700 l/s cryo pump are installed in the loading chamber for rough evacuation, a 500 l/s ion pump and a 2000 l/s NEG pump are used in the preparation chamber, and two pairs of an ion pump and a 2000 l/s NEG pump have been installed upstream and downstream the cathode holder (see Fig. 2). The vacuum pressures at the loading, preparation, and high voltage chambers are 7 $\times 10^{-9}$

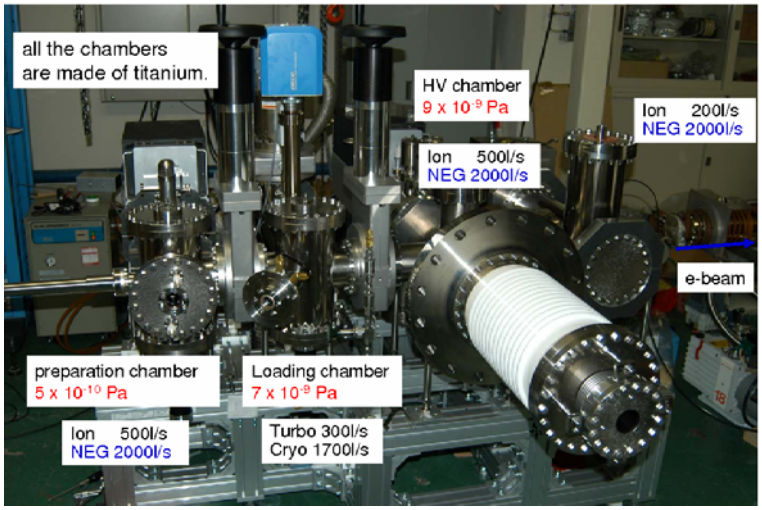

FIGURE 2. Preparation, loading, and HV chambers from left to right.

Pa, 5 $\times 10^{-10}$ Pa, and 9 $\times 10^{-9}$ Pa, respectively. A hot cathode type ionization vacuum gauge (AxTRAN [9]) whose measuring range is from 1 $\times 10^{-1}$ to 5 $\times 10^{-11}$ Pa has been installed at each chamber.

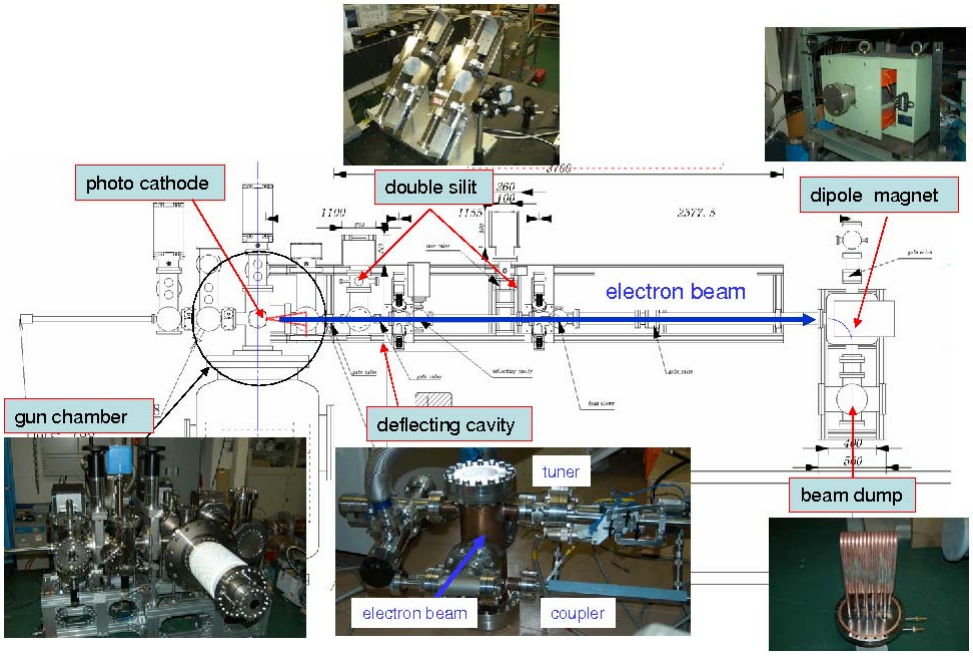

FIGURE 3. A diagnostic beam line for JAEA photocathode electron gun.

The typical quantum efficiency (QE) of GaAs cathode right after Cs activation is 4 % with a laser diode at wavelength of 670 nm. We have generated 1 μA beam at 150 kV using HeNe laser of 2.4 mW. This corresponds to QE of 0.08 %. The small value of QE may be attributed to short life time of the cathode and poor alignment of the cathode center along the downstream beam axis.

We have constructed a diagnostic beam line downstream of the gun chamber consisting of a double silt system for emittance measurement, a deflecting cavity for bunch length measurement, a dipole magnet to deflect the beam to a water cooled beam dump for beam current measurement. The diagnostic beam line is shown in Fig. 3. A 83.3 MHz Ti:sapphire laser with 500 mW average power has been installed for further experiments. The laser pulse length will be varied 5-20 ps (FWHM) by temporal shaping technique with birefringent crystals [10].

DESIGN STUDY OF 500 KV GUN

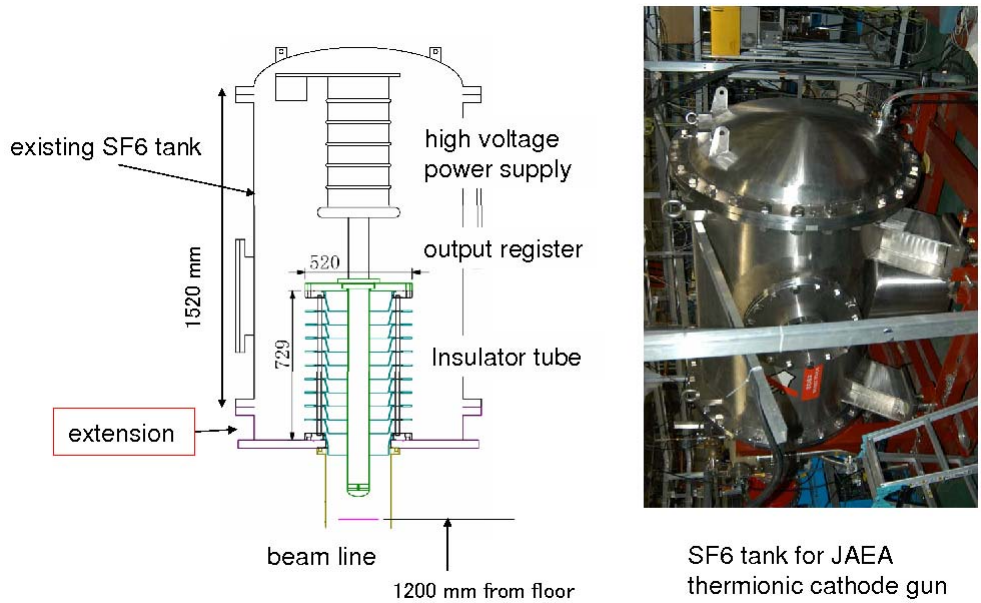

FIGURE 4. A schematic of SF6 tank for 500 kV gun.

We have started design of 500 kV 10 mA gun for the Compact ERL. A Cockcroft Walton power supply which can deliver beam current up to 10 mA will be constructed by March 2009. The maximum voltage is 550 kV, and the voltage ripple is less than 10^{-4}. The size is 400 mm in diameter and 700 mm in height. The design is similar to the existing high power supply for 250 kV prototype gun.

We designed a segmented insulator tube where ten ceramics are stacked in series. Kovar ring electrode is sandwiched between two ceramics and blazed. The diameters of the ceramics, and flange are 400 mm and 520 mm, respectively. The height of the tube is 730 mm. The insulator tube is similar to that for JAEA thermionic cathode gun used for FEL experiments [11] and that for polarized electron gun at Nagoya university [12].

The diameter of a rod supporting cathode electrode has been determined to be 106 mm for the field on the rod to be minimum. The guard ring attached to each electrode is optimized to suppress secondary electron emission from the ceramics by preventing field emitted electrons from reaching ceramics. The voltage between two consecutive electrodes is limited to 50 kV over 65 mm space. This segmented electrode configuration

may help to avoid electric field concentration on some particular point of the ceramics.

The design of SF6 tank is shown in Fig. 4 where the high voltage circuit, output register and insulator tube are placed in a straight line. This configuration will help one get an axially symmetrical field around the tube and power supply. The existing SF6 tank for JAEA thermionic cathode gun shown in the right of Fig. 4 will be reused as the SF6 tank for 500 kV gun for cost reduction, although an extension tank needs to be added. The top height is estimated to be 3.5 to 3.8 m from the floor when the beam line is 1.2 m high.

We also need to design cathode preparation system consisting of loading and NEA preparation chambers. We will fabricate these two chambers by March 2009.

SUMMARY

We have developed a 250 kV photo-emission DC gun and generated 150 keV, 1μA electron beam. We have designed 500 kV segmented insulator tube with optimized guard rings as well as a SF6 tank with symmetrical configuration. We will design and begin construction of cathode preparation system for 500 kV gun soon.

ACKNOWLEDGMENTS

This work was partially supported by Grants-in-Aid for Scientific Research (Grants No. 20360424) from the Ministry of Education, Culture, Sports, Science and Technology of Japan.

REFERENCES

1. C. Hernandez-Garcia *et al.*, “A High Average Current DC GaAs Photocathode Gun for ERLs and FELs”, Proc. of PAC2005, 3117 (2005).
2. J. Grames *et al.*, “Measurements of Photocathode Operational Lifetime at Beam Currents up to 10 mA using an Improved DC High Voltage GaAs Photogun”, Proc. of the 17th International Spin Physics Symposium and Workshop, Kyoto, Japan, 2–7 October 2006, 1037.
3. T. Kasuga *et al.*, “Status of R&D Efforts toward the ERL-based Future Light Source in Japan”, Proc. of PAC2007, 1016 (2007).
4. S. Sakanaka *et al.*, “Progress in R&D Efforts on the Energy Recovery Linac in Japan”, Proc. of EPAC2008, (2008) 205.
5. R. Hajima *et al.* (ed.), KEK Report 2007-7/JAEA-Research 2008-032 (2008) [in Japanese].
6. N. Nishimori *et al.*, “Development of an Electron Gun for the ERL Light Source in Japan”, Proc. of ERL07 (2007) (to be published).
7. R. Hajima *et al.*, “Proposal of Nondestructive Radionuclide Assay Using a High-Flux Gamma-Ray Source and Nuclear Resonance Fluorescence”, J. Nucl. Sci. and Tech. 45, 441 (2008).
8. H. Kurisu *et al.*, J. Vac. Sci Technol. A21, L10 (2003).
9. AxTRAN, ULVAC, Inc., `http://www.ulvac.com/vacuum/vacgauge_axtran.asp`.
10. S. Zhou *et al.*, Applied Optics 46, 8488 (2007).
11. N. Nishimori *et al.*, “A Thermionic Electron Gun System for the JAERI Superconducting FEL”, Proc of EPAC2000, 1672 (2000).
12. M. Yamamoto *et al.*, “200 keV Polarized Electron Source for Linear Collider”, Proc of LINAC2002, 680 (2002).

KSI's Cross Insulated Core Transformer Technology

Uwe Uhmeyer

Kaiser Systems, Inc, 126 Sohier Road, Beverly, MA 01915

Abstract. Cross Insulated Core Transformer (CCT) technology improves on Insulated Core Transformer (ICT) implementations. ICT systems are widely used in very high voltage, high power, power supply systems. In an ICT transformer ferrite core sections are insulated from their neighboring ferrite cores. Flux leakage is present at each of these insulated gaps. The flux loss is raised to the power of stages in the ICT design causing output voltage efficiency to taper off with increasing stages. KSI's CCT technology utilizes a patented technique to compensate the flux loss at each stage of an ICT system. Design equations to calculate the flux compensation capacitor value are presented. CCT provides corona free operation of the HV stack. KSI's CCT based High Voltage power supply systems offer high efficiency operation, high frequency switching, low stored energy and smaller size over comparable ICT systems.

Keywords: High Voltage Power Supply, HVPS, Insulated Core Transformer, ICT, Cross Core Transformer, CCT, Flux Compensation, corona free
PACS: 29.25.Bx

INTRODUCTON

Dr. James Cross developed Cross Transformer Technology (CCT) for high voltage (HV) generation improves upon existing techniques for HV generation at higher power levels. CCT builds upon Insulated Core Transformer (ICT) techniques adding several significant innovations. Dr. Cross was awarded US patents #5,631,815 and 6,026,004 for his inventions. Kaiser Systems is the exclusive worldwide licensee of the CCT patents. CCT power supplies have been demonstrated from 25 kV to 1000 kV at power levels up to 200kW and are suitable for SF_6, oil or solid insulation systems.

A design issue for conventional HV transformers is the creepage distance in the insulation system between the HV secondaries and the transformer core. Ferrites are conductive (~ 10^6 Ω/cm) and will draw corona. A 500 kV HV transformer with a conventional core would require several inches of creepage between secondary windings and the core in addition to the size of the windings and core itself, resulting in large size, high weight and high cost. Electrically, the drawbacks of large magnetic structures are increased leakage inductance and decreased efficiency.

CCT and ICT have similar basic features. The HV DC output is produced by multiple sections wired in series. Sections are stacked one above the other. Each section has its own secondary winding(s) and rectifiers associated with its own piece of magnetic core material, electrically connected to its rectified output, but insulated

from its neighbors. The core-to-winding insulation requirement for each section is never more than the localized Vdc output of that section.

Conventional ICT implementations use 3 phase line frequency excitation. Each 20kV (typical stage voltage) stage contains three series output arc limiting resistors, six rectifiers/capacitors and three magnetic core pieces and secondary windings. Stage sections vary as higher turns ratio are needed on higher stages to keep similar output voltage per stage. The most common regulation technique is a motor driven variable transformer to vary primary voltage and as such, control BW is limited to tens of Hz.

A conceptual diagram of an ICT system is shown in Fig 1. Take note that the secondary windings are in close proximity to their respective core sections. Each section has its own ferrite sections that are insulated from the decks above and below. At the fringes of the insulated gaps in the magnetic circuit, magnetic flux leaks out.

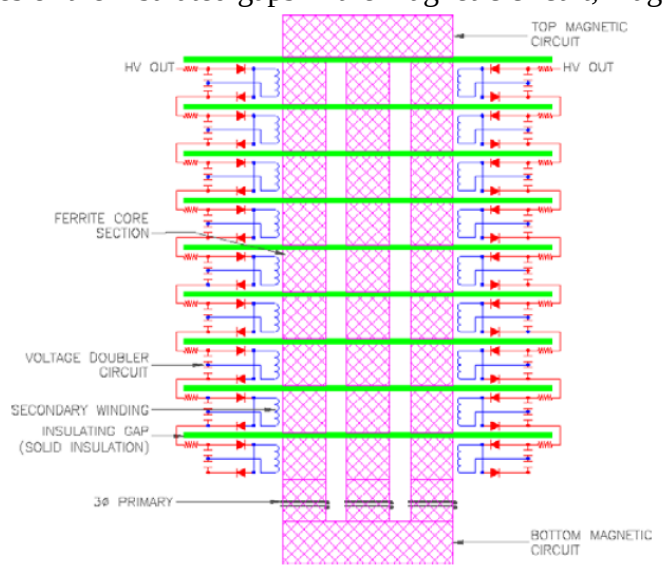

FIGURE 1. Conceptual drawing of ICT System. Note the middle phase circuitry is not shown

Less magnetic flux produces less voltage resulting in a reduction of voltage efficiency. A 25 stage nominal 500kV HVPS ICT will serve as an example. If each stage produced 20kV, then the total output should be 500kV. However, due to flux leakage, each successive stage produces only 98.5% of the previous stage; the total HV output will only go to 420kV. An ICT design trade off is to decrease the number of stages at the expense of higher stage-to-stage voltage. Often the deck transformer turns ratio is increased with each higher stage to keep stage-to-stage voltage the same.

CROSS TRANFORMER TECHNOLOGY (CCT):

CTT has many advantages over ICT. The most significant is a uniform stage-to-stage voltage due to compensation of flux leakage. Additional benefits include extremely low stored energy, fast transient response time, greater efficiency and an inherently corona-free design. This translates into higher reliability.

Figure 2 shows a 500 kV CCT stack. Each of the 40 stack cards are identical, producing up to 12.5 kV. The magnetic circuit is formed by the ferrite bars at top and bottom and joined by the ferrite tiles associated with each section. At the outside of

the assembly, grading rings control the electrical field towards the enclosure vessel that houses the stack. The dome at the top of the stack is the output of the power supply. A wire or cable can be attached at that point.

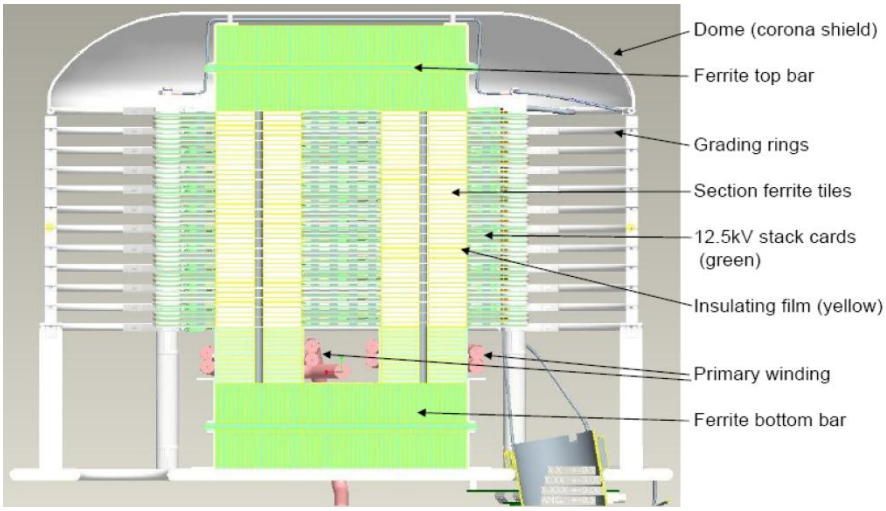

FIGURE 2. 500 kV CCT Stack Example

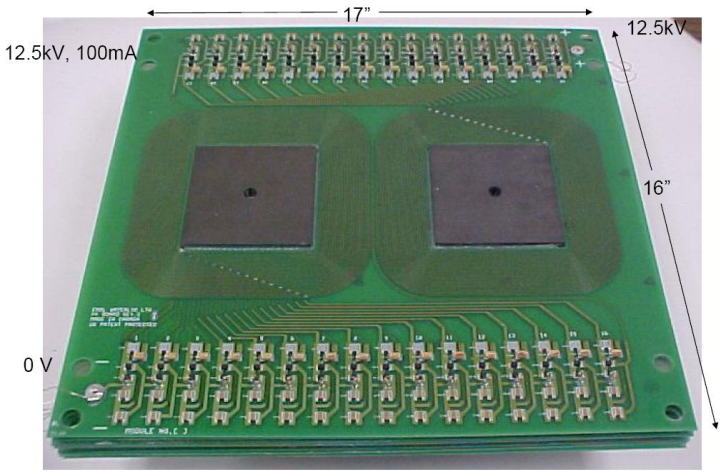

FIGURE 3. CCT HV Card

Figure 3 shows a CCT HV stack card. The card contains thirty-two identical circuits connected in series. Sixteen circuits at the top are fed from transformer secondaries from the right side ferrite tile, while the other 16 circuits from the left side ferrite tile. With 32 circuits connected in series, the card produces up to 12,500 Vdc.

Each circuit, as shown in Fig. 4, is composed of a fuse, voltage doubler, a flux compensating capacitor and an output arc current limiting resistor and is capable of producing up to 400 Vdc. Using low voltage components in a HV environment, there is minimal voltage stress across the stack board. The components in the circuit see less than 400V. The local electrical field is no more than 1 kV/inch. The corona inception voltage is never exceeded. [1] There is no gradual degradation of insulating materials by corona. Fault tolerance is provided by the fuse which will blow should a stage be damaged. The stage will generally fail in a shorted mode, thereby maintaining its

series connection and the output current path. The rest of the circuit elements continue to operate and the power supply functions but with a small loss of voltage efficiency.

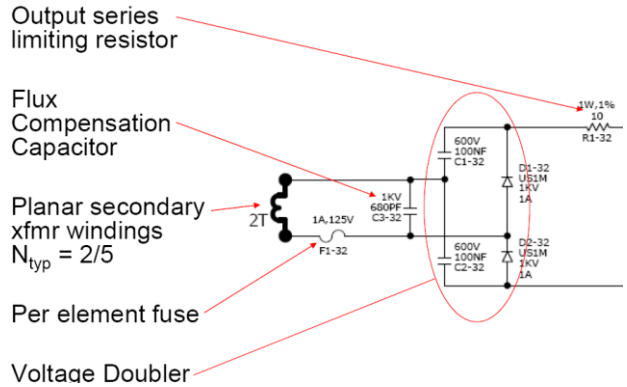

FIGURE 4. Basic CCT circuit element

An important benefit of the topology is very low stored energy. With only 50 nF (0.05uF) of capacitance per stage stored energies of only 0.98J, 4.88J and 7.32J for 100kV, 500kV and 750 kV systems, respectively, are present. These low stored output energies minimize arc currents and their duration should arcs occur.

The construction technique employed in CCT design lowers costs. The stack cards use inexpensive 2-layer Printed Wiring Board technology. Planar transformer design (PCB traces to form transformer windings) removes the need for individually wound secondary windings. Surface Mount Technology (SMT) components are low cost and can be assembled with automated SMT equipment. Lastly, all stack cards in HV stacks are identical to each other. Only one type of spare HV stack card is needed.

FLUX COMPENSATION:

From Patent 6,026,004: "The segmentation of the magnetic core in the transformer introduces gaps in the magnetic structure with permeability essentially that of air. This greatly increases the reluctance of the magnetic structure and produces leakage of magnetic flux. As a result, the upper sections of the magnetic core carry less flux than the lower sections of the core, which results in lower generated voltage per turn on the secondary windings" [2]. Flux compensation restores the lost magnetomotive force (MMF) per gap. The energy associated with the 'leaking' fields is associated with the value of the 'leakage inductance" parameter of transformers. Compensating for the leakage flux, in effect, cancels out the leakage inductance.

$$C = \frac{R}{N^2 \omega^2} \tag{1}$$

$$C = \frac{l}{\mu_0 A N^2 (2\pi f)^2} \tag{2}$$

Dr. Cross ends patent 6,026,004 with Eq. 1. KSI derived Eq. 2 based on Eq. 1 as a more useful form. Examination of the equation reveals that the value of the flux compensation capacitor C is a function of only the transformer physical properties and the operating frequency. It is independent of the output voltage or current. A fixed frequency sinusoidal voltage waveform is required at the primary of the transformer.

SUMMARY

TABLE 1. Selected Characteristics For A Typical 750 kV, 100 mA HV System.

Description	Value
Output Voltage and Operating Range	Meets all the efficiency, stability and regulation specifications over its normal operating voltage range of 100 kV to 750 kV
High Voltage Section Insulation	Pressurized SF6 gas, maximum pressure of 5 atm, absolute (59 psig)
HV Driver	Separate cabinet with control module and inverter module system. Inverters require water cooling
Power Supply Input Voltages	
Inverter supply	480Vac ±10%, 3-phase, 50-60 Hz
Controls and interlocks power	120 Vac ±15%
Efficiency	> 80% overall. Typically 92% at full voltage
Line and Load Regulation	< ±0.5% for a change of ±10% (lower values available on request)
Stability & Ripple	±0.5% total variation for fixed output voltage, current and temperature. (lower values available on request)
Temperature Coefficient	< 200ppm/°C (lower values available on request)
Reproducibility	< 0.5% after 1 hour warm-up (lower values available on request)
Operating Temperature	15°C to 40°C

Typical specifications for a CCT system are shown above in Table 1. KSI has delivered practical implementations using Phase Shift Modulation (PSM) topology operating at 90 kHz. PSM allows for Zero Voltage Switching (ZVS), which greatly reduces switching losses at mid-level to full power operation.

CCT builds upon ICT but has several advantages. The flux compensation technique minimizes stage-to-stage voltage differences yielding a higher efficiency design. Uniform stage-to-stage voltages allow all deck cards to be identical without compromising the voltage rating of the components on the higher stages. The uniform stage-to-stage voltage ensures inherent scalability of the topology over a very wide range of output voltages. The use of multiple low voltage circuits connected in series minimizes electric field stress, creating a corona free design, providing longer life and higher reliability. The lower cost SMT components and automated assembly make for an easier-to-assemble, and therefore lower cost, implementation. Low stored energy minimizes arc energy and also allows for excellent transient response.

ACKNOWLEDGMENTS

Contributions to this presentation include the work and input from David Johns, Yuri Botnar, Ken Kaiser and Steve Swech, all employees of Kaiser Systems, Inc.

REFERENCES

1. US Patent #5,631,815 “High Voltage Power Supply”, Inventor: Cross; James D. (41 Allen Street East, Waterloo, Ontario, CA)
2. US Patent #6,026,004 “Modular high voltage power supply with integral flux leakage compensation”, Inventor: Cross; James D. (Waterloo, CA)

Low Emittance Electron Gun for XFEL Application

C.Gough, M.Paraliev and S.Ivkovic

Paul Scherrer Institute, Villigen, Switzerland

Abstract. The Paul Scherrer Institute (PSI) in Switzerland is planning to build a cost-effective X-ray Free Electron Laser (XFEL) facility for 0.1-10 nm wavelength and 10-100 fsec pulse length, requiring only 6 GeV electron energy. The facility will consist of a Low Emittance electron Gun (LEG) with high gradient acceleration and advanced accelerator technology for preserving the emittance during acceleration and bunch compression. To demonstrate feasibility of the project, a 4 MeV test stand followed by a new 250 MeV test stand will be used at PSI. An emittance of <0.1 mm-mrad is desired, and this extreme value has prompted the development of several novel features: gated field emitting array, a pulsed high gradient gun, combined photo-field emission, pulsed solenoid focusing and a two-frequency cavity. The LEG should give stable emission of >200 pC, with >700 keV energy and >125 MV/m gradient.

Keywords: relativistic electron beams, electron sources, electron guns.
PACS: 29.25.Bx, 79.70 +q.

TEST STAND OVERVIEW

Figure 1 shows the present 4 MeV test stand. The initial acceleration of electrons is across a ~4 mm anode-cathode gap. After initial solenoid focusing, the electrons pass through a 2-cell, 1.5 GHz cavity, two further DC solenoids before passing into an emittance monitor. Details of the LEG development are given [1-3].

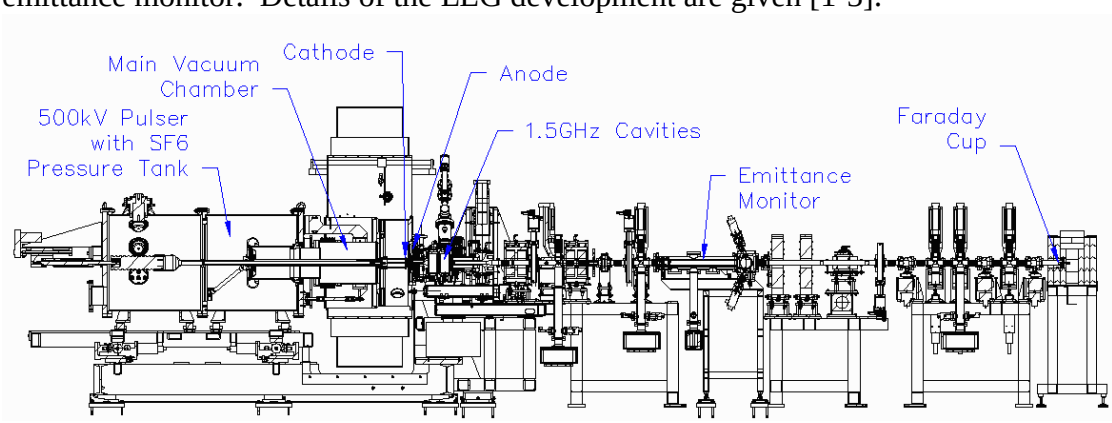

FIGURE 1. Cross-section of 4 MeV test stand.

The pulsed cathode voltage is generated by an optimized Tesla coil [4]. The shortest possible pulse was wanted to minimize the risk of breakdown, but this was balanced against the need for reasonable lifetime and low jitter for a long development program

of field emitting arrays and photoemission studies. Finally, thyratron switches with a Tesla coil were found to be our best compromise. There is a practical limit to the pulse width possible from a Tesla coil; in our case, ~17 secondary turns mean over 20 meters of secondary conductor, and due to speed of light constraints, this limits the FWHM pulse length to the range of ~250 ns.

ELECTRODE MEASUREMENTS

Figure 2a shows a rather primitive cathode electrode that was used for earlier tests. It was expected that the unpolished sharp transition from flat to elliptical geometry would give such high field enhancement that breakdown must occur on this circular line. Surprisingly, no breakdowns occurred there, but rather in random locations over the newly machined flat surface. Figure 2b shows one of several surprising features of this surface were found with an electron microscope.

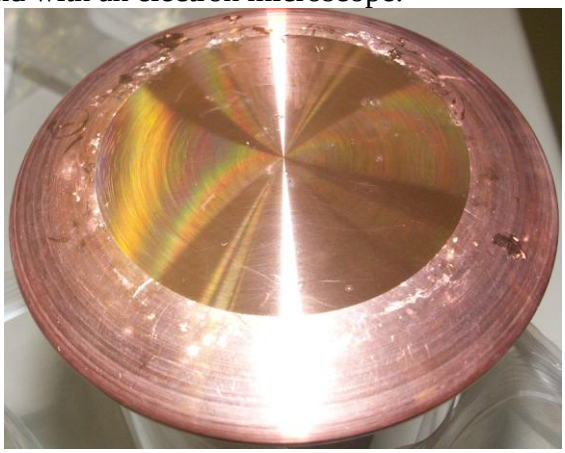

FIGURE 2a. Elliptical copper electrode, 80 mm in diameter, but with the front surface machined flat and not polished.

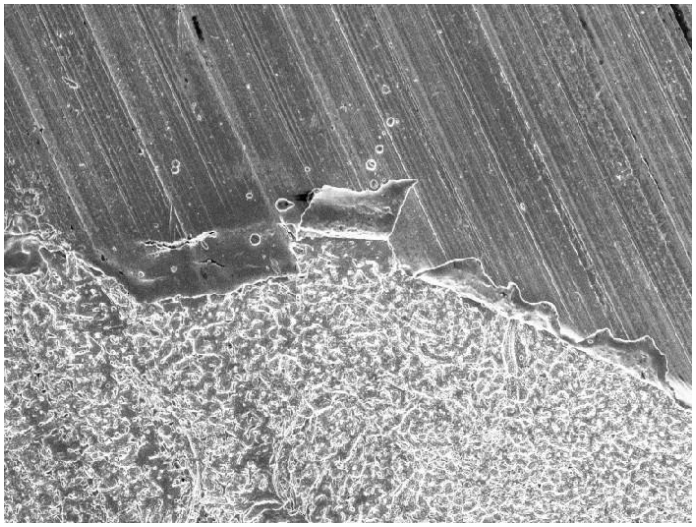

FIGURE 2b. Enlargement of one breakdown site, image width ~100 μm. In the lower part, the copper has been melted. The upper part shows a hardened surface of ~1 μm thickness which has peeled back. Surprisingly, these sharp edges with high β were not sites for later breakdowns.

FIGURE 3. Copper cathode and corresponding copper anode plate, after multiple breakdowns.

Figure 3 shows the results from another rather primitive test, where the anode was flat, but perforated by holes from 1 mm to 6 mm in diameter, and the cathode was a polished copper elliptical electrode. The expectation was that the rather sharp geometry changes around the holes would give preferential breakdown at these sites. Fig.3 shows that most breakdowns (in the 30-40 MV/m range) were not related to the anode holes with right angle edges.

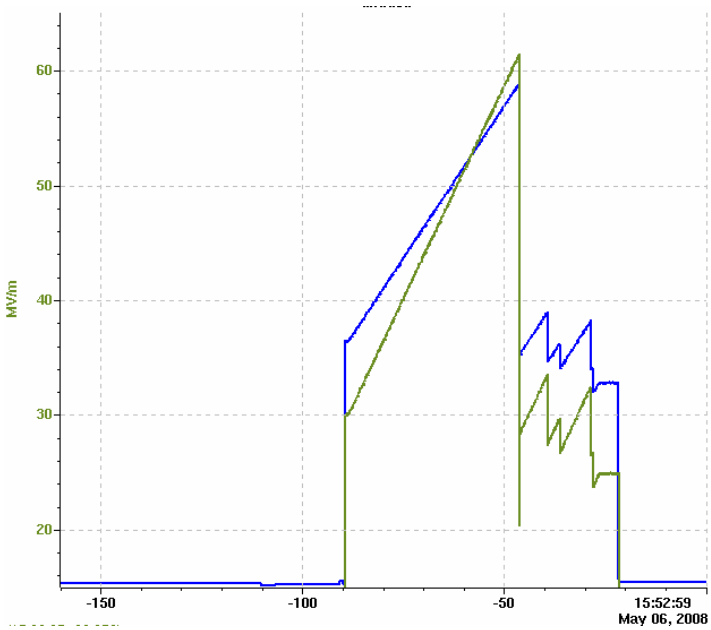

FIGURE 4. Voltage and gradient curves during a typical breakdown test. The gradient started at 30 MV/m and reached 61 MV/m about 45 minutes later before the first breakdown occurred. This event destroys the electrode surface and thereafter the breakdown gradient is around 35 MV/m.

From these results, we have a general knowledge of what is important for controlling breakdown, and that is solely the surface polishing. The following are <u>not</u> dominant in determining breakdown up to 130 MV/m:

- electrode geometry
- material type and purity
- surface scratches
- anode thickness
- argon discharge cleaning
- vacuum pressure
- surface cleanliness
- time in vacuum
- time in service and voltage ramp-up rate

Improving skills in hand polishing gave ever higher breakdown gradients, but also practical difficulties: X-ray emission was completely absent before breakdown so there is no warning of impending breakdown; the first breakdown completely destroys the surface; and to permit uniform polishing, the electrode surfaces should not have a transition from flat to curved geometry on the front surface.

PULSED SOLENOID

A novel feature of the gun is the use of a pulsed focusing solenoid after the initial acceleration, as shown in Fig.5. In this limited space, a DC solenoid would have a limited number of turns, making field asymmetry a problem. To solve this, a pulsed primary solenoid together with a precision stainless steel cylinder as a secondary "winding" was developed.

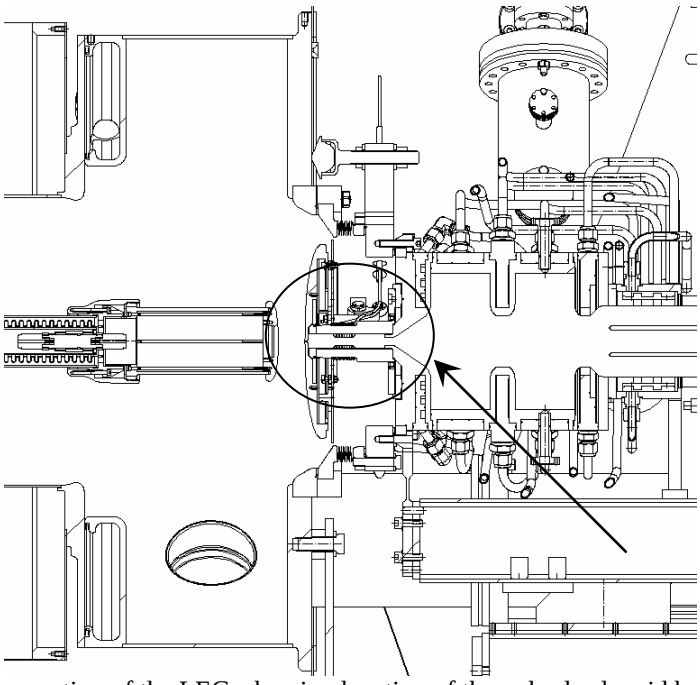

FIGURE 5a. Cross-section of the LEG, showing location of the pulsed solenoid between AK gap and RF cavity.

The primary and the stainless steel cylinder "secondary" are mounted in a precise ceramic flange, with tolerances in the +/-20 µm range. The operation is shown in Fig.5b. A pulsed current is applied to the primary for about 150 µsec; initially, there is a modest circulating

current in the secondary which opposes the change of flux. The primary current is then turned off rapidly; the opposing secondary current is then in the kiloamp current range, and decays with a time constant of ~30 μsec. During this time, the magnetic field is from the secondary only, and has near-perfect centering and symmetry. Additional advantages of the pulsed solenoid are the zero leakage field at the cathode and low thermal dissipation.

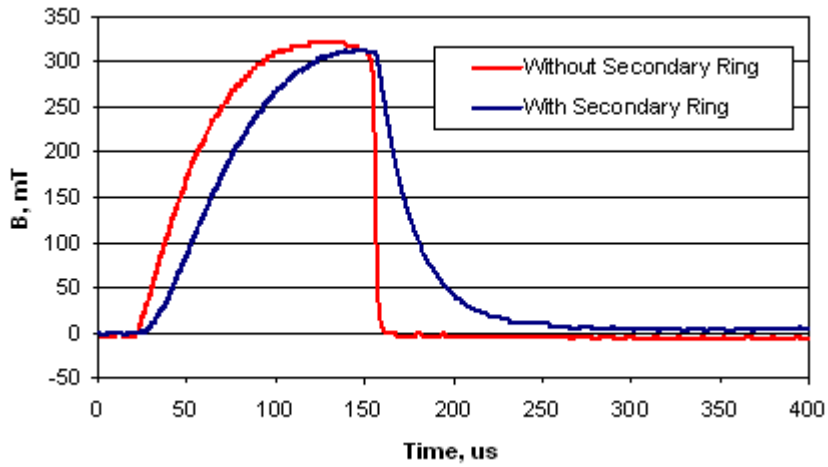

FIGURE 5b. Magnetic field waveforms. Without the secondary, the field is switched rapidly to zero. With the secondary, the field decays with a time constant ~30 μs.

SUMMARY AND PRESENT STATUS

Over 45 electrode pairs have been tested in the LEG pulser and considerable experience was gained with different materials and surface conditions. Another 40+ pairs are scheduled for testing in the first half of 2009.

Breakdown is presently limited by surface polishing. A gradient of 60 MV/m is standard for most materials, and well polished electrodes could reach 130 MV/m. Stainless steel has become our standard material because of low cost and ease of polishing.

Improvement in surface treatment by electron beam melting and surface deposition is being investigated. Gradients of >200 MV/m at 400 kV have been reached but further tests are needed to confirm this result.

REFERENCES

1. R.Ganter et al., *Phys Rev.Lett.* **100**,064801 (2008)
2. F.Le Pimpec et al., FEL 2008 Conference, Gyeongju, Korea (2008).
3. Project overview and publications are available from http://fel.web.psi.ch
4. M.Paraliev et al., IEEE Pulsed Power Conference, Monterey, USA (2005).

Ion bombardment in RF guns

E. Pozdeyev, D. Kayran and V.N. Litvinenko

Brookhaven National Laboratory, Upton, NY 11973-5000

Abstract. We use the ponderomotive potential of the RF field to study the motion of ions in an RF gun. We apply this method to the BNL 1/2-cell SRF photogun and demonstrate that a significant portion of the ions produced in the gun can reach the cathode if no special precautions are taken. Also, we propose simple mitigation techniques that can reduce the rate of ion bombardment.

Keywords: electron source, ion bombardment, cathode, RF gun, ponderomotive potential
PACS: 29.25.Bx,85.60.Ha

INTRODUCTION

Operational experience with DC guns has demonstrated that ion backbombardment is the major cause of degradation of the quantum efficiency of GaAs cathodes. Numerical simulations described in publications [1],[2] revealed that ion backbombardment also can occur in RF guns. In this paper, we use the method of a rapidly oscillating field [3] to analyze the motion of ions in an RF gun. We briefly describe the method and examine the ion motion in the BNL 1/2-cell SRF gun. We would like to note that electron backbombardment and multipacting also can affect the cathode lifetime in an RF gun. However, we do not discuss this phenomenon herein.

MOTION OF IONS IN A RAPIDLY OSCILLATING RF FIELD

The motion of an ion with the mass m and charge q in a rapidly oscillating electromagnetic field can be described as a superposition of a fast oscillating term, $\mathbf{a}$, and a term describing the ion motion averaged over the fast oscillations, $\mathbf{x}(t) = \overline{\mathbf{r}(t)}$: $\mathbf{r} = \mathbf{x} + \mathbf{a}$. If the RF electric field has the following form $\mathbf{E} = \vec{\mathscr{E}}(\mathbf{r})\cos(\omega t + \psi)$ where $\omega t + \psi$ is the RF phase, the fast oscillating term is given by

$$\mathbf{a} = -\frac{\lambda^2}{4\pi^2}\frac{q\vec{\mathscr{E}}\cos(\omega t + \psi)}{mc^2} \tag{1}$$

and the equation for the averaged motion is given by

$$\ddot{\mathbf{x}} = -\frac{\lambda^2 c^2}{16\pi^2}\left(\frac{q}{mc^2}\right)^2 \nabla\vec{\mathscr{E}}^2, \tag{2}$$

where λ is the RF wavelength. The method is applicable provided that the amplitude of the fast oscillations, $|\mathbf{a}|$, is small compared to the characteristic size of the inhomogeneity of the RF field, L: $|\mathbf{a}|/L \ll 1$.

Equation (2) shows that the effect of the RF field averaged over the fast oscillations can be described by the effective potential energy

$$U_e = \frac{mc^2}{16\pi^2}\left(\frac{\lambda q\vec{\mathscr{E}}}{mc^2}\right)^2 \tag{3}$$

The potential energy (3) frequently is referred to as the "ponderomotive" potential energy. If an external static electromagnetic field is present, the Lagrange function of the averaged motion is

$$L = T_e - U_e - U + \frac{e}{c}\mathbf{A}\cdot\dot{\mathbf{x}}, \tag{4}$$

where U and $\mathbf{A}$ are the scalar and vector potentials of the external field, respectively, and T_e is the effective kinetic energy $m\dot{\mathbf{x}}/2$.

In treating the ion motion, we assume that the ions are generated only in collisions of the electron beam with the residual gas. The energy transferred in the ionization process is mostly absorbed by knocked out electrons. Therefore, the cross section of collisions with a large energy transfer to an ion is much smaller than the ionization cross section. Thus, we can assume that ions originate at rest and find the initial effective velocity $\dot{\mathbf{x}}_0$:

$$\dot{\mathbf{x}}_0 = -\frac{\lambda c}{2\pi}\frac{q\vec{\mathscr{E}}\sin(\phi_0)}{mc^2}, \tag{5}$$

where ϕ_0 is the ionization RF phase. The associated initial effective kinetic energy is given by:

$$T_{e0} = m\frac{\dot{\mathbf{x}}_0^2}{2} = \frac{mc^2}{8\pi^2}\left(\frac{\lambda q\vec{\mathscr{E}}}{mc^2}\right)^2 \sin^2(\phi_0) = 2U_e\sin^2(\phi_0). \tag{6}$$

BNL 1/2-CELL SRF GUN

Brookhaven National Laboratory and Advanced Energy Systems, Inc. are jointly developing a 1/2-cell superconducting radio-frequency (SRF) photogun [4]. Figure 1 shows the SuperFish [5] model of the gun. The gun will operate with the following nominal parameters: a beam energy of 2 MeV, an accelerating gradient of 29 MeV/m, a fundamental RF frequency of 703.75 MHz, a bunch repetition rate of 9.38 MHz, a charge per bunch up to 5 nC, and an average beam current up to 50 mA.

The motion of ions on the gun axis is one-dimensional because of the axial symmetry of the gun. The electric field on the gun axis was calculated by SuperFish. The program Parmela [6] was used to calculate the RF phase at which electron bunches pass a given coordinate, yielding the ionization phase ϕ_0 as a function of z. In this simulation, the initial beam phase was chosen to minimize the beam emittance. Figure 2 shows the effective potential energy (in red) of H_2^+ ions on the gun axis. Also, Figure 2 shows the total effective energy of H_2^+ ions as a function of the ionization coordinate. The total energy curve is divided into two branches: Ions whose velocity $\dot{\mathbf{x}}_0$ points towards the cathode (in green) and those whose velocity points out of the gun (in blue). The total

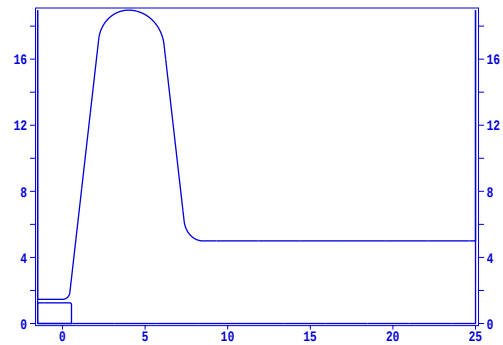

FIGURE 1. SuperFish model of the BNL 1/2-cell SRF gun. The horizontal axis corresponds to the gun axis.

effective energy of ions originating at $z < 3.4$ cm is larger than the effective potential energy at the cathode. Thus, those ions originating at $z < 3.4$ cm will reach the cathode. All other ions produced at $z \geq 3.4$ cm will be expelled from the gun.

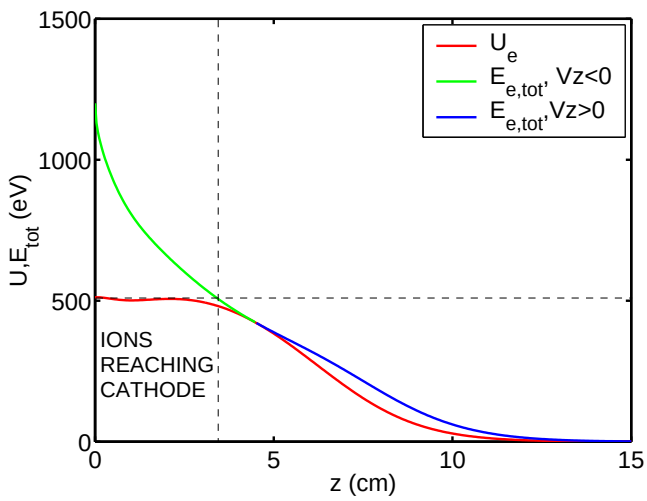

FIGURE 2. The effective potential energy (red) and the total effective energy (green and blue curves) of H_2^+ ions in the BNL 1/2-cell SRF Gun. The green and blue curves, respectively, show the total energy of ions with the effective velocity $\dot{\mathbf{x}}_0$ pointing towards the cathode and away from the cathode.

Off-axis, ions experience a deflecting force. The effective potential energy off the gun axis is given to the second order in r by

$$U_e = \frac{mc^2}{16\pi^2}\left(\frac{\lambda q}{mc^2}\right)^2\left(\mathscr{E}_a^2 - \frac{\mathscr{E}_a}{2}\left(\mathscr{E}_a'' + \frac{\mathscr{E}_a}{\lambda^2}\right)r^2 + \frac{(\mathscr{E}_a')^2}{4}r^2\right), \tag{7}$$

where $\mathscr{E}_a(z)$ is the electric field on the gun axis, and $'$ denotes a derivative with respect to z. Because we assumed that ions originate at rest, the equation for the average ion radius can be written as $m\ddot{r} = -\partial U_e/\partial r$. This equation has to be solved simultaneously with the Lagrange equation for z. However, because we are interested only in ion trajectories with a small deviation from the gun axis, we can assume that the axial motion does not depend on r and use the value of $\dot{x}_z$ on the gun axis.

Generally, the equation for the radial motion has to be solved numerically. Its solution also can be found by iterations. If the trajectory radius changes little, we can limit the solution to the first iteration and solve the problem analytically. Figure 3 shows a deviation of ion trajectories from the initial radius calculated at the cathode and normalized to the initial radius vs. the ionization coordinate. The blue curve shows a result of numerical solution of the equation of the radial motion. The green curve depicts the first iteration obtained analytically. The points show results of particle tracking in a SuperFish field map conducted to validate the results obtained by using the ponderomotive potential. There is a good agreement among all the results for $z < 3$ cm. The first iteration fails to predict the motion of ions correctly for ions originating at $3 < z < 3.4$ cm.

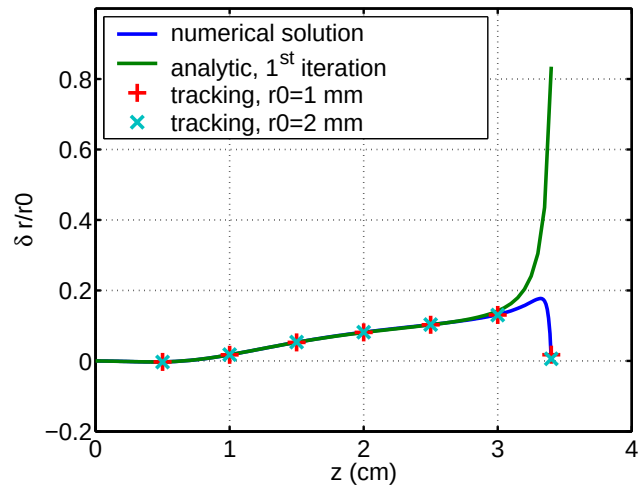

FIGURE 3. Normalized deviation of ion trajectories from the initial radius at the cathode as a function of the ionization coordinate. Tracking results for $r_0 = 1$ mm and $r_0 = 2$ mm practically coincide with each other, confirming the linearity of ion motion close to the gun axis.

The described results were obtained without including the field of the beam. Simple estimates of the beam field that are not presented here show that we can disregard the beam field up to a beam current of a few hundred milliamperes.

Rate of ion bombardment. Comparison to a DC gun.

The number of ions bombarding the cathode normalized to the extracted charge is given by

$$\frac{\mathrm{d}N}{\mathrm{d}Q} = \frac{n_i}{e}\int_0^D \sigma(E(z))\mathrm{d}z, \tag{8}$$

where n_i is the particle density of the residual gas, σ is the ionization cross section, and D is the distance from which ions can reach the cathode. For a residual hydrogen pressure of $5 \cdot 10^{-12}$ Torr and a distance D of 3.4 cm, equation (8) yields $(\mathrm{d}N/\mathrm{d}Q)_{\mathrm{BNL}} = 1.7 \cdot 10^6$ ions/C. We can compare this number to the number of ions produced in a high voltage DC gun. For this example, we choose the following parameters: a beam energy of 650 keV, an accelerating gap of 5 cm, and the residual gas pressure the same as that in the

example of the BNL gun, viz., $5 \cdot 10^{-12}$ Torr. With these parameters, equation (8) yields $(\mathrm{d}N/\mathrm{d}Q)_{\mathrm{HVDC}} = 2.4 \cdot 10^6$ ions/C.

This example indicates that rates of cathode ion bombardment can be comparable in RF and DC guns. However, in reality, a cross-comparisson of the cathode lifetime between these two types of guns based on the over-all rate of ion bombardment can be inaccurate. First, the ion energy spectra in the two differ substantially. Second, DC guns are frequently operated with the laser spot shifted from the cathode center. Therefore, a detailed knowledge of the ion spectra and the efficiency of QE damage as a function of the ion energy are required to predict the cathode lifetime with a reasonable accuracy.

MITIGATION TECHNIQUES

The dependence of the initial drift velocity $\dot{\mathbf{x}}_0$ on the accelerating phase can be employed to suppress ion bombardment in a single-cell gun. Assuming the RF field is accelerating in the phase range from $-\pi/2$ to $\pi/2$, the initial drift velocity $\dot{\mathbf{x}}_0$ of all ions will point away from the cathode if the RF phase changes between 0 and $\pi/2$ during the acceleration of electron bunches. Ions with the total effective energy greater than the effective potential energy will exit the gun. Only a small portion of ions originating close to the cathode still will be able to strike the cathode because positively charged ions are accelerated towards the cathode immediately after ionization.

The phasing method described above is not applicable to a multi-cell gun because the accelerating phase cannot be limited to the range between 0 and $\pi/2$. Cathode biasing can be used in this case. Also, cathode biasing can be effective in a single-cell gun. For the BNL gun, a bias voltage of 800 V might suffice to significantly reduce the rate of ion bombardment.

ACKNOWLEDGMENTS

We would like to thank Ilan Ben-Zvi for bringing the subject of ion bombardment in RF guns to our attention. This work was performed under the auspices of the U.S. Department of Energy.

REFERENCES

1. R. Fliller, T. Anderson, H. Edwards, H. Bluem, T. Schultheiss, C. Sinclair, and M. Huening, “Progress on Using NEA Cathodes in an RF Gun,” in *Proceedings of PAC 2005, Knoxville, Tennessee, 2005*, IEEE, Piscataway, New Jersey, 2005, p. 2708.
2. J. W. Lewellen, *Phys. Rev. ST Accel. Beams* **5, 020101** (2002).
3. L. D. Landau, and E. M. Lifshitz, *Mechanics (Course of Theoretical Physics)*, Butterworth-Heinemann; 3rd edition, 1982.
4. R. Calaga, I. Ben-Zvi, M. Blaskiewicz, X. Chang, D. Kayran, and V. Litvinenko, *Physica C* **441**, 159 (2006).
5. K. Halbach, and R. Holsinger, *Particle Accelerators* **7**, 21 (1976).
6. L. Young, Parmela, Tech. Rep. LA-UR-96-1835, LANL (1996), documentation by J.H. Billen, rev. 2004.

High-Fidelity RF Gun Simulations with the Parallel 3D Finite Element Particle-In-Cell Code Pic3P

A. Candel, A. Kabel, L. Lee, Z. Li, C. Limborg, C. Ng, G. Schussman and K. Ko

SLAC National Accelerator Laboratory, Menlo Park, CA 94025, USA

Abstract. SLAC's Advanced Computations Department (ACD) has developed the first parallel Finite Element 3D Particle-In-Cell (PIC) code, Pic3P, for simulations of RF guns and other space-charge dominated beam-cavity interactions. Pic3P solves the complete set of Maxwell-Lorentz equations and thus includes space charge, retardation and wakefield effects from first principles. Pic3P uses higher-order Finite Element methods on unstructured conformal meshes. A novel scheme for causal adaptive refinement and dynamic load balancing enable unprecedented simulation accuracy, aiding the design and operation of the next generation of accelerator facilities. Application to the Linac Coherent Light Source (LCLS) RF gun is presented.

Keywords: higher-order finite element time domain (FETD), electromagnetic particle-in-cell (PIC), space charge, electron dynamics, moving window, parallel computing
PACS: 41.20.Jb, 14.60.Cd, 41.75.Fr, 03.65.Pm, 02.60.Cb, 02.70.Dh

INTRODUCTION

A detailed understanding of emission, acceleration and transport phenomena is necessary for advancing the development of high-quality electron guns for next-generation light sources and colliders to be operated at ever more demanding parameter regimes. Joining in this effort, SLAC has developed the first high-performance higher-order Finite Element (FE) 3D Particle-In-Cell (PIC) code Pic3P, for realistic modeling of low energy, space-charge dominated electron dynamics in injectors. Running on large-scale supercomputing facilities, Pic3P provides advanced capabilities that enable RF gun simulations with unprecedented accuracy and speed.

THE PARALLEL CODE PIC3P

In Pic3P, the full set of Maxwell's equations is solved numerically in time domain using parallel higher-order FE methods. Electron macro-particles are pushed self-consistently in space charge, wake- and external drive fields.

Finite Element Time-Domain Field Solver

Ampère's and Faraday's laws are combined and integrated over time to yield the inhomogeneous vector wave equation for the time integral of the electric field $\mathbf{E}$:

$$\left(\varepsilon\frac{\partial^2}{\partial t^2}+\sigma_{\text{eff}}\frac{\partial}{\partial t}+\nabla\times\mu^{-1}\nabla\times\right)\int^t\mathbf{E}(\mathbf{x},\tau)\,\mathrm{d}\tau=-\mathbf{J}(\mathbf{x},t), \tag{1}$$

with permittivity ε and permeability μ. The effective conductivity σ_{eff} provides a simple model for damping in lossy materials.

The computational domain is discretized into curved tetrahedral elements and $\int^t\mathbf{E}\,\mathrm{d}\tau$ in Equation (1) is expanded into a set of hierarchical Whitney vector basis functions $\mathbf{N}_i(\mathbf{x})$ up to order p within each element:

$$\int^t\mathbf{E}(\mathbf{x},\tau)\,\mathrm{d}\tau=\sum_{i=1}^{N_p}e_i(t)\cdot\mathbf{N}_i(\mathbf{x}). \tag{2}$$

Substituting Equation (2) into Equation (1), multiplying by a test function and integrating over the computational domain results in a system of linear equations for the coefficients e_i, second-order in time. Numerical integration is performed with the unconditionally stable implicit Newmark-Beta scheme [1]. More detailed information about the employed methods has been published earlier [2].

Higher-Order Particle-Field Coupling

Electron macro particles are specified by position $\mathbf{x}$, momentum $\mathbf{p}$, rest mass m and charge q. The total current density $\mathbf{J}$ in Equation (1) is then approximated as

$$\mathbf{J}(\mathbf{x},t)=\sum_i q_i\cdot\delta(\mathbf{x}-\mathbf{x}_i(t))\cdot\mathbf{v}_i(t), \tag{3}$$

with $\mathbf{v}=\frac{\mathbf{p}}{\gamma m}$, $\gamma^2=1+|\frac{\mathbf{p}}{mc}|^2$. The classical relativistic collision-less Newton-Lorentz equations of motion are integrated using the standard Boris pusher, an explicit method splitting the momentum update into one magnetic and two electric contributions [3].

Maintaining numerical charge conservation during the self-consistent simulation of charged particles and electromagnetic fields is achieved by starting with proper initial conditions and then fulfilling the discrete versions of Equation (1) and the continuity equation

$$\frac{\partial\rho}{\partial t}+\nabla\cdot\mathbf{J}=\mathbf{0} \tag{4}$$

simultaneously during time integration.

The use of higher-order finite elements not only significantly improves field accuracy and dispersive properties [4], but also leads to intrinsic higher-order accurate particle-field coupling equivalent to, but much less laborious than, complicated higher-order interpolation schemes commonly found in finite-difference methods.

Causal Moving Window

The methods used in Pic3P are based on unstructured meshes of up to second-order curved tetrahedral elements – this allows modeling of small geometric features and scattering effects with high accuracy. In combination with higher-order field representation, highly efficient use of computational resources and unprecedented simulation accuracy are obtained.

Furthermore, orders of magnitude in computational resources can be saved, without sacrificing modeling accuracy, by restricting field computations to the causal field region around the particle bunch. This 'moving window' technique can be efficiently implemented using adaptive p-refinement – every element in the overall domain uses an individual basis order $p \geq 0$.

Figure 1a) shows a Minkowski spacetime diagram indicating the causal domain for a bunch transiting through a compact structure. Figure 1b) shows the corresponding parallel dynamic load balancing of the causal field domain during a typical RF gun PIC simulation with Pic3P, where both the field calculation and communication efforts are balanced.

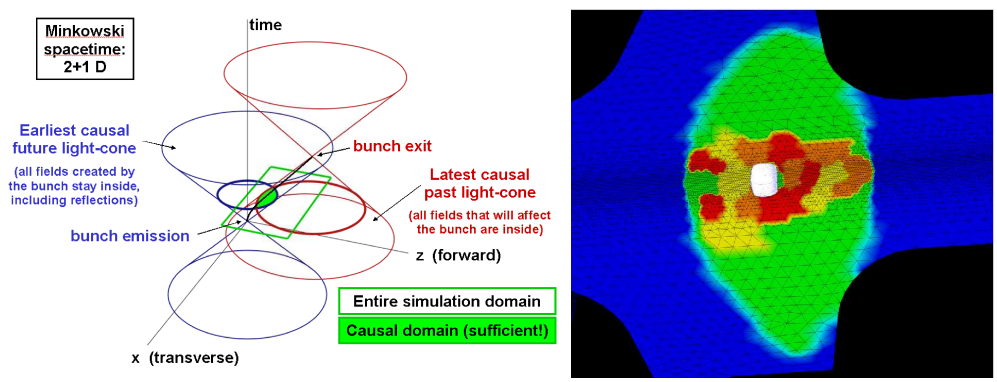

(a) (b)

FIGURE 1. Snapshot in time during bunch transit through compact structure with causal moving window technique. (a) Minkowski spacetime diagram indicating the causal domain.
(b) Pic3P simulation of a quarter model of an RF gun with particle bunch in transit. Elements in non-causal domain are omitted in the field computations ($p = 0$). Elements and fields in the causal domain ($p > 0$) around the particle bunch are partitioned onto all CPUs with dynamic parallel load balancing.

RESULTS

PIC simulations of the 1.6-cell S-band LCLS RF gun are presented [5]. In the simulations, the gun is driven by the π-mode with a peak accelerating field gradient of 120 MV/m at the cathode (the cavity wall). A cold, uniform, 10 ps flat-top, cylindrically symmetric electron bunch of 1 mm radius is emitted, centered around a phase of -58° with respect to the crest. Solenoidal focusing fields are neglected for simplicity. These parameters allow comparisons between the 3D results from simulations with Pic3P and PARMELA and the 2D results from simulations with Pic2P and MAFIA.

For Pic3P simulations, a conformal, unstructured 3D (1/4) mesh model with 305k tetrahedral elements is used, with mesh refinement along the center of the beam pipe. High fidelity cavity mode fields are obtained with the parallel FE frequency domain code Omega3P and directly loaded into Pic3P as drive fields. Figure 2a) shows a comparison of transverse emittance results by the different codes and Figure 2b) shows the parallel scalability of Pic3P.

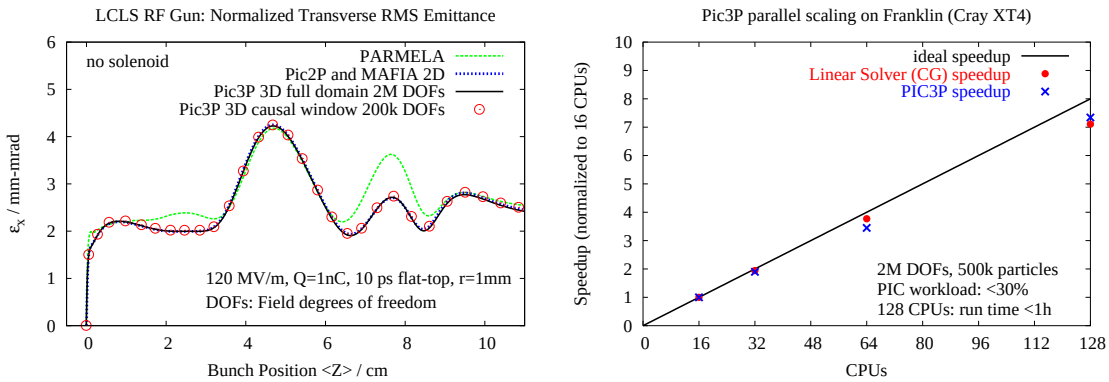

(a) (b)

FIGURE 2. (a) Comparison of normalized transverse RMS emittance as a function of beam position in the LCLS RF gun as calculated with PARMELA, Pic2P and MAFIA 2D (both agree), and Pic3P, where the causal moving window technique reduces the problem size by one order of magnitude.
(b) Parallel scalability of Pic3P for the full domain simulation with 2M DOFs.

Excellent agreement between 3D results from Pic3P and the 2D results from Pic2P and MAFIA is found, as expected from the high cylindrical symmetry in the fields and the convergence behavior of the codes. PARMELA results differ as space-charge effects are significant, presumably because wakefield and retardation effects are ignored, as detailed in a previous study [2].

Pic3P allows large-scale 3D PIC simulations of RF guns with realistic particle distributions, including intra-bunch effects. Starting with an initial particle distribution obtained from measurements, another LCLS RF gun simulation was performed. Figure 3a) shows a snapshot of the scattered fields during bunch transit. Figure 3b) shows the transverse and longitudinal phase phase of the particle bunch near the exit of the gun.

CONCLUSIONS

The first successful implementation of a parallel Finite Element 3D electromagnetic PIC code is presented. The new code Pic3P was used to model space-charge effects in the LCLS RF gun from first principles, including wakefield and retardation effects. It employs state-of-the-art parallel Finite Element methods on conformal, unstructured meshes with unconditionally stable time integration and self-consistent higher-order particle-field coupling. In combination with novel causal moving window techniques and dynamic load balancing, Pic3P allows unprecedented accurate and efficient simulations of low-emittance electron injectors, aiding the design and operation of the next generation of light sources and colliders.

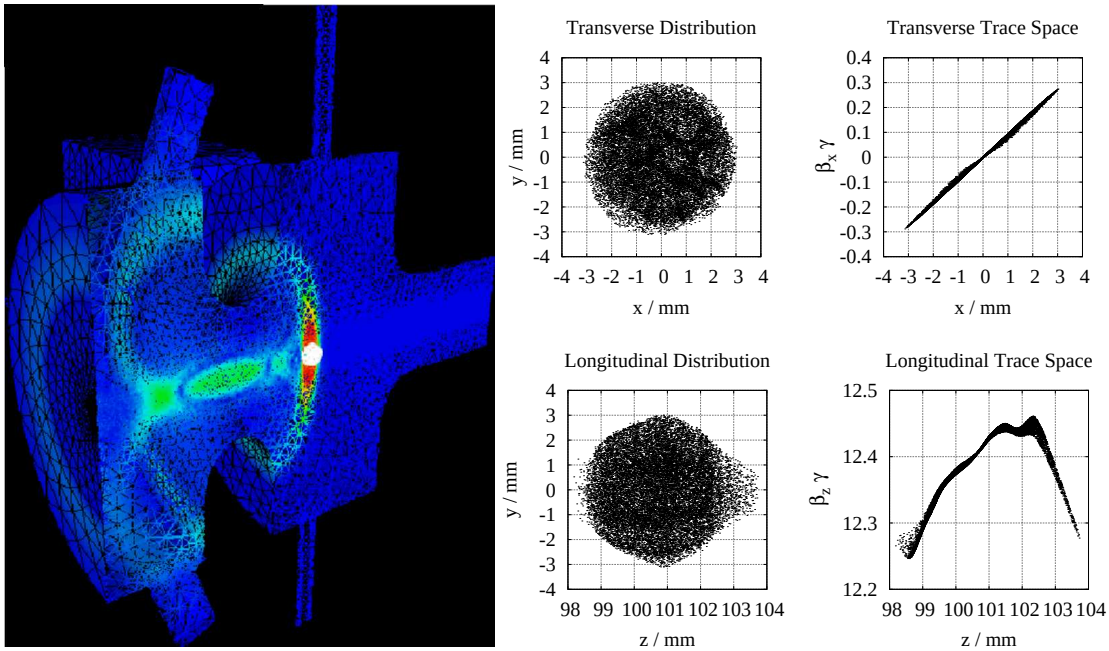

(a) (b)

FIGURE 3. Snapshot during LCLS RF gun simulation with Pic3P, starting with a non-uniform electron bunch distribution obtained from measurements. (a) Scattered electric fields (b) Phase space

ACKNOWLEDGMENTS

This work was supported by the US DOE ASCR, BES, and HEP Divisions under contract No. DE-AC002-76SF00515. This research used resources of the National Energy Research Scientific Computing Center, and of the National Center for Computational Sciences at Oak Ridge National Laboratory, which are supported by the Office of Science of the U. S. Department of Energy under Contract No. DE-AC02-05CH11231 and No. DE-AC05-00OR22725. – We also acknowledge the contributions from our SciDAC collaborators in numerous areas of computational science.

REFERENCES

1. N. M. Newmark, “A method of computation for structural dynamics”, Journal of Eng. Mech. Div., ASCE, vol. 85, pp. 67-94, July 1959.
2. A. Candel et al., “Parallel Higher-order Finite Element Method for Accurate Field Computations in Wakefield and PIC Simulations”, Proc. ICAP 2006, Chamonix Mont-Blanc, France, Oct. 2-6, 2006.
3. J. P. Boris, “Relativistic plasma simulation-optimization of a hybrid code”, Proc. Fourth Conf. Num. Sim. Plasmas, Naval Res. Lab, Wash. D.C.,pp. 3-67, Nov. 2-3, 1970.
4. M. Ainsworth, “Dispersive properties of high-order Nedelec/edge element approximation of the time-harmonic Maxwell equations”, Philos. trans.-Royal Soc., Math. phys. eng. sci., vol. 362, no. 1816, pp. 471-492, 2004.
5. L. Xiao et al., “Dual Feed RF Gun Design for the LCLS”, Proc. PAC 2005, Knoxville, Tennessee, May 15-20, 2005.

The Superconducting RF Photoinjector at ELBE – First Operational Experience

J. Teichert[a], A. Arnold[a], H. Büttig[a], D. Janssen[a], M. Justus[a], U. Lehnert[a], P. Michel[a], P. Murcek[a], A. Schamlott[a], C. Schneider[a], R. Schurig[a], F. Staufenbiel[a], R. Xiang[a], T. Kamps[b], J. Rudolph[b], M. Schenk[b], G. Klemz[c], and I. Will[c]

[a]*Forschungszentrum Dresden-Rossendorf, P.O. Box510119, 01314 Dresden, Germany.*
[b]*BESSY, Albert-Einstein-Str. 15, 12489 Berlin, Germany.*
[c]*Max-Born-Institut, Max-Born-Str.2A ,12489 Berlin, Germany.*

Abstract. An RF photoinjector with a superconducting cavity (SRF gun) for installation at the Radiation Source ELBE was developed within a collaboration of BESSY, DESY, FZD, and MBI. This new and promising injector type allows CW operation and has the potential for the production of high-brightness electron beams. The gun cryostat, the electron diagnostic beamline, and the driver laser with optical beamline were installed. In November 2007 the first beam was produced. Results of the beam parameter measurements with Cs_2Te photo cathodes are presented.

Keywords: electron source, photo electron injector, superconducting cavity, SRF gun, radio frequency acceleration, cesium telluride photo cathode.
PACS: 07.77.Ka, 29.25.Bx, 29.27.Ac, 29.27.Fh.

INTRODUCTION

One of the main concerns in the development of electron guns for future accelerator based light sources is the combination of high beam brightness and high average current. State-of the-art normal conducting RF photo injectors have demonstrated very high brightness at large bunch charges. The success based on direct generation of short electron bunches by laser pulses and the immediate strong acceleration of the electrons from the surface of the photo cathode in the RF field. By exploiting superconducting technology the RF power losses can be minimized and operation in continuous wave (CW) mode with high average current is possible. In the Research Center Dresden-Rossendorf (FZD) a superconducting RF photo injector (SRF gun) with a 3½-cell niobium cavity has been developed. The SRF gun is installed at the superconducting electron accelerator ELBE, a user facility for the production of electro-magnetic radiation (infrared, x-rays, gamma radiation) and secondary beams (neutrons, positrons).

The SRF gun project at FZD, carried out in collaboration with BESSY, DESY, and MBI, has two main goals: the installation of a high-brightness photo-injector for ELBE, and contributing to the SRF gun development as a promising future technology. Now the new SRF gun has opened an unique opportunity for experimental

studies like long term studies of photo cathodes operation and lifetime, cavity quality degradation, or emittance compensation methods.

On November 12, 2007, the first accelerated electron beam was generated which was extracted from a Cu photo cathode. In March 2008 the cathode transfer system was mounted and the first set of Cs_2Te photo cathodes was produced. Since May 2008 the gun has been operated with these cathodes. This paper reports on the operational experience and on beam parameter measurements within the first operation run until October 2008. The RF properties of the SRF gun cavity are presented in a separate paper [1]. An overview of the SRF gun design is published in ref. [2].

PHOTO CATHODES AND DRIVE LASER

During the commissioning and the first measurement period two types of photo cathodes were used: a Cu cathode and later semiconductor cesium telluride (Cs_2Te) cathodes. The Cu cathode was mounted into the cavity during the assembly of the cryomodule. It was used during the commissioning until the cathode transfer system was installed. The quantum efficiency (QE) was about 1×10^{-6}, which was rather low. However, an electron beam could be produced and observed on YAG screens.

After installation of the cathode transfer system, the first set of Cs_2Te photo cathodes for the SRF gun was produced in May 2008 in the preparation lab with QE of 4-5 %. After transfer to the gun the QE dropped down to 0.05 %. The first Cs_2Te cathode was in operation for 44 h. This cathode and all the others of the first set were damaged due to an accidental venting during the summer shut down.

A second set of Cs_2Te photo cathodes was prepared and transported to the SRF gun in July 2008. One was installed in the gun and was in operation for about 350 h until the end of the measurement period. Its QE after preparation was 3 %. Again the QE measurement in the SRF gun after insertion delivers a much lower value of about 0.1 %. Although the vacuum of 10^{-9} mbar in the transportation chamber was now good enough the worse vacuum during cathode exchange in the transfer chamber causes the drop-down. Nevertheless the QE was high enough to produce bunch charges up to 200 pC and to conduct the beam parameter measurements. The QE measurement was regularly repeated without any further significant changes during the whole measurement period.

The cathode cooling, support and transfer system worked properly. The cooling of the cathode with liquid N_2 was efficient. As desired the cathodes can be exchanged without warming-up.

In order to fulfill the requirements of the SRF gun specifications, a UV laser system with two channels has been developed. The two channels have different oscillators, but jointly used amplifier and UV conversion. At present, the 500 kHz channel is used for the experiments. The frequency-quadrupled Nd:YLF system for CW operation consists of a mode-locked oscillator with 26 MHz, a regenerative amplifier, and a two-stage frequency conversion. The Pockels cells in the amplifier allow variable repetition rates up to 500 kHz. The laser has a Gaussian temporal beam shape with a width of 15 ps FWHM. The laser spot is enlarged with a telescope on the laser table. Then the beam is cut with an aperture to obtain a circular flat top profile with 2.7 mm diameter.

BEAM PARAMETER MEASUREMENTS

For the electron beam characterization a diagnostic beam line has been installed [3]. The beam properties were measured using the following parameters: cavity acceleration gradient of 5 MV/m, photo cathode about 2.5 mm retracted, 5 kV DC voltage at the cathode, and the gun was operated in CW.

In a laser phase scan the arrival time of the laser pulse onto the cathode is varied with respect to the RF phase while measuring the bunch charge in a Faraday cup at constant laser pulse energy. In Fig. 1 such a measurement is shown for the whole phase range from -180° to 180°. The RF field is given by $B_z(z) = B_{z0}(z)\sin\varphi_{RF}$ and the z-axis corresponds to the beam direction. Due to its negative charge, electrons are emitted in the phase range -180° to 0°, whereas emission is suppressed between 0° and 180°. This behavior is clearly seen in the measured curve. The curve delivers important information on synchronization, phase jitter, and proper operation of the laser system. But the main purpose of the measurement is the determination of the optimum laser launch phase.

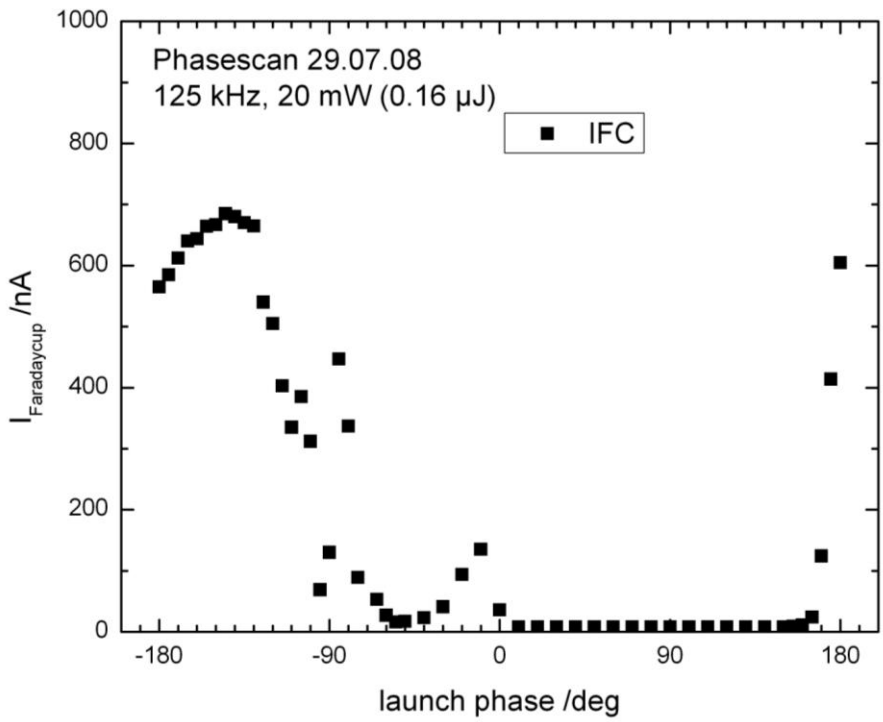

FIGURE 1. Laser phase scan with low bunch charge measured for a full RF period from -180° to 180° (T = 1/f = 769.2 ps). The dark current measured in the phase range between about 0° and 180° is 8 nA.

The phase scan has been carried out for different laser pulse repetition rates from 125 kHz down to 1 kHz with nearly the same laser power of 20 mW for each scan. Whereas the average current is about the same, the bunch charge is increasing with lower laser pulse rate. With increasing laser pulse energy and correspondingly higher electron bunch charge, the space charge effect in front of the cathode becomes more and more important. As visible in Fig. 2, this effect smoothes the curve structures and causes the saturation in the bunch charge. Except these space charge effects, the

behavior of the curves is independent of the laser repetition rate which confirms the proper laser synchronization.

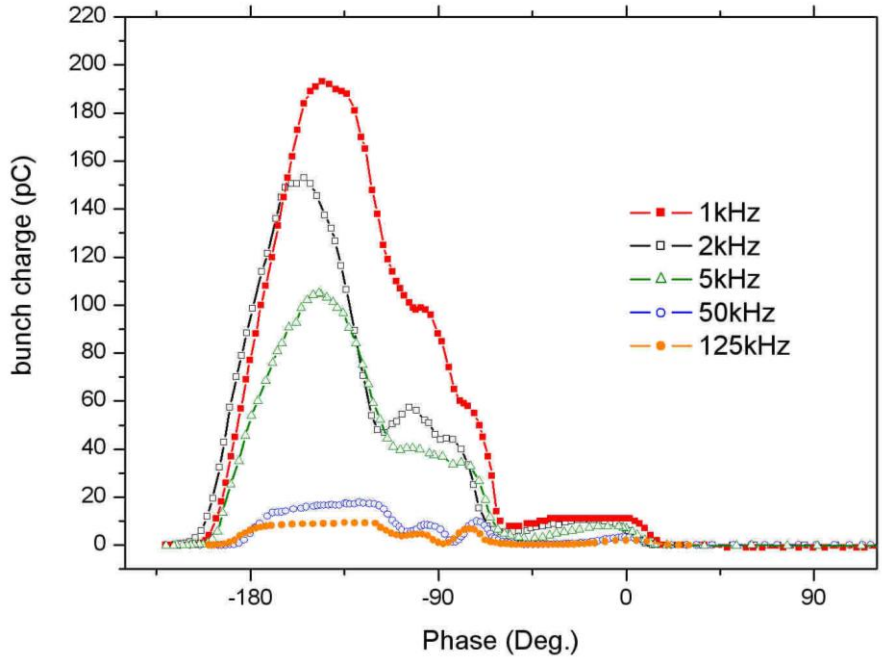

FIGURE 2. Bunch charge versus laser launch phase measured for different laser repetition rates.

The beam energy as a function of launch phase is presented in Fig. 3 with a maximum beam energy of 2.06 MeV. The comparison with the laser phase scan in Fig. 2 shows that the energy drops down at phases > -160° whereas the emission current is still constant until -120°.

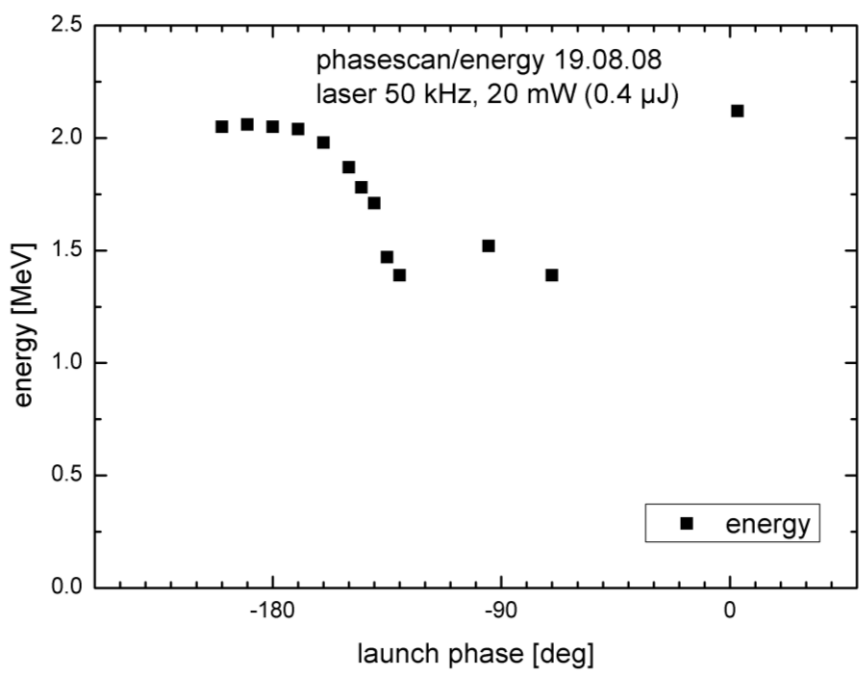

FIGURE 3. Electron beam energy versus launch phase measured by means of the 180° bending magnet in the diagnostic beam line.

The transverse emittance have been measured with the solenoid scan method. For these measurements the gun solenoid and two following screens have been used. Between the solenoid and the screens there is only a drift space of 38 cm and 170 cm, respectively. The magnetic axial field distribution of the solenoid was precisely measured. Thus the focal strength in dependence on the excitation current I can be calculated. The measured beam size $\sigma^2_{x,y}$ on the screen is a parabolic function in I^2 containing the phase space ellipse parameters. From a quadratic fit these parameters and the emittance can be determined. In order to establish the operation phase of the gun, the tranverse emittance was first measured as a function of laser phase. Considering also the other results the laser operational phase was set to -160°. For this laser phase the transverse emittance as a function of bunch charge has been measured with the results in Fig. 4. Measurements were carried out till 70 pC. For higher bunch charges the method could not be applied. The strong space charge effect causes a solenoid current dependence of the beam size which could not be fitted with the theoretical curve. Furthermore the beam shows an increasing halo. To measure the beam size CCD camera images with 8 bit and 660 x 495 pixels were produced, the camera gain was adapted, back ground subtracted and a region of interest (RoI) selected. In the RoI the beam spot size was obtained by a direct rms analysis or by a Gaussian fit to the projected profiles. All theses measurement points are shown in the figure.

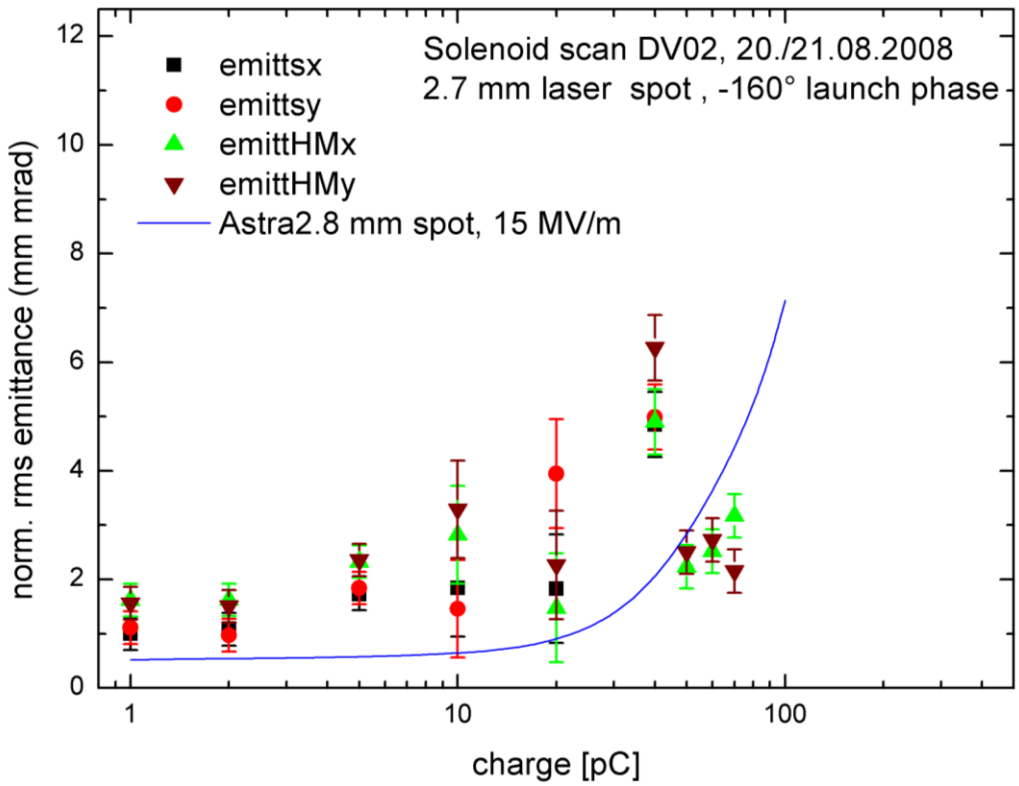

FIGURE 4. Normalized transverse emittance as a function of bunch charge at -160° laser launch phase measured with the solenoid scan method using beam spot on screen 2. Measurement in horizontal (x) and vertical (y) direction, direct rms beam spot size (emittHM), and Gaussian fit (emits).

In Fig. 4 the curve shows an ASTRA simulation result with parameters corresponding to the present experimental situation. The peak value of the RF field was chosen to 15 MV/m, the cathode 2 mm retraced, for the launch phase the optimum value was taken for each bunch charge. In the simulation bunches could be accelerated up to a bunch charge of about 100 pC. For higher bunch charges particle loss occurs due the space charge in front of the cathode. The transverse emittance starts with about 0.5 mm mrad and increases to about 7 mm mrad at 100 pC. This simulation agrees rather well with the experimental data. Especially there is a good agreement in the predicted space charge limit.

For the next runs of the SRF gun in 2009 it is planned to deliver beam to the ELBE accelerator for user operation. Thereby bunch charges above 100 pC are important. It is obvious that the present low acceleration gradient of the gun is the crucial point. As reported in [1] the acceleration gradient could be increased to about 18 MV/m peak field by means of RF high power processing. Furthermore the space charge effect can be reduced by a larger laser spot size. Both changes can improve the electron beam parameters. For a prediction ASTRA simulations have been carried out with 18 MV/m peak field. The cathode position, laser launch phase and laser spot size have been optimized. It turned out that for the higher field and enlarged laser spot of 5.2 mm diameter the space charge limit at the cathode is about 750 pC. The limitation is the transverse emittance now. If 10 mm mrad are acceptable, bunch charge up to about 500 pC can be delivered.

ACKNOWLEDGMENTS

We acknowledge the support of the European Community-Research Infrastructure Activity under the FP6 “Structuring the European Research Area” programme (CARE, contract number RII3-CT-2003-506395) and the support of the German Federal Ministry of Education and Research grant 05 ES4BR1/8.

REFERENCES

1. Arnold, et al., "Rossendrof SRF-Gun Cavity Characteristics," these proceedings.
2. Arnold, et al., "Development of a Superconducting Radio frequency Photo Electron Injector," Nucl. Instr. and Meth. A **577**, 440-454 (2007).
3. T. Kamps, et al., "Electron beam diagnostics for a superconducting radio frequency photoelectron injector," Rev. Sci. Instrum. **79**, 093301 (2008).

Rossendorf SRF-Gun Cavity Characteristics

A. Arnold[a], H. Büttig[a], D. Janssen[a], M. Justus[a], T. Kamps[b], G. Klemz[d], U. Lehnert[a], P. Michel[a], K. Möller[a], P. Murcek[a], J. Rudolph[b], A. Schamlott[a], M. Schenk[b], Ch. Schneider[a] R. Schurig[a], F. Staufenbiel[a], J. Teichert[a], V. Volkov[c], I. Will[d], R. Xiang[a]

[a]*Forschungszentrum Dresden-Rossendorf, P.O. Box 510119, 01314 Dresden, Germany.*
[b]*BESSY, Albert-Einstein-Str. 15, 12489 Berlin, Germany.*
[c]*BINP, 11, akademika Lavrentieva prospect, Novosibirsk, 630090, Russia.*
[d]*Max Born Institute, Max-Born-Str. 2A , 12489 Berlin, Germany.*

Abstract. At the Forschungszentrum Dresden-Rossendorf the development and the setup of the 2nd superconducting radio frequency photo electron injector (SRF-Photo-Gun) is finished. This new injector is placed next to the existing thermionic gun of the superconducting linear accelerator ELBE. A connection between the accelerator and the SRF-Gun will provide improved beam parameters for the users at the second half of 2009. At the moment the commissioning is fully under way. We will report on important results concerning cavity commissioning like measurements of: Q vs. E, microphonics, Lorentz detuning, tuner parameters, pressure sensibility and in-situ fundamental mode field distribution calculated from measured pass band.

Keywords: superconducting cavity, radio frequency acceleration, photo electron injector, SRF-Gun.
PACS: 07.77.Ka, 29.25.Bx, 29.25.Pj, 29.27.Ac.

INTRODUCTION

For future FEL light sources and high energy linear accelerators a high current electron gun with high brilliance is absolutely essential. Thus, an innovative superconducting RF photo injector test bench (SRF-Gun) is in use at the Forschungszentrum Dresden Rossendorf (ELBE) since November 2007. This electron source was developed by a collaboration of BESSY, DESY, MBI and FZD and supported by the European Community.

The use of a superconducting cavity allows CW mode operation with an average beam current of 1 mA and electron energy up to 9.4 MeV. Moreover, the source can deliver short pulses and high-brightness electron beams, as known from the conventional normal conducting RF photo injectors.

Table 1 shows the important cavity design parameters. A detailed description of the cavity and cryomodule is published elsewhere [1]. In this paper we will report on important RF cavity properties measured during the first period of operation. Further results concerning the first beam parameter measurements are presented in [2].

TABLE 1. RF cavity parameters calculated with MWS© and normalized to 50MV/m peak axis field.

Parameter	Value
stored energy U	32.5 J
quality factor Q_0	$1x10^{10}$
dissipated power P_C	25.8 W
geometry factor G	241.9 Ω
Acceleration voltage V_{acc}	9.4 MV
Acceleration gradient E_{acc}	18.8 MV/m
shunt impedance $R_a = V_{acc}^2 / 2Pc$	$1.72x10^{12}$ Ω
R_a/Q_0	166.6 Ω
E_{peak}/E_{acc}	2.66
B_{peak}/E_{acc}	6.1 mT/(MV/m)

1ST COOL DOWN

The first cool down of the SRF-Gun took place in August, 2007. For cooling and filling with liquid nitrogen two days were needed. Then the cavity was cooled down with He gas (10 K) for about 24 h. After a break in which the two ELBE modules were cooled with He gas, the tank was filled with liquid He. Finally, the tank was pumped to 30 mbar in order to get the working temperature of 2 K. Pressure stabilization is performed with cold compressors for all three cryostats of ELBE together using a pressure sensor near the first ELBE cryomodule. During the cool-down, the frequency of the π-mode (acceleration mode) was monitored (Fig. 1).

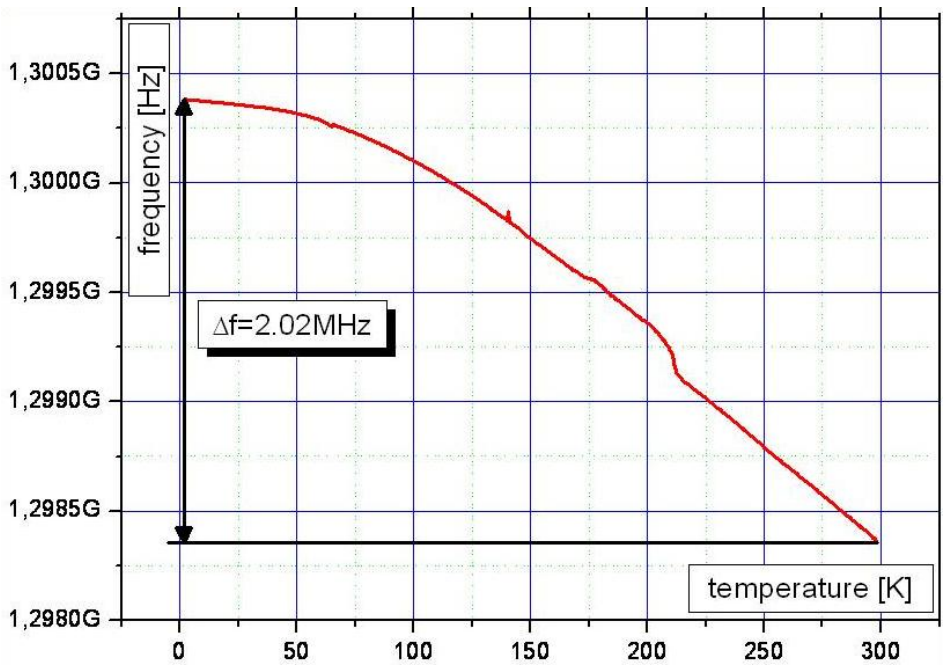

FIGURE 1: Cool down curve of the SRF-Gun cryomodule: cavity resonance frequency versus temperature. The final temperature was 2.0 K.

For the frequency shift from room temperature (RT) to 2 K a value of 2.02 MHz was found which is equal to the shift of TESLA resonators in the ELBE cryomodules. Due to the uniformly shrinkage of the cavity, the coefficient of thermal expansion can be calculated to:

$$\alpha = \frac{f_0}{f_0 + \Delta f} - 1 \rightarrow \alpha \;\; 300K - 2K \;\; = \Delta l / l = -1.55 \cdot 10^{-3} . \qquad (1)$$

Unfortunately, the pre-stress adjustment of the SRF-Gun tuners was wrong. Thus, the final frequency obtained is about 400 kHz higher than expected. For the next operation period in 2009, this was corrected by another adjustment.

PRESSURE SENSITIVITY

To estimate the pressure sensitivity of the cavity, the resonant frequency and the pressure of the helium liquefier were measured at the same time. The result is shown in Fig. 2. To get the pressure dependence of the resonant frequency, the time domain signal versus the pressure variation is plotted for the same time. The linear fit function of this plot gives a slew rate (SR) of approximately SR=230 Hz/mbar. In comparison to the measured value of SR=35 Hz/mbar for the ELBE modules, the value is seven times higher. This could be a problem for operations at high dissipated power which causes slow oscillations of the helium pressure and thus the phase controller could exceed its regulation limit. To improve the frequency behavior the design of a new cavity was modified. Further a control loop using the phase signal and the forward power as process variable and the cavity tuner as actuator can be used at the existing cavity.

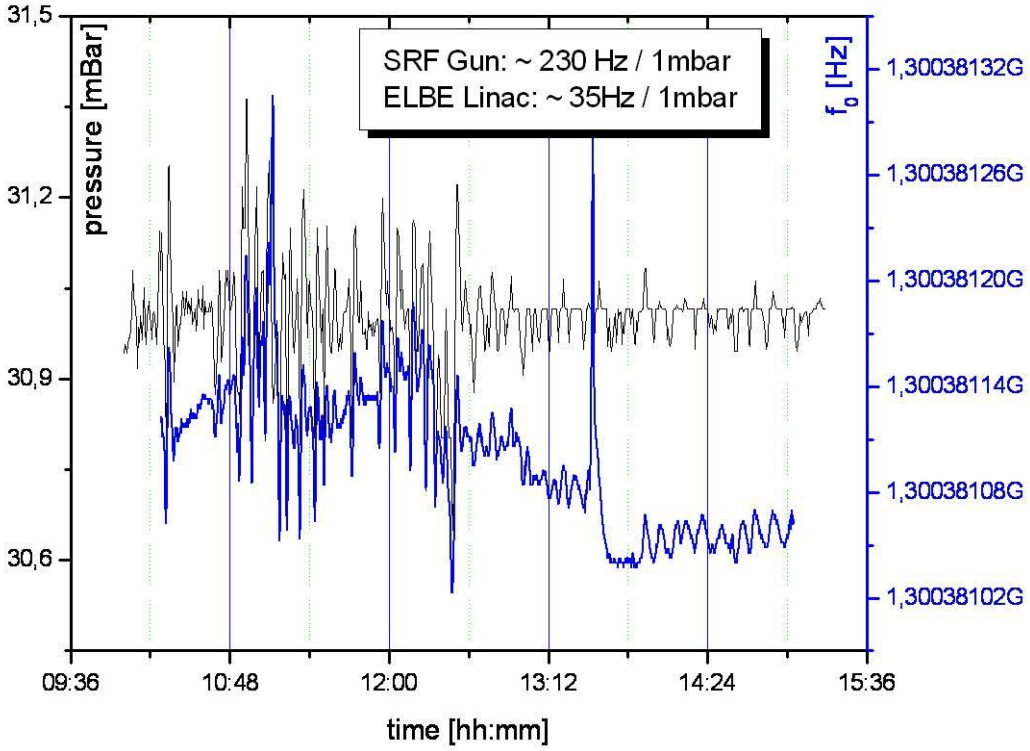

FIGURE 2. Time domain plot of the resonant frequency and the helium pressure.

PASSBAND AND ON-AXIS FIELD DISTRIBUTION

In a mathematical model the RF properties of the 3½-cell cavity can be described by an eigenwert problem. The eigen values are the passband resonance frequencies and the eigen vectors are the field amplitudes in the four cells. Then, the field distribution of the cavity in operation can be calculated from its fundamental mode passband measured at a temperature of 2K. The initial point for that calculation is the last measured cavity state right before the final BCP treatment. The change of the passband frequencies caused by cool down shrinking, change of permittivity and the final BCP cleaning must be taken into account. A detailed explanation of the used algorithm can be found elsewhere [3]. The measured frequencies are shown in Table 2. The obtained field distribution is in good agreement with the design values of 60% in the half cell and 100% in the Tesla cells.

TABLE 2. Measured pass band frequencies at 2 K and calculated acceleration field distribution.

¼ π [MHz]	**½ π [MHz]**	**¾ π [MHz]**	**π [MHz]**
1267.346959	1282.669318	1294.920031	1300.381168
↓	↓	↓	↓
half cell	**1st TESLA cell**	**2nd TESLA cell**	**3rd TESLA cells**
63.1%	100%	96.6%	97.0%

CAVITY TUNER

Due to the different mechanical stiffness, the cavity has two tuners, one for the three TESLA cells, and one for the half-cell. The 3D model and a simplified principle of the mechanism are shown in Fig. 3. Detailed information can be found in [1].

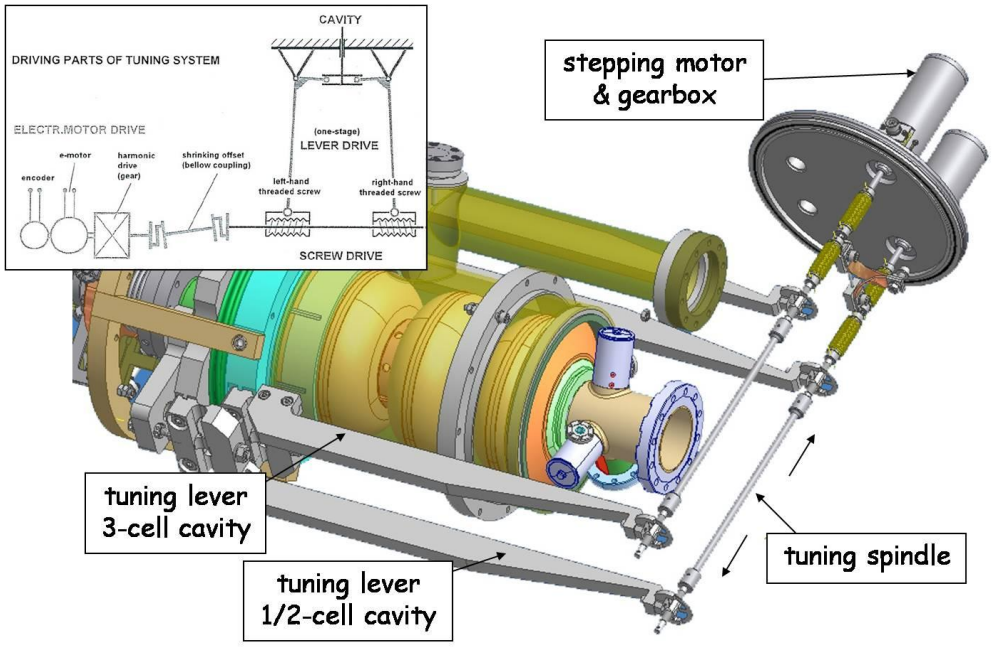

FIGURE 3. 3D model and simplified principle of both tuner systems.

In order to quantify the resolution, the frequency shifts of both tuners were measured versus motor steps while they were moved ±900 steps around the point of origin. To find the overall tuning range the frequency was measured at the mechanical end positions. The results are arranged in Table 3.

TABLE 3. Summary of the measured tuner parameters.

Parameter	Unit	½ cell	3 cells
tuning span	kHz	± 78	± 225
mechanical resolution	nm / step	1.3	2.1
frequency resolution	Hz / step	0.3	0.9

A strong hysteresis, found during the first measurement, could be corrected. The achieved tuning span and the resolution are sufficient for CW operation and in good agreement with the design values.

LORENTZ FORCE DETUNING

In order to measure the Lorentz force detuning of the SRF-Gun cavity, a network analyzer (NWA) was used as a driver for the klystron amplifier. Due to the fact that an increasing RF field detunes the cavity frequency downward, the NWA has to sweep the klystron from higher frequencies over the cavity resonance to lower values. Otherwise the maximum field could not be reached. To increase the cavity field, the output power of the NWA was raised in steps of 1dB while the gradient was calculated from the calibrated pickup voltage. Using this method, the achieved resonance curves for different forward power levels are shown in Fig. 4.

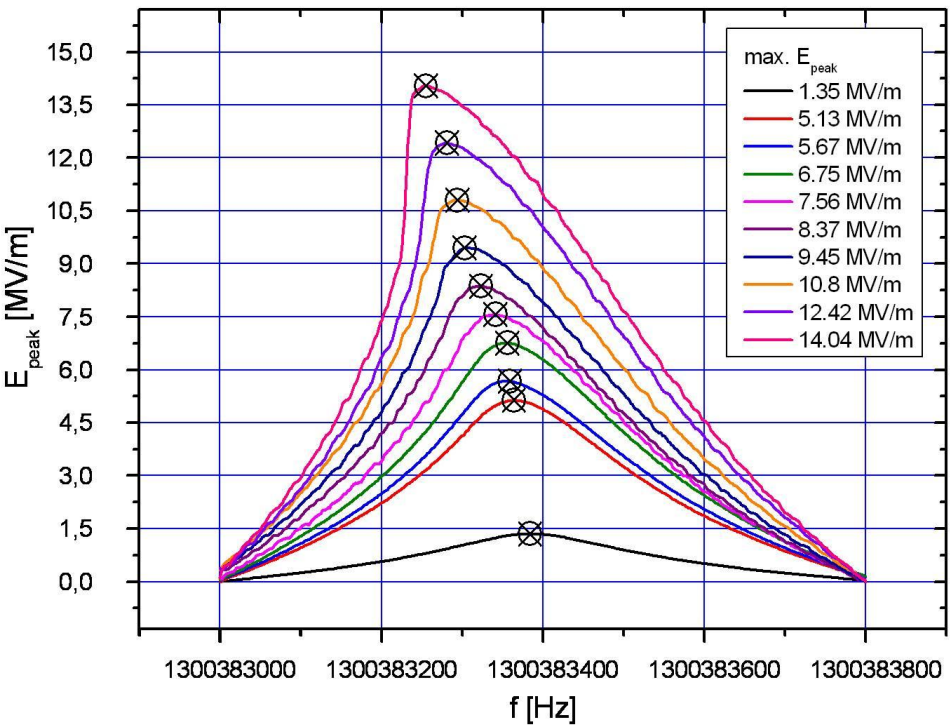

FIGURE 4. Measurement of the peak axis field in the TESLA cells for increasing gradients.

If the frequency shift on crest is plotted versus the applied peak field in the cavity, one can find a quadratic dependence. The determined constant of proportionality is:

$$\Delta f = -k \cdot E_{peak}^2 \quad ; \quad k = 0.7 Hz / \ MV / m^{\ 2} . \tag{2}$$

In comparison to TESLA cavities (with k=-0.25 $(MV/m)^2$), the detuning of the SRF-Gun is about three times higher. The reason is the mechanical weakness of the half cell. At present, for gradients of E_{acc} = 5-6 MV/m the frequency shift is in the order of one bandwidth and causes no operational problems.

MICROPHONICS

Microphonics is known as an excitation of the mechanical eigen modes of the cavity. This results in a permanent detuning of the acceleration mode frequency. Due to the low bandwidth and the weak niobium walls this is typically a problem for superconducting cavities. The mechanical vibrations are induced by pumps, compressors and other heavy machinery next to the SRF-Gun module as well as from helium pressure fluctuation.

The cavity detuning results in a phase shift and amplitude drop of the acceleration mode. In order to stabilize both, a low level RF system is used [4]. The residual detuning (error signal) is measured via the demodulated low level phase controller signal in time domain. A following fast Fourier transformation (FFT) of the stored time signal shows the corresponding discrete power spectral density (PSD). The integrated PSD gives the variance of the measured phase deviation which can be seen as a weighted spectral distribution (Fig. 5).

The overall phase noise up to 1000 Hz of the closed loop operation is σ = 0.055 ° (RMS). This is comparable to the known value of σ ≤ 0.05 ° (RMS) measured at the four ELBE cavities and ensures an energy spread of the accelerated electrons below 10^{-3} [4].

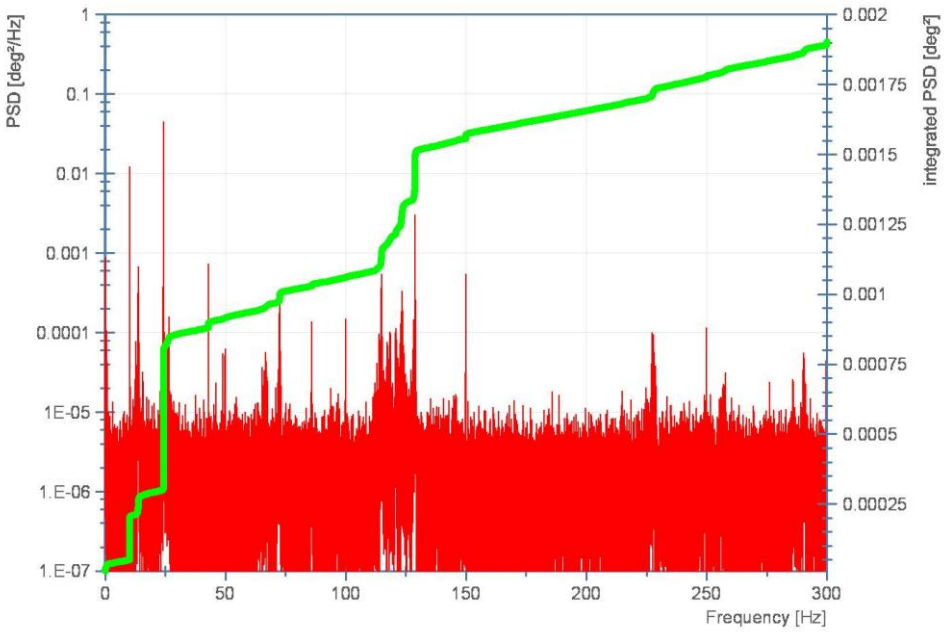

FIGURE 5. Red curve: discrete power spectral density (PSD); Green curve: integrated PSD or $\sigma(f)^2$

CAVITY PERFORMANCE & HIGH POWER PROCESSING

The SRF-Gun cryostat has an electrical heater in the helium tank. For regular operating conditions, the liquid He flow into the cryostat is constant. The different consumption due to variations of the acceleration gradient is compensated by adequate changes of the heater power. It is controlled by a level sensor in the He tank. Therefore the change of the heater power between the status RF-off and a given gradient is equal to the RF loss of the cavity. These values were measured as function of the acceleration gradient E_{acc}. The on-axis peak field E_{peak} in the TESLA like cells is related to the acceleration gradient by a factor of 2.7, i.e. $E_{peak} = 2.7 \times E_{acc}$.

In Figure 6 the second measurement on September 19, 2007 and the eighth measurement on August 28th, 2008 are compared. For the second measurement the red curve shows the corresponding radiation level caused by field emission in the cavity. The maximum achievable field is only one third of the designed value (E_{peak}=50MV/m) and the unloaded Q at low field levels is 10 times lower than measured in the vertical test before assembling. Possible reasons are the pollution of the inner surface during clean room preparation or frozen magnetic flux produced by RF cables, screws and other ferrous materials inside the µ-metal shielding. Especially the last assumption was strengthened by a magnetized RF feed through found during the last maintenance. Nevertheless, it is obvious that the drop down of Q_0 is caused by field emission. Fortunately, after one year of operation the use Cu and Cs_2Te cathodes did not changed the cavity performance.

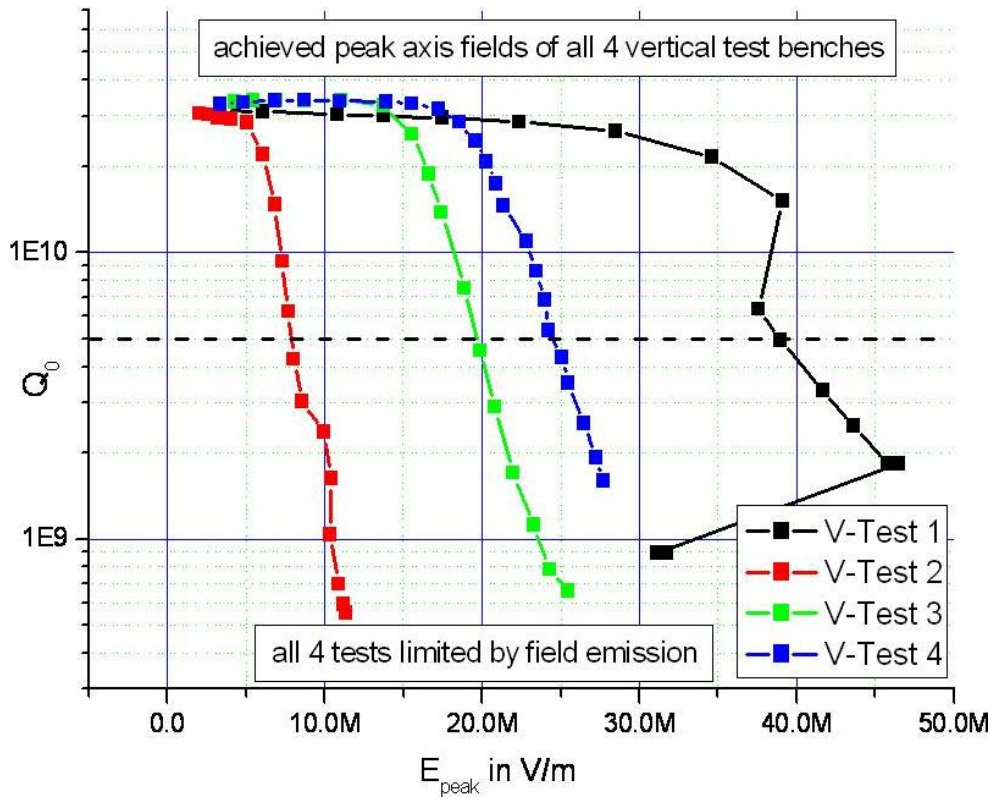

FIGURE 6. Comparison of the cavity performance, unloaded quality factor Q_0 versus peak field E_{peak}, before and after high power RF processing of the cavity in September 2008.

In order to increase the quality factor at a certain RF field level, high power RF processing (HPP) of the SRF-Gun cavity was done at the end of the first measurement period in September 2008. Therefore the RF klystron was pulsed with a low duty cycle (30ms/1000ms) to reduce the dissipated power. Within the short pulses a maximum field of E_{peak} = 25 MV/m was reached. The 9th measurement in Fig. 6 shows, that this results in a stable CW operation up to E_{peak}=17.6 MV/m or E_{acc} = 6.5 MV/m which is a reduction of the dissipated power by a factor of two at the same field level. Above this level the cavity starts to quench. The higher gradient allows maximal particle energy of 3 MeV at the exit of the electron source.

ACKNOWLEDGMENTS

We acknowledge the support of the European Community-Research Infrastructure Activity under the FP6 “Structuring the European Research Area” programme (CARE, contract number RII3-CT-2003-506395) and the support of the German Federal Ministry of Education and Research grant 05 ES4BR1/8.

REFERENCES

1. A. Arnold, et al., “Development of a Superconducting Radio Frequency Photo Electron Injektor”, Nucl. Instr. and Meth. A 577, 440 (2007).
2. J. Teichert, et al., “The Superconducting RF Photoinjector at ELBE – First Operational Experience”, these proceedings.
3. A. Arnold, “Field Reconstruction by Band Pass Frequency Measurement at the Rossendorf SRF-Gun Cavity”, Proc. SRF 2007, Peking, China.
4. A. Büchner, F. Gabriel, H. Langenhagen, “Noise Measurements at the RF System of the ELBE Superconducting Accelerator” EPAC’2002, Paris, June 2002.

The Polarized SRF Gun Experiment

Jőrg Kewisch[a], Ilan Ben-Zvi[a], Triveni Rao[a], Andrew Burrill[a], David Pate[a], Erdong Wang[a], Rob Todd[a], Hans Bluem[b], Doug Holmes[b], Tom Schultheiss[b]

[a]*Brookhaven National Laboratory, Upton, NY 11973*
[b]*Advanced Energy Systems, Medford, NY*

Abstract. An experiment is under way to prove the feasibility of a super-conducting RF gun for the production of polarized electrons. We report on the progress of the experiment and on simulations predicting the possibility of success.

Keywords: Polarization, electron sources, quantum efficiency
PACS: 29.25.Bx, 29.27.Hj

INTRODUCTION

Photo-cathode RF electron guns are superior to DC guns in producing high brightness electron beams, because the electric field on the cathode can be much higher without the technical difficulty of voltages higher than 100 kV. However, all successful existing guns for polarized electrons are DC guns because the environment inside an RF gun is usually hostile to the GaAs cathode material necessary for polarization. Ions created by scattering of electrons on residual gas can be accelerated back into the cathode. The number of back-scattered ions is proportional to the vacuum pressure inside the gun and while the typical vacuum pressure in a DC gun is better than 10^{-11} Torr the vacuum in an RF gun is in the order of 10^{-9} Torr. The cathode can also suffer damage from electrons which are emitted from the cavity walls or the cathode itself and are accelerated during the negative RF phase to impact the cathode with high energy.

Experiments at BINP Novosibirsk in the late 1990s demonstrated the following effects [1, 2]: the quantum efficiency in a pulsed normal-conducting 2.8 GHz RF gun was destroyed in as little as 10 pulses. We are now working to repeat this experiment with modifications that we hope will give a positive result: First, instead of a normal-conductive gun we use a superconductive gun. Since the RF fields will not heat up the cavity walls we avoid out-gassing. In fact, the cold walls will act as a cryogenic pump and we expect the vacuum pressure to be better that 10^{-11} Torr. Secondly, we will use a lower frequency half cell gun (1.3 GHz) which will help to avoid electron multipacting involving the cathode.

THE EXPERIMENT

The experimental setup has two parts. The first is the electron accelerator, where the gun is placed in a 100 liter cryostat. The layout is shown in Fig. 1. The gun points upwards, so that the beam exits the cryostat on the top and is bend by a 90 degree dipole (shown in Fig. 2) into a Faraday cup. A window on top of the dipole is used for the laser. The polarization of the beam is not measured, since we are only interested in the decay of the quantum efficiency. In order to measure the beam current the gun is insulated from the rest of the apparatus with a ceramic break, which is protected from mechanical stress by a G10 sleeve.

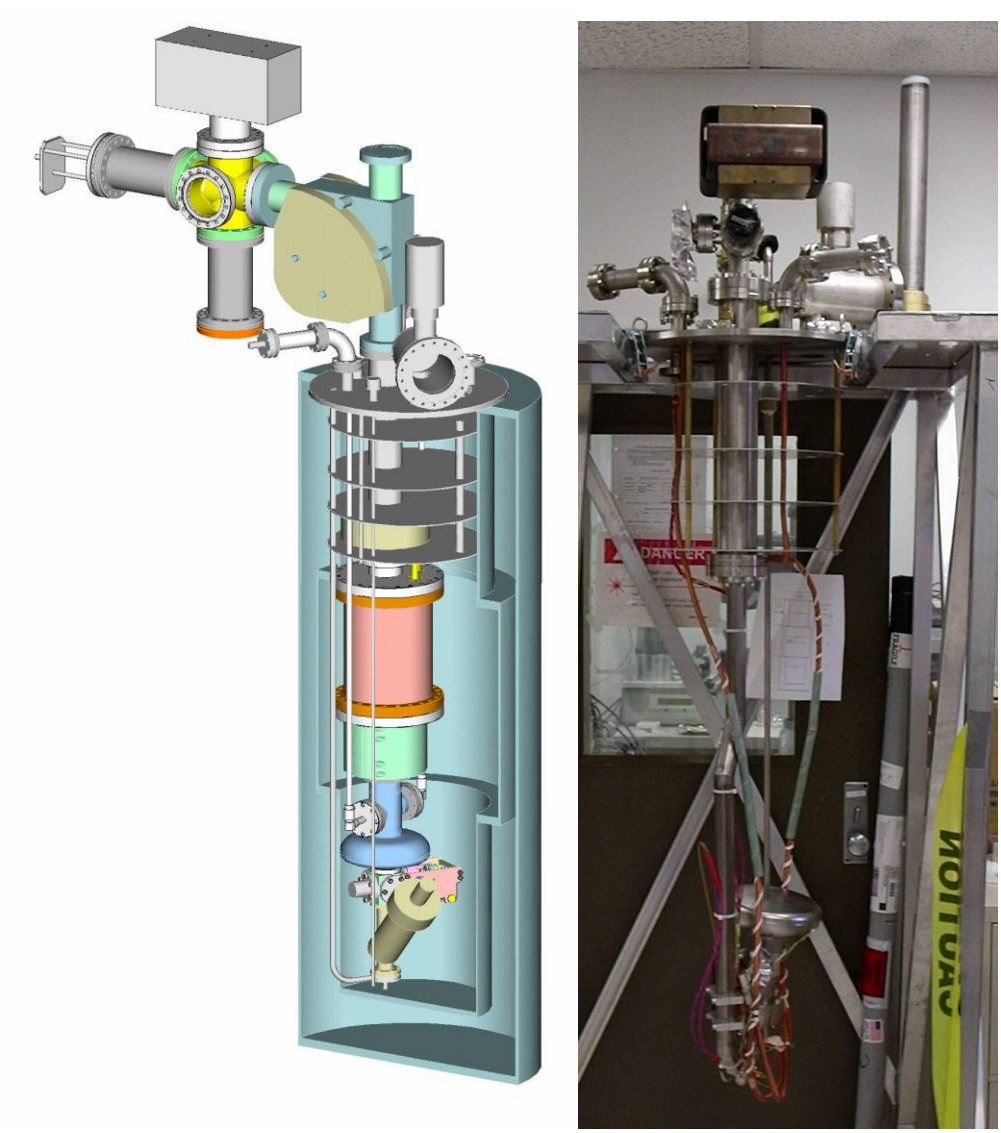

FIGURE 1. Layout of the experiment and gun assembly as used in the first cool-down. The gun is mounted upside-down in this test to prevent particulate from dropping into the gun cavity. The ion pump on to of the assembly was used during the cool-down to measure the vacuum pressure.

A tank filled with NEG pumps close to the gun is maintaining the vacuum when the gun is warm and is not cryo-pumping. Another NEG pump and an ion pump is placed next to the Faraday cup, where the impact of the beam will cause degradation of the vacuum. A set of four aluminum baffles insulates the liquid helium from the top plate and a high temperature superconducting focusing solenoid is placed between the lowest baffles, where a temperature of 17 K was measured

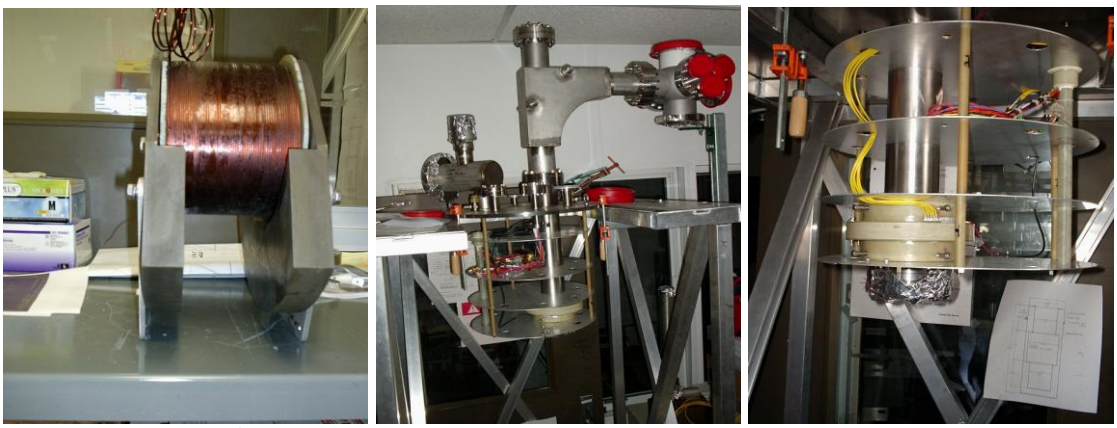

FIGURE 2. The 90° bending dipole and its 3-way vacuum chamber and the high temperature super-conducting focusing solenoid.

The other part is the cathode preparation system, which allows heating the GaAs cathode to 600° C for cleaning and the deposition of a mono-layer of Cesium. In normal-conducting guns the preparation system is integrated into the gun, in our case it must be separate with a transporter which allows transfer of the cathode without breaking the vacuum.

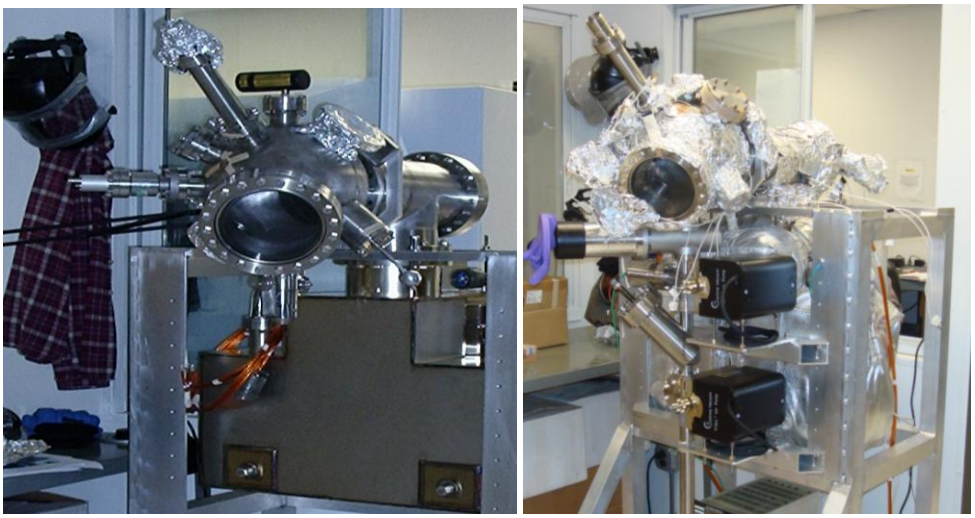

FIGURE 3. The preparation system on the left with attached TSP and on the right wrapped for baking with attached cathode transporter. The two ion pumps are part of the transporter.

FIRST COOL-DOWN

In the first cool-down the Q of the cavity was verified and the thermal properties and vacuum pressure of the system was measured. After the cryostat was filled the ion pump was turned off and the pressure fell by cryo-pumping alone below the range of the pressure gauge. The heat load of the system was approximately 5 Watts.

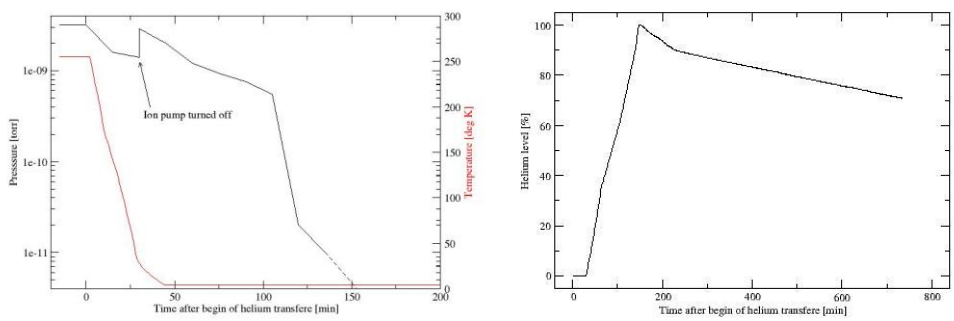

FIGURE 4. The preparation system on the left with attached TSP and on the right wrapped for baking with attached cathode transporter. The two ion pumps are part of the transporter.

ION AND ELECTRON BOMBARDMENT

The above measurement gives us confidence that the vacuum pressure will be comparable or better than found in DC guns. Also, only a fraction of the generated ions will return to the cathode and the impact energy will be significantly lower than in a DC gun [3]. But as suggested by Aleksandrov [2], electron bombardment may be the cause of the short cathode lifetime in the BINP experiment.

Electrons emitted from the cathode at the RF phase between approximately 100 and 180 degrees in the RF phase will not leave the gun cavity, but will be accelerated backwards and impact the cathode, in our case with energies up to 350 MeV.

The effect is twofold: one is the damage to the cathode; the other is to lift thousands of secondary electrons from the valence band into the conduction band. These electrons will drift under the influence of the RF field to the surface and leave the cathode due to the negative affinity.

A tracking program was developed to investigate the possibility of multipacting involving the negative affinity cathode. The program calculates the maximum phase advance from an emission of an electron to the emission of its secondary electrons including the motion inside the GaAs, were the penetration depth of the electric field and the dependence of the drift velocity on the field must be considered.

The results are shown in Fig. 5, where the maximum phase advance of the electron impact and the emission of the last secondary electron are plotted vs. the gradient at the cathode. The condition for multipacting is that the phase advance is 360 degrees. Therefore, if the range overlaps the 360 degree line multipacting must be expected.

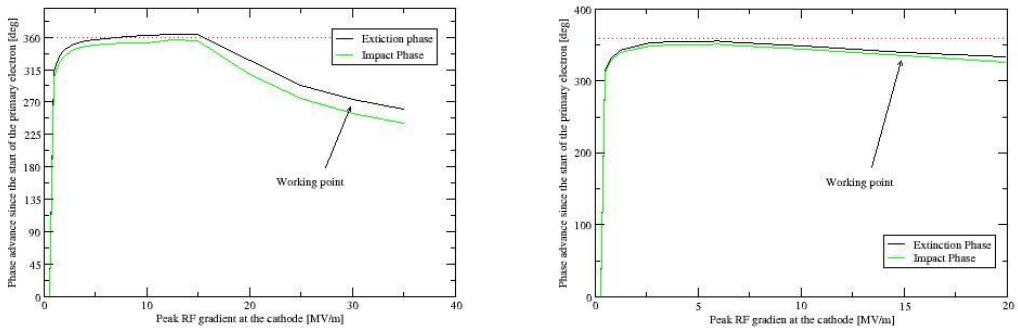

FIGURE 5. Maximum phase advance between the emissions of an electron to the emission of its secondary electrons, on the left for a pill box cavity similar to the BINP gun, on the right for our 1.3GHz gun. Since the exact dimensions of the BINP gun were not available, the gun shape was approximated by a pill box cavity, matching the data given in [1]. The green curve shows the impact, the black curve the last emitted secondary electron.

We see that this is the case for the BINP gun while the in the electric gradient range between 10 and 15 MV/m. This agrees with the observation that dark current was observed above 10 MV/m. In order to improve the vacuum in the gun the RF was pulsed. Therefore the multipacting condition was fulfilled every pulse. The calculations for our experiment show that we escape this disaster, but with little room to spare.

These calculations were done assuming bulk GaAs with p-doping of $10^{18}/cm^3$. The skin depth is in our case 45μ. In strained GaAs, where only a 5 nm thick surface layer is doped, it will be important to make the cathode crystal thin enough to prevent multipacting.

ACKNOWLEDGMENTS

Work performed under contract No. DE-AC02-98CH10886 with the Department of Energy of the United States.

REFERENCES

1. A. V. Aleksandrov et.al.: “A Prototype of RF photogun with GaAs photocathode for injector of VEPP-5”, 1996 European Particle Accelerator Conference.
2 A. V. Aleksandrov et.al.: “Experimental Study of GaAs Photocathode Performance in RF Gun”, 1999 Particle Accelerator Conference
3. E. Pozdeyev: these proceedings.

Non Evaporable Getter (NEG) Pumps: a Route to UHV-XHV

Paolo Manini

SAES Getters SpA, Viale Italia 77, 20010 Lainate (MI), Italy

Abstract. Non Evaporable Getter (NEG) technology has been developed in the 1970's and since then adopted by industry, R&D labs, research centres and in large physics projects like accelerators, synchrotrons and fusion reactors. NEG pumps are very compact and vibration-free devices able to deliver very high pumping with minimal power requirement and electromagnetic interference. In the present paper, main features and performances of getter pumps are reviewed and discussed with a special focus to photocathode gun application, where UHV or XHV conditions are mandatory to ensure adequate gun life. NEG coating and future challenges for NEG technology are also discussed.

Keywords: Non evaporable getter, NEG pumps, photocathode gun, UHV-XHV.
PACS: 07.30.Cy, 81.65.Tx, 81.20.Ev.

NEG PUMP GENERAL FEATURES

NEG pumps are capture pumps which remove, by a chemical reaction, molecules impinging on their surface. They use high surface area reactive alloys, generally made of Zr or Ti. NEG pumping speed and sorption capacity is optimized by selecting getter alloy composition, its geometrical and physical configuration and the operating temperature [1]. NEG pumps, are generally combined with sputter ion [2], turbo-molecular [3] or cryo- pumps [4], to improve the final vacuum, reduce the evacuation time and increase bake-out effectiveness in vacuum systems.

They generally operate in the 10^{-5} $^{-}10^{-11}$ Pa range and present some distinctive features:

- High pumping speed for H_2, the main residual gas in UHV-XHV systems
- Irreversible sorption of all active gases, like O_2, CO, CO_2, H_2O, N_2.
- Constant pumping speed in UHV-XHV regime
- Minimal power requirements.
- Oil and vibration-free.
- Negligible interference with electro-magnetic fields.
- Extremely compact and light, can be mounted inside the vacuum system.

NEG do not pump noble gases and CH_4, a relatively stable molecule difficult to dissociate at room temperature. Pumping of CH_4 is however possible at higher temperatures (250-350°C), while sorption of larger and less stable hydrocarbons and organics, like toluene, decane and methyl-metacrylate, occurs at room temperature [5].

Principles of Operation

To sorb gases, NEG pumps need first to be “activated”. The activation process is carried out under vacuum (or noble gas atmosphere) heating the getter at moderate temperature (350-500°C) for a short time (typically ~ 1 hour). This treatment allows surface oxides and carbides covering the surface to decompose and diffuse inside the getter material bulk structure, leaving a clean and reactive metal surface, ready to chemi-sorb impinging molecules [6, 7].

As the getter surface progressively gets saturated by chemisorbed molecules, pumping efficiency slows down. When the pumping speed drops below a specified value (application dependent), the getter needs to be activated again (“reactivation”). Getters can be re-activated many times providing a long lasting and low total cost of ownership pumping solution.

Range of Configurations

The getter material can be configured in many different ways and geometries [1, 8]. They can be laminated onto a metal strip which can be mounted inside a chamber to provide distributed pumping.

The strip can also be folded into concertina-like or wafer panel (WP) modules having higher trapping efficiency for gases [9]. This allows achieving very large speed in compact volumes. Getter powder can also be sintered as high porosity bodies like disks or fins. These are arranged into high efficiency cartridges which are then assembled in a range of NEG pumps [2-4, 8]. Depending on the pump model and the flange size, speeds from 20 to 2000 l/s (H_2) are available. Larger, custom made pumps have been also realized with speed exceeding 10,000 l/s for H_2 [10].

In most of these configurations, the getter material is activated by radiation (e.g. emitted by a heating element integrated in the cartridge) or, as in the case of the WP, by direct passage of current across the strip. Passive activation during the chamber bake-out is also a possibility.

Another possible configuration is obtained depositing ~50-100 micron getter powder onto a thin metal sheet which undergoes a vacuum sintering process [11]. The outcome is a well adhered getter layer onto a flexible support which can be also pre-cut or folded to fit specific shapes (HPTF or High Porosity Thick Film).

Sputter deposited thin getter films (~ 1micron thick) have been also proposed. They find applications in MEMS [12] and other micro-devices as well as in the vacuum pipes of accelerators and synchrotrons [13].

In particular, CERN has investigated a range getter alloys [14] (composition centered around $Ti_{40}V_{30}Zr_{30}$) activatable at low temperature (<200°C), compatible with most of the accelerator bake-out procedures. The getter film is here directly sputtered onto the internal surface of the accelerator beam pipe [13]. After activation, it displays large in-situ pumping which is particularly beneficial for long and narrow gap pipes, like insertion devices, which can be hardly otherwise pumped due to conductance issues**.** In the past 5 years, NEG coating has been successfully adopted by an increasing number of accelerators, boosting their vacuum performances [15-17].

Examples of Applications

NEG pumps cover a broad range of applications, encompassing surface science, vacuum equipments for material preparation and characterization, semiconductor processing, inspection and review tools or metrological equipments. Being very compact and with minimal power requirements they are ideal in portable and miniaturized equipments (like hand-held mass spectrometers, radioactivity counters or UHV suitcases). The absence of electromagnetic interference allows to mount NEG pumps very close to ion/electron sources, like in the case of scanning and transmission electron microscopes and lithographic equipments, where vacuum is most critical.

NEGs are also used in the main rings and beam lines of colliders and synchrotron machines as well as in a number of other experimental facilities [8].

Application to Photoelectron Guns

Photoelecron guns are one of the most demanding applications, vacuum wise. Most of the photo-cathodes require very good vacuum conditions to deliver stable currents for a long time. Gases present in the gun chamber can poison the cathode surface or damage it by ion back bombardment, both effects reducing the cathode useful life.

To avoid cathode deterioration, pressures in the range of 10^{-8} -10^{-10} Pa are required. This poses serious challenges in term of gun chamber design, material selection and processing as well as the choice of the pumping group. The use of arrays of NEG pumps mounted inside the gun chamber is one of the preferred choices to achieve very low pressure [18-21]. A typical configuration is based on the use of WP modules which, thanks to their design, can be mounted side by side inside the gun to cover a large area and provide extremely large pumping speed for H_2, the main residual gas. An example is showed in Fig.1, where pumping speed exceeding 20,000 l/s has been reported [18].

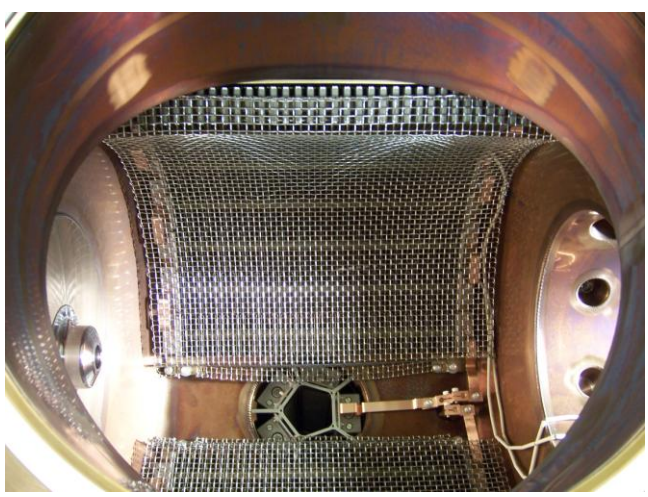

FIGURE 1. An array of WP 1650-St 707 modules is placed inside the photocathode gun chamber , A few modules are also placed inside the ion pump pumping port (Courtesy of Cornell University).

The use of cartridge pumps mounted in the cathode chamber as well as in the preparation and load-locked chambers [21, 22] is also quite popular (Fig.2).

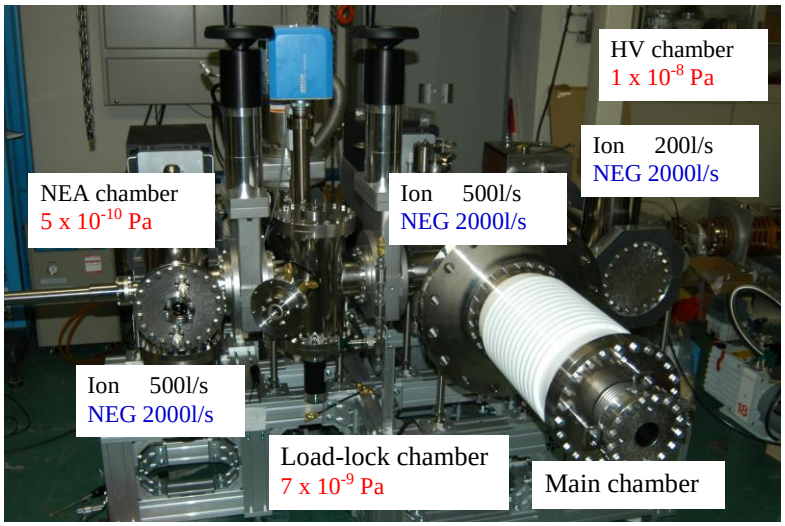

FIGURE 2. NEG cartridge pumps (Capacitorr D 2000 model) mounted in the NEA, preparation and main chambers of the DC gun developed for the ERL project at JAEA (Courtesy of JAEA).

NEG coating has also been proposed to reduce H_2 out-gassing and improve the vacuum [19, 23]. To deposit films with large pumping speed, careful control and optimization of the sputter deposition parameters is key. This is not always easy in chambers with irregular geometries but has definitively an impact on the quality and reproducibility of the deposited getter film [24]. If this aspect is not taken into account, lower than expected speed and modest vacuum improvement may be obtained [23].

LIMITATIONS AND ULTIMATE PERFORMANCES OF NEGS

The use of NEG pumps, coupled with a small sputter or turbo pump for inert gases, is one of the best routes to achieve XHV. The ability of NEG to reach ~$3x10^{-12}$ Pa was measured at CERN [25] in a series of experiments where the NEG was the main pump, backed by small sputter ion pumps for the pumping of noble gases and CH_4.

The two main mechanisms which can intrinsically limit NEG pumps in achieving extremely low pressures are the generation of methane and the H_2 emission due to the equilibrium always existing between H_2 in the gaseous phase and hydrogen atoms in solid solution in the getter lattice.

CH_4 can be released from a getter surface due to the reaction of surface carbon atoms and hydrogen present in the getter volume or coming from the vacuum system. However, due to the difficulty of the measurement (CH_4 can be in fact generated also by hot filaments and gauges and emitted by other sources), the identification of a clear and unambiguous mechanism for CH_4 generation is still controversial.

At low H_2 concentration and moderate temperature, NEG alloys used in pump applications, follow Sievert's law [1]. This has been confirmed also in the case of Ti-V-Zr based NEG coatings in the 100-250°C range and down to 10^{-9} Pa [26]. However, no data are available in XHV regime, due to the complexity of measuring equilibrium

isotherms in a controlled and reproducible way below 10^{-10} Pa. For St 707 ($Zr_{57}V_{36}Fe_7$), Sievert's law extrapolated at 25°C and 100 l x Pa(H_2)/g(alloy) gives an equilibrium value of ~2 x10^{-14} Pa. This might be considered as an indication of the pressure limit for this alloy. Other getter alloys have been developed which have lower equilibrium pressure than St 707, so in principle, lower pressure could be even reached using different getters. Specific investigation is ongoing at SAES Getters on this point.

These considerations suggest that NEG pumps can be definitively effective also in new, more demanding, electron sources at present under study or being built. From this point of view it must be stressed however, that achieving extreme performances in such sophisticated guns is possible only when the integration of the NEG pumps in the vacuum system is optimized and carefully designed to avoid interferences between sub-systems. Being a reactive surface, the NEG can in fact release and/or adsorb gases during the various different phases of evacuation, conditioning and baking procedures. This has to be taken in due account to avoid, for example, that gases released by the getter during the activation, contaminate the system or partially load the other installed pumps or, vice-versa, that a fully active getter surface is saturated during bake-outs or degassing procedures, thus preventing the achievement of the best performances.

REFERENCES

1. B. Ferrario "Getters and Getter Pumps" in *Foundation of Vacuum Science and Technology*, edited by J.M.Lafferty, John Wiley & Sons, 1998, pp. 261-315.
2. R. Caloi et al, *Proceedings 14th Italian Vacuum Association Conference*, Vicenza, Italy, 5-7 May, 1998 (Ed. Compositori, Bologna, Italy)
3. R. Giannantonio et al., *Vacuum*, **55**, 1999, pp 27-37
4. R. Giannantonio et al. , *J. Vac.Sci. Technol*., A **15**(1), Jan/Feb. 1997, pp 187-191
5. A. Conte, *Proceedings 55th AVS Conference*, Boston, 2008
6. K. Ichimura et al, , *J. Vac.Sci. Technol*., A **5**(2), 1987, pp 220.
7. M. Sancrotti et al, *J. Vac.Sci. Technol*., A **9**(2), Mar/Apr 1991, pp 182-189
8. F. Mazza , *Non Evaporable Getters for UHV application*, SAES literature , 2002
9. B. Ferrario and L. Rosai, *Proceedings 7th Int.Vac. Conference*, Wien (Austria), 1977, pp. 359-362
10. R. Giannantonio et al., *J. Vac.Sci. Technol*., A **17**(4), Jul/Aug 1999, pp 2093-2098
11. E. Giorgi, *Journal of Vac. Sci. & Technol.* A **7** (2), Mar/Apr. 1989, pp. 218-222
12. M. Moraja et al. *Proceeding of SPIE Photonic West 2004*, 2003, Vol.4980.
13. A. Conte et al *Proceedings Particle Accelerator Conference*, 2007, Albuquerque, USA.
14. C. Benvenuti et at., Vacuum, **53** , 1999, pp 219-225
15. P. Chiggiato, 41st IUVSTA workshop, Brdo ori Kranju, Slovenia, June 2004
16. C. Herbeaux et al., *Proceedings European Particle Accelerator Conference*, 2008, Genova, Italy
17. H. Huang et al. *Proceedings European Particle Accelerator Conference*, 2006, Edinburgh, UK
18. B.M. Dunham et al *Proceedings Particle Accelerator Conference*, 2007, Albuquerque, USA
19. C. K. Sinclair, *Physical Review Special Topics- Accelerators and Beams*, **10**, 2007, 023501
20. S. Pastuszka et al. *Journal of Applied Physics*, **88**(11), December 2000
21. M. Yamamoto et al, *Proceedings LINAC 2004*, 2004, Lubeck Germany
22. N. Nishimori et al, *Proceeding ERL07*, 2007, Daresbury Laboratory, UK
23. M.Poelker et al. *Proceedings Particle Accelerator Conference*, 2007, Albuquerque, USA
24. A. Bonucci et al *Proceedings Particle Accelerator Conference*, 2007, Albuquerque, USA
25. C. Benvenuti, *Proceedings Particle Accelerator Conference*, 2001, Chicago, USA, pp 602-606
26. A. Rossi, *Proceedings European Particle Accelerator Conference*, 2006, Edinburgh, UK

Sensitive Ion Pump Current Monitoring Using an In-House Built Ion Pump Power Supply

J. Hansknecht, P. Adderley, M. L. Stutzman and M. Poelker

Thomas Jefferson national Accelerator Facility
12000 Jefferson Ave., Newport News, VA 23606

Abstract. Ion pumps are common vacuum pumps on DC high voltage photoguns and baked-accelerator beamlines. Commercial ion pump power supplies provide a measure of the electrical current drawn by the pump, but typically have resolution to only ~ 0.1uA, which corresponds to pressure ~ 10^{-9} Torr, a value considerably higher than the minimum pressure required by photoguns and nearby beamline. This submission describes a very sensitive in-house-built ion pump power supply with current monitoring capability good to less than 1nA, and corresponding pressure in the low-10^{-11} Torr range. Besides providing "free" pressure monitoring on a scale equivalent to the best available commercial pressure gauges, the ion pump power supply also serves as a sensitive diagnostic for detecting field emission from the photogun cathode electrode and bad electron beam orbits that could diminish photogun operating lifetime. Since its inception, this ion pump power supply has become an invaluable tool for operating the CEBAF polarized electron source. It is also a very useful low-cost diagnostic for ultrahigh vacuum studies in the laboratory.

Keywords: Ion pump; Polarized electron source
PACS: 29.25.Bx; 29.27.Hj; 07.30.Cy; 07.30.Dz

INTRODUCTION

Ion pumps have been used for decades at particle accelerators [1] and are common components on DC high voltage polarized electron sources [2], where they serve to pump gas species not effectively pumped by non-evaporable getter (NEG) pumps, for example, argon and methane. At the heart of the ion pump is the Penning cell [3], which is used to ionize and capture residual gas. There are different types of ion pumps, composed of different electrode materials, with different shapes and electrical configurations. The "diode" ion pump is widely used and well suited for UHV systems. The term "diode" describes a Penning cell composed of a positively biased tubular anode situated between grounded cathode plates, immersed in a magnetic field created by permanent magnets affixed to the outside of the ion pump vacuum chamber. Energetic free electrons provided by the cathode travel in long helical trajectories, trapped by the applied magnetic field, striking and ionizing residual gas along the way. Ions generated by these collisions are only weakly affected by the magnetic field (because of their relative mass compared to electrons). They are repelled by the biased anode and accelerated toward the cathode end plates. Gas is removed from the vacuum chamber when these ions are embedded within the cathode end plates. If the cathode end plates are made of titanium, there is the added benefit of

chemical gettering that results when titanium is sputtered away, which boosts pump speed, especially for hydrogen gas.

It has long been known that the electrical current associated with the ion-pump process is an indication of the vacuum level, or pressure inside the chamber. This is illustrated in Fig. 1, which shows ion pump current measured using a sensitive in-house built ion pump power supply [4], as a function of pressure inside one of the polarized electron sources at CEBAF/Jefferson Lab. Pressure was measured using a Leybold extractor gauge [5] while gradually venting the chamber to atmospheric pressure with hydrogen gas, prior to photocathode replacement. The pressure values in Fig. 1 are "raw", i.e., uncorrected for gas species. Ion pump current increases with pressure, following a typical and expected power rule relationship to produce a straight line on the log/log plot. The slope of the line depends on specific features of the Penning cell(s) used inside the pump, like anode geometry, anode bias voltage, and magnetic field. The remarkable feature of Fig. 1 is that data extend to less than 1 nA, while commercial ion pump power supplies are limited to ~ 0.1uA, more than a factor of 100 larger. This submission describes the inexpensive in-house built ion pump power supply with sub-nA current monitoring capability that provides accurate and "free" pressure monitoring into the low-10^{-11} Torr vacuum range. Besides providing a measure of static vacuum inside UHV systems, the device has become a useful diagnostic for photogun set-up, characterization and troubleshooting. Some examples are presented below.

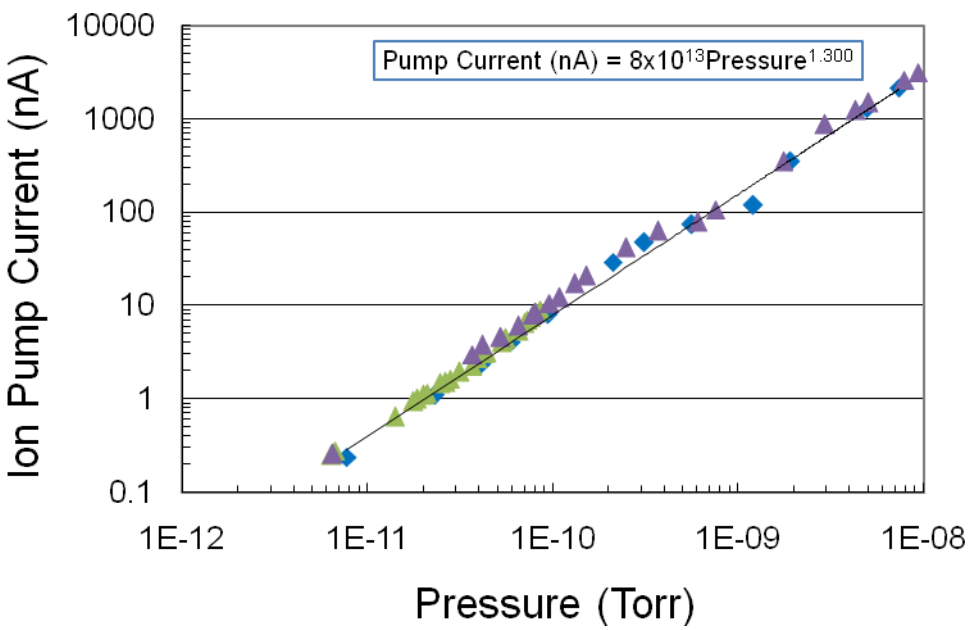

FIGURE 1. Ion pump current v. pressure inside a CEBAF/Jefferson Lab DC high voltage GaAs photogun. The data were obtained while venting the photogun to atmospheric pressure with hydrogen gas prior to photocathode replacement. The three data sets correspond to three different photocathode installations. The expected functional form $I_p=kP^x$ provides a good fit to the data.

ELECTRICAL DESIGN

At the heart of the ion-pump power supply is a high voltage transformer with "floating" secondary winding circuit attached to a pico-ammeter (Fig. 2). Good electrical isolation between the two windings ensures that any current flowing through the ion pump also flows through the pico-ammeter, and this current is not "contaminated" by uninteresting current from other parts of the circuit. The design relies on a high frequency transformer (~ 400kHz) that provides a number of benefits, including; 1) it shrinks the size and weight of the power supply while increasing electrical efficiency, 2) higher frequencies are easier to rectify and filter and, 3) it permits the use of a Cockcroft-Walton multiplier to raise voltage to the ultimate desired level. Since the transformer runs at lower voltage, the potential for leakage to ground is greatly reduced. Pump current as low as ~ 100pA can be accurately measured while the total cost for all components is modest, < $500. The only disadvantage of this design compared to commercial power supplies is that pump current must be < 0.5mA, which limits operation of the ion pump to 10^{-7} Torr.

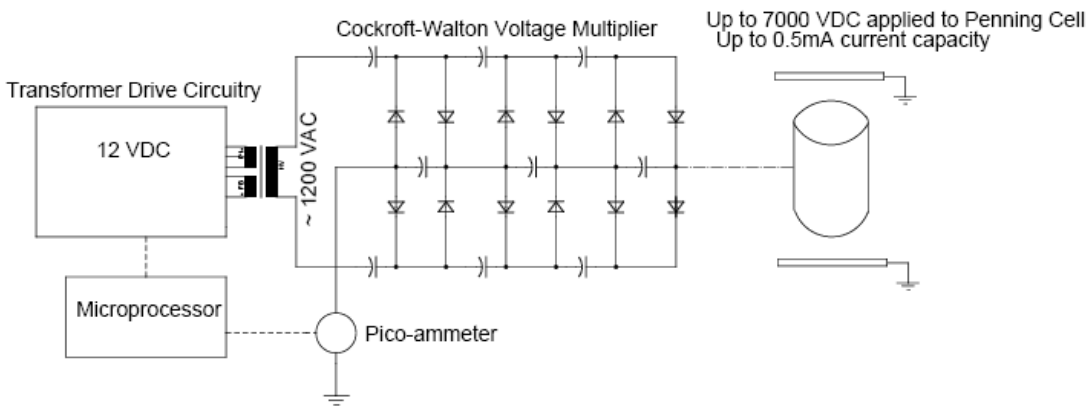

FIGURE 2: Schematic of ion pump power supply with sensitive current monitoring capability.

APPLICATIONS

Field emission from the cathode electrode inside a DC high voltage GaAs photogun is problematic. Large amounts of field emission lead to dramatic reduction of photocathode quantum efficiency, and can be easily identified. Small amounts of field emission however, also spell trouble for the photogun, contributing to shorter than expected operating lifetime, but can be more difficult to diagnose. The ion pump power supply with sensitive current monitoring capability has proven to be a very useful tool for detecting small amounts of field emission inside CEBAF/Jefferson Lab GaAs polarized photoguns. Figure 3 shows ion pump current versus applied photogun bias voltage, indicating vacuum degradation (due to electron stimulated desorption of gas associated with field emission striking the photogun anode electrode and/or vacuum chamber wall) when bias voltage exceeds 100kV. From Fig. 3, it would appear field emission is an obvious problem, however it must be pointed out pressure

inside the photogun remains very good, with ion pump current < 1nA, even at bias voltages that produce field emission. This information cannot be obtained using a commercial ion pump power supply because small changes in ion pump current (tens to hundreds of pA) cannot be resolved. And it would be difficult to obtain similar data using a conventional vacuum gauge, since hot filament gauges produce light that generate electron beam from the activated GaAs photocathode, thereby degrading vacuum in a similar (or worse) manner, masking the problem associated with field emission.

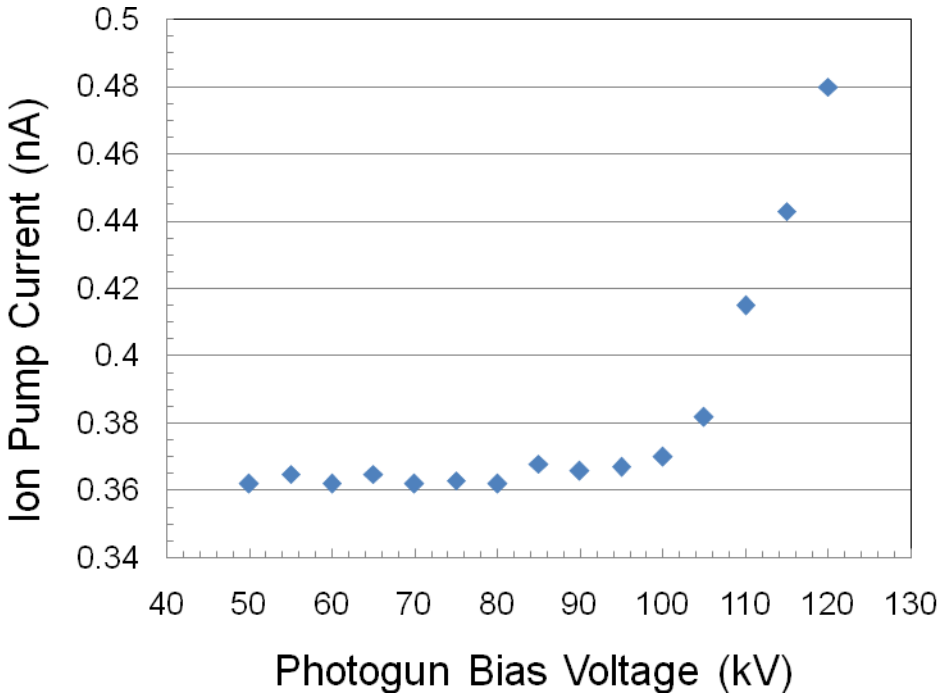

FIGURE 3. Ion pump current versus applied photogun bias voltage. Low-level field emission degrades vacuum inside the photogun for bias voltage > 100kV that can be easily detected using the ion pump power supply with sensitive current monitoring capability.

Another example illustrating the utility of sensitive ion pump current monitoring can be seen in Fig. 4, which shows a time-dependent "chart-recorder" trace of ion pump current for five ion pumps downstream of the CEBAF/Jefferson Lab GaAs polarized photoguns. These data were obtained while inadvertently operating one of the photoguns with a bad beam orbit – a very small portion of the electron beam was striking a retracted phosphorescent view screen. Electrons would accumulate on the view screen, causing an electrostatic deflection of the electron beam. Charge on the view screen would build and eventually arc to ground, thereby restoring the normal beam orbit. This "back and forth" beam motion was disrupting the physics program at one the CEBAF endstations. Pinpointing the origin of the problem was difficult using conventional beam position monitors but easily tracked to a specific location by analyzing the relative intensity of the vacuum bursts associated with each event. All of the beamline ion pumps near the CEBAF photoguns operate with less than 70nA current – these vacuum bursts would not have been visible using commercial ion

pump power supplies. Accelerator operators now monitor ion pump current to prevent these types of beam orbit problems.

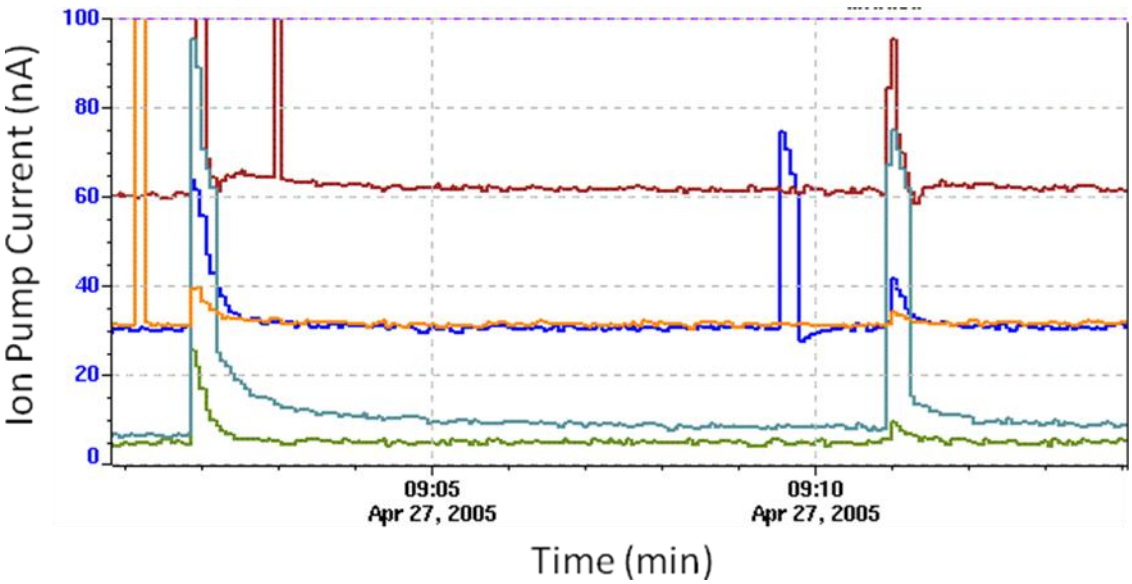

FIGURE 4. Ion pump current versus time, for five ion pumps attached to a baked beamline near the GaAs photoguns at CEBAF/Jefferson Lab. Vacuum "bursts" correspond to charging-discharging of a retracted phosphorescent view screen, due to a bad beam orbit.

CONCLUSION

An ion pump power supply with extremely sensitive current monitoring capability has been constructed that exploits the relationship between pump current and pressure to provide "free" pressure monitoring of the CEBAF/Jefferson Lab DC high voltage GaAs photoguns and injector beamline, at a level equivalent to the best available commercial vacuum gauges. The device has also proven useful for characterizing and troubleshooting photogun performance.

ACKNOWLEDGEMENTS

Authored by Jefferson Science Associates, LLC under U.S. DOE Contract No. DE-AC05-06OR23177.

REFERENCES

1. K. Welch Capture Pumping Technology (Elsevier, Amsterdam, 2001), p33
2. C. K. Sinclair, P. A. Adderley, B. M. Dunham, J. C. Hansknecht, P. Hartmann, M. Poelker, J. S. Price, P. M. Rutt, W. J. Schneider, and M. Steigerwald, Phys. Rev. ST Accel. Beams 10, 023501 (2007).
3. F.M. Penning, Philips Technical Review, 2 (1937) 201.
4. Ultra-high vacuum ion pump power supply with pump current resolution < 1 nA. Model EOS-902, from Eye On Science LLC, 527 Lakeshead Dr., Williamsburg, Va 23185.
5. Leybold extractor gauge, model IE 514 with IONIVAC IM 520 controller.

High Brightness and High Polarization Electron Source for Spin-LEEM

T. Nakanishi[1], N. Yamamoto[1], A. Mano[1], Y. Nakagawa[1], T. Konomi[1], M. Yamamoto[1], S. Okumi[1], X. Jin[2], T. Ujihara[2], Y. Takeda[2], T. Ohshima[3], T. Kohashi[3], T. Yasue[4], T. Koshikawa[4], T. Saka[5], and T. Kato[6]

[1]*Graduate School of Science, Nagoya University, Nagoya 464-8602, Japan*
[2] *Graduate School of Engineering, Nagoya University, Nagoya 464-8601, Japan*
[3] *Central Research Laboratory, Hitachi Ltd. Tokyo, 185-8601, Japan*
[4]*Fundamental Electronics Research Center, Osaka Electro-Communication University, Osaka 572-8530, Japan*
5Daido Institute of Technology, Nagoya 457-8531, Japan
[6]*Daido Steel Co. Ltd., Nagoya 457-8531, Japan*

Abstract. A point-like emission mechanism is required for a GaAs polarized electron source to produce an electron beam with high brightness. This is realized by changing the direction of injection laser from a front-side to a back-side of the photocathode. Based on this concept, a 20keV gun (JPES-1) was constructed and a transmission photocathode including an active layer of a GaAs-GaAsP superlattice was installed. It produced a laser spot diameter as small as 1.3μm for the 760~810nm laser wavelength, and the brightness of ~2×10^7A·cm^{-2}·sr^{-1} corresponding to a reduced brightness of ~1.0×10^7 A·cm^{-2}· sr^{-1}·V^{-1} was obtained for an extracted current of 5.3μA. This brightness is still smaller than those of W-field-emitters, but one order of magnitude higher than those of LaB_6 emitters. The peak polarization of ~90% was achieved at the same time by the photocathode which has an inserted GaAs thin layer between the GaAsP substrate and the GaAaP buffer layer. It demonstrated that the strain-control of the GaAsP buffer layer is indispensable to achieve the highest polarization. The charge density lifetime of 1.8×10^8 C/cm^2 was observed for an extracted current of ~3μA. The second gun system (JPES-2) was already constructed and mounted to a LEEM apparatus operated at OECU..

Keywords: Polarized electrons, LEEM, SPLEEM, transmission photocathode
PACS: 29.25.Bx, 79.60.-i

MOTIVATION

Low Energy Electron Microscopy (LEEM) is a powerful tool to observe the structure and morphology of ultra-thin metal film grown on the metal substrate [1]. Using polarized electron beam for LEEM (SPLEEM) the magnetic domain structure can be observed, since the magnetic sensitivity is based on the spin-dependent exchange scattering between beam and specimen. Images of the spin-up and spin-down asymmetry can pick up the exclusive features that purely originate in the magnetism of the sample [2].

In order to enable a real time observation of the film growth, one image should be taken within 0.1 seconds and it has been realized already by LEEM with the LaB_6

emitter but it takes more than 10 seconds by the available SPLEEM, as shown in Table 1. The motivation of this work is to overcome such a dilemma by improving the brightness of the PES by two order magnitude or more.

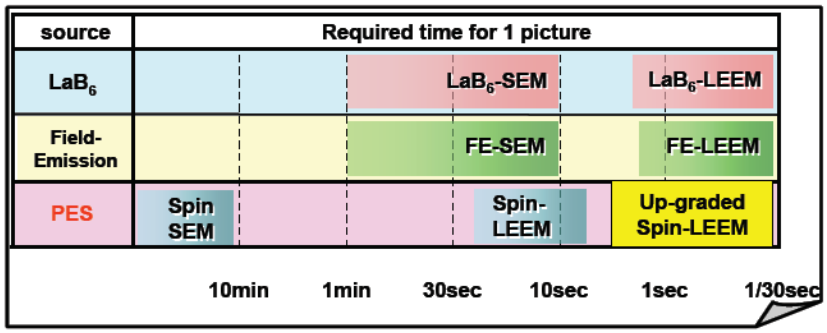

TABLE 1. Required time for taking one picture by various microscopes.

KEY TECHNOLOGY

In order to minimize the beam spot, a new geometry is proposed as shown in Figure1, where the laser lights transmit through the photocathode and the excited electrons are emitted in the forward direction. Using this transmission type photocathode, the distance between a focus lens and the photocathode can be shortened to a few mm and the laser spot size less than 10μm will be easily obtained.

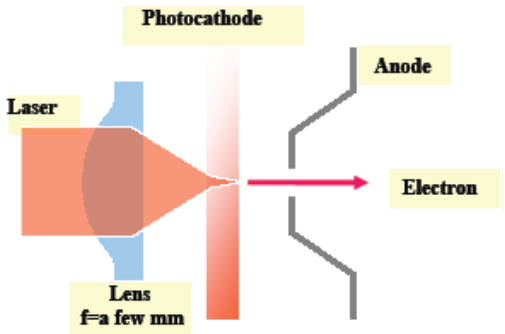

FIGURE 1. Conceptual view of transmission type photocathode to minimize electron source size.

EXPERIMENTAL EQUIPMENT

Laser optical system

The design of our laser optical system is based on that developed by one of the authors (T.O.) for a 1keV-SEM source with high brightness and mono-chromaticity [3]. The components of our laser system and the measured laser spot profile are shown in Figure2 [5]. The input laser light is guided to the gun by a single mode optical fiber. Its output light is collimated and converted to circularly polarized light by combination of a polarizing beam splitter and a quarter wave-plate, and finally focused on the active layers of the photocathode by the focusing lens (f=4.2mm, NA=0.5). The

focusing lens is mounted on a translation XYZ stage to optimize the laser illumination conditions.

The laser focusing spot size was monitored by using reflected laser light from the surface of photocathode. The 180° reflected light is separated by a polarizing beam splitter and focused on a CCD by an imaging lens (f=100.0mm). Combining an image magnification factor of 23.8 on the CCD and 1pixel size of 4.65μm, the resolution of this CCD monitor is expected to be 0.20μm/pixel, and the obtained laser spot size was 1.3~1.4μm (FWHM) for 780nm laser wavelength.

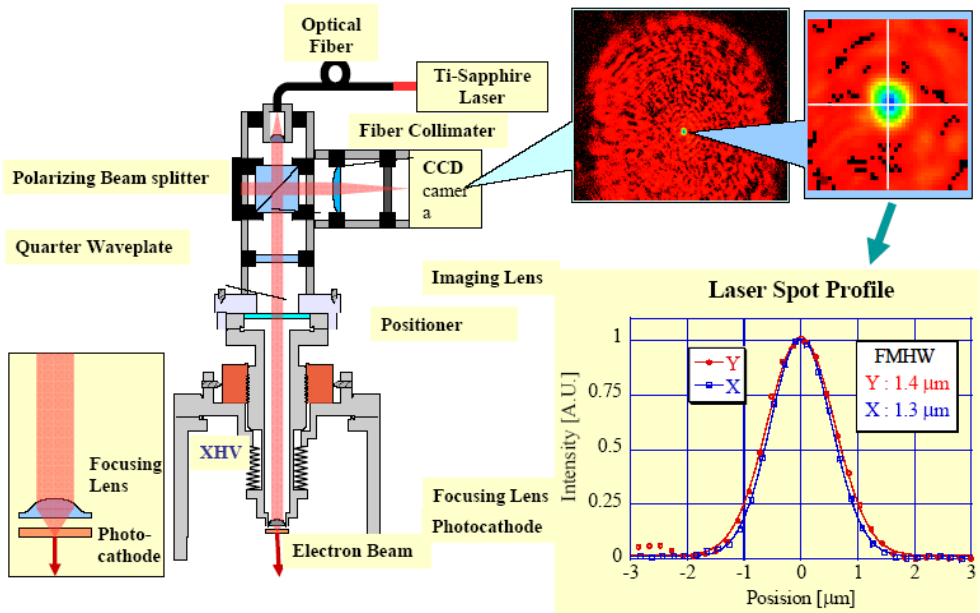

FIGURE 2. Components of laser optics equipment and the laser spot profiles on the photocathode

20keV gun

A schematic illustration of our PES system (named JPES-1) is shown in Figure3 [5]. The JPES-1 consists of four vacuum chambers including the activation chamber, the gun chamber, and other chambers for measurements of beam brightness and spin polarization. The activation chamber has the vacuum level of ~10^{-9}Pa, and the gun chamber maintains the ultrahigh vacuum environment of an order of 10^{-10}Pa near the photocathode surface.

The heat cleaning and NEA activation are done in the activation chamber and the photocathode pack is installed in the electrode using load lock mechanism. The beam brightness is measured at the downstream of the gun. The beam is deflected by 90° angle using a spherical condenser to change the polarization vector from longitudinal to transverse, and the beam polarization is measured by a 100kV Mott chamber analyzer.

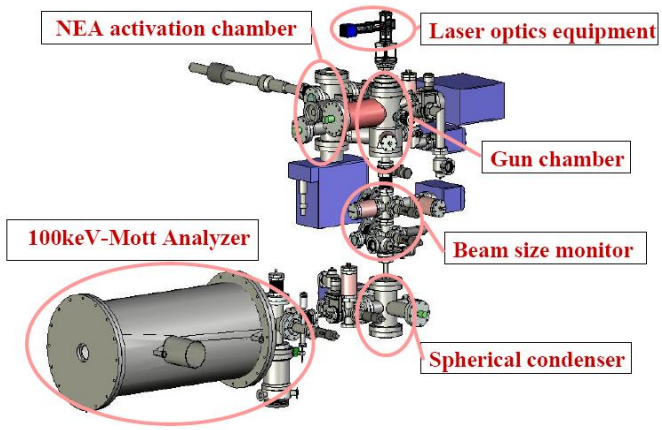

FIGURE 3. Transmission-type polarized electron source for high brightness performance

As the beam energy of the LEEM operated at OEC Univ. is 20keV, the same beam energy is employed for the gun. A gap distance of electrode is set to be 4mm, and the electric field gradient to be 5MV/m. In order to minimize the dark current, Mo and Ti are used for the cathode and the anode materials, respectively [4]. The electrode surface was finished by the electro-buff-compound polishing, and the dark current was well suppressed below 6nA level at 25kV bias voltage.

Transmission photocathode and spin polarization

The GaAs/GaAsP strained superlattice layer is used to produce the highly polarized electrons (≥85% @780nm) [5, 8]. As a substrate material GaP is chosen, since it is transparent for 780nm laser light due to the wide band-gap corresponding to 550nm.

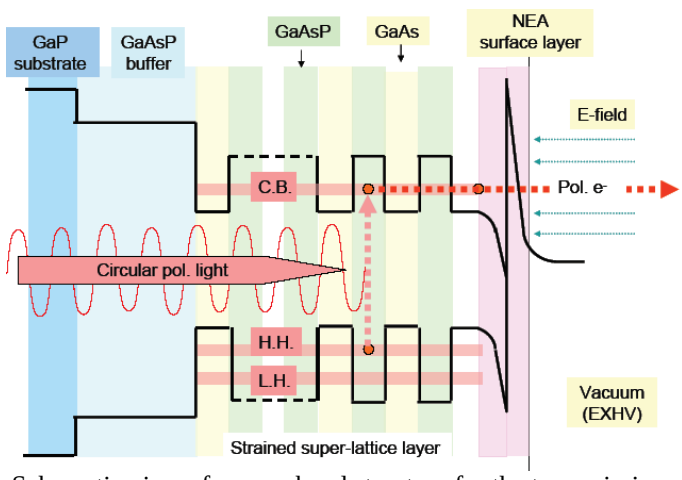

FIGURE 4. Schematic view of energy band structure for the transmission photocathode

We fabricated two types of photocathode to achieve 90% polarization, as shown in Figure5. Maximum polarization was limited to below ~60% using the first photocathode. Polarization improved to ~90% by using a thin GaAs interlayer between the GaP substrate and the GaAsP buffer layer [6, 7]. It is the same magnitude

of electron polarization obtained by the conventional photocathode with the same superlattice structure but grown on the GaAs substrate [8].

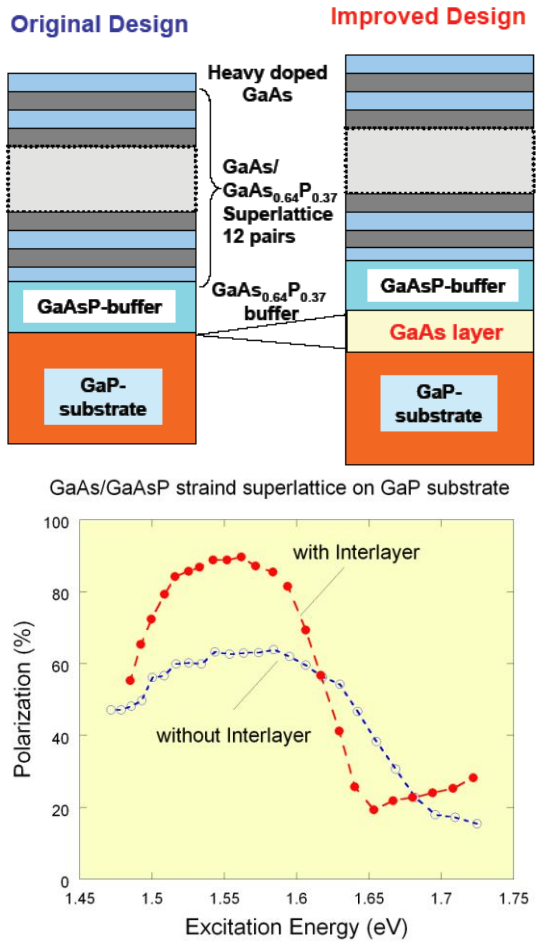

FIGURE 5. Two designs for photocathodes and the corresponding polarization spectra

The large difference between the maximum polarizations clearly shows the importance of strain control in the buffer layer. With the various studies on strain property of our crystals it was concluded that the spin-polarization of electrons produced from the photocathode was strongly related to the types of defects induced in the buffer layer. The tensile strain in the buffer layer was relieved by cracks, while the compressive strain was relieved by dislocations, and those cracks and dislocations propagated into the active superlattice layer. From our data, it was demonstrated that the cracks parallel to the polarized electron escape direction slightly influenced to the polarization, while the dislocations intersecting with escape direction caused the sizable spin-flip depolarization [7]. The quantum efficiency for the 90% polarization photocathode was ~0.1% at 790nm laser wavelength.

Brightness measurements

The procedure of brightness measurement is shown in Figure 6 [5]. The beam profile was measured using a pair of knife-edge slits located 53.1cm downstream from the photocathode, and the beam radius (FWHM) was determined by Gaussian fit of this profile. The reduced brightness can be derived using parameters of this beam radius, the estimated electron source radius and the emission current by using the formula in Figure 6, where the obtained value is also shown.

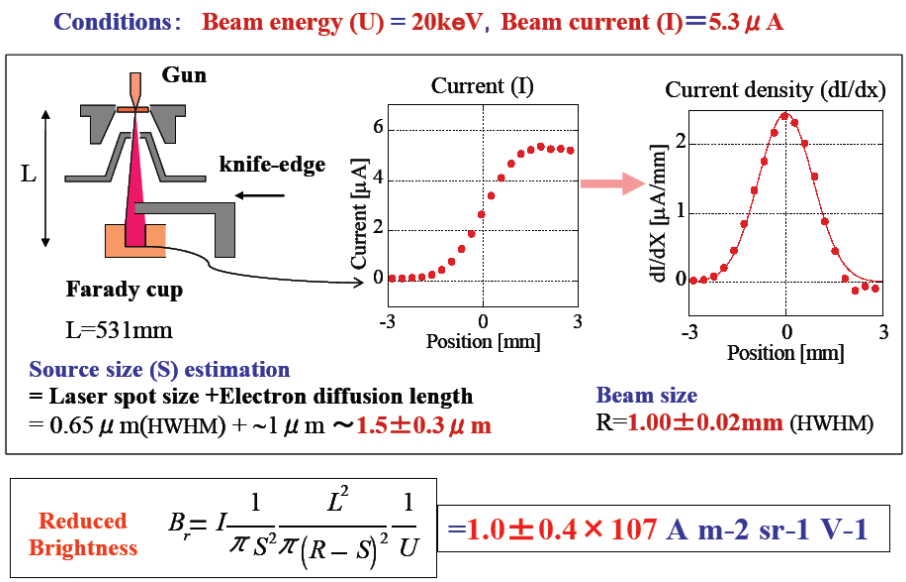

FIGURE 6. Procedure of beam brightness measurement and the obtained brightness results

The dependence of reduced brightness on the extracted voltage was measured and the result is shown in Figure 7 (left), where the saturation behavior is obviously observed above 10kV bias voltage. The current dependence of the reduced brightness was also studied at 20kV with the beam source radius kept at 0.95~1.00mm and the result is also shown in Figure 7 (right), where the reduced brightness increases linearly up to the maximum current of 5.3μA. For this current, the angular current density and the current density were estimated to be 250mA/sr, ~5.1A/mm^2 respectively, and the reduced brightness to be (1.0±0.4)×10^{7}A/m^2/sr/V. This brightness is three orders of magnitude higher than that of the available polarized electron source. Moreover, it still smaller than those of the W-field-emitters, but one order of magnitude higher than those of LaB_6 emitters. The charge density lifetime of 1.8×10^8 C/cm^2 was observed for an extracted current of ~3μA [5].

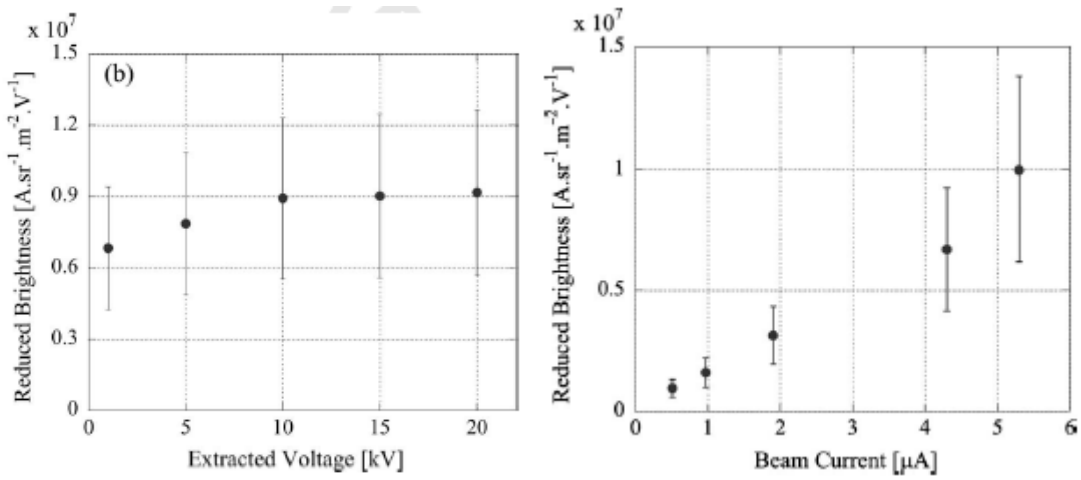

FIGURE 7. Reduced brightness dependence on the extracted voltage and beam current

By the work with JPES-1, we could demonstrate that the polarized electron source with transmission photocathode is highly effective to achieve high brightness and high polarization simultaneously. Based on this work, the second gun system (JPES-2) was already constructed at Nagoya Univ. and now it was mounted for the LEEM apparatus operated at OECU.

ACKNOWLEDGEMENTS

This work has been financially supported by the Japan Science and Technology (JST) Agency as a technology development program for advanced measurements and analysis (program leader: T. Nakanishi).

REFERENCES

1. E. Bauer, T. Duden and R. Zdyb: “Spin-polarized low energy electron microscopy of ferromagnetic thin films”, J. of Phys. D: Appl. Phys., 35 (2002) pp. 2327-2331.
2. K. L. Man et al.: “Growth morphology, structure, and magnetism of ultrathin Co films on W (111)”, Phys. Rev. B 67, p. 184402 (2003).
3. T. Ohshima and M. Kudo: “Electron Beam Brightness from Negative-Electron-Affinity Photocathodes for Scanning Electron microscopy Application”, Jpn. J. Appl. Phys., Vol.43, No.12 (2004) pp. 8335-8340.
4. F. Furuta, T. Nakanishi, et al.: “Reduction of field emission dark current for high-field gradient electron gun by using molybdenum cathode and titanium anode”, Nucl. Intrum. Methods A538 (2005) pp. 33-44.
5. N. Yamamoto, T. Nakanishi, A Mano, X. Jin, T. Ujihara et al., “High brightness and high polarization electron source using transmission photocathode with GaAs-GaAsP superlattice layers” J. Appl. Phys., Vol.103, No. 6 (2008), 064905.
6. X. Jin, N. Yamamoto, T. Ujihara, T. Nakanishi et al.,“Super-high brightness and high spin-polarization photocathode” Appl. Phys. Express Vol. 1 (2008), No. 4, 045002.
7. X. Jin, N. Yamamoto et al., “Highly spin-polarized electron photocathode based on GaAs-GaAsP superlattice grown on mosaic-structure buffer layer” J. of Crystal Growth 310 (2008) pp. 5039-5043
8. T. Nishitani, T. Nakanishi, et al.: “Highly polarized electrons from GaAs-GaAsP and InGaAs-AlGaAs strained-layer superlattice photocathodes”, J. Appl. Phys., Vol.97, No.9, 094907 (2005).

Ab Initio Calculation of Effective Sherman Functions in MeV Mott Scattering

K. Aulenbacher, V. Tioukine

Institut f. Kernphysik der Universität Mainz,
J.J. Becherweg 45, D-55099 Mainz, Germany, F. R.

Abstract. A Mott polarimeter operating at energies from 1 to 3.5 MeV and at backward scattering angle of 164 degree has been installed at the MAMI accelerator. Its detection system is based on magnetic spectrometers allowing for efficient background suppression. The useful range of primary currents is between 10 nA and 100 μA, hence adapted to the typical beam currents at MAMI. The reduction of analyzing power due to multiple scattering can be calculated directly from the cross sections with the help of Monte Carlo simulation.

Keywords: Pol. beams, multiple scattering, Polarization in interactions and scattering
PACS: 29.27.Hj -11.80.La -13.88+e

INTRODUCTION

Mott detectors determine the beam polarization P_{beam} by measuring the experimental asymmetry $A_{exp} = P_{beam} \cdot S_{eff}$ in elastic scattering of polarized electrons off targets with high nuclear charge, typically gold. P_{beam} can then be determined once that the effective analyzing power S_{eff} is known. The statistical efficiency $Q = S_{eff}^2 \cdot (I_{scat}/I_0)$ (I_{scat} =scattered current, I_0 = primary current on target) reaches a maximum at about 25 keV beam energy and then decreases since I_{scat} is proportional to the differential cross section being roughly proportional to $1/E^2$. It seems therefore not attractive to use higher energies since the size of the apparatus increases, whereas the statistical efficiency decreases. However, both effects are only of minor concern at the MAMI accelerator, which evidently provides high energies and where the low efficiency is compensated for by high beam currents. Hence, in our case, the following advantages of 'high' energies - in the range of several MeV - become effective:

- MeV beam energies could allow for better reproducibility, e.g. because of lower sensitivity with respect to varying magnetic fields, high pointing stability and low geometric emittance.
- The reduction of the effective analyzing power with target thickness is much less pronounced thus allowing to use much thicker -i.e. less delicate- targets.
- The energy loss dE/dx is lower; leading to less heat dissipation in a thin target.
- In a single scattering experiment, the effective analyzing power S_{eff} can only be determined if the analyzing power S_0 which corresponds to single elastic scattering has been calculated theoretically. As an input for such calculations details of the electronic and nuclear charge distribution are required. However, the momentum transfer at 3.5 MeV and backward scattering angle is sufficiently high that the

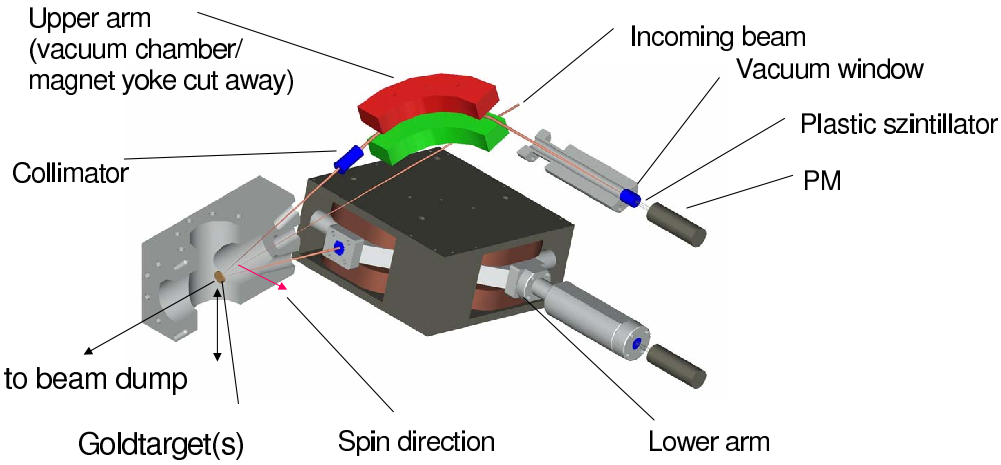

FIGURE 1. Mott polarimeter with two magnetic spectrometers for backward scattered electrons

atomic electrons become rather unimportant for scattering whereas the momentum transfer is still small enough to make the nucleus appear as a point charge. The variation of S_0 for a point nucleus in comparison to an exact calculation with realistic nuclear and atomic charge distributions is only 1% (relative). The uncertainty introduced by the model dependence of charge distributions is therefore negligible.

APPARATUS AT MAMI

After passing the 3.5 MeV injector linac, the electron beam is deflected from the main beam line towards the Mott polarimeter (fig. 1). The energy may be varied by changing the r.f.- phase of the third acceleration section of the linac, which allows to achieve energies as low as 1 MeV. Typically the spin direction is rotated into the horizontal transverse direction with a Wien filter before entering the linac [1]. The Mott asymmetry is then observed for up/down scattered electrons, the scattering angle being 164 degree. The solid angle is defined by cylindrical diaphragms with 4 mm aperture located at 240 mm distance from the scattering center. Double focusing 90 degree spectrometers are used. Because the detectors lie out of the line of sight to the target the background is effectively suppressed. Electrons are sufficiently energetic to pass a 0.3 mm thick aluminium vacuum window and reach the air mounted plastic szintillators. Gold targets of different thicknesses ($d = 0.1, 0.25, 0.5, 1, 15 \mu m$) can be moved into the beam, alternatively a szintillation screen can be used for inspection of beam shape and position.

RESULTS

Statistical efficiency: Typically, a scattering rate of 1.7 kHz is observed per μA of beam current hitting a 1 μm thick gold target, which is in agreement with the expected rate from the elastic cross section. Figure 2 also shows that for the thickest target (15 μm), the rate is increased over-proportionally, which results from the multiple scattering

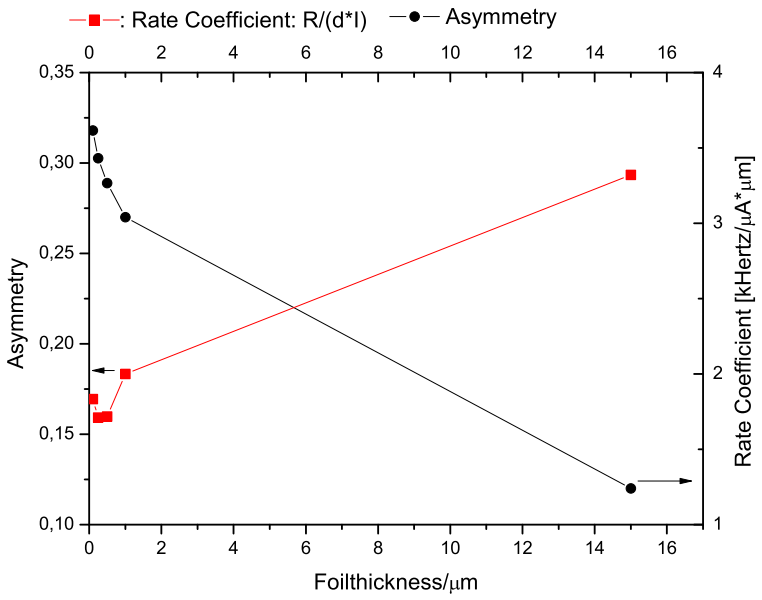

FIGURE 2. Rate coefficient and asymmetry vs. target thickness. Beam energy 3.5 MeV.

processes to be discussed below. Multiple scattering is also the main reason for the dramatic reduction of effective analyzing power $S_{eff} = A_{exp}/P_{beam}$ for the 15μm target. However, if statistical efficiency is considered, this is more than compensated by the higher rate. Therefore asymmetry measurements have the highest efficiency if performed with the 15 μm target, leading to a measurement time of 1 hour for 1% accuracy at a primary beam current of 10 nA. Measurement times at the higher beam currents which are characteristic for electron scattering experiments are of the order of a few seconds. One may worry that ionization losses in the target will lead to eventual destruction due to heating. Such problems may be alleviated by using the thinner targets, since radiative surface cooling should remain the same but the dissipated power is $\propto d$. We have already tested the $0.1\mu m$ target at the maximum beam current possible at MAMI, $100\mu A$.

Reproducibility: Several beam parameters (position of the foil, beam current, beam movement in position and angle) were varied, the asymmetry being insensitive to this manipulations at a level of $\Delta A/A < 1\%$. Long term observations showed a relative drift of asymmetry by 0.3% in 8 hours, which may be due to a change of beam polarization because of cathode aging. An independent simultaneous monitor is presently under construction in order to disentangle changes of polarization from apparative drifts.

AB INITIO CALCULATION OF S_{eff}

In a real experiment the single elastic scattering analyzing power S_0 is modified, which leads to an 'effective' analyzing power S_{eff}. For example, a determination of S_{eff} must take into account the reduction of S_0 due to multiple scattering. Analytic approaches [2] in order to extrapolate to zero target thickness introduce errors: we estimate presently

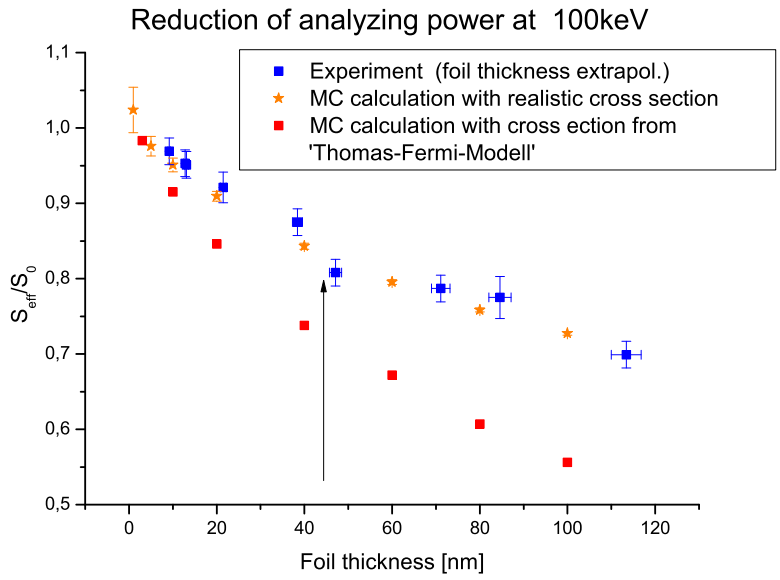

FIGURE 3. Comparison of MC simulation and data based on extrapolation (100keV).

the relative error caused by the extrapolation for our apparatus to be 4%. However these ambiguities can be reduced if the reduction is determined by a Monte Carlo (MC-) simulation, which was successfully demonstrated by M. Khakoo et al. [3] for energies up to 120 keV. Such 'ab initio' calculations are limited in accuracy only by the input accuracy of the cross sections and the corresponding spin rotation parameters. The MC results then predict the reduction of analyzing power for a target of finite thickness, hence eliminating the need for an extrapolation. We have checked this method for previous results obtained by us with a 100 keV Mott and found good agreement (fig. 3). Besides the agreement, figure 3 reveals that good knowledge of the atomic charge distribution is important, a simple atomic model with a Thomas Fermi charge distribution which reproduces cross section and Sherman function at large angles does not reproduce the data. This probably happens because the forward cross sections at angles below 5 deg are not correct in this model. At thicknesses larger than $d \approx 40\,nm$ an increasing number of electrons is subject to energy losses larger than the energy resolution of the experimental set up and does not contribute to the signal. This results in a change of slope, which is indicated by the arrow in fig. 3. For larger d the MC results therefore depend on the value assumed for the detector resolution. Albeit a reasonable value for the energy resolution was chosen, it should be noted that a highly accurate determination for large thicknesses requires a corresponding knowledge of the properties of the detection system.

Preliminary results for 1 and 2 MeV are shown in figure 4 which are the result of 100 hours runtime each on a conventional PC, the statistical accuracy can be increased easily by using a small PC farm. The experimental data points are normalized to the extrapolated asymmetry at d=0, which leads to the above mentioned 4% error bar. The MC data are normalized to S_0 and carry statistical error bars. Even for the limited

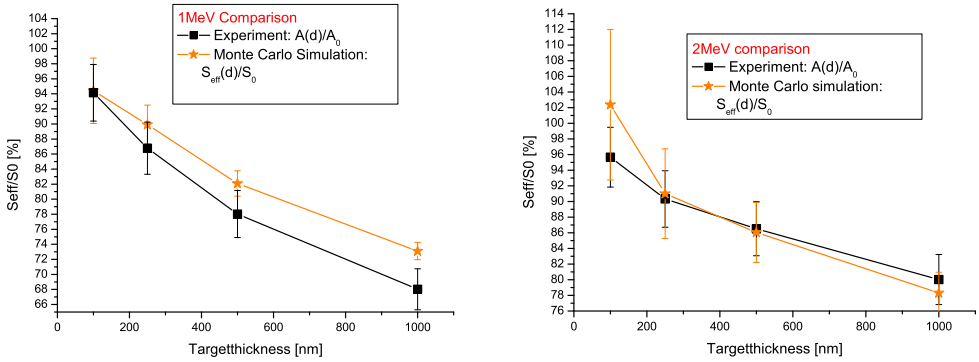

FIGURE 4. Decrease of analyzing power with target thickness for 1 and 2 MeV.

statistical accuracy some discrepancy seems to be present at 1 MeV. This is probably due to the fact that, since at these energies high accuracy cross section calculations as provided by [4],[5] are not available to us, a Thomas-Fermi model was used again. However, the extension of high accuracy cross section calculations to higher energies seems to be no principal problem.

CONCLUSION

A 3.5 MeV Mott polarimeter is in operation at the accelerator MAMI in Mainz. It offers sufficient measurement speed and good reproducibility for primary currents in the range 0.01-100 μA which coincides with the current requirements of most MAMI experiments. The effective analyzing power of the targets for elastic scattering can be simulated by a MC calculation which takes into account the microscopic cross sections ('ab initio' calculation). It seems possible to increase the accuracy of the Mott polarimeter by supporting the foil thickness extrapolation method by MC data. We believe that a reduction of the total systematic error below 2% is possible.

ACKNOWLEDGMENTS

This work was supported by the SFB 443 of the Deutsche Forschungsgemeinschaft.

REFERENCES

1. V. Tioukine and K. Aulenbacher, *NIM* **A 568** *537* (2006).
2. T.J. Gay et al. , *Rev. Sci. Instrum.* **63 (1)** *114* (1992).
3. M. A. Khakoo et al. , *Phys. Rev.* **A 64** *052713* (2001).
4. G. Holzwarth and H.J. Meister, *Nucl. Phys.* **59** *56* (1964).
5. A. W. Ross and M. Fink, *Phys. Rev.* **A 38,(12)***6055* (1988).

Compton Polarimetry at ELSA

Wolfgang Hillert, Bastian Aurand, and Jürgen Wittschen

Physikalisches Institut, Universität Bonn,
Nussallee 12, D-53115 Bonn, Germany

Abstract. Part of the future polarization program performed at the Bonn accelerator facility ELSA will rely on precision Compton polarimetry of the stored transversely polarized electron beam. Precise and fast polarimetry poses high demands on the light source and the detector which were studied in detail performing numerical simulations of the Compton scattering process. In order to experimentally verify these calculations, first measurements were carried out using an argon ion laser as light source and a prototype version of a counting silicon microstrip detector. Calculated and measured intensity profiles of backscattered photons are presented and compared, showing excellent agreement. Background originating from beam gas radiation turned out to be the major limitation of the polarimeter performance. In order to improve the situation, a new polarimeter was constructed and is currently being set up. Design and expected performance of this polarimeter upgrade are presented**.**

Keywords: Compton scattering; Microstrip detector; Polarimetry; Polarization
PACS: 13.60.Fz; 29.40.Wk; 95.75.Hi; 29.27.Hj

INTRODUCTION

The experimental hadron physics program at the **EL**ectron **S**tretcher **A**ccelerator ELSA ([1], see Fig. 1) is based on the availability of polarized beams and polarized solid state targets. A beam of polarized electrons is generated with a dedicated source [2] and post accelerated in a linear accelerator, the booster synchrotron and the stretcher ring. During post acceleration in the stretcher ring, crossing of depolarizing resonances will cause significant beam depolarization unless these effects are being compensated by application of sophisticated correction schemes [3]. Therefore, precise determination and monitoring of the beam polarization is mandatory and is performed in the low energy beam-line (by means of Mott polarimetry) and the external high energy beam-line to the experiment (by means of Møller polarimetry). In order to measure the polarization of the stored electron beam in the stretcher ring directly on a time scale of minutes, a Compton polarimeter has been developed [4] and installed at ELSA, and is currently being upgraded. It is based on Compton backscattering of circularly polarized photons off the stored beam of transversely polarized electrons. The electron beam polarization is extracted from measuring the shift of the center of the backscattered photon spatial distribution when switching the polarization of the incoming photons from right-handed to left-handed. In order to record the intensity profile of the backscattered photons, a counting silicon microstrip detector [5] is utilized.

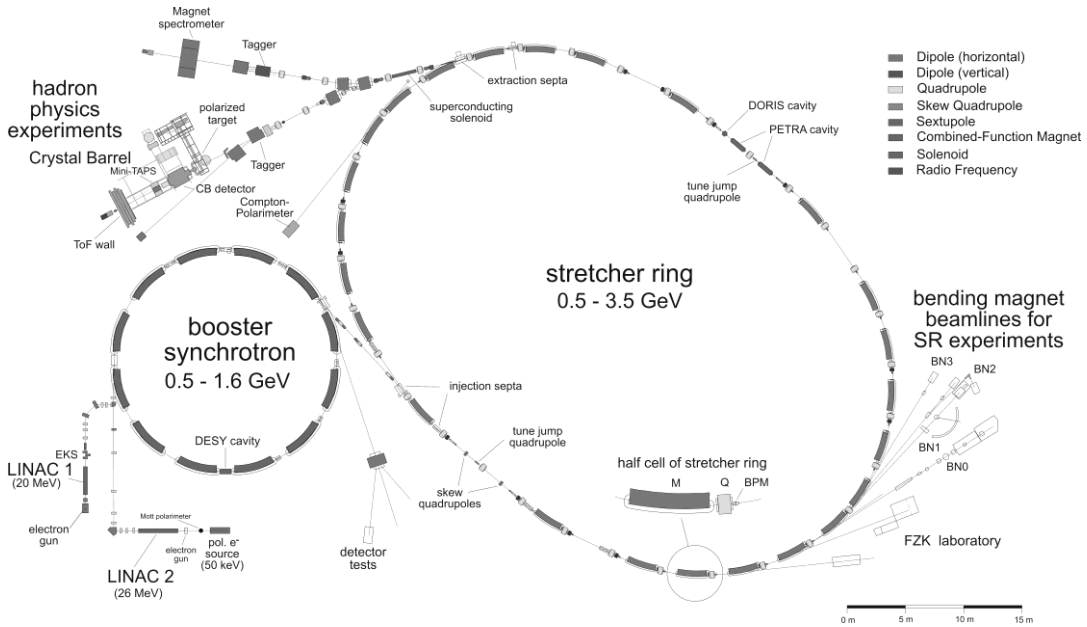

FIGURE 1. The Electron Stretcher Accelerator ELSA at Bonn University.

POLARIMETER SET-UP

In order to achieve a minimum electron beam divergence, the crossing region of photon and electron beams is placed in a defocusing quadrupole magnet of the stretcher ring. A crossing angle of about 3 mrad was chosen to protect the final dielectric deflection mirror, which is mounted off axis in vacuum, from synchrotron radiation emitted by the electron beam (see Fig. 2 (b)). Compton-scattered photons are detected 15 m away from the interaction region. Assuming typical vertical beam widths of the electron and the photon beam of about 2 mm, the interaction length is below 1.4 m. In order to suppress background produced by beam gas radiation, the interaction region was placed in one of the shortest straight sections of the stretcher ring, where a defocusing quadrupole magnet is directly surrounded by dipole magnets, as shown in Fig. 2 (a).

The photon counting detector is based on a silicon microstrip sensor of type BABAR 1 (size 38.4 mm x 41.3 mm), which contains 768 horizontally oriented strips with a pitch of 50 microns. In the first version of the detector electronics, every second strip was read out using dedicated front-end chips (see [5]), partially developed by the ATLAS pixel group of Bonn University [6].

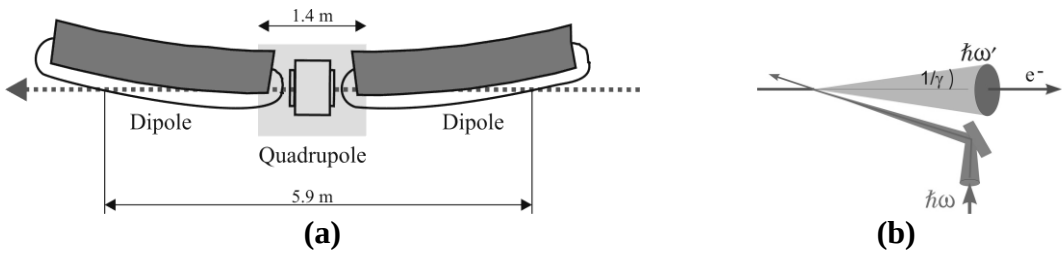

FIGURE 2. The interaction region in ELSA. Photon and electron beams are crossed in a defocusing quadrupole magnet, directly surrounded by dipole magnets (a). The crossing angle is 3 mrad in order to protect the deflection mirror from synchrotron radiation (b).

In order to be detected, the Compton-backscattered photons (with energies in the MeV-range) are pair converted in a lead converter of two radiation lengths thickness, which is placed directly in front of the sensor.

NUMERICAL SIMULATIONS

The photon counting rate was calculated for each of the 384 sensitive strips of the sensor by numerical integration over the 5-dim phase space of a 100% transversely polarized electron beam of fixed energy (chosen in the range between 1 and 3 GeV) and a 100% circularly polarized photon beam (wavelength λ = 514.5 nm). Each strip was divided into 41 sections and the number of photons $\dot{N}$ impinging on a section centered at (x_d, z_d) was derived by solving

$$\dot{N}\left(x_d, z_d\right) = \int_{S_0}^{S_1} ds \int_{z_{\min}}^{z_{\max}} dz \int_{x_{\min}}^{x_{\max}} dx \int_{z'_{\min}}^{z'_{\max}} dz' \int_{x'_{\min}}^{x'_{\max}} dx' \; \frac{\partial(\vartheta^*, \varphi^*)}{\partial(x, z)} \cdot \rho_e \cdot \rho_\gamma \cdot \frac{d\sigma}{d\Omega^*} \cdot \eta(E_\gamma) \quad (1)$$

where electron and photon beams are represented by their phase space distribution functions ρ_e and ρ_γ. The Compton cross-section $d\sigma/d\Omega^*$ was taken from [7], and the pair conversion efficiency $\eta(E_\gamma)$ for a 1.7 radiation lengths converter was derived from [8] using Compton kinematics to determine E_γ.

The shift of the center of the profile of backscattered photons was determined from subtraction of the weighted sums

$$\Delta\bar{z} = \sum_{i,j} z_j \dot{N}^+(x_i, z_j) - \sum_{i,j} z_j \dot{N}^-(x_i, z_j) \quad (2)$$

over the calculated 2-dim profiles in case of right-handed ($\dot{N}^+$) and left-handed ($\dot{N}^-$) circularly polarized photons and is presented in Figure 3.

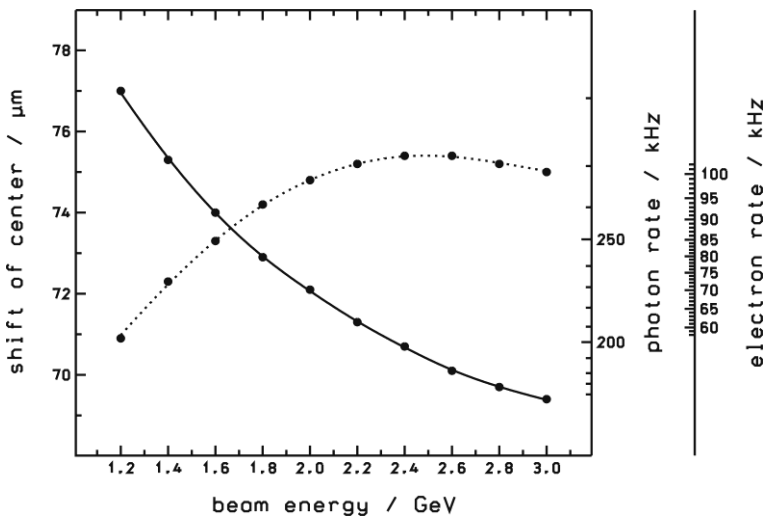

FIGURE 3. The shift of the center of the profile of backscattered photons (solid line) and pair converted electrons / positrons (dashed line) in case of switching from right-handed to left-handed circular polarization of the laser beam. Corresponding overall counting rates are indicated at the right hand side of the figure for a laser power of 10 W and an electron beam current of 100 mA.

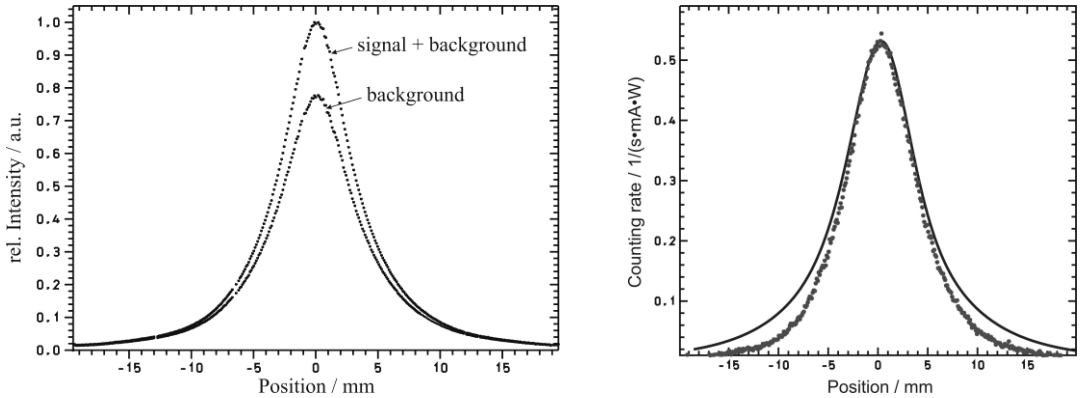

(a) **(b)**

FIGURE 4. Measured and calculated intensity profiles of pair converted backscattered photons. The left figure (a) shows profiles derived with the argon ion laser switched on (signal + background) and off (background). The right figure (b) presents a comparison of the measured signal (dots) and a simulated profile (solid line), normalized to 1 mA beam current and 1 W laser power.

COMPARISON WITH MEASURED DATA

First measurements were carried out using a 10 W cw argon ion laser (green line) and the prototype version of a counting microstrip detector in combination with a two radiation lengths lead converter. Background produced from beam gas radiation was derived from an additional measurement with the laser beam switched off.

Figure 4 (a) shows the measured intensity profiles in case of a 2.3 GeV, 20 mA stored electron beam. Due to the limited laser power and moderate vacuum conditions in the interaction region (pressure in the 10^{-7} mbar regime) the signal to background ratio is less than 1:3. Due to this considerably low value, a measuring time of about one hour is expected in order to reach a polarization error of 2 %.

Figure 4 (b) presents a comparison of measured and calculated profiles of backscattered photons, both normalized to 1 mA electron beam current and 1 W laser power. The profiles agreement is excellent for the center part. Slightly lower counting rates observed in the wings of the measured profile may be attributed to the difference in radiation lengths of the lead converters used in the measurement (2 X_0) and the numerical simulation (1.7 X_0).

POLARIMETER UPGRADE

In order to significantly enhance the signal to background ratio, a new 2x20 W two-beam solid state laser system was purchased and is currently being set up at the accelerator. In addition, the vacuum chamber of the interaction region was replaced by a newly developed one including electron beam position monitoring, water cooling, and an additional ion getter pump. With these improvements, a signal to background ratio of at least 3:1 is expected.

Figure 5 shows the set-up of the laser system and the beam-line in the accelerator tunnel. The two laser beams become circularly polarized by means of rotatable quarter wave plates. Two beam telescopes focus the beams to rms diameters of less than 3 mm in the interaction region, where the beams are crossed. Each laser beam polarization is

monitored after the interaction by means of a second quarter wave plate, a polarizing beam splitter and two photo-diodes. The correct positioning of the laser beams can be controlled online using two four-element photo-diodes, detecting the small fraction of laser light being transmitted through the dielectric mirrors which deflect the laser beams to the polarization analyzer box.

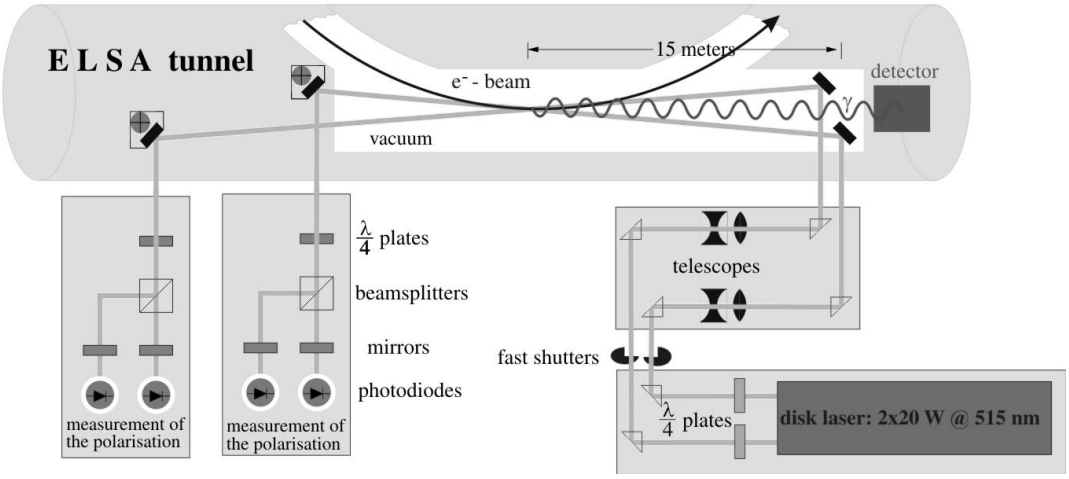

FIGURE 5. Set-up of the upgraded Compton polarimeter based on a 2x20 W two-beam solid state laser system and a counting silicon microstrip detector with improved LVDS micro-electronics.

The improved electronics of the silicon microstrip detector consists of six front end chips, each having 128 channels in order to read out all 768 strips of the sensor. Each channel consists of a low noise charge sensitive amplifier, a CR-RC shaper, a comparator, and a 13 bit asynchronous binary counter. The digital part of the front end chips is built in low voltage differential signal (LVDS) technology which offers a high rate acceptance of up to 150 MHz. With a spatial resolution of 14 microns, the position error turns out to be below 0.7 microns, which results in an achievable absolute error of polarimetry of less than 1 %. Due to the high signal to background ratio and laser power, a polarization measurement error of 2 % should be obtained within minutes of measuring time.

REFERENCES

1. W. Hillert, *Eur. Phys. J.* A **28** s01, 139-148 (2006).
2. W. Hillert, M. Gowin, and B. Neff, "The 50 kV inverted source of polarized electrons at ELSA", in Proceedings of the 14th international Spin Physics Symposium SPIN2000, edited by K. Hatanaka et al., AIP Conference Proceedings 570, American Institute of Physics, Melville, NY, 2001, pp. 961-964.
3. M. Hoffmann et al, "The polarized electron beam at ELSA", in Proceedings of the 14th international Spin Physics Symposium SPIN2000, edited by K. Hatanaka et al., AIP Conference Proceedings 570, American Institute of Physics, Melville, NY, 2001, pp. 756-760 (2001).
4. W. Hillert et al., "The Compton Polarimeter at ELSA", in Proceedings of the 12th international Symposium on High Energy Spin Physics SPIN96, edited by C.W. de Jager et al., World Scientific, Singapore, 1997, pp. 785-787.
5. D. Doll et al., *Nucl. Instrum. Methods* A **492**, 356-364 (2002).
6. P. Fischer, *Nucl. Instrum. Methods* A **378**, 297-300 (1996).
7. F.W. Lipps, and H.A. Tolhoek, *Physica* **20**, 395-405 (1954).
8. D.H. Fitzgerald et al., Nucl. Instrum. Methods **192**, 193-203 (1982).

A Green Fabry-Pérot Cavity for Jefferson Lab Hall A Compton Polarimetry

Abdurahim Rakhman[†], Sirish Nanda[*], Paul Souder[†]

[*]*Thomas Jefferson National Accelerator Facility, Newport News, VA 23606, USA*
[†]*Department of Physics, Syracuse University, Syracuse, NY 13244, USA*

Abstract. A green laser (CW, 532 nm) based Fabry-Pérot cavity for high precision Compton Polarimetry is under development in Hall A of the Jefferson Laboratory. In this paper, we present the principle and the preliminary studies for our test cavity.

Keywords: Fabry-Pérot Cavity, Compton Polarimetry
PACS: 01.30.Cc

INTRODUCTION

Many experiments at Jefferson Lab require accurate knowledge of the polarization of the electron beam. In Hall A, beam polarization measurement is achieved by using both Møller and Compton Polarimeters. The Møller Polarimeter will be suitable only at low current (typically 10 μA) and the measurement cannot be done simultaneously with the experimental data taking. A Compton Polarimeter gives a non-intrusive measurement for higher current beam in which the electrons are scattered from the photons trapped in a high-finesse Fabry-Pérot cavity [1]. The presently operational Polarimeter uses an infra-red (1064 nm, 1.16 eV) laser as its photon source which is not capable of giving good accuracy at beam energies below 2 GeV. To reach 1% accuracy for high precision parity violation experiments like PREx [2] in Hall A, a green (532 nm, 2.33 eV) Fabry-Pérot cavity was proposed [3]. In this paper, we explain the principle of power buildup inside such a cavity and present some preliminary results from our test setup. As a conclusion, we also discuss how to achieve our design goal before installing the new system in the beam line.

THE COMPTON POLARIMETER

In a Compton Polarimeter, the longitudinal polarization P_e of the electron beam is calculated from the measurement of the experimental asymmetry A_{exp} in elastic scattering of circularly polarized (P_γ) photons off the electrons.

$$A_{\exp} \equiv \frac{n^+ - n^-}{n^+ + n^-} = P_e P_\gamma \langle A_l \rangle \tag{1}$$

where n^+ and n^- are the counting rates of scattering events before and after the electron spin flip ($P_e \rightarrow {}^-P_e$). The asymmetry $< A_l >$ on the Compton cross section with longitudinally polarized electrons is calculated in the framework of QED. The longitudinal asymmetry A_l is plotted on Figure 1 as a function of the normalized energy of the scattered photons.

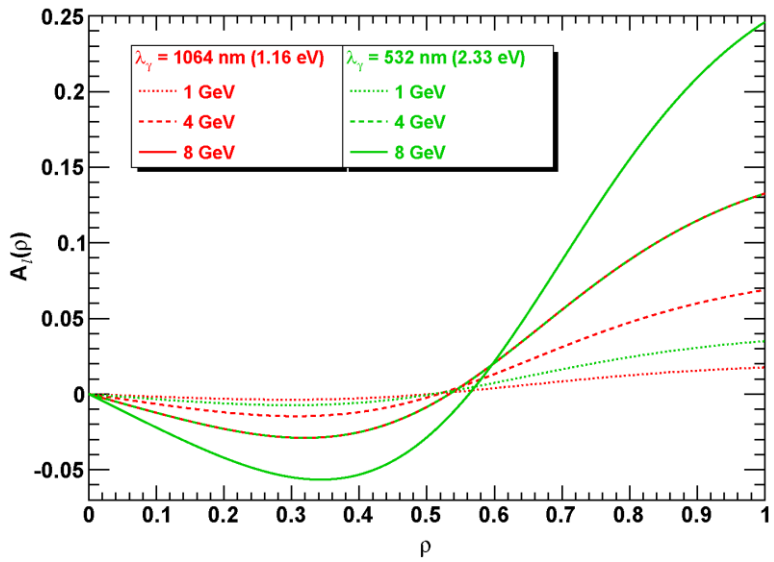

FIGURE 1. Longitudinal asymmetry for a 1 GeV, 4 GeV, 8 GeV electron beam and a green (2.33 eV) and an IR (1.16 eV) laser beam versus the scattered photon energy normalized to the maximum scattered photon energy.

The time needed to get the electron beam polarization with a statistical precision ($\Delta P_e / P_e$) is given by [4],

$$t \approx \frac{1}{L\left(\frac{\Delta P_e}{P_e}\right)^2_{stat} P_e^2 P_\gamma^2 \sigma_t \left\langle A_l^2 \right\rangle} \tag{2}$$

where σ_t and $< A^2_l >$ are the total cross section and the squared theoretical asymmetry. For 1 GeV electrons, if the IR laser was used, the maximum value of A_l is 1.8 %, whereas with the green laser, its value is 3.5 %. The luminosity L can be calculated using the relation [4],

$$L \approx \sqrt{\frac{2}{\pi}} \frac{I_e}{e} \frac{P_L \lambda}{hc^2} \frac{1}{\sqrt{\sigma_e^2 + \sigma_\gamma^2}} \frac{1}{\sin\alpha} \tag{3}$$

where I_e is the electron beam current, P_L is the power of the laser beam, σ_e and σ_γ are the Gaussian width of the electron and laser beams at the Compton Interaction Point (CIP), α is the crossing angle between the beams. Using Eq. 2 and Eq. 3, one can evaluate the time of measurement to get a 1% level statistical error. The proposed

alternative [3] will use a tunable CW green laser (532 nm) coupled with optical cavity to increase the L and $< A^2_l >$ respectively.

The schematic of the Compton Polarimeter at Jefferson Lab is shown in Figure 2. A Fabry-Pérot cavity provides a high-density circularly polarized photon target at the CIP. A magnetic chicane is used for vertical displacement of the electron beam and optimizing the crossing of the electron and photon beams. The back-scattered photons are collected by the photon calorimeter. The silicon micro-strips in the electron detector tag the momentum of the scattered electrons at the end of the third dipole and provide a complimentary polarization measurement.

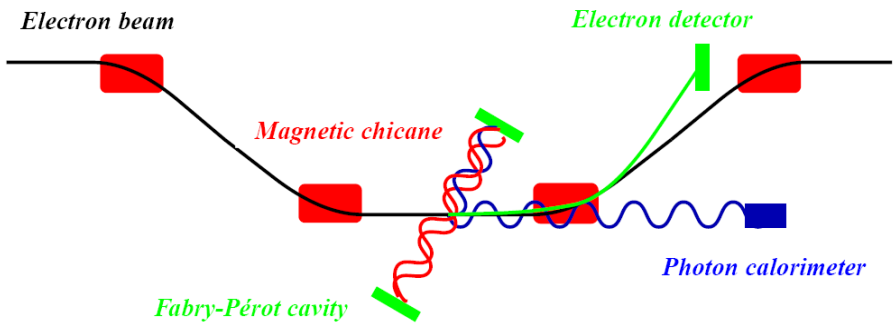

FIGURE 2. A schematic of Compton Polarimeter in Jefferson Lab hall A

THE FABRY-PÉROT CAVITY

The Fabry-Pérot cavity is made of two high reflective (R > 99 %) mirrors separated by integral multiple of the half wavelength of the input light. When the focusing of the injected Gaussian laser light correctly matches the fundamental TEM_{00} mode of the cavity, the circulated light inside the cavity is amplified by a large factor with respect to the incident beam power. The amplification factor or cavity gain is defined by the properties of the mirrors and the optical coupling of the light to the cavity. In other words, the cavity mirrors should be high reflective and low loss type. Maximum coupling is achieved by good alignment of the laser beam to the optical axes of the cavity and proper focusing of it at the cavity center. However, a small variance in the cavity length brings a large change in the cavity resonance frequency and we always have to keep the laser frequency adjusted to the change in cavity resonance frequency. The critical part of Fabry-Pérot cavity system is sustaining the TEM_{00} resonance mode of the cavity in order to have continuous high power inside the cavity. One of the most widely used techniques is the Pound-Drever-Hall (PDH) locking scheme [5] which controls the laser frequency based on the analysis of the reflected light by the cavity.

Our laser (Prometheus, Innolight Gmbh [6], Hannover, Germany) is a diode pumped solid-state NPRO laser which has a primary wavelength of 1064 nm. After single pass frequency doubling with a PPKTP crystal, it delivers up to 100 mW of CW green laser (532 nm) with longitudinal mode TEM_{00} and a narrow linewidth (1 kHz over 100 ms). Frequency tunability is achieved changing the frequency of the pump laser by means of a temperature (SLOW) control of the NPRO crystal with a tuning range of 60 GHz or of a voltage (FAST) applied to a piezoelectric bonded to the crystal with a dynamic range of 200 MHz.

Our test cavity (Figure 3.) consists of two identical high reflective (manufacturer specification R = 99.9 %) concave mirrors (from CVI Laser, ROC = 0.5 m, 0.5 in. diameter) separated by 0.85 m. They are mounted on gimbal mount on two ends of the cavity and can be controlled remotely by picomotors. Our home-made locking system uses the PDH scheme. Based on an Analog Devices 32-bit microprocessor, the system automatically scans for a TEM_{00} cavity mode and engages the feedback servo to acquire lock. The shape of the resonance mode is monitored by a Spiricon CCD camera. From the transmitted and the reflected power measured by two pre-calibrated photodiodes (PDT and PDR), one can estimate the intra cavity power and the optical coupling as well. The purpose of this test cavity is to check the locking electronics and understand the basics of optical setup.

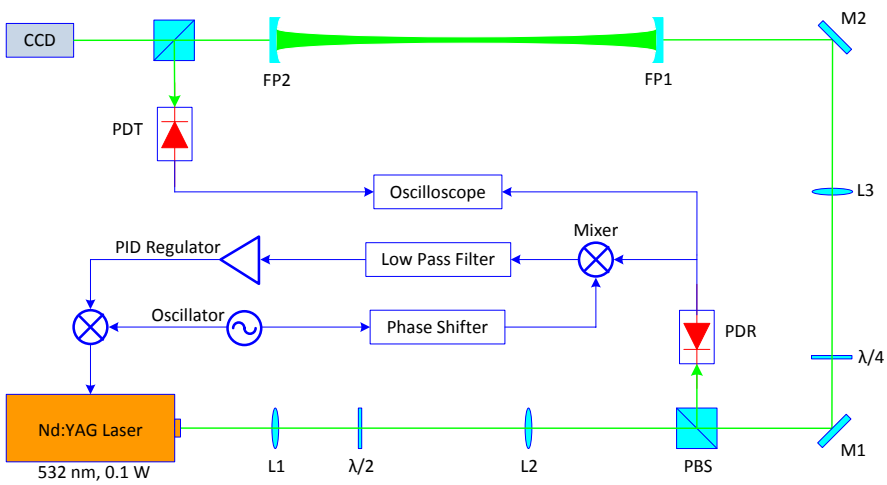

FIGURE 3. A schematic of the optical setup for the test cavity

RESULTS AND DISCUSSION

Our PDH feedback servo system was able to lock this test cavity successfully. During cavity locking tests, no careful optimization of the input optics was performed resulting in poor optical coupling. Furthermore, substantial loss (absorption, scattering) in these stock mirrors limited the power gain in the cavity. With 55 mW injected laser power, the intra-cavity power was about 6 Watts. We measured the finesse of the mirrors from cavity decay time as well as cavity bandwidth, to be 2695 corresponding to a reflectivity of 99.896 %. Losses in the mirrors were estimated to be 500 ppm.

In order to improve optical coupling efficiency, the laser beam was analyzed with the Spiricon Laser Beam Analyzer. Lens positions were determined by simulation of the transport optics with OptoCad [7] to achieve better mode-matching. The simulated and measured beam profiles agree reasonably well (Figure 4). To control losses in mirrors, new sets of super-polished (surface RMS roughness = 0.5 Å) low-loss mirrors (from General Optics, Moorpark, CA) were ordered. We expect to achieve less than 10 ppm losses in the new mirrors, thus substantially improving cavity gain. The feedback servo system needs to be re-optimized for higher gain cavities. Our goal for

operational green cavity for high precision Compton Polarimetry is to get 1500 W intra cavity power.

The future goal also includes the polarization transfer function of laser beam in the system. The accurate determination of the circular polarization of the beam at the CIP is crucial to electron beam polarization measurement.

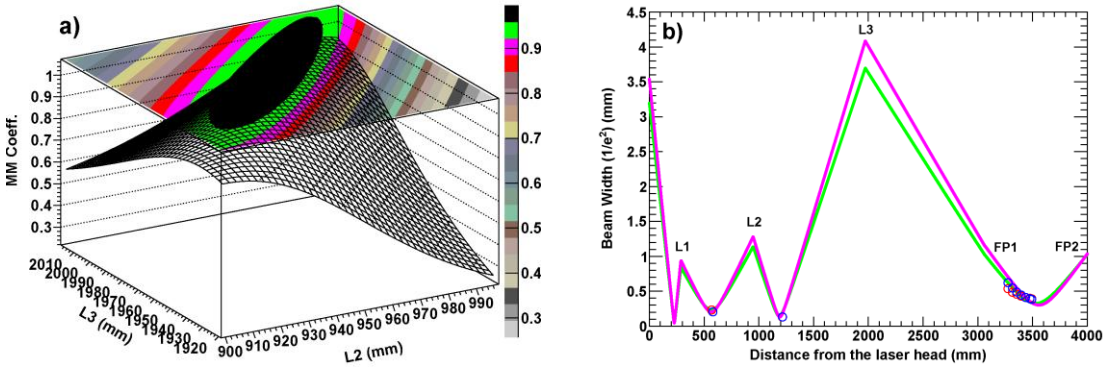

FIGURE 4. a) The calculated mode matching coefficients for L2 and L3 lens configurations, while L1 is fixed, b) calculated and measured beam diameters along the beam path from the laser head. The green (magenta) curve corresponds to the calculated value of tangential (sagittal) component. The red (blue) circles show the measured value of tangential (sagittal) component with Spiricon Laser Beam Analyzer.

CONCLUSIONS AND OUTLOOK

A new green Fabry-Pérot cavity for high precision Compton Polarimetry is under development. We have developed our own feedback control system based on PDH scheme. Test cavity has been assembled and tested for mechanical and ultra-high vacuum integrity. Low power gain locking has accomplished. More work is necessary to improve the light coupling to the cavity. We are working on developing a proper mirror cleaning and handling method to minimize losses. We are also working on feedback electronics, in order to get 1500 W power with a higher gain cavity. Alternative ways, such as injecting more green power to lower gain cavity is also an option, provided we have tunable high power green laser available.

REFERENCES

1. N. Falletto et al., *Nucl. Instrum. Methods A*, **459** (2001), 412-425.
2. K. Kumar et al., CEBAF experiment E06002, http://hallaweb.jlab.org/parity/prex/
3. S. Nanda and D. Lhuillier, “Conceptual Design Report of a Hall A Compton Polarimeter Upgrade”, Jefferson Lab, 2004.
4. G. Bardin et al., “Conceptual Design Report of a Compton Polarimeter for CEBAF Hall A”, CEA-Saclay, 1996.
5. R. V. Pound, *Rev. Sci. Instrum.* **17**, 490 (1946); R. W. P. Drever, J. L. Hall, *Appl. Phys. B: Photophys. Laser Chem.* **31**, 97 (1983); R. W. P. Drever et al., *Appl. Phys. B* **31**, 145 (1983)
6. I. Freitag, InnoLight GmbH, http://www.innolight.de/
7. R. Schilling, The Rechenzentrum Garching (RZG), http://www.rzg.mpg.de/~ros/OptoCad/

Polarimetry at the Superconducting Darmstadt Electron Linac S-DALINAC

C. Eckardt*, R. Barday*, U. Bonnes*, M. Brunken*, R. Eichhorn*, J. Enders*, C. Heßler*, W.F.O. Müller†, M. Platz*, Y. Poltoratska*, B. Steiner†, M. Wagner* and T. Weiland†

*Institut für Kernphysik, Technische Universität Darmstadt, Germany
†Institut für Theorie Elektromagnetischer Felder, Technische Universität Darmstadt, Germany

Abstract. A spin polarized electron source will be installed at the S-DALINAC to extend the existing experimental capabilities polarization. In order to manipulate and monitor the beam polarization a Wien filter and different polarimeters will be installed. The already installed Wien filter and 100 keV Mott polarimeter and the planned 5 MeV Mott, 30-130 MeV Møller and Compton transmission polarimeters are described.

Keywords: S-DALINAC, Polarimetry
PACS: 29.20.Ej, 29.25.Bx, 29.27.Hj, 29.27.Fh, 24.70.+s

The superconducting Darmstadt electron linac S-DALINAC [1] will soon start its polarized beam program. As a first step a laser-driven GaAs electron source [2] at 100 keV has been set up at a separate test stand [3, 4] for development purposes. The source will be moved to the S-DALINAC in 2009. The beam line set up of the test stand includes a Wien filter to switch from longitudinally polarized beam for experiments to transversally polarized beam for polarimetry and to adjust for spin precession through the bending magnets. A 100 keV Mott polarimeter [5] is installed to measure the polarization of the electron beam produced by the source. As the S-DALINAC has an adjustable energy range of about 4 up to 130 MeV and many bending magnets because of its two recirculations it is necessary to determine the polarization at different positions close to the experimental sites as indicated in Fig. 1. For this purpose a 5-10 MeV Mott polarimeter will be installed at the low-energy experimental area, a 30-100 MeV Møller polarimeter in the extraction section and Compton transmission polarimeters at the end of the beam line at different experimental sites.

100 KEV MOTT POLARIMETER

The 100 keV Mott polarimeter has been installed and tested in the low energy beam line section at the test stand of the polarized source. A description of the test stand status can be found in these proceedings in ref. [6]. The Wien filter is placed on the beam axis to switch the polarization into the transverse direction for Mott polarimetry and to account for the bending magnets of the S-DALINAC. Inside the Mott polarimeter four silicon surface-barrier detectors are placed, one in each quadrant at 120° with respect to the beam. This allows one to measure both transverse beam polarizations.

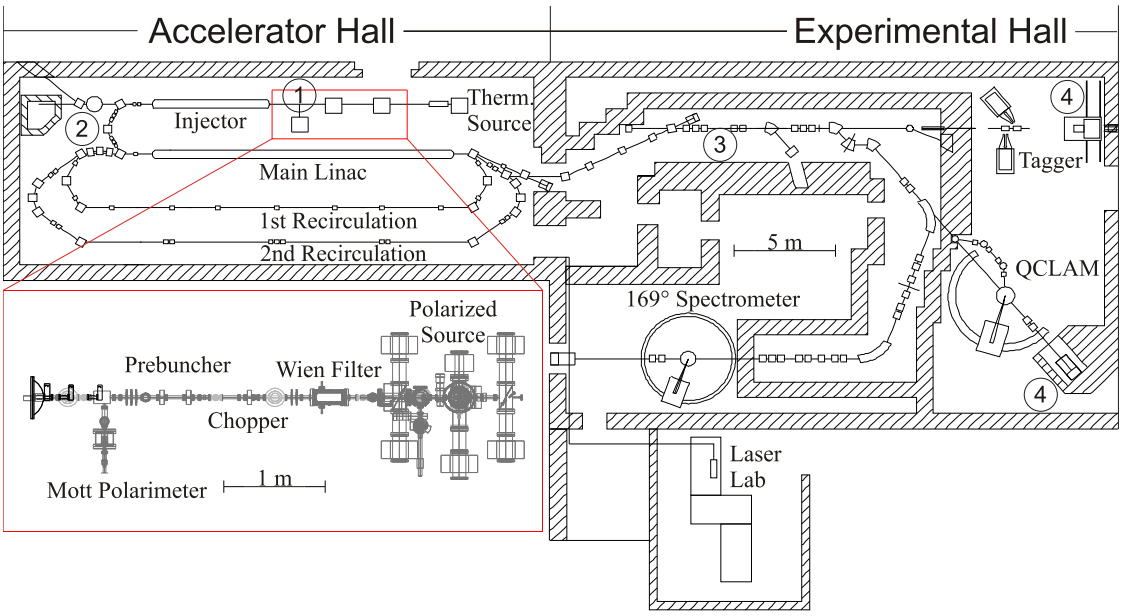

FIGURE 1. Layout of the S-DALINAC. The polarized source seen in the lower left will be installed between the thermionic source and the injector part of the linac. The laser beam runs through a fiber or an evacuated laser beam transport line originating in the laser lab. The position of the different polarimeters is as follows: 1. 100 keV Mott polarimeter 2. 5-10 MeV Mott polarimeter 3. 30-130 MeV Møller polarimeter 4. Compton transmission polarimeter

A target wheel with an empty slot for the beam, a BeO target to monitor the beam position and several self-supporting gold foils ranging from 42.5 to 500 nm is positioned in front of the detectors. Targets with different thicknesses are needed to extrapolate to a target thickness of zero, as the analyzing strength is only known for this target thickness. With this set up an asymmetry was measured at the test stand and it has been possible to determine the beam polarization for bulk GaAs to 35.5±1.4% and to 86±3% respectively for strained superlattice GaAs at a laser wavelength of 830 nm.

5-10 MeV Mott Polarimeter

A 5-10 MeV Mott polarimeter will be installed behind the injector section of the S-DALINAC, in front of the low energy experimental area. Here an energy up to 10 MeV and currents up to 60 μA are possible. This polarimeter has to be installed to monitor the beam polarization after the acceleration to the MeV range. Again, self-supporting gold foils of various thickness will be used for the extrapolation of the asymmetry to thickness zero. The uncertainty due to the foil thickness is smaller at higher energies. Due to limited space of only 0.5 m at the beam line the optimal angle for the Sherman function of 173° for 5 MeV or 176.5° for 10 MeV cannot be selected, instead an angle of 165° is chosen. The polarimeter will be installed with two scintillators for the detection of the scattered electrons.

30-130 MEV MØLLER POLARIMETER

A 30-130 MeV Møller Polarimeter will be installed at the beam extraction section behind the main accelerator. Energies up to 130 MeV with a maximum current of 20 μA are possible while typical values are 30-80 MeV with beam currents of a few μA only. (This prohibits, e.g. the use of a laser-backscattering Compton polarimeter). At this energy range Møller scattering is the method of choice. The polarized beam hits a polarized target, in this case a 20 μm vacoflux foil rotated by 20° with respect to the beam polarized by the magnetic field of two Helmholtz coils. As space is limited to 1 m and the scattering angle shows a large variation over this energy range, a large-acceptance compact magnet set up has to be developed to separate the scattered Møller electrons from the beam and to focus these electrons on the focal plane of a plastic scintillator detector array for coincident detection of the scattered and the recoiling electrons near a center of mass scattering angle of 90°. Present design considerations include a quadrupole magnet with collimators to separate the scattered electrons from the direct beam that has undergone small-angle scattering and a dipole magnet to bend the Møller electrons for momentum analysis. The main beam has to be safely dumped. The schematic layout of the Møller polarimeter and the energy dependence of the scattering angle are shown in Fig. 2. Note the logarithmic scale. Further information can be found in ref. [7].

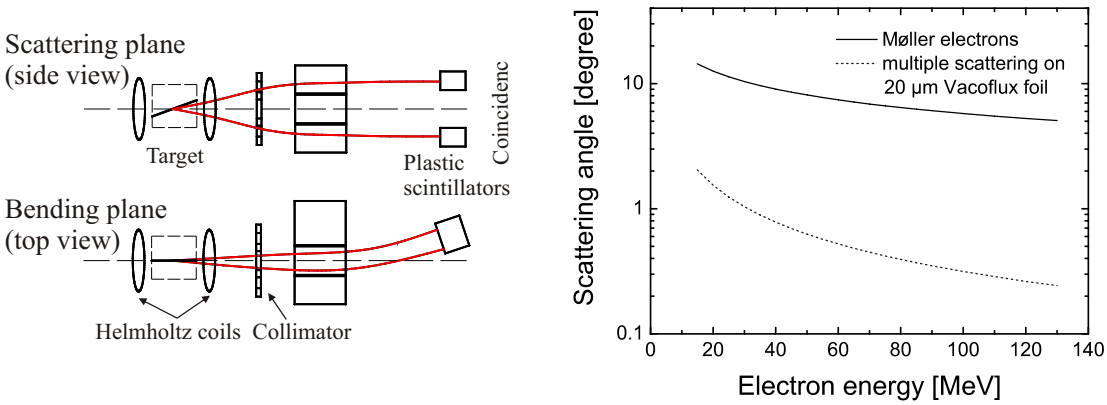

FIGURE 2. Schematic layout of the Møller polarimeter. The magnetic field of the two Helmholtz coils polarizes a Vacoflux foil. Scattered electrons are separated by a quadrupole and collimator and bent by a dipole magnet out of the beam path. On the right the energy dependence of the scattering angle for Møller electrons and multiple scattered electrons is shown.

COMPTON TRANSMISSION POLARIMETER

In the experimental hall three experimental sites are in use, the NEPTUN photon tagging system, the QCLAM spectrometer with 180° chicane and the 169° spectrometer. The NEPTUN tagger and the QCLAM spectrometer have experiments planned with polarized electrons. Therefore it is necessary to monitor the polarization of the electron beam for both experimental sites. The tagger is placed behind the Møller polarimeter.

The beam line to the QCLAM spectrometer is bent by 40°. To monitor the polarization at the spectrometer during long experimental runs a Compton transmission spectrometer is foreseen. A similar device has recently been developed for the A4 experimental setup at Mainz [8]. The use of Compton backscattering polarimeters is not possible because of the limited current at these experimental sites.

SUMMARY

The polarized beam program at the S-DALINAC is soon going to start. First planned experiments are sketched in ref. [9]. The test stand set up for the polarized source has been completed and the installation at the S-DALINAC will soon proceed. Necessary beam diagnostic elements to monitor the polarization of the beam at different areas of the beam line are completed or planned. First experiments with polarized beams will start in 2010 and collaboraters for further experiments are welcome.

ACKNOWLEDGMENTS

The S-DALINAC and this work are supported by the Deutsche Forschungsgemeinschaft through SFB 634. We would like to thank K. Aulenbacher and V. B. Asgekar for helpful discussions in the development of the 100 keV Mott polarimeter and H. Schmieden and co-workers for support with the polarization measurement of the vacoflux foil. The author likes to thank the SPIN 2008 organizing committee for financial support.

REFERENCES

1. A. Richter, "Operational Experience at the S-DALINAC," in *Proc. of the 5th EPAC*, 1996, p. 110.
2. D. Pierce, et al., *Rev. Sci. Instrum.* **51**, 478 (1980).
3. C. Heßler, *Konzeption, Aufbau und Test einer Quelle spinpolarisierter Elektronen für den supraleitenden Darmstädter Elektronenlinearbeschleuniger S-DALINAC*, Doctoral thesis D17, TU Darmstadt (2008).
4. C. Heßler, et al., "Comissioning of the Offline-Teststand for the S-DALINAC Polarized Injector SPIN," in *Proc. of the 11th EPAC*, 2008, p. 1482.
5. Y. Poltoratska, *Setup and Design of a 100 keV Mott-Polarimeter for the future S-DALINAC Polarized Injector*, Diploma thesis, Kharkiv Karazin National University and TU Darmstadt (2005).
6. Y. Poltoratska, et al., Polarized eletrons in Darmstadt: recent developments, these proceedings (2008).
7. R. Barday, et al., "Electron beam polarimetry at S-DALINAC," in *Proc. of the 11th EPAC*, 2008, p. 1476.
8. C. Weinrich, *Eur. Phys. J. A* **24**, 129 (2005).
9. C. Eckardt, et al., Polarized Eletrons for Experiments at Low Momentum Transfer SPIN @ S-DALINAC, these proceedings (2008).

Benchmark studies among own and commercial beam tracking codes on fundamental conditions

Naoto Yamamoto*, Akihiko Mizuno†, Kai Masuda**, Koichi Kan‡, Shuji Matsumoto§ and Masashi Yamamoto¶

*Graduate School of Engineering, Nagoya University, Furo-cho, Chikusa-ku, Nagoya, Aichi,464-8602 Japan
†JASRI/SPring-8, Mikazuki, Sayo, Hyogo 679-5198, Japan
**Institute of Advanced Energy, Kyoto University, Uji, Kyoto 611-0011, Japan
‡The Institute of Scientific and Industrial Research (ISIR) Osaka University, Mihogaoka 8-1, Ibaraki, Osaka 567-0047. JAPAN
§KEK. 1-1 Oho. Tsukuba-shi. Ibaraki-ken. 305- 0801. Japan
¶Accuthera Inc.,2-7-6 Kurigi, Asaoku, Kawasaki-city, Kanagawa, Japan

Abstract. In order to design accelerators or to analyze experimental data, commercially or non-commercially programs for tracking particles have been developed and used. However the reliabilities of those programs are not clear, especially if the beam quality is as high as that required for future applications. Therefore, for the purpose to study the reliabilities and to improve their accuracy, we planed to benchmark those programs. As a first step, the calculations were carried out in the both condition of free space and homogeneously accelerating-field by using three own codes and three commercial codes (MAGIC, PARMELA, and GPT)

Keywords: beam tracking, electron source, simulation cord
PACS: 29.25.Bx, 41.75.-i

INTRODUCTION

The generation and transportation of low emittance and high brightness electron beams are important technologies for future generation accelerators. For example, an energy recovery linac requires a beam emittance of 0.1 π mm mrad with a peak current higher than 4 A at the source [1].

To design accelerators satisfied with such requirements, particle tracing become a very powerful tool. For this purpose, some simulation cords such as PARMELA [2], GPT [3] and MAGIC [4], have been provided commercially and some researchers have developed their own cords.

One of authors (N. Y) has also developed his own cord to design polarized electron sources (PESs). The cord is possible to trace thousands of macro particles through complex electromagnetic fields taking all 3D effects, space-charge forces and image-charge forces near the source material into account by using 4th-order Runge-Kutta method as a function of time. In fact, this tracing cord was successfully used to design a emittance measurement system for the 200–kV PES [5] and a high brightness gun for the 20–kV PES [6] [7] at Nagoya University.

Though the tracing cords described above have been used in various reseach groups, the reliabilities of those cords are not clear in the especially case that the beam perfor-

mances are as high as that required for future applications. Therefore, for the purpose to study the reliabilities and to improve those accuracies, we planed to benchmark those tracing cords. We have to note that the purpose of our bench mark is not to decide the superiority or inferiority of the codes.

In this report, the collaborator and their cords, the assignment for benchmarking are described. A example of benchmarking result is also reported, however, the data analysis and detail discussions will be given in a forth coming paper.

SIMULATION CORDS

The benchmark studies have been carried out with 6 researchers in Japan and using 6 codes. The list of tracing cords is shown in Table 1. There are three own cords and two (own cord 1 & 2) of them can trace macro particles by using 3D point to point method. One of them (own cord 3) uses the method of particle in cell instead of 3D point to point. Detail descriptions of own cord 1 and 3 were given in ref [8] and [9] respectively. In addition to three own cords, three commercially cords are also employed. Those are MAGIC, PARMELA and GPT.

BENCHMARK ASSIGNMENT

For the benchmarking test, we decided the definition of beam parameters (beam size, bunch length, energy spread and emittance) and four conditions of benchmarking test written below have been assigned.

- Comparison with numerical analysis (Envelop Equation)
  1. Beam envelop in free space
  2. Beam envelop in DC / RF fields
- Comparison with experimental results
  3. RF-gun system in Osaka Univ. (ISIR) [10]
  4. SPring-8 Compact SASE Source (SCSS) [11]

The conditions of 1 and 2 were assigned for the purpose to find the basic character of each cord, such as dependences of accuracy on beam energy, charge densities in bunch, number of macro particles. In addition, in these conditions, the result can be compared with analytical result calculated by the envelop equation [12], as follows:

TABLE 1. the list of simulation cords.

index name in this paper	calculation method	cord name & collaborator	
own cord 1	3D point to point	own cord	A. M
own cord 2	3D point to point	own cord	N. Y
own cord 3	2D particle in cell	own cord	K. M
MAGIC	2D particle in cell	MAGIC	S. M
PARMELA	2D	PARMELA	K. K
GPT	3D particle in cell & point to point	General Particle Tracer	M. Y

$$\frac{d^2x}{ds^2} = \frac{eQ}{4\pi\varepsilon_0\, m_0c^2\, \gamma^3\beta^2\, x} \frac{1}{\sqrt{\frac{L^2}{4} + \frac{x^2}{\gamma^2}}} \tag{1}$$

$$\frac{d^2z}{ds^2} = \frac{eQ}{4\pi\varepsilon_0\, m_0c^2\, \gamma^3\beta^2\, R^2\, z} \left(\sqrt{4z^2 + \frac{R^2}{\gamma^2}} - \sqrt{\frac{R^2}{\gamma^2}} - 2z \right) \tag{2}$$

where, x and z are a transverse distance and a longitudinal distance from bunch center, z is a longitudinal distance of bunch center from the origin, R and L are a radial beam size and a bunch length, and β and γ are relativistic factor of the electron.

Simultaneously, we planed to be compared our calculation to experimental results obtained by various groups. At present, RF-gun system in Osaka Univ (ISIR) and SPring-8 Compact SASE Source (SCSS) was scheduled.

PRELIMINARY RESULT

As examples, comparison of calculation results with each cord and the envelop equation are shown in Fig 1. In this calculation, a electron beam in free space was traced for the traveling distance of 1 m and the beam paremeter at the traveling distance of 0 m was set with initial conditions of charge per bunch of 1 nC, a beam diameter of 1 mm flat-top, a beam bunch length of 200 mm and a beam energy of 500–kV. The alphabets (a, b, c and d) of each plot indicate the comparison results of beam radius, pulse length, normalized emittance and energy spread, respectively.

In Fig 1, we obtained good agreement for the envelop of beam radius and pulse length between each cord and the envelop equation. On the other hand, the disagreements were apparent on the envelop of normalized emittance and energy spread. Though other data was not shown in this report, similar behaviors were obtained with the different initial conditions, which is a beam bunch length of 3 mm and beam energies of 1, 3 and 6 MeV.

As results of this series of calculations, however this is only one example of our achievements, it is found that some cords do not have enough accuracy in the range of low energy, which mean the conditions that the energy of particles is less than or around equal to a few MeV. Futhermore, we considered that differences in calculation methods and inital distribution of particles between tracing cords caused these disagreements. Then additional calculations have been made with more optimized conditions.

SUMMARY

The benchmark studies have been carried out by using three own cords and three commercial cords (MAGIC, PARMELA, and GPT). As a first step, the calculations in the both conditions of free space and homogeneously accelerating-field were carried out and some discrepancies were apparent on the envelop of normalized emittance and energy spread. Additional benchmark studies have been made to understand the reason of those discrepancies and to improve our own cords. The detail descriptions will be given in a forth coming paper.

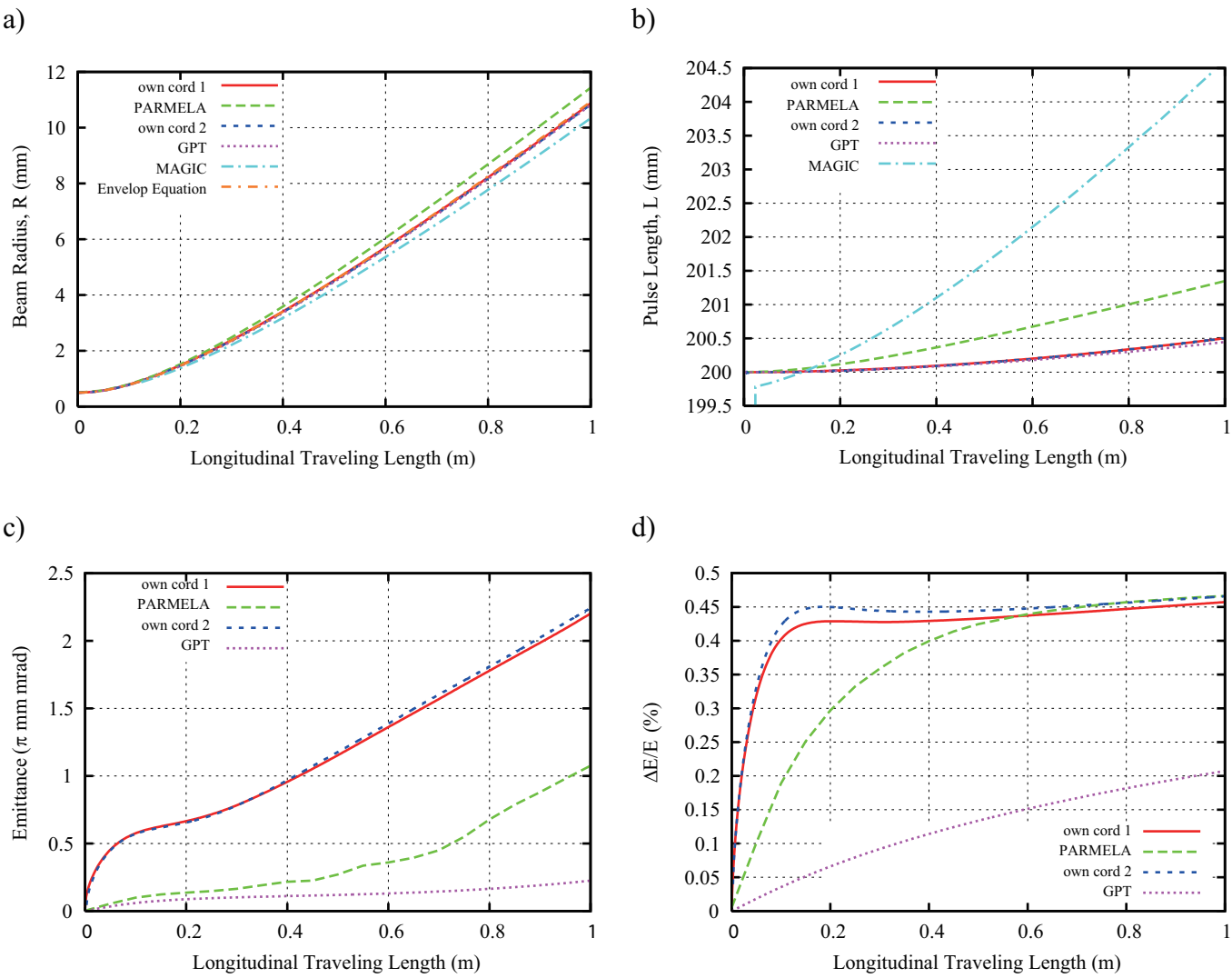

FIGURE 1. Comparison of calculation results in free space by each cord as a function of the longitudinal traveling distance. The alphabets of each plot indicate a) beam size, b) pulse length, c) normalized emittance and d) energy spread. The initial beam parameters are a energy of 500–kV, charge per bunch of 1 nC, a beam diameter of 1 mm flat-top and a pulse length of 200mm

Simultaneously, the calculation in the accelerating field and more realistic conditions, such as RF Gun system in Osaka University and SPring-8 compact SASE Source have been started.

ACKNOWLEDGMENTS

They wish to thank Dr. J. Yang and T. Shintake for providing the detail information of experimental setup and experimental results at each facility. One of authors (N. Yamamoto) extends his gratitude to Professor T. Nakanishi for the continuous encourage-

ments of his tracing cord developing research. He has been financially supported by the Hori Information Science Promotion Foundation.

REFERENCES

1. S. M. Gurner, D. Bilderback, I. Bazarov, K. Finkelstein, G. Krafft, L. Merminga, H. Padamsee, Q. Shen, C. Sinclair, and M. Tigner, Review of Scientific Instruments **73**, 1402 (2002).
2. L. Young and J. Billen, Tech. Rep., LA-UR-96-1835 (1998).
3. M. de Loos and S. van der Geer, in *Proc. 5th Eur. Particles Accelator Conf* (1998).
4. B. Goplen, L. Ludeking, D. Smith, and G. Warren, Computer Physics Communications **87**, 54 (1995), ISSN 0010-4655.
5. N. Yamamoto, M. Yamamoto, M. Kuwahara, R. Sakai, T. Morino, K. Tamagaki, A. Mano, A. Utsu, S. Okumi, T. Nakanishi, et al., Journal of Applied Physics **102**, 024904 (2007).
6. N. Yamamoto, T. Nakanishi, A. Mano, Y. Nakagawa, S. Okumi, M. Yamamoto, T. Konomi, X. Jin, T. Ujihara, Y. Takeda, et al., Journal of Applied Physics **103**, 064905 (2008).
7. N. Yamamoto, X. Jin, A. Mano, Y. Nakagawa, and Nakanishi, this Proceedings (2009).
8. A. Mizuno, T. Asaka, H. Dewa, T. Kobayashi, S. Suzuki, T. Taniuchi, H. Tomizawa, K. Yanagida, H. Hanaki, and M. Uesaka, Nuclear Instruments and Methods in Physics Research Section A: Accelerators, Spectrometers, Detectors and Associated Equipment **528**, 387 (2004), ISSN 0168-9002, proceedings of the 25th International Free Electron Laser Conference, and the 10th FEL Users Workshop.
9. K. Masuda, K. Yoshikawa, M. Ohnishi, Y. Yamamoto, H. Toku, M. Sobajima, and J. Kitagaki, Microwave Theory and Techniques, IEEE Transactions on **46**, 1180 (1998), ISSN 0018-9480.
10. J. Yang, T. Kondoh, K. Kan, T. Kozawa, Y. Yoshida, and S. Tagawa, Nuclear Instruments and Methods in Physics Research Section A: Accelerators, Spectrometers, Detectors and Associated Equipment **556**, 52 (2006), ISSN 0168-9002.
11. T. Shintake, T. Tanaka, T. Hara, K. Togawa, T. Inagaki, Y. Kim, T. Ishikawa, H. Kitamura, H. Baba, H. Matsumoto, et al., Nuclear Inst. and Methods in Physics Research, A **507**, 382 (2003).
12. A. Mizuno (2006), unpublished electronic article, URL `http://acc-web.spring8.or.jp/~workshop/e-gun/benchmark/envelop.pdf`.

3D Modeling of the ALICE Photoinjector Upgrade

J.W. McKenzie, B.L. Militsyn, Y.M. Saveliev

STFC Daresbury Laboratory, Warrington, WA4 4AD, United Kingdom

Abstract. The injector for the ALICE machine (Accelerators and Lasers In Combined Experiments) at Daresbury Laboratory is based around a 350 kV DC photocathode electron gun. An upgrade is proposed to introduce a load-lock GaAs photocathode preparation facility to allow rapid transfer of photocathodes to the gun without breaking the vacuum system. In the current design this requires side-loading of the photocathodes into the cathode ball. An alternative is to relocate the ceramic insulator vertically which will allow back-loading and also back-illumination of the photocathodes. 3D electrostatic simulations of the gun chamber are presented for both options along with 3D beam dynamic simulations for an off-axis photocathode, introduced to increase photocathode lifetime by reducing damage by ion back-bombardment. Beam dynamic simulations are also presented for the entire injector beamline as well as for a proposed extension to the injector beamline to include a diagnostic section.

Keywords: Electron sources; linear accelerators; electron and positron beams
PACS: 29.25.Bx; 29.20.Ej; 41.75.Fr

INTRODUCTION

ALICE is a 35 MeV energy recovery linac undergoing commissioning at Daresbury Laboratory [1]. The injector is based around a 350 kV DC photocathode gun which is a modified version of the gun developed for the Jefferson Laboratory Infra-Red FEL [2]. Electron bunches with charge 80 pC are produced from a GaAs photocathode illuminated by laser pulses of wavelength 532 nm. Currently the photocathodes are activated *in situ* in the gun chamber by means of a Cs and NF_3 or O_2 "yo-yo" procedure. Replacing the photocathode takes weeks due to the requirement to break the vacuum, replace the photocathode, and then restore the vacuum to the operational level of 10^{-11} mbar. An upgrade is planned to introduce an external load-lock photocathode preparation facility to reduce changeover downtime to a matter of hours [3]. Details of this three-chamber design can be found in [4]. This facility will use new GaAs photocathodes currently under development [5], with a reduction in diameter from 25 mm, as currently used in ALICE, to 10 mm.

SIDE-LOADING GUN OPTION

It is proposed that the photocathodes are loaded from the preparation chamber into the side of the gun, in order to avoid disruption to the existing ALICE infrastructure. This involves a re-design of the cathode ball from the present rear-loading mechanism. The

ball requires a slot in the side for loading of the photocathode. This has been positioned on the cylindrical part of the ball surface to keep the field distortion low. The photocathode then has to be moved forward into position, requiring a second slot further back in the cathode ball for insertion of a magnetic screwdriver to drive the winding mechanism. A third slot, perpendicular to the loading slot, might be required as a viewport to ensure the photocathode is loaded properly. Figure 1 shows the electric fields at 350 kV on the cathode ball surface, modelled in CST Studio [6]. The electric field has been kept lower than 10 MV/ on the curved surface of the ball and also around the edges of the slots. A focussing electrode has been added and optimised by performing beam dynamic simulations in ASTRA [7]. Figure 2 shows that the transverse beam properties for the new gun design compared to the existing gun which lacks the focussing electrode.

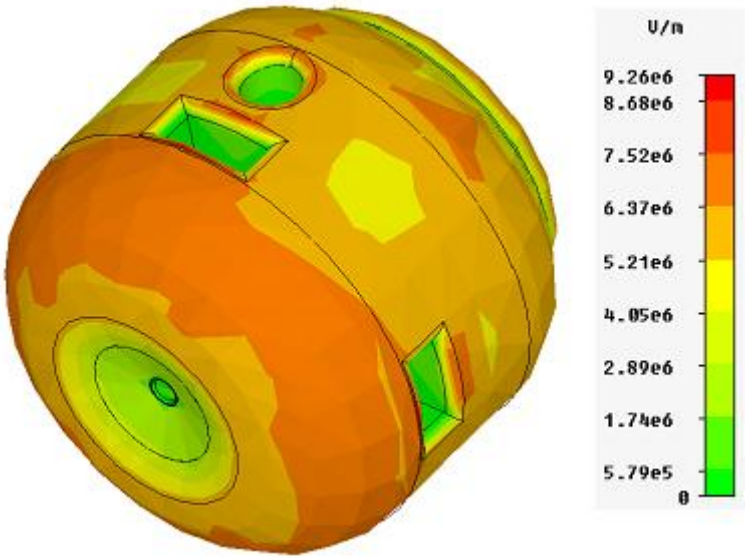

FIGURE 1. The cathode ball with slots and focusing electrode showing electric fields.

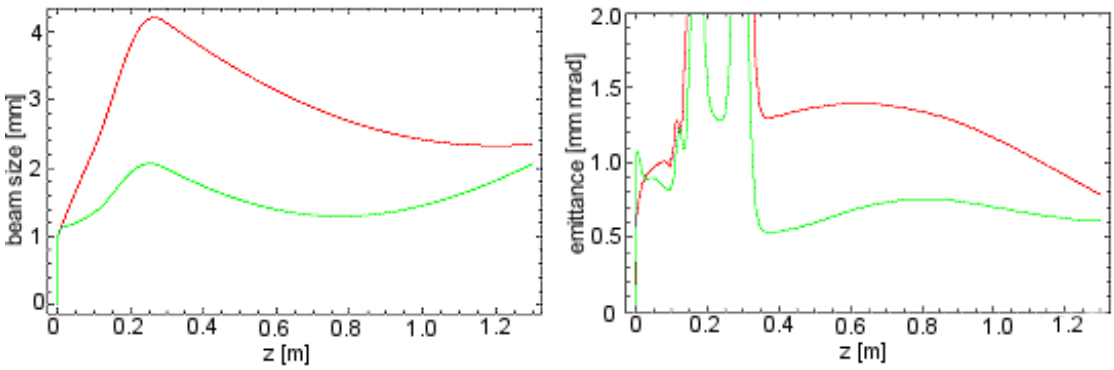

FIGURE 2. RMS beam size (left) and transverse emittance (right) for the new gun design (green) compared to the current gun (red) including a 330 G solenoid at 0.25 m.

VERTICAL CERAMIC GUN OPTION

As an alternative to the side-loading design, the ceramic insulator can be relocated vertically to allow back-loading of the photocathodes. This would also allow back-

illumination of transmission-mode photocathodes and should be more mechanically stable. However, this requires relocation of the gun power supply and ancillary equipment. Electrostatic simulations have been performed using CST Studio, shown in figure 3. The cathode stem introduces a vertical component of electric field along the electron beam trajectory, peaking at 1.5 kV/m. This is small compared to the peak of the longitudinal electric field of 5 MV/m. 3D fieldmaps were extracted and used in GPT [8] to perform particle tracking simulations with space charge. These show that the vertical field displaces the beam by an almost negligible amount.

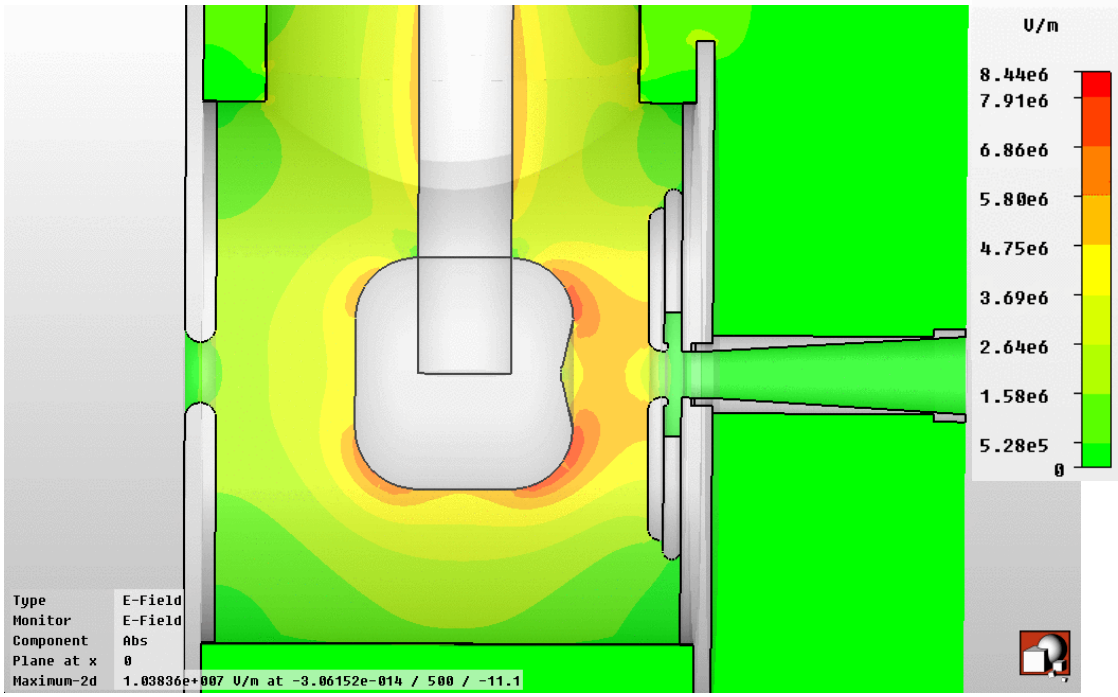

FIGURE 3. Electric fields in the gun chamber for the vertical ceramic design at 350 kV.

OFF-AXIS BEAM TRANSPORT

The lifetime of photocathodes is a major issue for regular operation of photoelectron guns. The principle cause of photocathode degradation is ion back-bombardment. When the gun is in operation, ions are produced by collision of the electron beam with residual gases and accelerated directly back towards the cathode. These ions acquire a large acceleration but little transverse displacement. Therefore, citing the photocathode off-centre should result in fewer ions striking the photocathode surface, thus increasing the photocathode lifetime. One method currently in use is to direct the drive laser off-centre on the photocathode [9]. When designing a new gun, two further options present themselves - situating the photocathode off-centre on the cathode ball, or situating the whole cathode ball off-axis. Previous GPT simulations [10] show that for the offset ball, the electron beam still moves parallel to the optical axis, thus ion damage should remain the same, whereas the off-centre photocathode produces a beam which moves directly away from the photocathode. Both horizontal and vertical steering coils are placed around the beampipe at the same position as the solenoid and

simulations in GPT show that these can be used to steer the beam parallel to the beampipe whilst retaining an emittance of 1 π mm mrad, as can be seen in figure 4.

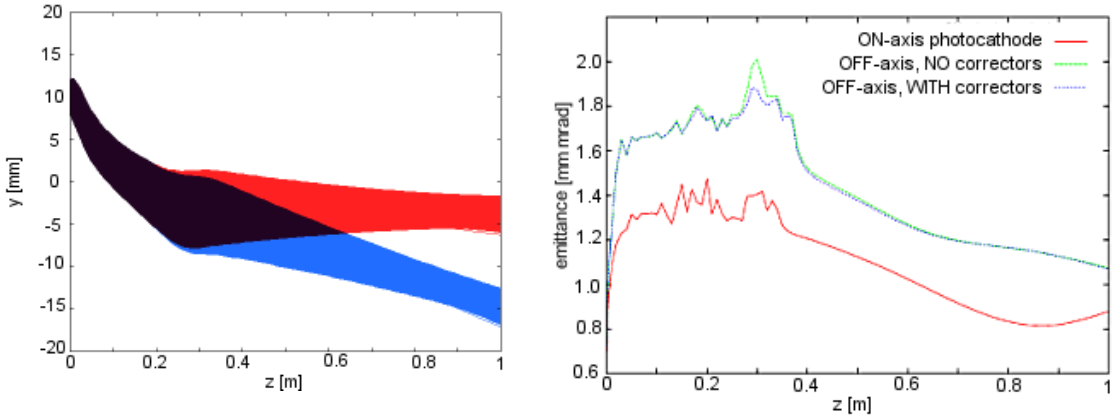

FIGURE 4. (a) Particle trajectories for a 10 mm off-centre photocathode including a 300 G solenoid both with (blue) and without (red) steering coils. **(b)** Transverse emittance for the off-centre photocathode compared to the on-axis version.

GUN BEAMLINE UPGRADE

During the ALICE gun commissioning phase a dedicated diagnostic beamline was used to characterize the beam. For the commissioning and operation of the full ALICE machine, this was removed, leaving just two focusing solenoids, three sets of steering coils, a buncher cavity, and a single YAG screen before the superconducting booster cavity. An extension to the current gun beamline is proposed to reinstate some diagnostics. The layout is shown in figure 5.

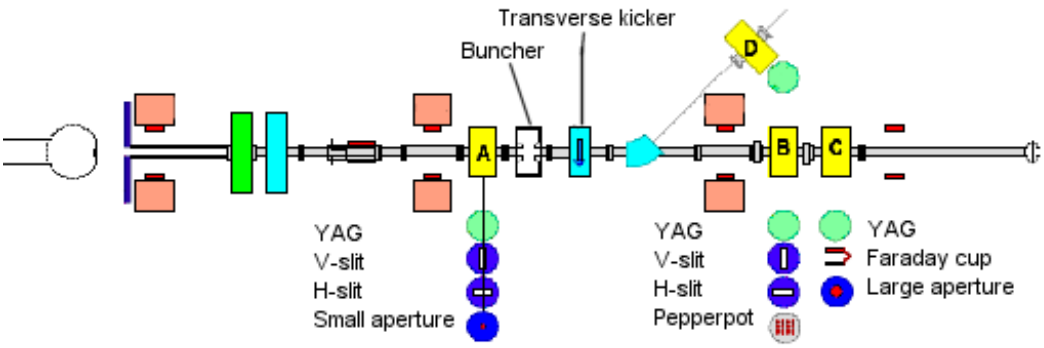

FIGURE 5. Schematic of the gun beamline upgrade showing components in each diagnostic unit.

A RF transverse kicker and dipole leading to a YAG screen orientated above the gun beamline will allow for longitudinal profile, energy, and bunch length measurements. A pair of horizontal and vertical slits plus a pepperpot provide the ability for emittance measurements and an insertable Faraday cup will be used for measuring the bunch charge. Two apertures are included: one small (~1 mm) to give the option of operating ALICE at low bunch charges without having to reset the setup of the photocathode gun; and one larger aperture to cut off any halo that may be produced along with the core beam. The positions of the first diagnostic unit, buncher and second solenoid have been reversed from the initial gun beamline in order to

perform measurements with the solenoid switched on. An additional solenoid and set of steering coils are needed to provide good beam transport into the booster module for this extended beamline. The total additional length of the beamline is 1.2 m which involves moving the entire gun and power supply systems backwards. The extra length of this beamline means that there is a smaller range of parameters for good beam transport. Figure 6 shows the results of beam dynamics simulations performed using ASTRA, compared to the existing injector design. They show that although there is an increase in transverse emittance, there is a decrease in both bunch length and longitudinal emittance which combined with the benefit of the added diagnostics, will improve the operation of the ALICE facility.

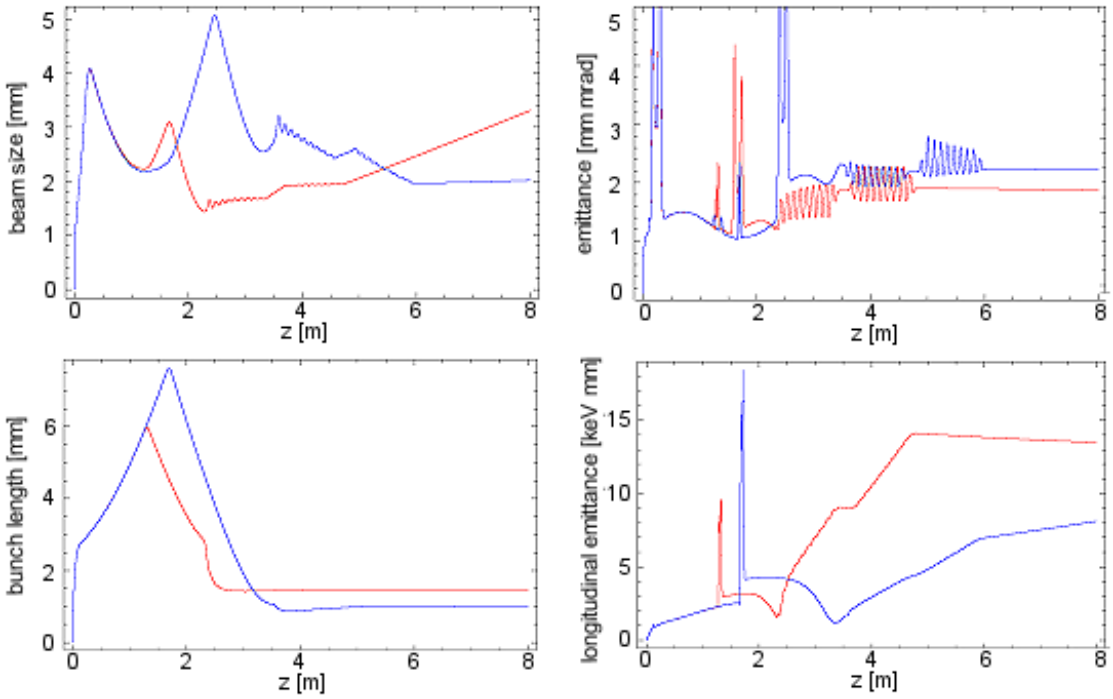

FIGURE 6. Beam dynamic simulations comparing the current gun beamline (red) with the upgraded beamline design (blue).

REFERENCES

1. L.B. Jones et al., *"Status of the ALICE Energy Recovery Linac"*, these proceedings
2. T. Siggins *et al.*, *"Performance of a DC GaAs photocathode gun for the Jefferson lab FEL"*, NIM A 475 (2001) 549-553
3. B.L Militsyn et al., *"Design of an upgrade to the ALICE photocathode electron gun",* Proceedings of EPAC 2008
4. K.J. Middleman et al., *"Photocathode preparation system for the ALICE photoinjector"*, these proceedings
5. L.B. Jones et al., "*Cooled transmission–mode NEA–photocathode with a band–graded active layer for high brightness electron source"*, these proceedings
6. CST Studio Suite, http://www.cst.de
7. K. Flöttmann, ASTRA, http://www.desy.de/~mpyflo
8. M.J. de Loos and S.B. van der Geer, General Particle Tracer, http://www.pulsar.nl/gpt
9. C. Hernandez-Garcia et al., *"A high average current DC GaAs photocathode gun for ERLs and FELs"*, Proceedings of PAC 2005
10. J.W. McKenzie and B.L. Militsyn, *"3D simulations of a non-axisymmetric high average current DC photocathode electron gun"*, Proceedings of EPAC 2008

Polarized Positrons at Jefferson Lab

J. Dumas[a,b], J. Grames[b], E. Voutier[a]

[a]*Laboratoire de Physique Subatomique et de Cosmologie*
IN2P3/CNRS – Université Joseph Fourier - INP
53, rue des Martyrs, 38026 Grenoble Cedex, France
[b]*Thomas Jefferson National Accelerator Facility*
12000 Jefferson Avenue, Newport News, VA 23606, USA

Abstract. A novel concept for producing polarized positrons at Jefferson Lab using the CEBAF polarized electron photo-injector is presented. This approach relies on the polarization transfer from low energy highly polarized electrons to positrons via bremsstrahlung followed by pair production in a conversion target. An experiment to test this concept is discussed on the basis of GEANT4 simulations. It is shown that this low energy approach, which benefits from recent advances in high current high polarization electron sources, can yield positron longitudinal polarization up to 40%.

Keywords: Positron source, polarization transfer, electron sources.
PACS: 29.25.Bx, 41.75.Ht, 23.20.Ra, 07.77.Ka

INTRODUCTION

The high spin polarization of the electron beam at the Continuous Electron Beam Accelerator Facility (CEBAF) at Jefferson Laboratory (JLab) is a significant feature of this facility. More generally, the polarization of a beam is a key element for the completion of a physics program and the achievement of precision physics. In addition, the sensitivity of electromagnetic processes to the charge of a lepton beam is a fundamental property, revealing singular features of a system when comparing negative and positive lepton responses. In the JLab context, a *polarized positron beam* would offer a unique opportunity for the study of Generalized Parton Distributions [1] or the two-photon exchange mechanisms, and globally the deep scattering processes.

An efficient scheme for positron production, widely used in particle accelerators, relies on the creation of electron-positron pairs from high energy photons. A significant aspect of the process is the dependence on the polarization, in particular, the circular polarization of the photon transfers to the longitudinal polarization of the positron [2]. A concept to generate polarized positrons from undulator-generated polarized photons [3] has recently been demonstrated by the E-166 experiment [4], in view of its application to the International Linear Collider (ILC) project. There, circularly polarized photons (~10 MeV) are created via synchrotron radiation using very high energy electrons (~50 GeV) travelling through a helical undulator, and are then converted into positrons via pair-creation. In contrast with this scheme, a new concept using a low energy (10 MeV) highly polarized electron beam to produce polarized positrons for the JLab physics program is hereafter discussed.

JLAB POLARIZED POSITRON SOURCE CONCEPT

Similarly to pair creation, the bremsstrahlung process is a polarization sensitive mechanism. This property has been widely used at un-polarized electron accelerators to produce linearly polarized photon beams. In addition to the intrinsic linear polarization (L), the photons have a circular component (C) when the incoming electron beam is polarized, such that the bremsstrahlung of polarized electrons most generally lead to elliptically polarized photons [2,5]. The polarization component ratio C/L depends on the electron and photon energies, and is proportional to the electron beam polarization.

The proposed JLab polarized positron source concept takes advantage of recent advances of high-current high-polarization electron sources using GaAs-based photocathodes that simultaneously have both high electron polarization (>80%) and high quantum efficiency (~1%). Recent advances in electron gun performance have resulted in improved photocathode lifetime and sustainable high average current (1 mA) in a configuration suitable for an accelerator has been demonstrated [6]. At the CEBAF photo-injector a high intensity and highly polarized continuous electron beam would interact in a thin tungsten target foil to produce polarized positrons via bremsstrahlung followed by pair-creation. A thin target is chosen to limit the emittance of the positrons exiting the target as well as limit the extent of radiation. In this respect, a low electron beam energy (~10 MeV) helps limit photo-neutron production. The emitted positrons would then be selected in a given energy range, suitable for subsequent acceleration by the CEBAF system [7]. An experiment at the CEBAF photo-injector is presently considered to test and characterize this concept. Some key aspects are summarized in Table 1 along with those of the E-166 experiment. Practical ingredients for testing this concept are the pre-existing electron photo-injector and relatively small foot-print and cost for a conversion target and diagnostics beam line. An actual source for the CEBAF accelerator would be more sophisticated and costly, yet continue to be based upon the pre-existing photo-injector.

TABLE 1. Key aspects of the JLab and E-166 polarized positron generation schemes.

	JLab	**E-166 [4]**
Electron beam energy	~10 MeV	~50 GeV
Electron beam polarization	85 %	Un-polarized
Photon production	Bremsstrahlung	Synchrotron
Converter target	Tungsten foil	Tungsten foil
Positron polarization	40% (simulated)	80% (measured)

SIMULATIONS

To study the proposed concept, particle interactions in a material are simulated with GEANT4 [8]. In particular, we expect the production of particles to follow the bremsstrahlung and pair creation cross-sections which are respectively given in [9] and [10]. One consideration is the incident electron energy. The electromagnetic shower is larger for high energy electrons in a high Z (atomic number) medium and photons created with higher energy are more likely to produce positrons, however, the energy distribution of bremsstrahlung photons decrease as $1/E_\gamma$. Another consideration is the transfer of polarization in an electromagnetic shower, also implemented in

GEANT4 [11]. Using Stokes parameters [5], each particle is followed, step-by-step, including the polarization transfer for bremsstrahlung and pair creation calculated by Olsen and Maximon [2], as well as depolarization due to bremsstrahlung, ionization, Compton and Moller/Bhabha scattering. For these processes, the polarization transfer is determined [3] as a function of the particle kinematics. These kinematic quantities are also combined into two parameters that determine the Coulomb and screening corrections of the cross-section and polarization transfer coefficients. These corrections to the Born approximation have been evaluated for the ultra-relativistic and small angle limits, which are known to be inaccurate at small energy [12]. In particular for the JLab concept, where energy distribution of the photon is near the pair-creation threshold, it is legitimate to question the effects of the mass-less electron and Lorentz focusing approximations. This problem is presently under study in view of an improved implementation in GEANT4. In the context of these simulations, calculations are limited to an ultra-relativistic Coulomb correction [13] and to the complete screening approximation, which presently appears in GEANT4 as the prescription in the considered low energy range.

Finally, GEANT4 was used to simulate the energy, yield and polarization distributions for a CEBAF electron beam with total energy of E = 5 MeV, longitudinal polarization P = 85% and current I = 1 mA. The target used in the simulation is a 250 μm thick tungsten foil. A contour plot of the distribution is shown in Fig. 1 where the positron energy is normalized to incident electron beam energy. In this simulation, first moments of the distribution yield a positron polarization of 43% and energy of 1.5 MeV.

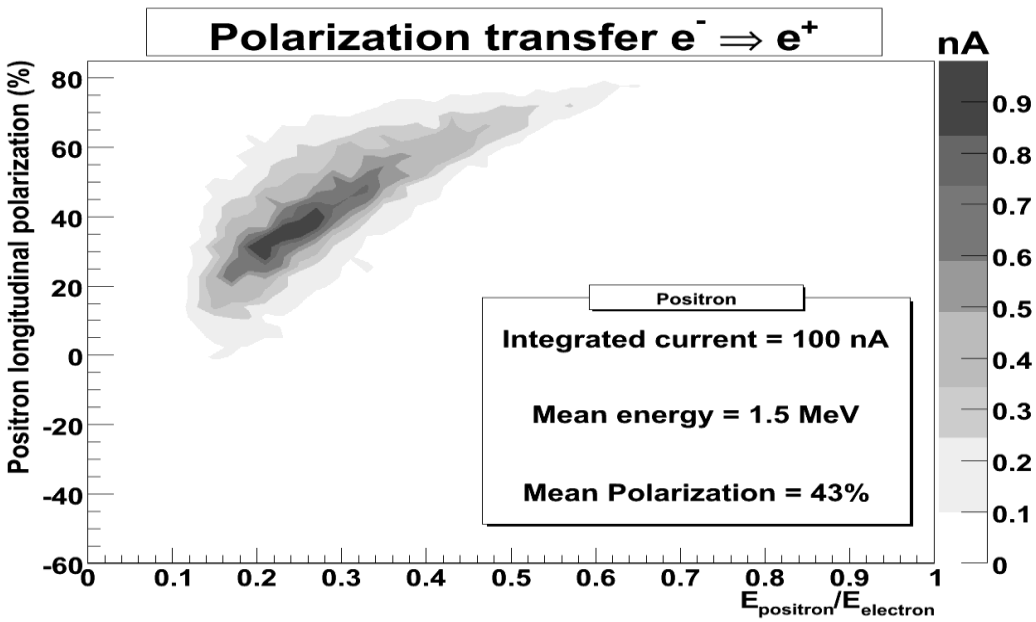

FIGURE 1. GEANT4 positron distribution of an electron beam E = 5 MeV, P = 85% and I = 1 mA incident on a 250 μm thick tungsten target foil.

TEST OF CONCEPT

An experiment is planned to test the proposed concept, making use of the existing CEBAF electron photo-injector. A highly polarized electron beam (>80%) is produced using a strained superlattice GaAs/GaAsP photocathode inside a 100 kV DC high voltage electron gun. Electron bunches are emitted from the photocathode using a high-power fiber-based laser pulsing synchronously (1497 MHz) with the accelerating frequency. The low energy (100 keV) electrons are bunched, captured and accelerated to intermediate energy (<10 MeV) with small emittance ($\varepsilon_{n,rms}$ < 1 mm-mrad) and low energy spread ($\delta E/E < 2 \times 10^{-5}$). At this point the electron beam may be deflected to a Mott polarimeter to measure the electron polarization, a diagnostics beam line to measure the electron beam momentum (energy) or transverse profile, or toward the main accelerator. To test the polarized positron concept a new beam line is required containing the conversion target and means to characterize the positron distribution, limit the background and dump the primary electron beam.

The converter target is an important part of the positron source. The target should have a high atomic number (Z) to be more efficient for the production of an electromagnetic shower, but have sufficiently high thermal conductivity and melting point to dissipate deposited beam energy loss. Tungsten (Z = 74) is a good choice with a high melting point (3695 K) and can be made in a thin foil. A thinner target reduces positron yield, however, collection becomes easier because the electromagnetic shower is limited. As an example, the total integrated positron yield and deposited power versus target thickness resulting from an incident 5 MeV electron beam with current of 1 mA is shown in Fig. 2. The optimum positron yield ($Ne^+/Ne^- \sim 10^{-4}$) occurs at a target thickness of 0.5 mm, corresponding to considerable power deposited in the target. To initially avoid high power issues a low duty factor pulsed electron beam may be used, however, optimization of target thickness, target cooling, positron yield and polarization are ultimately to be considered in any practical source operating a high average current.

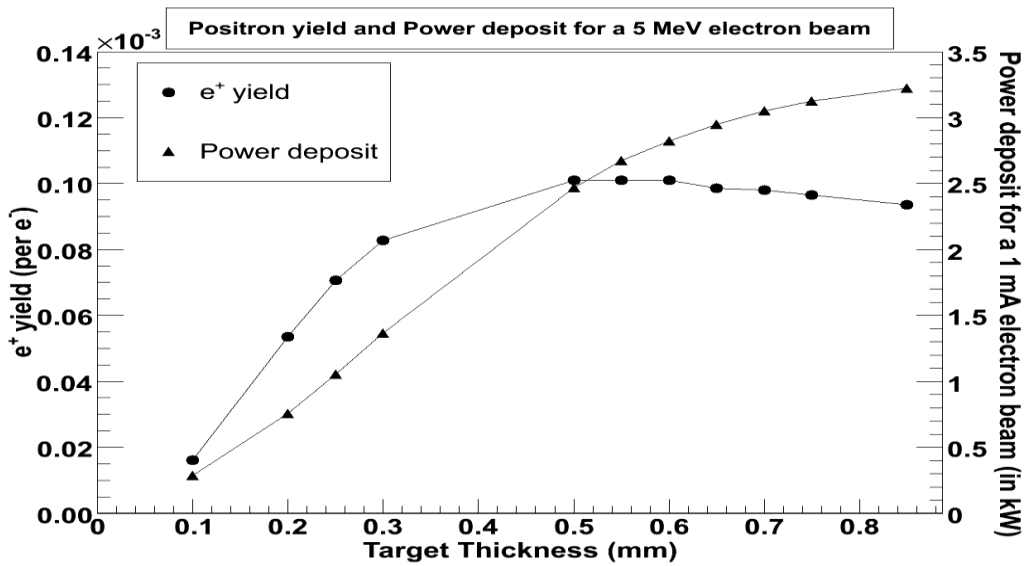

FIGURE 2: Positron yield (left axis) and deposited power (right axis) are plotted versus target thickness for a 5 MeV, 1 mA electron beam normally incident on a tungsten foil.

Ultimately, the shower of particles exiting the conversion target must be separated and isolated using a combination of spectrometer magnets and collimators to be analyzed and counted. Of interest are testing the positron and photon polarization when compared to the theory and simulation routines used by GEANT4, particularly at low energy and with respect to the aforementioned Coulomb and screening corrections. The intent is to measure the positron and photon polarization using a Compton transmission polarimeter [14].

SUMMARY & OUTLOOK

A novel concept for producing polarized positrons at Jefferson Lab using the CEBAF polarized electron photo-injector is presented. The concept relies on transferring the electron beam spin polarization, via bremsstrahlung and pair production in a conversion target, to the positrons. Initial GEANT4 simulations indicate a positron polarization of 40% should be accessible with the present CEBAF photo-injector. An experiment to test this concept, benchmark modeling tools and collect valuable technical information for the design of an actual source is planned.

REFERENCES

1. E. Voutier, *Proc. of the XVIIIth Symposium on Spin Physics*, Charlottesville (Virginia, USA), October 6-11, 2008.
2. H.A. Olsen, L.C. Maximon, *Phys. Rev.* **114** (1959) 887.
3. V.E Balakin and A. A. Mikhailichenko, in *Budker Institute of Nuclear Physics Report No. BINP 79-85* (1979).
4. P. Schuler et al, in *Phys. Rev. Lett.* **100** (2008) 210801.
5. W.H. McMaster, *Rev. Mod. Phys.* **33** (1961) 8.
6. J. Grames et al., in *Proc. of the 2007 Particle Accelerator Conference, THPMS064,* 3130.
7. S. Golge, in *Proc. of the 2007 Particle Accelerator Conference, THPMS067,* 3133.
8. S. Agnostinelli et al., Nucl. Inst. Meth. **A 506** (2003) 250.
9. H.W. Koch, J.W. Motz, *Rev. Mod. Phys.* **31** (1959) 920.
10. J.W. Motz, H.A. Olsen, H.W. Koch, *Rev. Mod. Phys.* **41** (1969) 581.
11. R. Dollan et al., *Nucl. Inst. Meth.* **A 559** (2006) 185.
12. E. Borie, *Nuo. Cim.* **A 11** (1972) 969.
13. H. Davies, H.A. Bethe, L.C. Maximom, *Phys. Rev.* **93** (1954) 788.
14. H. Schopper, *Nucl. Instr.* **3** (1958) 158.

Summary Report of PESP2008 - The Workshop on Polarized Electron Sources and Polarimeters

M. Poelker

Thomas Jefferson national Accelerator Facility
12000 Jefferson Ave., Newport News, VA 23606

Abstract. The Workshop on Polarized Electron Sources and Polarimeters (PESP2008) was hosted by Jefferson Lab October 1-3, 2008, in association with SPIN2008, continuing a tradition since 1983. The workshop was well attended with 84 registrants, 38 oral presentations and 17 posters. The usual topics were covered: DC and RF photoguns, high voltage issues, photocathodes, drive lasers, vacuum and polarimetry. Detailed accounts of each contribution (oral and poster) appear within these Proceedings. This submission summarizes some of the highlights of the workshop.

Keywords: polarized electrons
PACS: 29.25.Bx; 29.27.Hj

EXISTING PROGRAMS, NEW FACILITIES AND INITIATIVES

Highly productive nuclear physics experimental programs are being conducted using spin-polarized electron sources at three facilities worldwide: ELSA at the University of Bonn, Germany, the Mainz Microtron at the University of Mainz, Germany and at CEBAF/Jefferson Lab, Newport News, Virginia. The GaAs photoguns at these facilities are the product of years of research and development – they are very reliable, with adequate operating lifetime, beam current capability and polarization (80% or higher).

Other groups with an extensive history of polarized electron source development continue to conduct polarized photogun research, although the experimental nuclear and high energy physics programs at MIT-Bates and SLAC have ended. The group at Nagoya University, Japan, has made noteworthy progress developing a 200kV polarized electron source for the International Linear Collider (ILC) and they have also constructed a novel low-voltage (20kV) polarized electron source with a back-illuminated photocathode for materials science and commercial applications. The source group at the MIT-Bates accelerator has teamed with Brookhaven National Lab (BNL) to develop a high current polarized electron source to meet the requirements of eRHIC - the BNL proposal for an Electron Ion Collider (EIC). And the source group at SLAC has been actively involved in the ILC program, designing (among other things) the electron-beam photoinjector and drive laser. The speakers from these institutions addressed the unique requirements of proposed new accelerators and the need for continued photogun R&D.

It was gratifying to hear about the aspirations of polarized electron beam physics at the S-DALINAC, University of Darmstadt, Germany. The Darmstadt group has constructed a 100kV load locked polarized source and is working hard to install and commission this source at the accelerator during 2009.

PHOTOGUN DEVELOPMENT FOR LIGHT SOURCES: VERY HIGH VOLTAGE DC PHOTOGUNS

A number of accelerator-based light source programs use (or plan to use) DC high voltage photoguns to produce very bright electron beams, with small transverse and/or longitudinal emittance. Although these programs do not require polarized electrons, the photoguns at these facilities operate with GaAs photocathodes because this material provides very high quantum efficiency with readily available laser light. Extremely demanding emittance requirements necessitate extremely high bias voltage: typically -500kV or higher. A recurring theme of five presentations from photogun experts at the Jefferson Lab FEL, Cornell University, Daresbury Laboratory, and JAEA, related to high voltage problems, particularly field emission from components at high voltage and associated insulator damage that often leads to catastrophic vacuum loss. Eliminating field emission at gradients up to ~12 MV/m with bias voltage 500kV would be a major victory. Unfortunately, field emission-free operation for most labs seems limited to just ~ 7MV/m with associated maximum voltage of ~ 300kV. One topic of a lunchtime round table discussion was a desire for more robust insulators, particularly insulators with suitable bulk resistivity to “bleed off” accumulated charge stemming from field emission. Another approach uses segmented insulators incorporating metal shields to protect sensitive insulator regions from field emission. The possibility of using “inverted” insulators was discussed, where the insulator extends into the high voltage vacuum chamber eliminating the need for a metal cathode support structure that normally extends through the bore of a conventional insulator. The inverted insulator geometry has the advantage that electric field lines within the structure serve to direct field-emitted electrons toward the vacuum chamber wall at ground potential, rather than toward the insulator, preventing charge build up on the insulator and subsequent damage.

PHOTOGUN DEVELOPMENT FOR LIGHT SOURCES: WARM/COLD RF GUNS

The appealing feature of the RF gun rests in its ability to accelerate electrons to relativistic speed in a very short distance, thereby preserving good beam emittance. Beam energy from an RF gun would be in the ~ MeV range, and consequently an injector could be relatively compact, and with fewer components compared to injectors using DC photoguns. Indeed, numerous RF photoguns operate at laboratories worldwide however none produce polarized electrons and none operate CW. Prospects for producing polarized electrons from an RF gun seem distant mostly because GaAs (the only photocathode material providing polarized electrons to

accelerators today) is a delicate material, not capable of withstanding the relatively harsh environment of an RF gun – from a vacuum and field emission point of view.

DULY Research has long advocated a novel warm RF gun design called the Plane Wave Transformer (PWT), a structure with relatively low-Q but an open geometry that supports lots of vacuum pumping in the vicinity of the photocathode compared to standard RF cavity designs, which would satisfy the UHV requirement of GaAs. Removing heat from the structure (and preserving good vacuum), especially when operating in CW mode, seems to be the dominant challenge. DULY has teamed with Fermi National Accelerator Lab to construct a PWT warm-RF gun with a GaAs photocathode for the ILC and experimental results could be forthcoming in 2009. DULY is also modeling a lower energy PWT photogun for CEBAF.

The superconducting RF gun has long been considered the "holy grail" of photogun R&D because it naturally provides superb vacuum with high accelerating gradient in CW mode, without the thermal heat-load problems and concomitant cooling requirements of copper structures. Rossendorf-ZFD has constructed their second SRF gun using a Cs2Te photocathode (unpolarized). They have successfully extracted 1uA of CW beam for hundreds of hours – a significant achievement – however a number of technological challenges remain, including: reliable photocathode exchange and elimination of particulate contamination within the RF structure and subsequent field emission. They plan to operate at significantly higher average current during 2009. BNL has been working with Advanced Energy Systems to construct a very high average current SRF photogun (unpolarized) for their energy recovery linac program and more recently, their partnership has expanded to include polarized e-beam SRF gun development.

In general, SRF gun programs are costly endeavors requiring significant engineering resources and generous construction schedules. These factors make it difficult for some labs to "get in the game". Fortunately, at least two groups are working on this project and positive results could have dramatic impact on design of future accelerators.

PHOTOCATHODES

It is now common for electron beam polarization at experimental facilities to exceed 80%, a monumental achievement stemming from the development of the strained-superlattice photocathode, a structure composed of multiple pairs of very thin layers of lattice-mismatched III-V semiconductor material, for example GaAs grown atop GaAsP. The strain induced within the GaAs crystal serves to break a valence-band energy-level degeneracy that limits polarization from bulk GaAs to < 50%. By growing very thin layers (~ few nanometers thick), one ensures that the strain does not relax and by growing multiple GaAs/GaAsP layer pairs, one ensures sufficiently high QE. There is one commercial supplier of strained-superlattice photocathode material - SVT Associates - and they are now developing alternatives to their GaAs/GaAsP superlattice structure using different III-V elements, with the goal of improving QE and minimizing/eliminating problematic behavior known as "surface charge limit", where QE falls as the power of the incident light is increased. Surface charge limit is a very serious problem that reduces the effective operating lifetime of the

gun/photocathode, and likely represents one of the more serious challenges to new programs requiring high bunch charge and/or high average current. Surface charge limit is not well understood – e.g., onset, explanation of physical mechanism, prevention - and is one of the more interesting photogun research topics of the day.

The group at St. Petersburg State Polytechnic University, Russia has long been involved with development of high polarization photocathode material and they continue to model and grow new structures with success, both in terms of beam polarization and QE. A team of Japanese researchers led by T. Nakanishi of Nagoya University reported the development of a remarkable transmission photocathode, exhibiting excellent polarization and world-record beam brightness. The extracted beam is bright (i.e., the emittance small) because the transmission-style photocathode provides a means to illuminate the photocathode from behind using a short focal length lens. In this way, the drive laser beam can be made very small and consequently, the transverse dimensions of the extracted electron beam can be extremely small. The transmission photocathode is the central feature of a spin-polarized low-energy electron microscope (SPLEEM) they have built for material science research. Such a transmission photocathode could find application at accelerator-based physics research facilities, to improve beam quality/emittance and provide a means to simplify the vacuum beamline (no bend magnet required to introduce the drive laser beam into the photogun vacuum chamber, and no laser mirrors inside vacuum beamline downstream of the photogun).

LASERS

The telecommunications industry has made it possible to obtain inexpensive, high-power laser light at wavelengths ~1.06um and 1.56um, thanks to advances in Er and ErYb-doped fiber amplifier technology. This light can be converted to useful wavelengths for photoguns using conventional frequency conversion techniques. The noteworthy contribution to PESP2008 that illustrates the exciting potential of this approach was a description of the fiber-based drive laser developed at Cornell University for the 100mA energy recovery linac (ERL) program. A modelocked diode laser produces picosecond pulses at high pulse repetition rate (1.3GHz), which are delivered to high power fiber amplifiers, and then converted to green light using second harmonic generation to obtain over 15Watts average power. Such a laser system should be capable of producing the desired 100mA average beam current for the Cornell ERL, assuming the bulk GaAs photocathode inside the photogun can sustain reasonable QE (~ few %). A similar fiber-based laser system, albeit at lower average power (~ 2W), was developed at CEBAF/Jefferson Lab at 780nm wavelength suitable for high polarization photocathodes.

VACUUM

Vacuum technology and practice has always been a central issue for the polarized source community, because GaAs photocathodes can only survive within an ultrahigh vacuum environment. Initially, the challenge was to obtain suitably good vacuum to

avoid chemical contamination of the photocathode surface. Now the challenge relates to making vacuum improvements that will lead to longer operating lifetime while delivering beam, especially at high current, since lifetime of modern DC high voltage photoguns is limited by ion-backbombardment, where the extracted electron beam ionizes residual gas within the cathode/anode gap. These ions are back-accelerated toward the photocathode surface, sputtering away the chemicals used to produce a negative electron affinity condition and/or damaging the photocathode crystal. The loose consensus within the polarized source community is that polarized photoguns today operate in the low 10^{-11} Torr range. To improve vacuum further, these questions (and likely others) must be addressed:

- where does the gas inside the photogun come from?
- how to limit this gas load?
- how best to pump the gas away?
- how to accurately measure pressure at lower and lower pressure scales?

C. Sinclair of Cornell University reported very low outgassing rates (~ 10^{-14} Torr L $s^{-1}cm^{-2}$) from thin-walled stainless steel baked at 400°C for an extended duration (~ 100 hours) [1]. Similar results were obtained by baking in air or under vacuum, and this low outgassing rate was maintained after venting the chamber to atmospheric pressure with subsequent bakeout to just 150°C. However, thick end flanges are problematic, exhibiting "typical" outgassing of 10^{-12} Torr L $s^{-1}cm^{-2}$, even when baked at 400°C, which can mask the low rate of the thin-walled chamber if flange material constitutes a significant portion of the total surface area of the vacuum chamber.

Non-evaporable getter pumps, first developed at CERN, were embraced by the polarized source community about 10 years ago. These passive pumps have very large hydrogen pump speed and are now considered indispensible, providing most of the pumping in every polarized electron source used at accelerators today. P. Manini of SAES Getters presented a detailed overview of NEG technology, including the relatively new technique of coating the interior vacuum chamber wall with a thin layer of NEG material. He was unaware of limitations these pumps might have in terms of achieving better vacuum (< 10^{-12}Torr).

SUMMARY

This year's PESP workshop marked the first time photogun experts from un-polarized beam programs were invited to attend. By all accounts, the expanded scope contributed to the success of PESP2008. It was clear that both gun communities (polarized and un-polarized) face many shared technological challenges and it was mutually beneficial to learn what each group is doing. For example, the programs to develop very high voltage DC photoguns for light sources will benefit new polarized-electron beam accelerator initiatives such as the ILC, CLIC and EIC, because these same photoguns, in principle, could generate polarized electron beams by simply changing the photocathode material and drive laser wavelength. Operation at considerably higher voltage compared to today's standard 100kV is appealing because photoguns at higher bias voltage produce a "stiffer" beam, suffering less space-charge

induced emittance growth, especially when extracting high bunch charge which is a common attribute of electron beams at the new/proposed machines cited above. An ever-growing list of new workshops and conferences creates significant competition for experts and speakers - it might be difficult to gather the world's unpolarized-gun experts for each PESP workshop - but at a minimum, future PESP Organizers should invite gun experts from DC high voltage gun programs for light sources and CW-minded RF gun programs.

New accelerator proposals such as the ILC, CLIC, and EIC demand continued polarized photogun research. These machines are significantly different from today's machines. The polarized electron source community must continue to push the state of the art, even beyond the stated needs of host institutions, to eliminate potential objections to new facilities which might encounter criticism based on absence of required source technology. Some exciting R&D topics include very high average current operation, high bunch charge operation, beam handling at high average current and/or bunch charge, very high voltage operation, field emission suppression, surface charge limit reduction and extreme high vacuum.

REFERENCES

1. C. Park et al, JVST A **26**, 1166 (2008)

Workshop on Sources of Polarized Electrons and High Brightness Electron Beams	
7:30-8:30	Continental breakfast and Registration
Introduction (chair: M. Poelker)	
8:30-8:45	Welcome by Larry Cardman, Dir. Physics Division
8:45-9:15	Polarized electron beams: opening new doors to physics (Gordon Cates, Univ. of Virginia)
Polarized Guns/Programs (chair: W. Hillert)	
9:15-9:45	Status report of the new Darmstadt polarized electron injector (Y. Poltoratska, Darmstadt Univ.)
9:45-10:15	Status of 200keV beam operations at Nagoya University (Masahiro Yamamoto, Nagoya Univ.)
10:15-10:30	Coffee break
10:30-11:00	Recent polarized photocathode R&D at SLAC and future plans (Feng Zhou, SLAC)
11:00-11:30	High Intensity Polarized Electron Gun Studies at MIT-Bates (E. Tsentalovich)
11:30-12:00	Polarized Electron Beams from a Rubidium Spin Filter (Tim Gay, Univ. Nebraska)
12:00-13:30	Lunch on own, Option: JLab cafeteria adjacent to auditorium
Photocathodes (chair: J. Grames)	
13:30-14:00	Atomic hydrogen cleaning of superlattice cathodes (V. Tioukine, MAMI)
14:00-14:30	Atomic Hydrogen Cleaning at TSR Ring Heidelberg (A Terekhov and D. Orlov)
14:30-15:00	Ultra cold photoelectron beams for ion storage rings (D. Orlov, MPI Heidelberg)
15:00-15:30	Optimization of Semiconductor Superlattice for Spin-Polarized Electron Source (L. Gerchikov, St Petersburg State Polytechnic University)
15:30-15:45	Coffee Break
15:45-16:15	Study of the Activated GaAs Surface for Application as an Electron Source in Particle Accelerators (N. Chanlek, STFC Daresbury Laboratory)
16:15-16:45	Super-high brightness and high-spin-polarization electron source based on a novel transmission-type GaAs/GaAsP strained superlattice - Defects and polarization (Toru Ujihara, Nagoya Univ.)
16:45-17:15	Recent Progress toward Robust Photocathodes (Gregory Mulhollan, Saxet Surface Science)
17:15-17:45	Polarized Photocathode Development at SVT Associates (Aaron Moy, SVTA)
17:45-18:00	K2CsSb Photocathodes (J. Smedley, BNL)
18:00-20:00	Reception at CEBAF Center
20:00	Socialize at City Center, Location to be announced

Workshop on Sources of Polarized Electrons and High Brightness Electron Beams	
8:00-8:30	Continental breakfast and Registration
DC High Voltage Guns - Unpolarized (chair: B. Dunham)	
8:30-9:00 9:00-9:30 9:30-10:00	Status Jefferson Lab FEL High Voltage Guns (Carlos Hernandez-Garcia, JLab) Status Cornell High Voltage Gun (Karl Smolenski, Cornell Univ.) Status of the ALICE Energy-Recovery Linac (L. Jones, STFC Daresbury Laboratory)
10:00-10:15	Coffee Break
10:15-10:45 10:45-11:15	Photocathode Preparation System for the ALICE Photoinjector Gun, (K.J. Middleman, STFC Daresbury Laboratory) Development of an electron gun for an ERL based light source in Japan (Nobuyuki Nishimori, ERL Development Group, Japan Atomic Energy Agency
High Voltage	
11:15-11:45	KSI's Cross Insulated Core Transformer Technology (Uwe Uhmeyer, Kaiser Systems, Inc.)
11:45-13:30	Lunch Provided, CEBAF Center Room F113 Option1 – for interested participants: Lunch discussion concerning high voltage, insulators, field emission, etc. Option2 – tour of CEBAF injector and FEL Gun Test Stand. *Sign-up required.*
RF Guns (chair: K. Aulenbacher)	
13:30-14:00 14:00-14:30 14:30-15:00	Low Emittance Gun for XFEL Application (Christopher Gough, Paul Scherrer Institute) Ion Bombardment in RF Guns: Analytical Approach (E. Pozdeyev, BNL) High-Fidelity RF Gun Simulations with the Parallel 3D Finite Element Particle-In-Cell Code Pic3P (A. Candel, SLAC)
15:00-15:15	Coffee Break
15:15-15:45 15:45-16:15 16:15-16:45	Polarized Electron PWT Photoinjectors (David Yu, DULY) 15:45-16:15 The Superconducting RF Photoinjector at Elbe – First Operational Experience (J. Teichert, Forschungszentrum Dresden-Rossendorf, FZD) 16:15-16:45 The BNL Polarized SRF gun (J. Kewisch, BNL)
17:00-18:00	Poster Session at CEBAF Center Atrium
18:00-20:00	Conference Dinner at CEBAF Center Atrium
20:00-	Socialize at City Center, Location to be announced

Workshop on Sources of Polarized Electrons and High Brightness Electron Beams	
8:00-8:30	Continental breakfast
RF Guns (cont.)	
8:30-9:00 9:00-9:30	A Polarized SRF Gun for the ILC (D. Holmes, Advanced Energy Systems) Status of the 1.3 GHz Photoinjector for GaAs testing (A. Burrill, BNL)
Lasers (chair: M. Poelker)	
9:30-10:15	Status of the Cornell High Power Fiber-based Drive Laser (Dimitre Gueorguiev Ouzounov and Heng Li, Cornell Univ.)
10:15-10:30	Coffee Break
Vacuum	
10:30-11:00 11:00-11:30	Vacuum Considerations for GaAs Photoelectron Guns (C. Sinclair, Cornell Univ.) NEG Pump Technology (Paolo Manini, SAES Getters SpA)
11:30-13:30	Lunch Provided, CEBAF Center Room F113 **Option1** – for interested participants: Lunch discussion concerning photocathode issues **Option2** – tour of CEBAF injector and FEL Gun Test Stand. *Sign-up required.*
Other Applications of Polarized Electrons (chair: R. Suleiman)	
13:30-14:00	High brightness and high polarization PES for SPLEEM and/or High brightness PES with transmission photocathode (T. Nakanishi, Nagoya Univ.)
Parity Violation Experiments	
14:00-14:30	Sources of Helicity Correlated Beam Asymmetries (K. Paschke, UVa)
Polarimetry	
14:30-15:00 15:00-15:30	Ab initio calculation of effective Sherman function in MeV Mott scattering (K. Aulenbacher, MAMI) Compton Polarimeter at Bonn (W. Hillert, Univ. Bonn)
15:30-15:45	Coffee Break
Beam Modeling	
15:45-16:15 16:15-16:45	Benchmark studies among own and commercial beam tracking codes on fundamental conditions (Naoto Yamamoto, Nagoya Univ.) 3D Modeling of the ALICE Photoinjector Upgrade (J.W. McKenzie, STFC Daresbury Laboratory)
Closeout	

Posters (17 total)

- Ultrahigh Vacuum Ion Pump Power Supply with Sensitive Current Monitoring Capability (J. Hansknecht and P. Adderley, JLab)
- Fast and Inexpensive Pockels Cell Flipping (J. Hansknecht, JLab)
- Efficiency Measurements of the Nebraska Retarding Potential Mott Polarimeter (J. McCarter, JLab/UVa)
- Electron Spin Precession at CEBAF (Douglas Higinbotham, Marie-Isabelle Holdrinet, JLab)
- High Brightness Electron Source Using a Superlattice Photocathode with Long Life NEA-Surface (Tomohiro Nishitani, RIKEN)
- Photoemission Spectroscopic Study of Cesium Telluride Thin Film Photocathode (Harue Sugiyama, Synchrotron Light Application Center, Saga Univ., Japan)
- High Brightness and High Polarization Electron Source Using Transmission Photocathode (Naoto Yamamoto, Nagoya Univ.)
- New Transmission-Type Photocathode Structure Based on Strain-Compensated Superlattice (Xiuguang Jin, Nagoya Univ.)
- Cooled Transmission-Mode NEA- Photocathode with Band-Graded Active Layer for High – Brightness Electron Source (L. Jones, STFC Daresbury Laboratory, with A. Terekhov, Institute of Semiconductor Physics, Novosibirsk)
- Measurements of the Rossendorf SRF-Gun Cavity Characteristics (Andre Arnold, Forschungszentrum Dresden Rossendorf, FZD)
- Polarimetry and Planned Experiments at the Superconducting Darmstadt Electron Linac S-DALINAC (Christian Eckardt, Darmstadt Univ.)
- Hall C Compton Polarimeter with RF Pulsed Green Light (Gaskell/Chuyu, JLab)
- Surface Analysis of Damaged Superlattice Photocathode (M. Stutzman, JLab)
- Field Emission Measurements from Cathodes Electrodes Prepared Using Electro and Chemical Polishing (Ken Surles-Law, JLab)
- Polarized Positron Source at Jefferson Lab (J. Dumas, JLab)
- Benchmarking PARMELA against Beam-Based Measurements at the CEBAF Photoinjector (Ashwini Jayaprakash, K. Surles-Law, Y. Zhang, Old Dominion University and Jefferson Lab)
- Hall A Compton Polarimeter – DC Green Light and Optical Storage Cavity (Abdurahim Rakhman, JLab)

Adderley , Philip
Jefferson Lab
12050 Jefferson Avenue
Suite 500
Newport News, VA 23606
adderley@jlab.org

Arnold , Andre
Forschungszentrum Dresden
Rossendorf
Bautzner Landstraße 128
Dresden, Saxony 01314
Germany
a.arnold@fzd.de

Aulenbacher , Kurt
Institut für Kernphysik, Universität
Mainz
J.J. Becherweg 45
Mainz, RLP 55099
Federal Republik of Germany
aulenbac@kph.uni-mainz.de

Balling , Andreas
University of Bonn
Nussallee 12
Bonn, NRW 53115
Germany
balling@physik.uni-bonn.de

Bazarov , Ivan
Cornell University
373 Wilson Lab
Ithaca, NY 14853
ib38@cornell.edu

Benesch , Jay
Jefferson Lab
12000 Jefferson Avenue
Suite 19
Newport News, VA 23606
benesch@jlab.org

Benson , Stephen
Jefferson Lab
12000 Jefferson Avenue
Suite 19
Newport News, VA 23606
felman@jlab.org

Biallas, George
Jefferson Lab
12050 Jefferson Avenue
Suite 402
Newport News, VA 23606
biallas@jlab.org

Bullard, Don
Jefferson Lab
12000 Jefferson Avenue
Suite 17
Newport News, VA 23606
bullard@jlab.org

Burrill, Andrew
Brookhaven National Laboratory
MS 911A
Upton, NY 11973
aburrill@bnl.gov

Burrows, Ian
STFC Daresbury Laboratory
Keckwick Lane
Daresbury, Warrington WA4 4AD
United Kingdom
i.burrows@dl.ac.uk

Candel, Arno
SLAC National Accelerator Laboratory
2575 Sand Hill Road
Menlo Park, CA 94025
candel@slac.stanford.edu

Chanlek, Narong
STFC Daresbury Laboratory
Keckwick Lane
Daresbury, Warrington WA4 4AD
United Kingdom
n.chanlek@dl.ac.uk

Clendenin, James
SLAC National Accelerator Laboratory
2575 Sand Hill Rd.
Menlo Park, CA 94025
clen@slac.stanford.edu

Comer, Amy
Jefferson Lab
12000 Jefferson Avenue
Suite 19
Newport News, VA 23606
acomer@jlab.org

Dabiran, Amir
SVT Associates, Inc.
7620 Executive Drive
Eden Prarie, MN 55344
dabiran@svta.com

Dreiling, Joan
University of Nebraska
115 Ferguson Hall
Lincoln, NE 68588
jmdreiling2@gmail.com

Dumas, Jonathan
Jefferson Lab
12050 Jefferson Avenue
Suite 500
Newport News, VA 23606
dumas@jlab.org

Dunham, Bruce
Cornell University
373 Wilson Lab
Ithica, NY 14853
bmd29@cornell.edu

Eckardt, Christian
TU Darmstadt
Schlossgartenstrasse 9
Darmsradt 64289
Germany
eckardt@ikp.tu-darmstadt.de

Farkhondeh, Manouchehr
DOE Office of Nuclear Physics
SC-26.2, Germantown Building
Washington, DC 208585
manouchehr.farkhondeh@science.doe.gov

Gay, Timothy
University of Nebraska
116 Brace Lab
Lincoln, NE 68588
tgay1@unl.edu

Gerchikov, Leonid
St. Petersburg State Polytechnic University
Polytechnicheskaya 29
St. Petersburg 197373
Russia
lgerchikov@rambler.ru

Gough, Christopher
Paul Scherrer Institute
WSLA-015
Paul Scherrer Institut
Villigen AG 5232
Switzerland
christopher.gough@psi.ch

Grames, Joseph
Jefferson Lab
12050 Jefferson Avenue
Suite 500
Newport News, VA 23606
grames@jlab.org

Gulliford, Colwyn
Cornell University
610 Mitchell St
Ithaca, NY 14850
cg248@cornell.edu

Hernandez-Garcia, Carlos
Jefferson Lab
12000 Jefferson Avenue
Suite 19
Newport News, VA 23606
chgarcia@jlab.org

Hannon, Fay
Jefferson Lab
12000 Jefferson Ave.
Newport News, VA 23606
fhannon@jlab.org

Hansknecht, John
Jefferson Lab
12050 Jefferson Avenue
Suite 500
Newport News, VA 23606
hansknec@jlab.org

Higinbotham, Douglas
Jefferson Lab
12000 Jefferson Avenue
Suite 4
Newport News, VA 23606
doug@jlab.org

Hillert, Wolfgang
University of Bonn
Physics Institute
Nussallee 12
Bonn, NRW 53115
Germany
hillert@physik.uni-bonn.de

Hofler, Alicia
Jefferson Lab
12050 Jefferson Avenue
Suite 704
Newport News, VA 23606
hofler@jlab.org

Holmes, Douglas
Advanced Energy Systems
27 Industrial Blvd
Unit E
Medford, NY 11763
doug_holmes@mail.aesys.net

Jayaprakash, Ashwini
Old Dominion University
12000 Jefferson Avenue
Newport News, VA 23606
ashwini@jlab.org

Jones, Lee
STFC Daresbury Laboratory
The Cockcroft Institute, CCS 07
Keckwick Lane, Daresbury
Warrington, Cheshire WA4 4AD
United Kingdom
l.b.jones@dl.ac.uk

Kewisch, Jorg
Brookhaven National Lab
Building 911
Upton, NY 11973
jorg@bnl.gov

Klopf, Michael
Jefferson Lab
12000 Jefferson Avenue
Suite 19
Newport News, VA 23606
klopf@jlab.org

Li, Heng
Cornell University
214 Wilson Lab
Ithica, NY 14853
hl344@cornell.edu

Manini, Paolo
Saes Getters Spa
Viale Italia 77
Lainate 20020
Italy
paolo_manini@saes-group.com

McCarter, James
Jefferson Lab
12000 Jefferson Ave.
Newport News, VA 23606
mccarter@jlab.org

McKenzie, Julian
STFC Daresbury Laboratory
Keckwick Lane
Warrington, Cheshire WA4 4AD
United Kingdom
j.w.mckenzie@dl.ac.uk

Middleman, Keith
STFC Daresbury Laboratory
Keckwick Lane
Warrington, Cheshire WA4 4AD
United Kingdom
k.j.middleman@dl.ac.uk

Moy, Aaron
SVT Associates
7620 Executive Drive
Eden Prairie, MN 55344
moy@svta.com

Mulhollan, Gregory
Saxet Surface Science
3913 Todd Lane
Suite 303
Austin, TX 78744
mulhollan@saxetsurfacescience.com

Murcek, Petr
Forschungszentrum Dresden-Rossendorf
P.O. Box 510119
Dresden 01314
Germany
p.murcek@fzd.de

Nakanishi, Tsutomu
Nagoya University
Department of Physics, Graduate School of Science
Nagoya, Aichi 464-8602
Japan
nakanisi@spin.phys.nagoya-u.ac.jp

Neil, George
Jefferson Lab
12000 Jefferson Ave.
Newport News, VA 23606
neil@jlab.org

Nishimori, Nobuyuki
JAEA
2-4 Shirakata Shirane, Tokai-mura, Naka
Ibaraki 319-1195
Japan
nishimori.nobuyuki@jaea.go.jp

Nishitani, Tomohiro
RIKEN
Hirosawa 2-14
Wako, Saitama 351-0198
JAPAN
tnishitani@riken.jp

Orlov, Dmitry
MPI-K
Saupfercheckweg 1
69117 Heidelberg
Germany
orlov@mpi-hd.mpg.de

Ouzounov, Dimitre
LEPP, Cornell University
226A Wilson Lab
Ithaca, NY 14853
dgo4@cornell.edu

Paff, John
Spectra-Mat, Inc
100 Westgate Dr
Watsonville, CA 95076
john_paff@saes-group.com

Paschke, Kent
University of Virginia
Department of Physics
PO Box 400714
Charlottesville, VA 22904
paschke@virginia.edu

Poelker, Matt
12050 Jefferson Avenue
Suite 500
Newport News, VA 23606
poelker@jlab.org

Poltoratska, Yuliya
Darmstadt University of Technology
Institute for Nuclear Physics
Schlossgartenstrasse 9
64289 Darmstadt
Germany
yuliya@ikp.tu-darmstadt.de

Pozdeyev, Eduard
Brookhaven National Lab
Bldg. 911
Upton, NY 11973
pozdeyev@bnl.gov

Rao, Triveni
Brookhaven National Lab
Bldg. 911
Upton, NY 11973
triveni@bnl.gov

Silwal, Rupesh
University of Virginia
Department of Physics
PO Box 400714
Charlottesville, VA 22904
rs3te@virginia.edu

Sinclair, Charles
Cornell University (retired)
230 Wilson Lab
Ithaca, NY 14853
cks26@cornell.edu

Smedley, John
Brookhaven National Laboratory
Bldg. 911
Upton, NY 11973
smedley@bnl.gov

Smolenski, Karl
Cornell University
230 Wilson Lab
Ithaca, NY 14853
karl.smolenski@cornell.edu

Stoltz, Peter
Tech-X Corporation
5621 Arapahoe Ave
Boulder, CO 80303
pstoltz@txcorp.com

Stutzman, Marcy
Jefferson Lab
12050 Jefferson Avenue
Suite 500
Newport News, VA 23606
marcy@jlab.org

Sugiyama, Harue
Saga University
1 Honjo
Saga 840-8502
Japan
harues@hep.phys.saga-u.ac.jp

Suleiman, Riad
Jefferson Lab
12050 Jefferson Avenue
Suite 500
Newport News, VA 23606
suleiman@jlab.org

Surles-Law, Ken
Jefferson Lab
12050 Jefferson Avenue
Suite 500
Newport News, VA 23606
law@jlab.org

Teichert, Jochen
Forschungszentrum Dresden-Rossendorf
P.O. Box 510119
Dresden 01314
Germany
j.teichert@fzd.de

Tennant, Chris
Jefferson Lab
12000 Jefferson Avenue
Suite 19
Newport News, VA 23606
tennant@jlab.org

Terekhov, Alexander
Institute of Semiconductor Physics,
Russian Academy of Sciences,
Siberian Branch
Lavrentev ave., 13,
Novosibirsk 630090
Russian Federation
terek@thermo.isp.nsc.ru

Trantham, Kenneth
Fort Hays State University
600 Park Street
Physics Department
Hays, KS 67601
ktrantha@fhsu.edu

Tsentalovich, Evgeni
MIT-Bates
21 Manning Rd
Middleton, MA 01949
evgeni@mit.eduj

Tyukin, Valery
Inst. of Nuclear Physics
J.-J. Becherweg 45
Mainz 55099
Germany
tioukine@kph.uni-mainz.de

Uhmeyer, Uwe
Kaiser Systems, Inc
126 Sohier Road
Beverly, MA 01915
uuhmeyer@kaisersystems.com

Ujihara, Toru
Nagoya University
Furo-cho, Chikusaku
Nagoya, Aichi 4648603
Japan
ujihara@numse.nagoya-u.ac.jp

Voutier, Eric
LPSC/IN2P3/CNRS
Laboratoire de Physique Subatomique
et de Cosmologie
53 rue des Martyrs
Grenoble 38026
France
voutier@lpsc.in2p3.fr

Walker, Richard
Jefferson Lab
12000 Jeffereson Avenue
Suite 19
Newport News, VA 23606
richard@jlab.org

Williams, Gwyn
Jefferson Lab
12000 Jefferson Ave.
Newport News, VA 23606
gwyn@jlab.org

Xiuguang, Jin
Nagoya University
Furo-cho Chikusa-ku
Nagoya 464-8603
Japan
kim@mercury.numse.nagoya-u.ac.jp

Yamamoto, Masahiro
Nagoya University
Furo-cho Chikusa-ku
Nagoya 464-8603
Japan
yamamoto@spin.phys.nagoya-u.ac.jp

Yamamoto, Naoto
Nagoya University
Furo-cho Chikusa-ku
Nagoya 464-8603
Japan
naoto@nagoya-u.jp

Yu, David
DULY Research Inc.
1912 MacArthur Street
Rancho Palos Verdes, CA 90275
davidyu@pacbell.net

Zhang, Shukui
Jefferson Lab
12000 Jefferson Avenue
Suite 19
Newport News, VA 23606
shukui@jlab.org

Zhang, Yuhong
Jefferson Lab
12050 Jefferson Avenue
Suite 704
Newport News, VA 23606
yzhang@jlab.org

Zhou, Feng
SLAC National Accelerator Laboratory
2575 Sand Hill road
Menlo Park, CA 94025
zhoufeng@slac.stanford.edu